MICROSTRUCTURAL CHARACTERIZATION AND SHAPE MEMORY RESPONSE OF Ni-RICH NiTiHf AND NiTiZr HIGH TEMPERATURE SHAPE MEMORY ALLOYS

A Dissertation

by

ALPER EVIRGEN

Submitted to the Office of Graduate and Professional Studies of
Texas A&M University
in partial fulfillment of the requirements for the degree of

DOCTOR OF PHILOSOPHY

Chair of Committee,	Ibrahim Karaman
Committee Members,	Dimitris C. Lagoudas
	K. Ted Hartwig
	Ronald D. Noebe
	Xinghang Zhang
Head of Department,	Ibrahim Karaman

August 2014

Major Subject: Materials Science and Engineering

ABSTRACT

NiTiHf and NiTiZr high temperature shape memory alloys (HTSMAs) have drawn a great deal of attention as cheaper alternatives to Pt, Pd and Au alloyed NiTi-based HTSMAs while NiTiZr alloys also providing at least 20% weight reduction then its NiTiHf counterparts with the same stoichiometry. (Ti + Hf/Zr)-rich compositions were already reported to have high thermal hysteresis, poor dimensional and thermal stability due to their low matrix strength hampering their practical applications. However, Ni-rich compositions of NiTiHf alloys were shown to have very promising shape memory responses recently due to generation of fine Ni-rich particles after proper heat treatments not only strengthening the matrix but also leading to relatively high transformation temperatures. Comparable studies have not been performed on Ni-rich NiTiZr compositions. Furthermore, very few published work are present on these new Ni-rich NiTiHf and NiTiZr systems. Hence many critical characteristics still remains unknown and further investigation is necessary to reveal the effect of precipitation on the microstructures and its subsequent effect on the transformation characteristics and shape memory responses.

The present study focuses on the extensive microstructural and thermo-mechanical property characterizations of the Ni-rich NiTiHf and NiTiZr HTSMAs in order to develop the fundamental knowledge necessary for the optimization and development of reliable, cheap, lightweight HTSMAs operating up to 300 °C with improved thermal and dimensional stability. Several different compositions of Ni-rich

NiTiHf and NiTiZr HTSMAs are systematically precipitation heat treated for the microstructural control and then subjected to multi-scale microstructural and thermo-mechanical characterizations to achieve this goal. Differential scanning calorimetry measurements are conducted on the aged samples to reveal the transformation characteristics and furthermore generate the time-temperature-transformation temperature (TTT) diagrams of the individual alloy systems. The shape memory response and characteristics of the alloys are investigated through load-biased thermal cycling and superelasticity tests. The microstructures of the aged samples are extensively characterized using transmission electron microscopy (TEM) to build up microstructure-property relationships as well as providing deeper understanding of precipitate crystal structure, composition and morphology.

Such an experimental approach is crucial for the development of new ternary alloy compositions and for the careful control of the microstructure to obtain desired properties. The outcomes of the present study is expected to help to reveal the potential of these alloys to be utilized in a wide range of applications at elevated temperatures in aerospace, automotive and oil-gas industries.

To my family: my mother Zeynep Evirgen, my father Baki Evirgen and my brother Caner Evirgen for their never ending support and trust

ACKNOWLEDGEMENTS

It has been four tough years since I began my PhD studies in College Station. For four tough years I followed my career objective, the same one I've had ever since my undergraduate career. Despite all of the grueling work, these four years have been intellectually illuminating due to my scientific research and discoveries. These endeavors would not have been successful without the wonderful people I have met, YOU.

Prof. Ibrahim Karaman, I am not only grateful that I had the opportunity to have you as my advisor but more importantly I have developed a deep respect for you as a person. I would like to thank you for all your trust and the unconditional support you gave me during my PhD studies. I am very lucky to have had the chance to work under your supervision. In addition, Prof. Dimitris C. Lagoudas, Prof. K. Ted Hartwig and Prof. Xinghang Zhang, I would like to express my gratitude to you for serving on my committee and giving me advice on my studies and scientific work.

Dr. Ronal D. Noebe from NASA Glenn Research Center, Structural Materials Division, without your help this study would not have been successful and complete. I am especially thankful to you for all your guidance and valuable comments on our joint publications along with my dissertation and also serving as a member on my committee.

Prof. Jaume Pons and Dr. Ruben Santamarta, there was no other way that this study would have had successfull microscopy investigations without your help, your experience and your deep insights provided the framework for numerous scientific

discoveries. I am very glad to have met you and I am very thankful that I had the chance to work in your group at “La Isla Bonita” Mallorca, Spain. Furthermore, I would also like to thank you for all your suggestions and contributions on our joint publications.

Dr. Aaron Stebner from Colorado School of Mines, I would like to thank you for letting me use your MATLAB code in order to calculate the maximum strains of the alloys in the present study. I am also thankful to Dr. Raymundo Arroyave and Anjana Talapatra from Texas A&M University for carrying out DFT calculations to calculate elastic constants of the alloys in the present study.

Finally, the people of “MESAM Research Group”, I spent quite a significant time, not only of my PhD years but also of my life in room 102 of Doherty building. It was neither the laboratory nor the devices that made my stay here memorable and tolerable but it was the people. James A. Monroe, Nevin Ozdemir, Sonia M. Razavi, Ruixian Zhu, Nick Bruno, Nick Barta, Li Wei Tseng, Ankush Kothalkar, Liangfa Hu, Hande Ozcan, Taymaz Jo and Omer Karakoc, thank you all for being there when I needed help and for the birthdays and fun we had in laboratory. Ji Ma, thank you for your patience during my training and also your indepth explanations on my never ending questions. Brian Franco, dude, thanks for your help on fixing almost everything that no one else is capable of to do so and also frequent discussions on the “precipitate story” in shape memory alloys. Special thanks go out to Brian for the shooting trip and watching “Game of Thrones” on a huge wall projector. Pinar Karpuz, Ceylan Hayrettin and Ebubekir Dogan, guys we talked about politics, life, and almost everything whenever we

wanted a break. Thank you for all your support and help on my studies and also for the coffee and tea sessions. I wish you all the best with the rest of your careers.

Samet Mutlu, Mehtap Deniz Unlu, Tumer Yildirim and Ugur Cem Ozder, you guys are more like brothers and sisters to me. We have been far apart for years, even living in different continents, however you have always been beside me. Thank you for making me feel at home with your never ending support and belief in my endeavors.

And the beautiful people I met in College Station, Eda Aydogan, Gokhan Gungor, Nese and Emrah Yilmaz, Sema and Volkan Firat, Duygu and Ceylan Hayrettin, Kivanc and Meltem Ustun, Sema Asik, Tugba Oner, Sevil Sarikurt, Murat Cobanoglu, Tuba Aydin, Zeynep Dincer, Gokhan Ileri, Andreas Larsson, Amanda Cain, Aishwarya Sooresh, Youxing Chen, Miao Song and Shamik Basu, thank you for all the good time and the friendship in College Station. I hope to see you somewhere in future. Mehmet Tatli, the good guy of Antakya and my roommate, thanks for everything and being a brother to me.

I would like to thank the students I mentored during their studies, Fabian Basner, Paul Joan and Flavien Hatton, thank you for carrying out experiments and your contribution in several parts of the present work.

In addition, I would like to thank the people that made my stay in Spain and the Netherlands memorable, Esteban, Anca, Marysia, Karol, Sebastian, David, Corrado, Mario, Vincent, Sarah, Eleonora, Neera, Jennifer, Aquilina, Maude, Lucie and Anjana; a big thank you.

And finally I would like to thank my family, Baki Evirgen, Zeynep Evirgen and Caner Evirgen who deserve my biggest gratitude for their infinite support, help and advice during all my life making me the person that I am now.

NOMENCLATURE

A_f	Austenite finish
A_s	Austenite start
ATAT	Alloy theoretic automated toolkit
BSE	Back-scattered electron
CC	Clasius-Clapeyron
CSS	Critical shear stress
CVP	Corresponding variant pair
DFT	Density functional theory
DSC	Differential scanning calorimetry
EDM	Electrical discharge machining
EDS	Energy-dispersive spectroscopy
EDX	Energy-dispersive X-ray
EM	Electron microprobe
ε_{irr}	Irrecoverable strain
ε_{rec}	Recovered transformation strain
ε_{total}	Total strain
FC	Furnace cooling
FFT	Fast fourier transform
HRTEM	High resolution transmission electron microscopy
HTSMA	High temperature shape memory alloy

HV	Vickers hardness
ICP-AES	Inductively coupled plasma – atomic emission spectrometry
LIS	Lattice invariant shear
M_f	Martensite finish
M_p	Martensite peak
M_s	Martensite start
MT	Martensitic transformation
SADP	Selected area diffraction pattern
SE	Superelasticity
SEM	Scanning electron microscopy
SHT	Solution heat treated
SIMT	Stress induced martensitic transformation
SMA	Shape memory alloy
SME	Shape memory effect
σ_{SIM}	Critical stress to induce martensite
TEM	Transmission electron microscopy
TRIP	Transformation induced plasticity
TTT	Time-temperature-transformation temperature
XRD	X-ray diffraction
WDS	Wavelength-dispersive spectroscopy
WQ	Water quenched

TABLE OF CONTENTS

Page

LIST OF FIGURES

Page

LIST OF TABLES

Page

CHAPTER I

INTRODUCTION

This chapter focuses on the significance for the development of dimensionally and thermally stable new generation Ni-rich NiTi(Hf,Zr) high-temperature shape memory alloys (HTSMAs) as alternatives to expensive NiTi-based HTSMAs. The limitations of current NiTi-based HTSMAs are discussed briefly and the advantages of using Ni-rich compositions to overcome these limitations were summarized. In the final part, the main goals of the present work are given together with the experimental approach to achieve these objectives.

1.1 Motivation

Shape memory alloys (SMA) are a unique group of functional materials since they can recover their initial undeformed shape and show superelasticity (SE) and shape memory effect (SME) as a consequence of their diffusionless, solid-to-solid martensitic transformation (MT) from a high temperature, high symmetry austenite phase to a lower temperature, low symmetry martensite phase and its reverse transformation. Starting with the discovery of SME on Au-Cd [1] and In-Ti [2,3] in 1950's and later on equatomic NiTi in 1960's [4], NiTi based SMAs have been the most widely studied and well known SMAs due to their superior functional, mechanical properties, good ductility and excellent corrosion resistance [5]. These distinctive properties of NiTi SMAs lead to a wide range of applications such as couplings, valves, orthodontic wires, switches and

applications especially in biomedical industry where SE effect is utilized. Moreover, NiTi based SMAs can generate higher or competitive work output than many conventional hydraulic, pneumatic or electromagnetic actuators since they show recoverable shape changes of several percent of strain when subjected to high loads (stress levels up to 800 MPa) [6,7]. Therefore, they can be alternative materials to the conventional actuators in aerospace and automotive applications. However, the commercially available NiTi SMA materials are not suitable to use at elevated temperatures since they generally undergo phase transformations at around or below 100 ^{o}C.

Recent challenges in automotive, aerospace, transportation and energy exploration industries require enhanced operating efficiency of mechanical components at elevated temperatures as high temperature solid state actuators or superelastic components where NiTi binary SMAs are not suitable for use. Therefore, SMA systems showing transformation temperatures above 100 ^{o}C, namely high temperature shape memory alloy (HTSMA) systems, have drawn a great deal of attention recently since they may replace multi-component assemblies through providing single-piece, adaptive, lightweight and multifunctional components that can safely be employed at high temperatures. Up to present time, a variety of HTSMA systems like ordered Ni-Al [8-10], Ni-Mn [11-13] and Cu based alloys [14-18] and disordered β-Ti HTSMAs [19-24] have been developed for high temperature applications. However, all these systems have numerous disadvantages hampering their practical applications. Cubic to terragonal type martensitic transformation seen in Ni-Al and Ni-Mn based alloys leads to intergranular

failure and brittleness. Cu-based and Ni-Al based alloys suffer from chemical and thermal instability as well as poor dimensional stability. β-Ti alloys undergo remarkable plastic deformation along with martensitic transformation resulting in poor reversibility and large hysteresis. Moreover, β-Ti alloys show relatively low transformation strain levels due to incomplete transformation. Beside all these drawbacks, all these alloys are also highly sensitive to oxidation and have tendency to easily form carbides.

Despite these alloys, several NiTiX alloy systems (where X can be Au, Pd, Pt, Hf, Zr) have also been developed to increase the transformation temperatures of binary NiTi [25] above 100 ^{o}C and characterized to explore possible applications in the aforementioned fields. Among the others, NiTiPd and NiTiPt HTSMAs were extensively studied in the last decade as candidate materials to use as solid-state actuators for the aerospace, automotive and power generation industries. Although, NiTiPd and NiTiPt SMAs exhibit very small thermal hysteresis and high transformation temperatures, transformation-induced plasticity (TRIP) and creep facilitated at high operating temperatures manifest themselves as instable SME and lack of superelasticity in these alloys systems [25,26]. Nowadays, the current state of art on the HTSMAs has moved to the design, processing and characterization of cheaper alternatives such as NiTiHf and NiTiZr HTSMAs compared to NiTi(Au,Pt,Pd) HTSMAs [25] since there is an increasing need for relatively inexpensive, lightweight and high performance materials. The mechanical and shape memory properties as well as transformation characteristics of NiTiZr and NiTiHf systems are reported to be very similar. Moreover, NiTiZr alloys

also provide at least 20% weight reduction compared to its NiTiHf counterparts with the same composition.

Eckelmeyer [27] is the first researcher reported that the transformation temperatures of equatomic or Ti-rich binary NiTi SMAs can be increased through replacing Ti with Zr. It was shown that Zr additions above 10 at.% increase martensite start (M_s) temperature with a rate of 18 ^oC/at.% in NiTiZr alloys [28]. Other than these studies, Hsieh and his coworkers studied the martensitic transformation behavior, lattice parameters of martensite and the room temperature phases of (Ti+Zr)-rich NiTiZr alloys where Ni content is less than 50 at.% [29-31]. Furthermore, Firstov et al. investigated the high temperature shape memory behavior of (Ti+Zr)-rich NiTiZr alloys under compressive force [32]. Although, these (Ti+Zr)-rich NiTiZr alloys exhibit high transformation temperatures, they suffered from large thermal hysteresis and poor dimensional and thermal stability preventing their commercial use.

In the case of NiTiHf alloys, the increase in M_s is more prominent when Ti is replaced with Hf compared to NiTiZr alloys [33,34]. The increase is only around 5 ^oC/at.% up to 5-10 at.% Hf addition but reaches over 20 ^oC/at.% for further Hf addition. The majority of the past studies on the NiTiHf HTSMAs were carried out on the (Ti+Hf)-rich compositions (Ni ccontent less than 50 at.%) since they show high transformation temperatures [35-41]. However, numerous disadvantages such as low recoverable and transformation strains, poor thermal and dimensional stability, large hysteresis, poor shape memory response, brittleness and poor workability were also reported on these systems. Furthermore, these alloys were shown to have no superelastic

behavior and their thermal cycling response degreases with further cycling. All these disadvantages of (Ti+Hf)-rich NiTiHf alloys limit their potential and prevented their commercial use.

In both (Ti+Zr)-rich and (Ti+,Hf)-rich NiTiZr and NiTiHf HTSMAs, the large thermal hysteresis (80-100 ^{o}C vs. 10-40 ^{o}C in NiTi(Au,Pt,Pd)) is generally a consequence of the poor structural compatibility between the austenite and martensite phases and also their low matrix strength for defect generation [25]. The low resistance against slip also degrades the functional and dimensional stability of these alloys. Several methods were proposed to overcome the disadvantages of Ti-rich NiTi-based SMAs and improve the SME through strengthening the matrix: (1) work hardening (e.g. cold rolling), (2) quaternary alloying, (3) precipitation hardening and (4) thermal cycling [42]. However, in the case of (Ti+Zr)-rich NiTiZr SMAs, neither thermal cycling nor cold rolling were proven to improve the shape memory response. Microhardness values increased with thermal cycling and cold rolling but martensite start (M_s) temperatures decreased significantly. Furthermore, microstructural control and stability is a big concern in the (Ti + Zr)-rich NiTiZr alloys since large (Ti,Zr)Ni, $(Ti,Zr)_2Ni$ and λ_1 (a NiTiZr ternary solid solution) precipitates were observed which are not favorable to strengthen the matrix or improve the shape memory properties.

Work hardening is also not a feasible method to improve the shape memory response of (Ti+Hf)-rich NiTiHf alloys because they suffer from brittleness at room temperature. Several quaternary elements were also added to (Ti + Hf)-rich NiTiH alloys to improve the shape memory response and overcome the aforementioned limitations.

NiTiHfCu alloys were studied previously, since Cu alloying in binary NiTi SMAs was shown to improve thermal stability, ductility and hysteresis. However, instead of the good two-way shape memory effect of NiTiHfCu SMA, no favorable improvement was obtained over the shape memory response of the NiTiHf SMAs [43]. Furthermore, the shape recovery ratio and the cold workability of the NiTiHf alloys were improved through Nb quaternary alloying but transformation temperatures and transformation strain levels were decreased [44]. Beside these two methods, it was also shown that large Ti-rich Ti_2Ni-type particles were formed during the heat treatment of (Ti + Hf)-rich compositions which do not strengthen the alloy or improve the SME [35].

However, during aging treatment of Ni-rich NiTi SMAs (Ni content higher than 50 at.%), nanosize metastable Ni_4Ti_3 particles form which has a strong effect on the transformation temperatures as well as on shape memory characteristics, thermal and stress hysteresis and mechanical properties [45-49]. Compared to the equatomic or Ti-rich binary NiTi alloys, M_s is drastically reduced when the Ni content is higher than 50 at.%. [50]. Moreover, compared to the solution heat treated (SHT) conditions where there are no precipitates in the matrix, M_s temperatures decrease with the precipitation of a large density of nano-size and coherent Ni-rich Ni_4Ti_3 particles whereas M_s increases when the volume fraction of the precipitates increases and hence the Ni-content of the matrix diminishes. As a consequence, precipitation of these nanoparticles creates great flexibility to modify transformation temperatures via conducting simple aging treatments for microstructural control. Furthermore, these fine Ni-rich precipitates block the dislocation movement and result in an increase in the critical shear stress (CSS)

necessary for slip which will lead to excellent shape memory recovery and near-perfect dimensional stability.

To the author's best knowledge, Sandu and his co-workers are the first and only researches reported on the effect of aging on the microstructure, martensitic transformation temperature and mechanical behavior of a Ni-rich $Ni_{52}Ti_{42}Zr_6$ (at.%) SMA [51,52]. The TEM and EDX studies indicated that fine nanosize Ni-rich particles were present in the microstructure that are different than Ni_4Ti_3 type precipitates but with an unknown crystal structure after proper heat treatments. The authors showed that these nano particles increased the hardness of the alloy. Although, increase in aging time was shown to increase the transformation temperatures, they were still below 100 ^oC since the Zr addition was just 6 at.%. Furthermore, the load-biased shape memory response of the alloy was not reported. Beside the studies of Sandu on Ni-rich NiTiZr HTSMAs with low Zr content, the effect of precipitation on the shape memory characteristics and the microstructure of Ni-rich NiTiZr HTSMAs with higher Zr contents have not been reported to date.

Several past studies showed that precipitation hardening in Ni-rich NiTiHf SMAs through formation of Ni-rich nanosize particles after proper aging treatments is also an effective method to improve the shape memory response similar to the Ni-rich NiTi. The aging, transformation behavior, and shape memory response of Ni-rich NiTiHf alloys were studied by Meng and his co-workers [53-55]. Coherent Ni-rich nanosize particles forming after aging heat treatments improved the thermal stability and the shape recovery remarkably. More recently, a Ni-rich NiTiHf alloy has been shown to exhibit

high strength, outstanding microstructural and dimensional stability without any need of training when 10-20 nm Ni-rich particles are present while exhibiting relatively high transformation temperatures [56-58]. Furthermore, it was also shown that precipitation hardened Ni-rich alloys show good superelasticity while unaged alloys show no superelasticity because of their low matrix strengths [59].

As explained above, Ni-rich NiTiZr and NiTiHf HTSMAs could be cheaper and lighter alternatives for high temperature applications as compared to NiTi(Au, Pt, Pd) HTSMAs. They show very promising shape memory characteristics while aging results in great flexibility to modify transformation temperatures. However very few published work are present on these new alloys. Therefore, many critical characteristics such as transformation characteristics, shape memory response or microstructural characteristics are mainly unknown. Moreover, considering the previous studies on Ni-rich NiTiZr and NiTiHf alloys, no detailed investigation have been carried out to understand the effect of aging conditions on precipitate size and volume fraction and their subsequent impact on transformation characteristics such as transformation temperatures, thermal hysteresis and shape memory response. Additionally, the previous studies are far behind to generate a time-temperature-transformation temperature (TTT) diagram of the Ni-rich NiTiZr and NiTiHf alloys including the effect of precipitate size and volume fraction. Furthermore, since these alloys have nano-size precipitates which are different than the Ni_4Ti_3 precipitates, the crystal structure, composition or lattice parameters of the precipitates also are also not known.

In order to expand the pool of the knowledge on these new generation Ni-rich NiTiZr and NiTiHf HTSMAs, one should perform systematical experimental characterizations and extensive microstructural investigations to understand the influence of nanoprecipitates on the critical properties of these alloys such as thermo-mechanical response, transformation and unrecovered strain levels, transformation temperatures and dimensional and thermal stabilities. Knowing the effect of nanosize Ni_4Ti_3 precipitates on the shape memory response and transformation characteristics in binary NiTi SMAs, such an experimental approach will also lead to the development of new ternary alloy compositions and the careful control of the microstructure to obtain desired properties. Once the capabilities of these new generation HTSMAs are revealed, they will have the potential to be utilized in a wide range applications at elevated temperatures in aerospace, automotive and oil-gas industries.

1.2 Objectives

In quest of this motivation, the main goal of the present work is to combine material fabrication and extensive microstructural and thermo-mechanical characterization techniques to develop a fundamental knowledge necessary for the development and optimization of new generation Ni-rich NiTiZr and NiTiHf HTMSAs which can operate up to 300 ^{o}C with improved thermal and dimensional stability. This will be achieved through multi-scale microstructural and thermo-mechanical characterizations of several Ni-rich compositions of the alloys in which the microstructural control will be through precipitation heat treatments. The majority of the

proposed alloy compositions will be studied for the first time to the author's knowledge. The optimum microstructural features for the best dimensional and thermal stability, providing high transformation temperatures as well as good superelasticity and mechanical response will be analyzed and discussed.

The first aim of the present work is to study the size, morphology, composition, coherency and crystal structures of the precipitates along with their effect on martensite morphology and twinning relationships in these new Ni-rich NiTiZr and NiTiHf HTSMAs. Since only a little information is present on the precipitates of these Ni-rich systems, extensive transmission electron microscopy (TEM) and high resolution electron microscopy (HRTEM) studies are performed to achieve this goal.

The second goal is to study the effect of precipitation on the transformation characteristics such as transformation temperatures, thermal hysteresis and thermal stability and also the shape memory characteristics of these Ni-rich NiTiZr and NiTiHf HTSMAs. For this purpose, the experimental results were correlated with the microstructures investigated via TEM/HRTEM studies. The optimum microstructural features for the best dimensional and thermal stability, providing high transformation temperatures as well as good superelasticity are analysed and discussed.

And finally, the transformation characteristics and shape memory responses observed in the present study as a function of microstructure are compared to $Ni_{50.3}Ti_{29.7}Hf_{20}$ HTSMA. The $Ni_{50.3}Ti_{29.7}Hf_{20}$ was already shown to have very promising shape memory effect while exhibiting relatively high transformation temperatures.

More explicitly, the objectives of this study can be summarized as following:

1. Systematic precipitation heat treatments of several Ni-rich NiTiZr and NiTiHf HTSMA alloys followed by extensive TEM and HRTEM studies in order to study the size, morphology, composition, coherency and the crystal structures of the precipitates as a function of aging temperature and time. The composition of precipitates is determined using energy-dispersive x-ray (EDX) method during TEM investigations. The subsequent effect of precipitation on the martensite morphology and twinning relationships are also evaluated.

2. Microstructural characterization and investigation of transformation characteristics as well as shape memory response in Ni-rich $Ni_{50.3}Ti_{34.7}Zr_{15}$ and $Ni_{50.3}Ti_{34.7}Hf_{15}$ alloys through differential scanning calorimetry (DSC), TEM/HRTEM and load-biased isobaric thermal cycling tests. Studying the effect of precipitation on microstructure and hence on transformation characteristics such as transformation temperatures, thermal hysteresis and thermal stability and shape memory responses such as transformation and irrecoverable strains and stress dependency of transformation temperatures and thermal hysteresis. Using the DSC data, TTT diagrams for these alloys are also generated.

3. Studying the evolution of shape memory response and transformation characteristics in $Ni_{50.3}Ti_{29.7}Zr_{20}$ HTSMA with higher ternary element addition (20 at.%) through the combination of extensive experimentation and microstructural characterization studies. Develop a fundamental understanding on the effect of precipitation on many properties such as:

   a. Transformation temperatures, thermal hysteresis and thermal stability studied via DSC

b. Transformation and irrecoverable strains as well as the stress dependency of transformation temperatures and transformation hysteresis studied via isobaric thermal cycling tests and isothermal superelasticity tests

c. Lattice parameters and elastic constants of the transforming phases determined using X-ray diffraction (XRD)

d. Maximum theoretical strain levels in single crystal orientations using the lattice parameters

In addition, the correlation between all the experimental results or observations and the microstructural features like precipitate size and martensite morphology are built up and discussed. TTT diagrams for the $Ni_{50.3}Ti_{29.7}Zr_{20}$ is also generated using the DSC data.

4. Investigation of the differences and the similarities in the microstructural properties and shape memory responses of $Ni_{50.3}Ti_{29.7}Zr_{20}$ and its Hf counterpart $Ni_{50.3}Ti_{29.7}Hf_{20}$ HTSMAs. $Ni_{50.3}Ti_{29.7}Hf_{20}$ is chosen as a base model since it shows very promising shape memory properties. The two alloys are compared on the basis of points given in third objective. The mechanisms resulting in distinct shape memory behaviors are evaluated and discussed.

It is aimed that this study will bring in more insight on many properties of these new HTSMA systems critical for their potential applications in aerospace, automotive and energy industries. Furthermore, the results of the present study may also be inputs for microstructurally-informed micro-thermal mechanical models to map the macroscopic behavior of NiTiX HTSMAs.

CHAPTER II

BACKGROUND

This chapter provides a brief introduction to the shape memory effect and superelasticity for the reader to better understand the experimental investigations in the present work. It also summarizes the previous literature studies performed on the NiTiHf and NiTiZr alloys. Finally, the current state of art on the Ni-rich NiTiHf and NiTiZr alloy compositions are discussed and summarized.

2.1 Martensitic Transformations

2.1.1 Shape Memory Effect and Superelasticity

Shape memory effect is the ability of a deformed SMA at low temperature to recover its original shape after being heated. Superelasticity takes place at constant temperatures where a material can recover large amounts of strains induced by mechanical stress upon unloading of the material. Both behaviors are a consequence of solid-to-solid and diffusionless reversible martensitic transformation (MT) which can be activated by temperature, stress or magnetic field.

MT is a reversible solid state phase transformation from a high temperature austenite phase to a low temperature martensite phase upon cooling of the material. During transformation, the atoms in the unit cell undergo a shear movement for a very short distance while the atoms maintain their close neighbor relationships. Since the

crystal structure of the austenite is different than the martensite, a macroscopic shape change is obtained along with the transformation.

The local strains arising from the formation of martensite in austenite due to the difference in the crystal structures are large enough that they cannot be accommodated elastically. In an SMA system, this strain is accommodated through formation of twins in martensite. Under stress free conditions, a self accommodated martensite structure consisting of a number of martensite lattice correspondence variants forms. Generally the austenite phase is the high symmetry phase while the martensite phase is the low symmetry phase and the number of the martensite variants depends on the crystallographic nature of the transformation. For instance, there are 12 lattice correspondence variants that may be formed during B19' (monoclinic) martensite to B2 (BCC) austenite phase transformation [60]. All these variants have a different orientation relationship with the austenite phase and they are all energetically equivalent to each other under stress free conditions. Therefore, a large portion of the strain occurring due to the crystal structure change could be accommodated through formation of a self accommodated martensite structure having twin related lattice correspondence variants. This twin related variants generally follow a habit plane variant during formation and several other habit plane variants may also be formed, all together reducing the remaining amount of the strain. Hence, no shape change is expected under stress free conditions due to the formation of a self accommodated martensite structure. However, when an external bias stress is applied on an SMA, certain habit plane variants are energetically more favorable to form or grow rather than the others which is defined as

the martensite reorientation. On the other hand, some martensite may detwin under stress which will lead to formation or growth of the favorable lattice correspondence variant on the expense of the others. As a consequence of martensite detwinning or reorientation, a macroscopic shape change and a rise in the shape memory effect and superelasticity is observed. More details on the nature of martensitic transformations and structural descriptions of twinning in martensite and self accommodation can be found elsewhere [5,61-73].

The austenite to martensite transformation can be driven by either with the change in temperature or application of external stress as shown in Fig. 2.1 [25]. As seen from Fig. 2.1, the austenite transforms to self accommodated martensite (twinned martensite) upon cooling and it transforms to detwinned or single variant martensite under applied stress. With heating up, single variant martensite again transforms to austenite and in conditions where there is no external bias stress, the austenite will go back to self accommodated martensite structure upon cooing (Fig. 2.1).

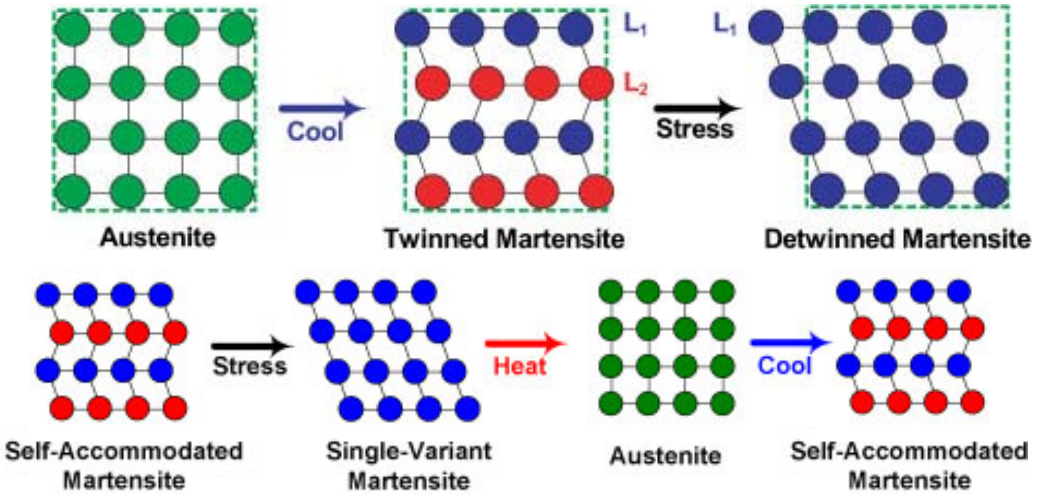

Figure 2.1 Illustritation of shape memory effect in shape memory alloys. Austenite transforms to self accommodated martensite under stress fee conditions upon cooling. The self accommodated martensite detwins or reorients and forms single variant martensite under applied stress. If the stress is released, the austenite can again go back to self accommodated martensite [25].

The martensitic transformation in SMAs takes place over some temperature ranges. When an SMA is being cooled to a lower temperature, the temperature where austenite starts to transform martensite is defined as martensite start temperature, M_s. The temperature where the austenite completely transforms to martensite, in other words where the forward transformation is completed, is described as the martensite finish temperature, M_f. For the martensite to austenite transformation, the temperature where austenite starts to form is the austenite start temperature, A_s and the temperature where reverse transformation is completed is the austenite finish temperature, A_f. These transformation temperatures follow a linear stress dependency under applied stress which is known as the Clausius-Clapeyron relationship. This relationship states that the necessary stress for unit change in transformation temperatures is constant, i.e. $d\sigma/dT$ is

constant, leading to a linear line in the stress-temperature, i.e. $\sigma - T$, diagram. If the Claisus-Clapeyron relationship for all transformation temperatures are drawn in the . $\sigma - T$ diagram, the phase diagram of the SMA is generated. Such an example of a phase diagram is shown in Fig. 2.2 which also defines the deformation response of the SMA as a function of transformation temperatures. As explained above, if the self accommodated martensite is loaded at a temperature below M_f, it detwins or reorients to a single variant martensite. When the material is unloaded, the martensite tends to maintain its detwinned or reoriented state while still keeping its deformed shape. Following heating up to the fully austenitic state and then subsequent cooling below M_f, the martensite will go back to its self-accommodated state in stress free conditions (Fig. 2.1) and the material will recover its original shape due to the shape memory effect in case there is no plastic deformation.

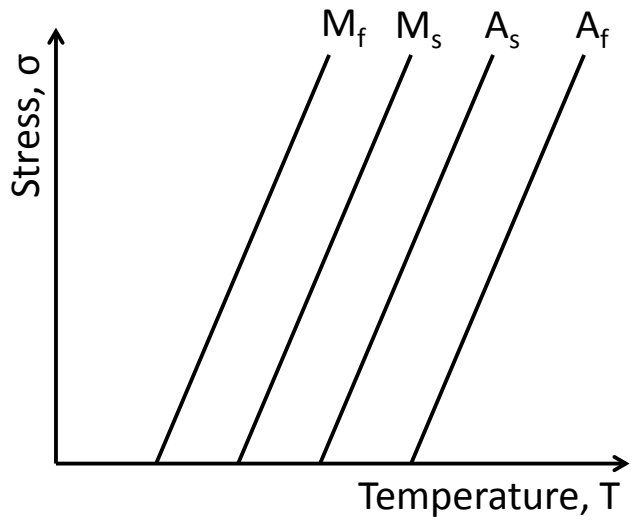

Figure 2.2 Demonstration of a σ – T phase diagram of an SMA for a martensitic transformation. The material is fully austenite above A_f and fully martensite below M_f.

If an SMA loaded to a certain strain level at a constant temperature above its A_f temperature (in austenite state), the material undergoes a stress induced martensitic transformation. When the material is unloaded, the stress induced martensite is not stable at that temperature (an imaginary temperature above A_f under no stress), the material will again transform back to austenite and the material will recover its original shape in the case of no plastic deformation. This kind of behavior in an SMA is known as superelasticity.

2.1.2 Characteristics of Shape Memory Effect and Superelasticity

Martensitic transformation is a phase transformation therefore the stress free transformation temperatures of an SMA system are one of the primary selection criteria for their practical applications. Generally, the transformation temperatures of an SMA

can be measured through differential scanning calorimetry (DSC) investigations, electrical resistivity measurements or dilatometry. In the present work, the transformation temperatures of the studied alloys were determined using DSC hence electrical resistivity measurements or the dilatometry methods are not discussed in the present chapter. In a typical DSC experiment, the forward transformation temperatures (M_s and M_f) and reverse transformation temparatures (A_s and A_f) are determined through slope extension method as shown in Fig. 2.3. As seen from the figure, the austenite to martensite transformation is exothermic while martensite to austenite transformation is endothermic. The thermal hysteresis (ΔT) under stress free DSC measurements is calculated as the difference in the A_f and M_s temperatures as ($A_f - M_s$).

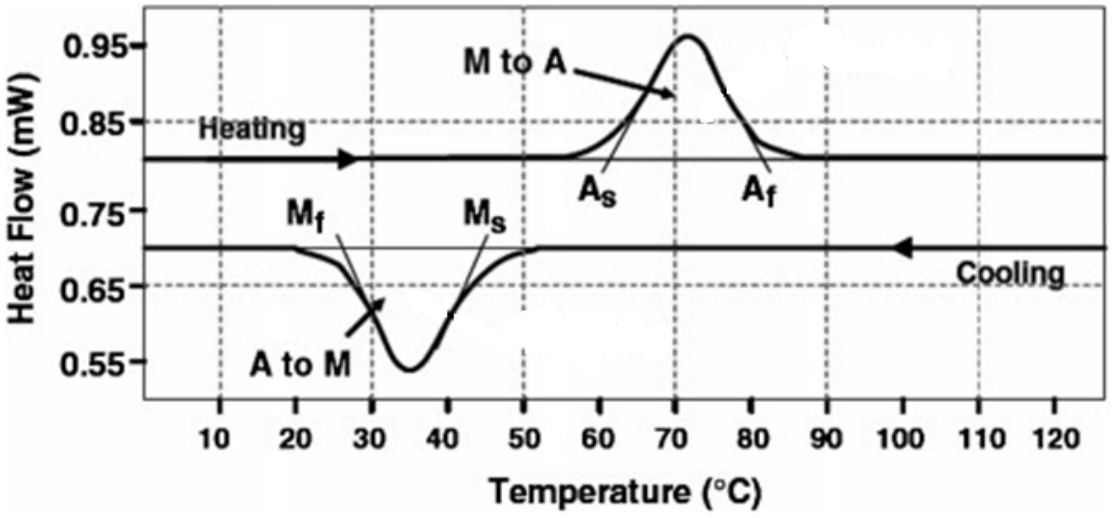

Figure 2.3 Schematic representation of how the transformation temperatures are measured using a typical DSC curve. The thermal hysteresis under stress free conditions is measured as the difference in A_f and M_s temperatures ($A_f - M_s$) [25].

Beside the transformation temperatures, it is also crucial to characterize the amount of shape change occurring during shape memory effect and superelastic behavior and its reversibility for practical applications of an SMA. In real applications of SMAs, they generally undergo phase transformations during thermal cycling under applied stress or during loading at constant stress as the stress induced martensitic transformation. The reversible shape change is characterized as the total amount of recovered strain after a complete shape memory or superelastic cycle and indicated as ε_{rec}. For shape memory effect, ε_{rec} arises from the elastic strain and the shape memory strain occurring from the detwinning/reorientation of the marteniste. For the superelasticity, ε_{rec} is the total recovery strain involving the elastic recovery (ε_{el}) and the superelastic strain (ε_{se}) due to the reverse SIMT after unloading of the material. The irreversible shape change is generally characterized as the unrecovered strain, ε_{irr}, and generally a consequence of the plastic deformation. Furthermore, if the martensite phase is stabilized in an SMA, there will be ε_{irr} contribution due to remnant martensite not transforming to austenite. This portion could still be recovered through heating the material to much higher temperatures than the A_f temperature.

As an addition to the recoverable and unrecoverable strain levels, the thermal (ΔT) and stress hysteresis ($\Delta\sigma$) are also important to evaluate for the practical uses of SMAs during a full transformation cycle. Both ΔT and $\Delta\sigma$ are a consequence of the energy dissipation associated to the MT. Several factors such as defect generations or heat generation due to the internal friction at martensite-austenite interfaces are effective on the dissipation during transformation. In practical uses of SMAs, the hysteresis is

decreasing the efficiency of SMAs especially in actuation application devices. For instance, larger hysteresis leads to wider heating and cooling ranges to provide transformation and hence larger energy is lost during transformation. The hysteresis in SMA systems can be reduced by several methods such as thermomechanical training and structural modifications, i.e. precipitation hardening and lattice compatibility of transforming phases.

The shape memory characteristics an SMA system under applied stress, are generally determined through constant stress thermal cycling experiments. The strain versus temperature response of the material under various applied stress levels are used to study the evolution of transformation temperatures, recovered and unrecovered strain levels and thermal hysteresis as a function of applied stress. An example of such a thermal cycle showing how the shape memory characteristics are determined is shown in Fig. 2.4a. Through measuring and plotting transformation temperatures for each stress levels, the stress-temperature phase diagrams, i.e. Clasius-Clapeyron relationships, are obtained. Thermal hysteresis for each cycle is calculated as the width from the middle points of heating and cooling curves. In these experiments, the measured ε_{rec} levels increase with increasing applied stress due to higher amount of detwinned or reoriented martensite but then reach to a peak point followed by a decrease due to plastic deformation at higher stress levels. In turn, the ε_{irr} levels are small initially but increases gradually with the increase in applied stress due to plastic deformation.

The superelastic properties are characterized through constant temperature loading and unloading experiments at a temperature above the A_f temperatures where

material is in fully austenitic state. In these experiments, the recovered and unrecovered strain levels as well as the stress necessary to induce SIMT (σ_{SIM}) can be evaluated. A typical superelastic cycle and the determination of the superelastic properties are shown in Fig. 2.4b. In the superelasticity experiments, the test temperatures are critical since if the difference between the test temperature and A_f is large then higher σ_{SIM} is necessary for SIMT. When the test temperature reaches to a temperature, M_d, the SIMT is not anymore the dominant deformation mode but instead it is the plastic deformation occurring prior to SIMT. Both recovered and unrecovered strain levels tend to increase with the increase in applied strain in a superelasticity test.

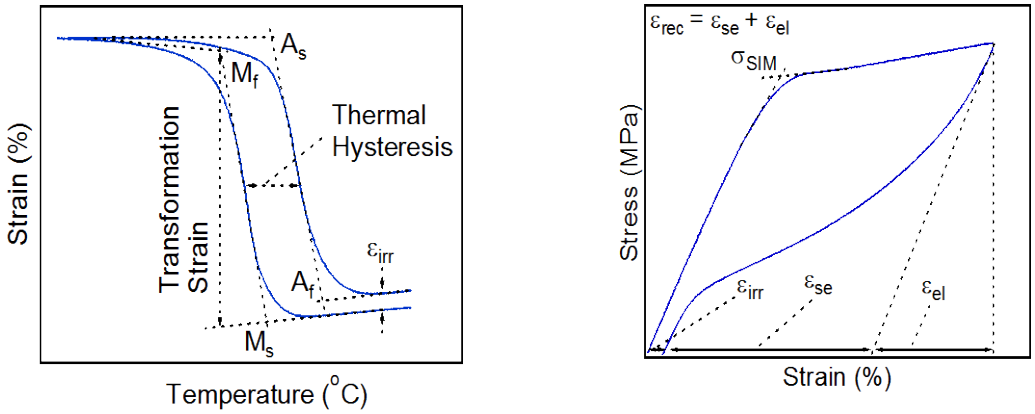

(a) (b)

Figure 2.4 Demonstration of shape memory effect and superelastic behavior. (a) constant stress thermal cycling experiments and (b) isothermal superelasticity testing. Transformation temperatures are measured using slope extension method and the thermal hysteresis is calculated as the width between the midpoint of heating and cooling curves in (a). ε_{irr}, ε_{se} and ε_{el} represents the unrecovered, superelastic and elastic strain while σ_{SIM} stands for the stress necessary for SIMT in image (b). ε_{rec} is the sum of elastic and superelastic strains.

2.2 High Temperature Shape Memory Alloys

As explained previously, NiTi alloys are not suitable for use at temperatures above 100 °C. Since NiTi is the most well known and widely studied SMA alloy, ternary alloying of NiTi is used as the most popular method to increase the transformation temperatures. However, there are other systems such as CuAlNi and NiAl SMAs that exhibit high transformation temperatures but suffer from microstructural instabilities. Decomposition occurs already at intermediate temperatures in Cu-based alloys [74] while martensite decomposes to Ni_5Al_3 phase which does not show reversible martensitic transformation in NiAl alloys [75,76]. These disadvantages have hampered

their applications. There are also Ru and Rh containing alloys which are extremely expensive and have not been investigated beyond some preliminary work [77]. Therefore, ternary alloying of NiTi alloys seem to be most advantageous and promising method to develop NiTiX alloys with improved transformation temperatures.

2.2.1 Effect of Ternary Alloying on NiTi

The Ni-content of the binary NiTi alloys significantly influences the transformation temperatures. Ni contents exceeding 50 at.% results in a sharp decrease in transformation temperatures whereas transformation temperatures are almost not effected in Ti-rich compositions since Ti_2Ni particles do not change the matrix composition.

When binary NiTi is alloyed with ternary elements less than 10 at.%, the transformation temperatures are either decreased or not changed. M_s decreases below -100 °C only with 1-6 at.% addition of Fe or Co at the expense of Ni or Al, Mn, V or Cr at the expense of Ti [27,78]. Adding Cu replacing Ni or Mn replacing Ti or Ni also does not remarkably affect the transformation temperatures of NiTi [79]. Beside these elements, Hf, Zr, Au, Pd and Pt additions were shown to successfully increase the transformation temperatures of NiTi. Fig. 2.5 summarizes the transformation temperatures (M_s or M_p) of NiTiX (X = Au, Pt, Pd, Hf, Zr) HTMSAs as a function of ternary element addition for 10 at.% or more alloying. As seen from the graph, NiTiZr and NiTiHf alloys may show higher transformation temperatures than the NiTiAu or NiTiPd HTSMAs for identical amount of ternary additions but they show comparable

transformation temperatures to NiTiPt HTMSAs for same amount ternary element addition.

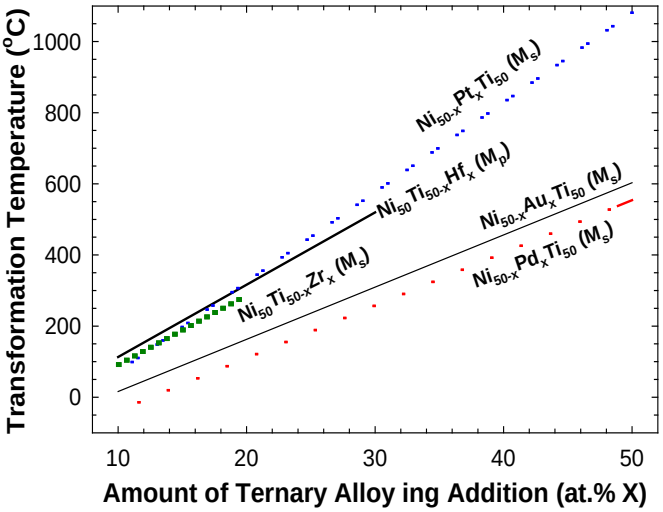

Figure 2.5 Effect of ternary alloying elements (Au, Pt, Pd, Hf, Zr) on the transformation temperatures of NiTi-based HTSMAs [77].

Ternary alloying also strongly modifies the thermal hysteresis of NiTi alloys through changing the martensite crystal structure. Binary NiTi with B19' martensite has a ΔT of 20-40 °C [80] whereas NiTiCu alloys only exhibit 10-15 °C of ΔT since it has B19 martensite [77]. Work hardening or low temperature aging in NiTi, NiTiCu and NiTiFe alloys lead to formation of R-phase leading to ΔT of only a few degrees. Nb additions on the other hand will move ΔT to almost 100 °C [81].

Although, NiTi(Au, Pt, Pd) HTSMAs were shown to exhibit high transformation temperatures, good thermal and dimensional stabilities, they are very expensive. Therefore, the current state of art on the HTSMAs systems has a focus on developing

cheaper alternatives such as NiTiHf and NiTiZr alloys which do not have numereous disadvantages. The following section will cover the general properties of the NiTiHf and NiTiZr alloys. For detailed information on the shape memory characteristics of NiTi(Au, Pt, Pd) alloys, the reader is suggested to refer literature.

2.2.2 NiTiHf and NiTiZr High Temperature Shape Memory Alloys

The primary reason on developing NiTi(Hf/Zr) HTSMAs is their cheaper cost as compared to Au, Pt or Pd alloyed NiTi-based HTSMAs. During alloying of NiTi with Hf or Zr, the ternary element is added at the expense of Ti. There is no continuous solid solution between NiTi and NiHf while the solubility of Zr in NiTiZr alloys is around 30 at.% at 700 °C [82]. Hf additions more than 3 at.% and Zr additions more than 10 at.% increase the transformation temperatures of NiTi. Addition of Hf increases M_s more efficiently than Zr does for more than 10 at% ternary addition: M_s increases with 20 °C/at.% rate in NiTiHf alloys [33] while with 18 °C/at.% rate in NiTiZr alloys [28]. The martensite peak temperature, M_p, in $Ni_{49}Ti_{36}Hf_{15}$ is found to be 190 °C [33] and 160 °C in $Ni_{49.5}Ti_{35.5}Zr_{15}$ alloy [29]. As long as the alloys are (Ti + Hf/Zr)-rich, the Ni-content of both alloys does not remarkably change the transformation temperatures. However a sharp decrease is observed when the Ni-content exceeds 50 at.% which is in accordance with the binary NiTi alloys as shown in Fig. 2.6 for the NiTiHf [25,83].

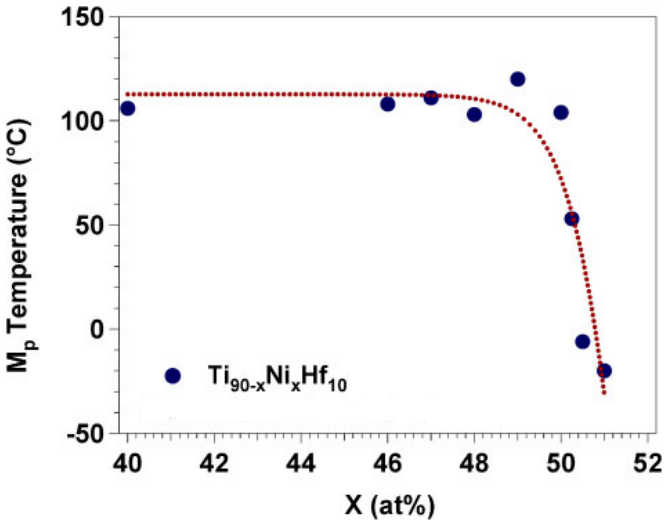

Figure 2.6 The effect of Ni composition on the M_p temperature of $Ni_xTi_{90-x}Hf_{10}$ alloys. No or negligible change is visible in the (Ti + Hf)-rich stoichiometry while M_p decrease sharply when Ni content is higher than 50 at.% [25,83].

Majority of the past studies on the NiTi(Hf/Zr) alloys were performed on the (Ti + Hf/Zr)-rich compositions with ternary additions less than 20 at.% ternary addition. These alloys were reported to have a monoclinic martensite structure of B19' and cubic austenite structure of B2 [29,84-86]. For ternary element additions above 20-25 at.%, the martensite phase becomes B19 (orthorhombic) and a B19 to B2 phase transformation takes place similar to the NiTiX alloys (X = Pd, Pt and Au) with higher ternary content [84].

When (Ti + Hf/Zr)-rich compositions are chosen to be processed in NiTi(Hf/Zr) alloys, large second phases are forming which influence the transformation temperatures, shape memory characteristics and also the stability of the alloys. In the case of NiTiZr system, $(Ti,Zr)_2Ni$ phase forms in (Ti + Zr)-rich compositions. Mulder et al. reported that NiTiZr Laves phase was present when the Zr content is higher than 7

at.% [87]. Hsieh and Wu stated that a NiTiZr intermetallic phase with an unknown crystal structure were observed in alloys containing 10 to 20 at.% of Zr rather than the $(Ti,Zr)_2Ni$ phase [31]. For the Ni-rich alloys, some mixture of $Ni_7(Ti,Zr)_2$, $Ni_{10}(Ti,Zr)_7$, NiZr and B2-Ni(Ti,Zr) phases are reported to be forming depending on their Zr content [87,88]. Ti_2Ni-type precipitates were also reported to be occurring in (Ti + Hf)-rich NiTiHf alloys. Meng et al. studied the effect of aging on the microstructure, transformation temperatures and room temperature tensile properties of the $Ni_{49}Ti_{36}Hf_{15}$ alloy [39]. The authors reported an increase in the size and volume fraction of the $(Ti,Hf)_2Ni$ phase with the increase in aging time at 700 °C. Same type of precipitates were seen in a $Ni_{44}Ti_{36}Hf_{15}Cu_5$ ribbon after aging at 500 °C for 1 h as shown in Fig. 2.7a [89]. Ti_2Ni-type precipitates are also shown to be present in the (Ti + Pd/Pt)-rich NiTiPt (Fig. 2.7b) and NiTiPd (Fig. 2.7c) [90]. Beside Ti_2Ni-type precipitates, oxide stabilized particles of Ti_4Ni_2Ox ($x < 1$) type particles are also found to be present in (Ti + Hf)-rich NiTiHf alloys depending on their interstitial oxygen level [34]. In general NiTiZr alloys seem to be less stable than NiTiHf alloys for fixed Ni and Ti contents since more type of secondary phases can be precipitated in NiTiZr alloys. The volume fraction of precipitates in the NiTiZr alloy also seems to be higher than the NiTiHf alloys for fixed compositions. Once the alloy compositions are more shifted to (Ti + Hf/Zr)-rich stoichiometry, the volume fraction of the precipitates increase.

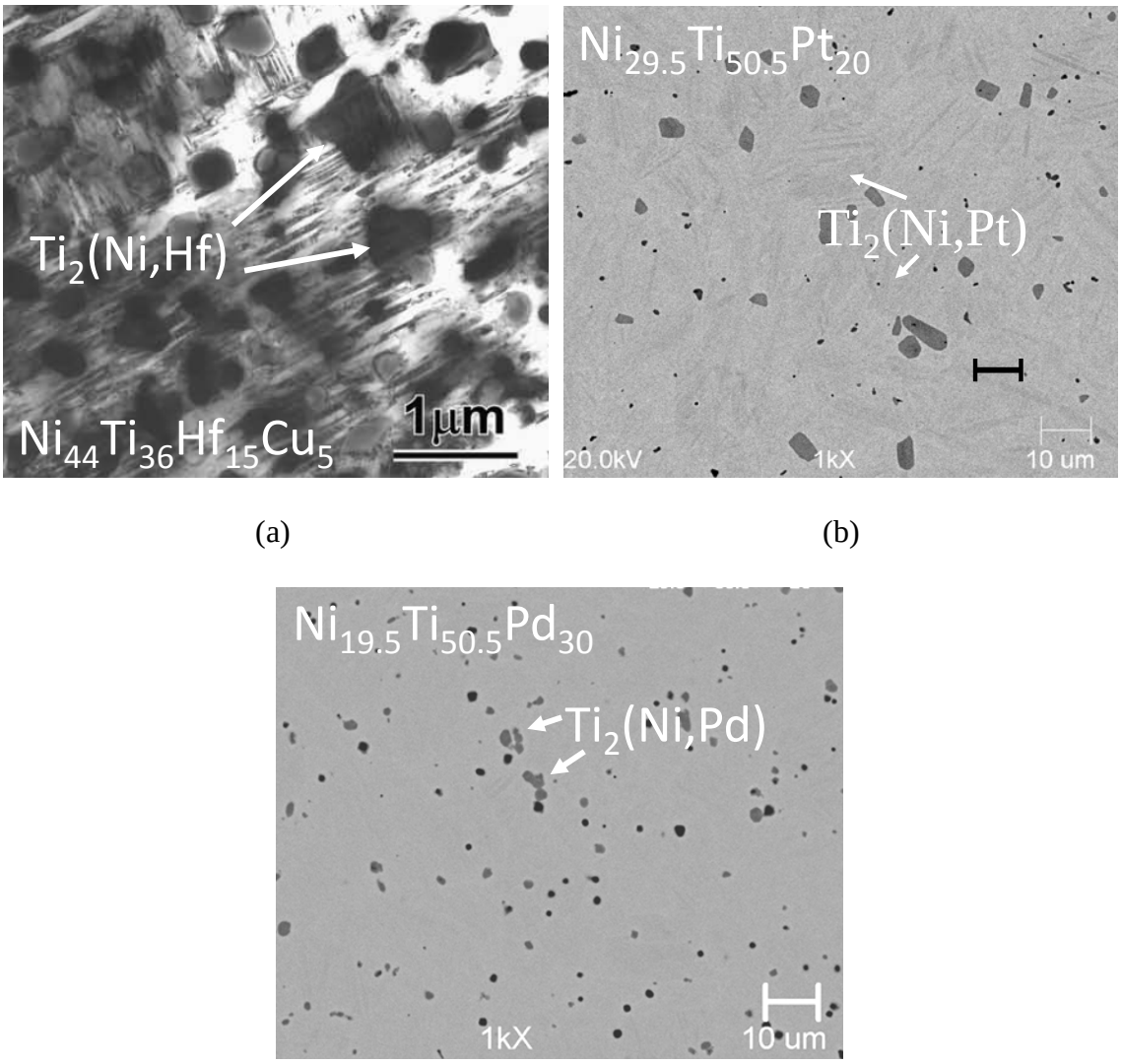

Figure 2.7 (a) Bright field TEM image $Ni_{44}Ti_{36}Hf_{15}Cu_5$ ribbon aged at 500 °C for 1 h and SEM images of as cast (b) $Ni_{29.5}Ti_{50.5}Pt_{20}$ and (c) $Ni_{19.5}Ti_{50.5}Pd_{30}$ HTSMAs. All the images show the presence of large Ti_2Ni-type particles in (Ti + Hf/Pd/Pt)-rich compositions [89,90].

Contrary to large particles seen in these alloys, Han et al. claimed that very fine, lenticular shaped and coherent precipitates which were face centered orthorhombic in crystal structure were forming in a $Ni_{48.5}Ti_{36.5}Hf_{15}$ alloy after aging at 600 °C for 150 h

[91]. These particles were different than the Ti_2Ni type particles which are expected to be precipitating in (Ti + Hf)-rich compositions.

Both NiTiHf and NiTiZr alloys suffer from room temperature brittleness in tension [29,40]. For instance $Ni_{49}Ti_{36}Hf_{15}$ only withstand a 7% elongation at room temperature [92]. However, the alloy can undergo 30% strain when deformed at 260 °C at fully austenitic state [40]. Ductility gets worse when the ternary element addition (Hf or Zr) is higher. Quaternary alloying of the same alloy with 0.1 at.% boron was also shown not to improve the ductility [93].

For solution heat treated $Ni_{49}Ti_{36}Hf_{15}$ alloys deformed at fully martensitic state, the material can recover 3% applied strain under room temperature bending [92] while it can well recover more than 80% of the 6% applied strain under tension at 80 °C [40] upon heating to austenitic state. The shape recovery was around 92% for samples subjected to 4.5% applied strain at deformation temperatures below 184 °C (lies between A_s and M_s of the material) [92]. This alloy also showed two way shape memory effect which deteriorates with thermal cycling. Olier et al. showed that $Ni_{50}Ti_{38}Hf_{12}$ alloy can recover the 80% of the 2.5% applied strain at room temperature [34]. However, the low recovery rate seen in this alloy was due to the large stress necessary for the detwinning of martensite (535 MPa) which was close to the stress to initiate slip in the material. The 4% strain which was applied in fully austenitic state triggering SIMT, can be recovered through heating of the material above A_f. Firstov and his co-workers obtained almost 3% recoverable strain for a $Ni_{49.42}Ti_{35.95}Hf_{14.63}$ alloy under compression [32]. The low recovery rate seen in these (Ti + Hf)-rich NiTiHf alloys were related to high stress

necessary for detwinning or reorientation of martensite as well as to the low resistance for dislocation slip due to their low matrix strength.

It has been reported that NiTiZr alloys with at least 15 at.% Zr content exhibit shape memory effect while alloys with 20 at.% Zr were too brittle for deformation in tension at room temperature and they can withstand only a small of applied strain [87]. $Ni_{50}Ti_{35}Zr_{15}$ can recover 1.8% applied strain at room temperature in bending while solution heat treated $Ni_{50}Ti_{30}Zr_{20}$ alloy can recover 1.6% applied strain in bending [84]. Moreover, Mulder et al. also reported that $Ni_{50}Ti_{35}Zr_{15}$ can recover all the 1.8% applied strain and the solution heat treated $Ni_{49.5}Ti_{35.5}Zr_{15}$ material can recover 85% of the 2.8% applied strain in compression at room temperature [28]. Pu et al. showed that the amount of fully recoverable strain decreases from 2.5% to 1.5% with the increase in Zr content during bending testing of alloys of NiTiZr alloys containing 5-20 at.% Zr, respectively [84]. Alloys containing 20 at.% or more Zr were reported to have a considerable amount of intermetallic phases leading to brittleness in these alloys. Alloys with more than 30 at.% Zr content exhibited no shape memory effect [86]. Based on these observations, it can be concluded that NiTiZr have inferior shape memory response and lower recovery rate as compared to NiTiPd and NiTiHf alloys. However, it should be noted that studies on NiTiZr alloys are limited and not too much effort is made to improve the shape memory response.

The presence of these large Ti_2Ni-type and several other phases in NiTi(Hf/Zr) alloys have an impact on the transformation temperatures, transformation characteristics, mechanical properties and also on the stability of the alloys. The transformation

temperatures, A_s and M_s, of $Ni_{49}Ti_{36}Hf_{15}$ alloys were decreased around 40 °C and 70 °C, respectively, after aging at 700 °C for 20 h due to formation of $(Ti,Hf)_2Ni$ particles [39]. The increase in the yield and ultimate tensile strength of the martensite after aging further supported precipitation in the alloy. The peak aging conditions was reached after 20 h and best improvement in the shape memory properties were obtained. The precipitation hardening effect is less efficient with further coarsening of the precipitates along with the prolonged aging.

One of the biggest issue of the NiTiHf and NiTiZr alloys is the the cyclic instability. Stress free thermal cycling lead to 40 °C decrease in transformation temperatures of the $Ni_{49}Ti_{41}Hf_{10}$ which is stabilizing after 20 cycles [36]. Thermal stability (a measure of stability in transformation temperatures) was much worse in the $Ni_{49.5}Ti_{30.5}Hf_{10}Zr_{10}$ alloy in which a 50-60 °C decrease was seen in transformation temperatures and also not stabilizing after 100 cycles [94]. Furthermore, thermal cycling was found to be diminishing half of the two way shape memory strain after 10 cycles that was obtained during bending.

The transformation temperatures of $Ni_{48.5}Ti_{31.5}Zr_{20}$ alloy were decreased during thermal cycling due to the precipitation in the alloy. Hsieh et al. investigated the transformation temperatures and the hardness of (Ti + Zr)-rich alloys. The transformation temperatures (M_p) decreased almost 50% in a $Ni_{49.5}Ti_{35.5}Zr_{15}$ alloy after 100 thermal cycles [94]. Hardness was also shown to be increasing along with precipitation in the alloy by a factor of 2-3 after thermal cycling. Pu et al., on the other hand show a 20-30 °C change in transformation temperatures after 100 thermal cycles in

(Ti + Zr)-rich alloys [84] which was lower than what Hsieh stated. The studies conclude that the thermal stability, which is a measure of stability in transformation temperatures, is much worse than any other NiTi-based HTSMAs such as NiTiPd or NiTiHf alloys. The reasons leading to large decreases in the transformation temperatures of NiTiZr alloys are not clear however increase in the hardness with thermal cycling was due to dislocation generation pointing out the low matrix strength of the alloys containing large second phases.

Beside the poor thermal stability and large decreases in transformation temperatures of (Ti + Hf/Zr)-rich NiTiHf and NiTiZr alloys which is summarized in Fig. 2.8a, they also possess large thermal hysteresis (ΔT) which would decrease the energy efficiency of SMA for actuation applications [25]. The thermal hysteresis in NiTiHf and NiTiZr alloys as a function of the ternary element (Hf or Zr) addition is represented in Fig. 2.8b [25]. The thermal hysteresis in these alloys is higher than the binary NiTi alloys but is comparable to each other. NiTiZr alloys with Zr content 20 at.% or less exhibit a ΔT of 50-60 °C while ΔT varies from 40 °C to 80 °C in NiTiHf alloys. The marteniste phase in the NiTiHf and NiTiZr alloys are found to be B19' similar to the binary NiTi. It has been shown in binary alloys that changing the marteniste structure from B19' to B19 can decrease the thermal hysteresis [95]. With a similar goal, Meng et al. added 1-5 at.% Cu to the $Ni_{49-x}Ti_{36}Hf_{15}Cu_x$ alloy, however Cu was found to have no effect on the martensite structure and increased the thermal hysteresis [96,97]. Additionally, the transformation temperatures were not affected with 5 at.% Cu addition but the transformation temperatures of the original $Ni_{49}Ti_{36}Hf_{15}$ alloy decreased by 20 °C

after 3 at.% Cu addition. Furthermore, Cu addition did not enhance thermal stability and the transformation temperatures were stabilized after 15-20 thermal cycles similar to the original $Ni_{49}Ti_{36}Hf_{15}$ alloy. On the other hand, Hsieh et al. worked on NiTiHfZr quaternary alloys with equal parts of ternary addition with transformation temperatures lying between the NiTiHf and NiTiZr alloys [94,98]. Although aging behavior and transformation temperatures were closer to NiTiHf system, the stability of transformation temperatures during thermal temperatures was found to be similar to NiTiZr alloys. Therefore, it can be concluded that the thermal stability was not improved in the quaternary alloys too. Finally, NiTiHfRh quaternary alloys were studied as melt spun ribbons but the transformation temperatures were decreased and the shape memory characteristics were not investigated [99].

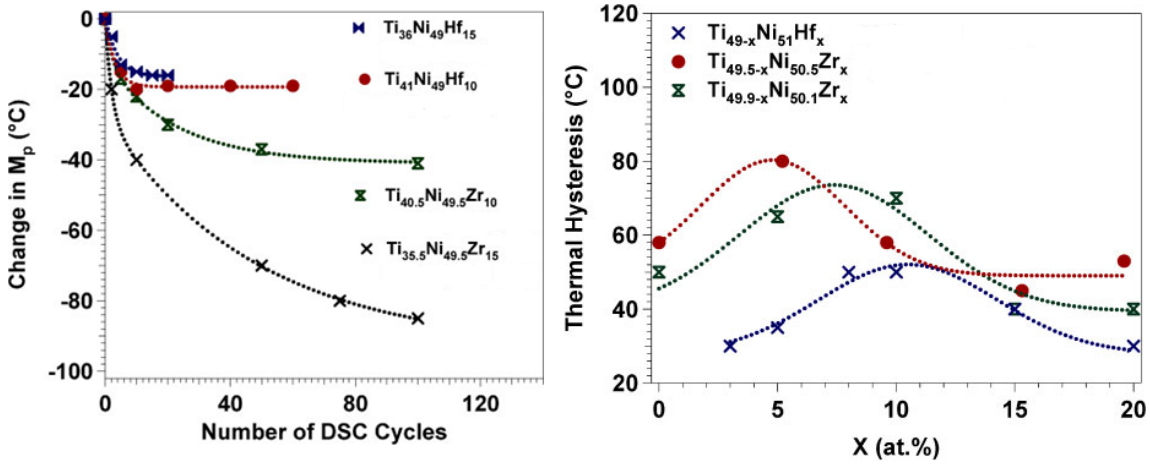

(a) (b)

Figure 2.8 (a) Decrease in the M_p of NiTiHf and NiTiZr alloys under stress free DSC cycling and (b) thermal hysteresis of NiTiHf and NiTiZr alloys as a function of ternary element content [25].

After this literature review on the (Ti + Hf/Zr)-rich NiTiHf and NiTiZr alloys, it can be concluded that the biggest issues resulting in poor shape memory response (low transformation strains and low recovery rate), large thermal hysteresis and poor thermal stability are the high detwinning stress and relatively low yield strength of austenite and martensite [32,34,37,40]. Due to the low matrix strength the resistance to plastic deformation is low and thus recovery rates are low or large amount of unrecovered strains occur. Otsuka et al. [42] proposed several methods to improve the shape memory response of the NiTi-based HTSMAs through increasing the strength of the transforming phases: i) work hardening, i.e. cold working, ii) quaternary alloying, iii) precipitation hardening and iv) thermal cycling. It has been discussed in detail previously that (Ti + Hf/Zr)-rich compositions generally are brittle at room temperature and therefore work hardening is not a proper method to improve the matrix hardness. One exceptional study was carried out on a $Ni_{49.8}Ti_{42.2}Hf_8$ alloy in which the material was subjected to equal angular channel extrusion leading to grain refinement and strengthening of the alloy [100]. However, although the alloy showed improved cyclic stability the recovered strain levels were also decreased. Quaternary alloys such as NiTiHfCu or NiTiHfZr also did not show favorable or improved shape memory responses as expected. Although thermal cycling also was shown to increase microhardness, it decreased the transformation temperatures and there is still lack of studies to characterize the effect of thermal cycling on the shape memory responses. Finally, the only favorable possibility left to improve the shape memory properties of these alloys is the precipitation hardening. There are rare studies showing that aging of Ti-rich compositions of the NiTiHf alloys may improve

the recovery rate as a consequence of precipitation hardening when the alloys is at peak aged conditions. Meng et al. stated that the shape recovery of the material after aging was not better than what Wang reported but still his study clearly showed the improved the recoverability in an aged sample as compared to an unaged one. But still in these compositions, large second phases (mainly Ti_2Ni-type) are present after aging (see Figure 2.7) which do not effectively strengthen the matrix. Therefore, even precipitation hardening is not a favorable method to enhance the shape memory responses of (Ti + Hf/Zr)-rich compositions in the NiTiHf and NiTiZr alloys. Beside these disadvantages, no favorable superelastic effect is observed in these alloys since plastic deformation becomes dominant over SIMT readily at temperatures over A_f again due to their low matrix strength.

It is well known that fine metastable Ni_4Ti_3 particles form during aging treatments of Ni-rich binary NiTi alloys which strongly influence transformation and shape memory characteristics as well as strengthening the matrix. With a similar fashion, recently Ni-rich compositions (Ni content > 50 at.%) of NiTiZr and NiTiHf have been shown to have nanosize particles after proper heat treatments not only recovering the transformation temperatures to relatively high temperatures and also improving the shape memory response and resulting in excellent shape memory recovery and good superelasticity as a consequence of precipitation hardening [51-59]. These studies on Ni-rich compositions will be discussed in the next section in detail along with the effect of nanoprecipitates on transformation characteristics.

2.3 Nanosize Precipitation in Ni-rich NiTi-based Alloys

NiTi was originally discovered as an intermetallic compound forming generally between 49-57 at.% Ni. Concerning the NiTi phase diagram provided by Otsuka and Ren [42], Ti has little solubility when Ni content is less than 50 at.% and only Ti_2Ni phase precipitates. Therefore, it is not possible to heat treat Ti-rich compositions in order to control the microstructure during precipitation. However, the phase diagram indicates that the microstructural control is permitted on the Ni-rich compositions (> 50 at.%). On this side, a series of metastable precipitates form: first Ni_4Ti_3 and later transforming to Ni_3Ti_2 and finally to stable Ni_3Ti phase. Ni_4Ti_3 precipitates are generally very small in size and Ni-rich in composition, therefore has different effects than large Ti_2Ni-type particles have on Ni-rich NiTi-based SMAs.

Ni_4Ti_3 particles have a strong effect on the transformation temperatures, transformation characteristics [45-50], shape memory response, superelastic behavior [101-103], fracture and fatigue behavior [104-106]. It is beyond the scope of the present study to discuss all the effects of these nanosize precipitates on the binary NiTi alloys, however as for the focus of the present work, the general effect of precipitation on the transformation temperatures and shape memory responses along with the studies on the Ni-rich NiTiHf and NiTiZr HTMSAs will be discussed.

2.3.1 General Effect of Precipitation and Composition on the Transformation Characteristics

The martensitic transformation temperatures of NiTi-based alloys are strongly affected by the composition, microstructure and also coherency stress fields generated through formation of nanosize precipitates. First of all, the M_s temperatures remain nearly constant when the Ni content is below 49.5 at.% but dramatically decreases when Ni content is higher than 50 at.%. This is analogous to the phenomenon seen in Ni-rich NiTiHf alloys when the Ni content is higher than 50 at.% (Fig. 2.6). However, M_s temperatures can be increased through precipitation of Ni-rich Ni_4Ti_3 particles depleting Ni from the matrix.

Secondly, martensitic transformation could be suppressed to lower temperatures as a consequence of small interparticle spacing [47]. When closely placed and densely distributed Ni_4Ti_3 particles are generated, the nucleation of martensite becomes harder. In these cases the extra strain energy to initiate martensitic transformation should be provided by the extra cooling of the material. Hence, M_s suppresses to lower temperatures which is in contradiction with the expected increase in M_s due to Ni-depletion of the matrix. Interparticle spacing is a function of aging time and temperature. Interparticle spacing is small when the precipitate size is small and their volume fraction is high. This is generally the case when the Ni-rich alloys are aged at low temperatures for short durations. However, with the increase in aging time or temperature, the particle size also increases leading to an increase in the interparticle spacing. So, with further aging interparticle spacing cannot be a dominant factor anymore on M_s and it increases.

This was exemplified by Panchenko et al. on Ni-rich compositions of binary NiTi alloys with 50.7, 50.8 and 51.0 at.% Ni content.

Beside the transformation temperatures, the thermal hysteresis occurring during transformation is also a function of precipitation and composition. The transformation hysteresis is generally a consequence of the energy dissipation due to resistance to austenite-martensite interfacial motion and defect generation. When the material is strengthened through precipitation hardening, defect generations such as dislocation formations are avoided and transformation shear is accommodated in elastic way resulting in lower thermal hysteresis. When the material is in single phase, i.e. no precipitates, the "geometric non-linear theory of martensite" (GNLTM) states that there is a relationship between the lattice compatibility of transforming phases and the thermal hysteresis [108,109]. The thermal hysteresis can be minimized by improving the lattice compatibility in an SMA system. This is rationalized with the second eigenvalue, λ_2, of the transformation matrix U. Transformation matrix, thus λ_2 is a function of the lattice parameters of the transforming phases. In a martensitic transformation where λ_2 approaches to 1 or equal to 1, the interfacial energy on the twin boundaries or any elastic transition layer is not necessary for transformation. Therefore, the lattice compatibility is good and the hysteresis is small. In NiTi, the λ_2 gets closer to 1 with the increase in Ni content and hence thermal hysteresis decreases [50]. For the ternary alloys the relationship between λ_2 and 1 is summarized in Fig. 2.9 [110].

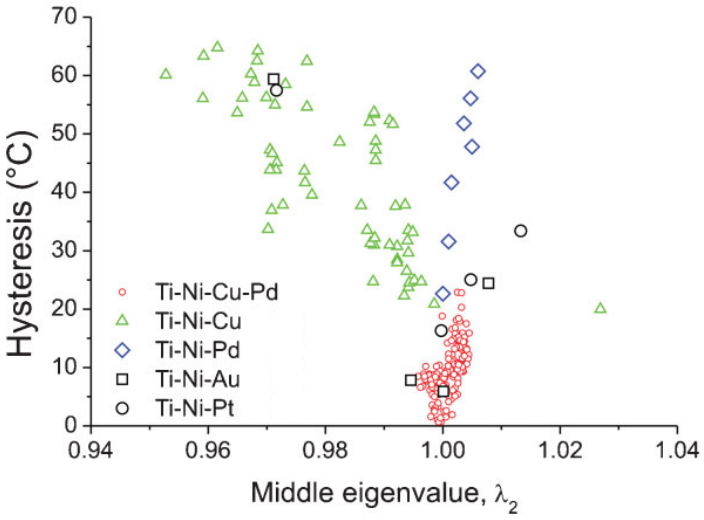

Figure 2.9 The thermal hysteresis values of ternary NiTi-based SMAs plotted against λ_2 [110].

It is also well known that the amount of unrecovered strains, ε_{irr}, is a function of the resistance to plastic deformation. During martensitic transformation, the local internal stresses arising can be much higher than the applied stress. Therefore, the material can undergo plastic deformation even if the applied stress levels are less than the yield strength of the material. So when nanosize Ni_4Ti_3 precipitates form in the binary NiTi matrix, the yield strength of the transforming phases will be increased and excellent shape recovery would be obtained. Indeed Kim and Miyazaki reported a dramatic increase in the critical stress for slip along with the increase in the density of Ni_4Ti_3 precipitates smaller than 15 nm in size [48]. The authors stated that the fine and dense nanoparticles block the dislocation motion and improve the shape recovery rate.

2.3.2 Effect of Precipitation on the Transformation Characteristics of Ni-rich NiTiHf and NiTiZr Alloys

To the best of our knowledge, Sandu is the only researcher published on the microstructure, martensitic transformation and mechanical behavior of a precipitation heat treated Ni-rich $Ni_{52}Ti_{42}Zr_6$ alloy [51,52]. The authors concluded that nanosize particles were formed in the microstructure exhibiting different diffraction patterns than the Ni_4Ti_3-type precipitates. Although aging increases transformation temperatures of the alloy and also lead to good superelasticity at room temperature, the transformation temperatures are below 100 °C since the Zr levels is just 6 at.%. Unfortunately, the load-biased shape memory response of the alloy was not characterized and no effort was made on any other Ni-rich NiTiZr alloys to understand the effect of nanoprecipitates on the shape memory response and transformation characteristics.

In 2006, Meng et al. showed that the transformation temperatures of Ni-rich $Ni_{50.6}Ti_{29.4}Hf_{20}$ alloy can be increased almost by 150 °C after aging at 550 °C for 2 h [53,54]. Such increase in transformation temperatures was attributed to the change in precipitate type from Ti_2Ni-type to Ni_4Ti_3-type precipitates which are coarsened with further aging. During stress free thermal cycling of the alloy, the transformation temperatures were decreased by 5-10 °C which was much lower than the Ti-rich compositions of NiTiHf alloys. The microhardness data also indicated that these fine precipitates were more efficiently strengthening the matrix as compared to Ti_2Ni-type precipitates. However, the information on the mechanical and shape memory properties of the alloy was lacking.

More recently, Bigelow et al. demonstrated an excellent shape memory response as well as perfect superelastic shape recovery on a Ni-rich $Ni_{50.3}Ti_{29.7}Hf_{20}$ alloy aged at 550 °C for 3 h while still showing relatively high transformation temperatures [57]. Coughlin et al. also showed that the precipitation heat treated alloy reaches to 1278 MPa yield strength at temperatures as high as 250 °C while showing very good superelasticity [59]. The same alloy also was shown to have excellent dimensional stability when cycled under 200 MPa applied stress by the scientists in NASA Glenn Researcher Center. The excellent superelasticity and excellent shape recovery as well as the improved dimensional stability as compared to any Ti-rich NiTi-based alloy was a result of formation of nanosize precipitates. For instance, as shown in Fig. 2.10a, the Ti-rich $Ni_{49.9}Ti_{50.1}$ alloy shows large amount of unrecovered strain levels even after the 1^{st} cycle (blue curve) and it stabilizes after 100^{th} cycle (black curve) [111]. Therefore, in order to reach dimensional stability, the material needs training. Along with the training, the material undergoes an accumulated plastic strain of around 7%. However, when the Ni-rich $Ni_{50.3}Ti_{29.7}Hf_{20}$ is aged at 550 °C for 3 h, precipitates smaller than 30 nm in size, are present (Fig. 2.10b) [56] and the material shows very good dimensional stability and very small amount of plastic strain after 100 cycles under 200 MPa applied stress (Fig. 2.10c) [90].

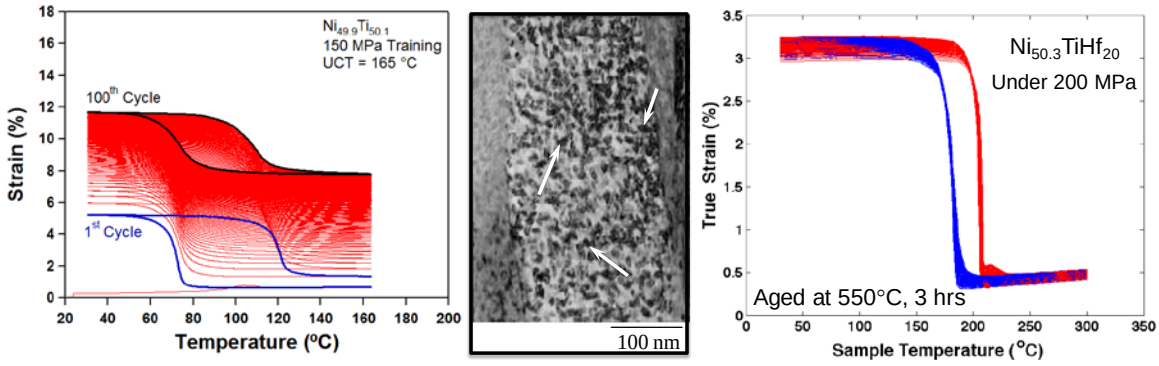

(a) (b) (c)

Figure 2.10 (a) Thermo-mechanical cycling response of a Ti-rich $Ni_{49.9}Ti_{50.1}$ SMA under 150 MPa demonstrating large dimensional stability. (b) Ni-rich $Ni_{50.3}Ti_{29.7}Hf_{20}$ aged at 550 °C for 3 h showing nanoprecipitates smaller than 30 nm in size [56] and (c) the corresponding thermo-mechanical response under 200 MPa applied stress for 100 cycles [90].

To sum up all these studies on Ni-rich compositions, one can argue that precipitation hardening is resulting in very promising shape memory responses in Ni-rich NiTiZr and NiTiHf alloys through hardening of the matrix. With the careful control of microstructure through precipitation, it would be possible to improve the shape memory responses which is the focus of this study.

CHAPTER III

EXPERIMENTAL METHODS

This chapter presents the details of the experimental procedures carried out throughout the present study. These details cover the fabrication and processing of the alloys and also the thermomechanical tests as well as the microstructural characterization studies performed in the study.

3.1 Materials Fabrication

High purity elemental materials of Ni, Ti, Zr and Hf (99.98 wt. %, 99.95 wt. %, 99.9 wt. % and 99.9 wt. % in purity, respectively) were used for vacuum induction melting of several different alloy compositions of Ni-rich NiTiZr and NiTiHf HTSMAs under Argon atmosphere using graphite crucibles. The molten materials were subsequently cast into a 25.4 mm diameter by 102 mm long copper mold. The resulting ingots were homogenized at 1050 ^{o}C for 72 hours and furnace cooled to room temperature under Argon atmosphere. The homogenized ingots were sealed in mild steel extrusion cans and hot extruded at 900 ^{o}C with an area reduction of 7:1. The extrusion cans were used to diminish the friction between the extrusion die and the ingot as well as preventing from oxidation during hot extrusion process.

3.2 Sample Preparation and Precipitation Heat Treatments

In this study systematic precipitation heat treatments were carried out on the alloys to study the effect of precipitation on the transformation characteristics and shape memory response as well as on the microstructure. For this purpose, firstly in order to investigate the transformation temperatures and thermal hysteresis, circular shaped DSC specimens with dimensions of 5 mm in diameter and 1 mm in thickness were cut from the extruded rod using electro-discharge machining (EDM). In order to prevent oxidation of samples during heat treatments, all the samples were sealed in quartz tubes under Argon atmosphere. All the samples used in the present study were first subjected to solution heat treatment (SHT) at 900 ^{o}C for 1h under Argon atmosphere and water quenched (WQ) through breaking the quartz tubes prior to precipitation heat treatments to dissolve any possible phases formed during alloy fabrication. Following the SHT, the samples were encapsulated in quartz tubes and then isothermal precipitation heat treatments at temperatures ranging from 400 ^{o}C to 600 ^{o}C with 50 ^{o}C increments for various durations shortest 1 hour and longest 200 hours were performed on the samples in order to control the precipitate size and volume fraction. In the $Ni_{50.3}Ti_{29.7}Zr_{20}$ alloy, in order to study the effect of controlled cooling on the transformation characteristics and the shape memory response, another set of samples were subjected to furnace cooling (FC) from 700 ^{o}C to 100 ^{o}C with various durations of 3 hours to 72 hours. The nominal alloy compositions fabricated and used in the present study as well as the applied heat treatments were summarized in Table 3.1.

Table 3.1 Nominal alloy compositions and the thermal treatments performed in the present study.

Alloy	at.% Ni	at.% Ti	at.% Zr	at.% Hf	Thermal Treatment
A	50.3	34.7	15	-	400 ^{o}C to 600 ^{o}C aging for 1 h to 200 h
B	50.3	29.7	20	-	400 ^{o}C to 600 ^{o}C aging and furnace cooling for 1h to 48 h
C	50.3	34.7	-	15	400 ^{o}C to 600 ^{o}C aging for 1 h to 72 h
D	50.3	29.7	-	20	No systematic heat treatments, several thermal treatments to provide distinct microstructures and compare with NiTiZr system
E	50.1	24.9	-	25	450 ^{o}C to 600 ^{o}C aging for 1 h to 24 h, only used for microstructural characterization

3.3 Differential Scanning Calorimetry

A TA Instruments, Q20^{TM} differential scanning calorimeter operated with a heating and cooling rate of 10 ^{o}C min^{-1}was used to measure the stress free phase transformation temperatures (martensite finish-M_f, martensite start-M_s, austenite start-A_s and austenite finish-A_f) of the as-received, SHT and heat treated samples. Before the DSC measurements, the surface of all samples were cleaned with grinding papers up to 600 grit in order not to leave any external stress on the sample. Using the DSC curves obtained from the experiments, the transformation temperatures were determined using the intersection points of the extended slope lines as shown in Fig. 2.3 (Chapter II). Each specimen was thermally cycled three times in order to study the cyclic stability of the

transformation temperatures and the difference between the first and third DSC cycle for the M_s temperature as (M_{s1} - M_{s3}) is calculated as a measure of thermal stability of the alloys. The stress free thermal hysteresis of the samples was also calculated as the difference between the first cycle A_f and M_s temperatures (A_f - M_s). Furthermore, using the data retrieved from DSC experiments, TTT diagrams for the alloys were generated to reveal the effect of precipitate size and volume fraction on the transformation temperatures.

3.4 Microstructural Characterization

3.4.1 Microstructure and Compositional Analysis

A Cameca SX-100 electron microprobe (EM) equipped with X-ray energy dispersive spectrometry (EDS) and wavelength dispersive spectrometry (WDS) was used to analyze the microstructures and chemical compositions of the solution heat treated samples. Back-scattered electron (BSE) imaging mode was used to investigate the present phases. The specimens for electron microprobe study were prepared by mechanical polishing down to a final step of 0.05 μm colloidal silica and investigated with no etching. As an addition to WDS, bulk samples were also analyzed with inductively coupled plasma – atomic emission spectrometry (ICP-AES) to validate the observations.

The samples for TEM/HRTEM studies were first machined as 3 mm in diameter discs and mechanically ground down to 100 μm thickness and finally prepared through double jet electropolishing using a 30% HNO_3 and 70% methanol solution at -20 ^oC and

a voltage of ~ 12 V. The TEM observations were conducted at room temperature using a Hitachi H600 conventional microscope operated at 100 kV and a JEOL 2011 high resolution transmission electron microscope with an LaB_6 filament, equipped with an energy-dispersive X-ray (EDX) sprectrometer and operated at an accelerating voltage of 200 kV.

3.4.2 Crystal Structures

The crystal structures of the transforming phases in the SHT and precipitation heat treated materials were investigated via a Bruker-AXS D8 X-ray diffractometer operated with CuK_α radiation (1.5406 Å). Since it was not possible to obtain a fully martensitic phase at room temperature for the alloy systems containing only 15 at.% ternary addition, e.g. $Ni_{50.3}Ti_{34.7}Zr_{15}$ and $Ni_{50.3}Ti_{34.7}Hf_{15}$, and since it was not possible to cool down in the present X-ray device, these experiments were only performed for the alloys containing 20 at.% ternary element namely $Ni_{50.3}Ti_{29.7}Zr_{20}$ and $Ni_{50.3}Ti_{29.7}Hf_{20}$. The X-ray diffraction (XRD) experiments were carried out between 2θ range of 20-80^o for the martensite phase at room temperature and the lattice parameters for the martensite phase were calculated using the obtained diffraction peaks. The d-spacing for the indexed planes was determined using the Bragg Law, $\lambda = 2d\sin\theta$, where the 2θ values of the planes and wavelength (λ) of the CuK_α radiation (1.5406 Å) were used as an input. In order to provide equivalent thermodynamically conditions and study the crystallographic compatibility, e.g. λ_2, of the transforming phases, the lattice parameters of the high temperature phase austenite should be extrapolated to room temperature.

Therefore, for the high temperature austenite phase, the XRD experiments were carried out at 5 different temperatures when the samples were at fully austenitic state such as M_s + 15 ^oC, M_s + 30 ^oC, A_f, A_f + 15 ^oC and A_f + 30 ^oC. For this purpose, the samples were first heated to a temperature 30 ^oC above their A_f temperature (A_f + 30 ^oC) to transform to fully austenite phase and then cooled to M_s + 15 ^oC temperature while the sample was still in fully austenitic state and the first XRD experiment was performed. Then the sample heated to next temperature, e.g M_s + 30 ^oC, and the experiment was repeated. The experimental temperatures were increased incrementally until A_f + 30 ^oC temperature and the experiments were repeated. The XRD measurements in the austenite state were conducted on a Pt heating strip and the samples were heated up through passing current from the strip. The temperature of the samples was controlled using an external K-type thermocouple placed on the surface of the samples. The experiments in the austenite state were restricted to 2θ range of 39-43^o since the highest intensity peak, e.g. from (111) plane, for B2 austenite appears in this range. Finally, the 2θ values for the obtained peaks were plotted as a function of experiment temperature and extrapolated to room temperature. Then the 2θ value for the room temperature was used to calculate the lattice parameters of the austenite phase using Bragg Law.

3.4.3 Maximum Theoretical Strains and the Elastic Constants

It has been formerly shown for several other SMAs such as binary NiTi that the maximum theoretical transformation strains could be calculated using their transformation matrix. The transformation matrix, U, describes the homogeneous

deformation that occurs during transformation of the austenite matrix to the martensite matrix [112]. Therefore, assuming that all austenite matrix will transform to martansite matrix and vice-versa without any remnant phase, one can calculate the maximum theoretical strain levels using the transformation matrix. Bhattacharya showed that the components of the transformation matrix are a function of lattice parameters of the transforming phases and for different crystal structures of the transforming phases the symmetry of the matrix as well as the number of martensite variants change. Therefore, the transformation matrix changes for the specific crystal structures of the transforming phases. Since the alloys used in the present study has an austenite crystal structure of B2, base centered cubic, and a martensite crystal structure of B19', monoclinic, the lattice parameters of transforming phases found via the XRD were used to generate the transformation matrix. More information on how to generate the transformation matrix of a B2 to B19' transformation can be found elsewhere. The generated transformation matrix was embedded in a MATLAB code in order to calculate the maximum theoretical of the alloys in several single crystal orientations. These calculations were performed for the $Ni_{50.3}Ti_{29.7}Zr_{20}$ and $Ni_{50.3}Ti_{29.7}Hf_{20}$ and compared with each other.

Furthermore, using the lattice parameters of the transforming phases measured via XRD studies, the elastic constants of the transforming phases were also calculated. The elastic constants were computed through imposing a set of strains, $\varepsilon = (\varepsilon_1, \varepsilon_2, \varepsilon_3, \varepsilon_4, \varepsilon_5, \varepsilon_6)$ on the crystal structures of the transforming phases [113]. Then the generated stresses (σ_i) as a consequence of the change in energy due to deformation were calculated. Using the Hooke's Law $\sigma_i = C_{ij}\varepsilon_j$, the stiffness tensor namely C_{ij} was

computed. Using the elements of the stiffness tensor, the bulk modulus (B) is computed as:

$$B = \frac{2}{9}\,(C11 + C12 + 2C13 + \frac{C33}{2})$$

Voight approximation was used to calculate the shear modulus as following:

$$G = \frac{1}{15}\,(2C11 + C33 - C12 - 2C13) + \frac{1}{5}\,(2C44 + \frac{1}{2}\,(C11 - C12))$$

The Young's modulus is calculated as:

$$E = \frac{9BG}{3B + G}$$

Finally the Poisson's ratio for the alloys is calculated using the following formula:

$$\nu = \frac{E}{2G} - 1$$

These elastic constants calculated were used to compare the mechanical properties of $Ni_{50.3}Ti_{29.7}Zr_{20}$ and $Ni_{50.3}Ti_{29.7}Hf_{20}$ systems.

3.4.4 Microhardness

In order to study the effect of precipitation on the microhardness of $Ni_{50.3}Ti_{29.7}Zr_{20}$ HTSMA, samples with 1 mm in thickness and 5 mm in diameter were cut from the extruded rod parallel to the extrusion direction using EDM. The extracted samples were SHT and then subjected to precipitation heat treatments at 550 ^{o}C and 600 ^{o}C for durations of 1 hour to 48 hour. Furthermore another set of the samples were SHT and subsequently furnace cooled from 700 ^{o}C to 100 ^{o}C for different durations varying from 3 hours to 72 hours. Vickers microhardness was measured using a Leco LM 300AT

microhardness tester applying 300 g load for 15 s. At least 10 indentations were made on the samples and averaged to find the microhardness of the samples.

3.5 Thermo-Mechanical Characterization

As explained previously, HTSMA systems, including the ones studied in the present study, are candidate materials for actuation applications. Therefore, the thermo-dynamical response of these alloys under service conditions where they undergo loading have a critical importance. In order to study the thermo-dynamical response of the present alloys, several different thermo-mechanical tests in tension were carried out on the materials. Primarily, load-biased thermal cycling tests were performed on the samples in order to study the shape memory response of the materials such as the evolution of transformation temperatures, recovered transformation strain (ε_{rec}), irrecoverable strain (ε_{irr}), and thermal hysteresis as a function of applied stress. Secondly, in order to characterize the superelastic response and the evolution of stress necessary for stress induced martensitic transformation (σ_{SIM}) as a function of temperature, isothermal and constant strain superelasticity tests were performed on the $Ni_{50.3}Ti_{29.7}Zr_{20}$ HTSMA. Since the mechanical response, e.g. ductility, as well as the strength of the transforming phases is also crucial for practical applications of the HTSMA systems, isothermal monotonic loading tests were also performed on $Ni_{50.3}Ti_{29.7}Zr_{20}$ HTSMA.

For the thermomechanical characterization experiments, dog bone shaped tension samples with 1.5 mm x 3 mm x 8 mm gage sections with the tension axis parallel to the extrusion direction were cut from the extruded rod with EDM. All the thermo-

mechanical experiments were carried out using a servo-hydraulic MTS test frame where the specimens were conductively cooled by flowing liquid nitrogen through the copper tubing wrapped around the grips and heated via resistive heating bands. The rate of the heating and cooling was kept as 10 ^{o}C min^{-1}. For the accurate measurement of the sample temperature during experiments, one side of the samples was polished for thermocouple attachment and the sample temperature was measured using a K-type thermocouple attached directly to the samples' gage section. The change in axial strain during the experiments was recorded with an MTS high-temperature extensometer attached directly to the gage section of the specimens. The extensometer consists of a pair of ceramic rods, 3.5 mm in diameter V-chisel ends applying 300 g force per rod on the sample preventing extensometer sliding during experiments. The gage length of the extensometer is 12.7 mm and maximum extension or compression level is ±2.54 mm. Since the gage section of the tension samples was 8 mm and the extensometer was attached to the gage section of the specimens, the measured strain values were updated taking into account the gage length of the specimen assuming that the inelastic deformation occurs only in gage section.

3.5.1 Load-Biased Thermal Cycling Experiments

Load-biased thermal cycling experiments were conducted on the samples showing relatively higher transformation temperatures, low thermal hysteresis and good thermal stability among the other samples in order to study the shape memory response of the alloys. In these experiments, the samples were loaded to a constant tensile stress

level at fully austenite state and underwent one thermal cycle between a temperature lower than its M_f and a temperature above its A_f while the change in axial strain is recorded as a function of temperature. Then, the stress was increased to the next level and the process was repeated for incremental levels of applied stress (e.g. 50, 100, 150, .. MPa) until the specimens failed. Shape memory characteristics like transformation temperatures, recovered transformation strain and irrecoverable strain levels (a measure of dimensional stability) and thermal hysteresis as a function of applied stress were determined using the thermal cycles of these experiments as shown in Fig. 2.4a given in Chapter II.

As seen from Fig. 2.4a, the total transformation strain (ε_{tot}) was measured as the strain during the forward transformation whereas the irrecoverable strain (ε_{irr}) was computed as the amount of the open-loop strain at the end of thermal cycle measured at A_f + 30 ^oC. The recovered strain (ε_{rec}) was recalculated as the difference between the total transformation strain and the irrecoverable strain. Thermal hysteresis was measured as the width between the midpoint of heating and cooling curve slopes. The transformation temperatures, M_f, M_s, A_s and A_f were determined according to the slope line extension method similar to DSC.

3.5.2 Isothermal and Constant Strain Superelasticity Experiments

Two different set of mechanical experiments were carried out to characterize the superelastic response of the $Ni_{50.3}Ti_{29.7}Zr_{20}$ samples. In the first group of tests, the samples were loaded in tension up to certain strain levels at a temperature 20 ^oC above

the (A_f) temperature and subsequently unloaded. These strain levels were incrementally increased until the samples showed failure. In the second group of sets, samples were tested under a constant 2–3% applied strain level at various temperatures to determine the temperature range of superelasticity and study the temperature dependency of the transformation stress levels. The test temperatures started at 20 ^oC above A_f and were incrementally increased until samples fractured within the applied strain level. All mechanical tests were conducted at a strain rate of 5 x 10^{-4} s^{-1}. The evolution of superelastic properties was studied as shown in Fig. 2.4b (Chapter II).

CHAPTER IV

PRECIPITATION IN Ni-RICH NiTiZr AND NiTiHf ALLOYS[*]

This study focuses on the effect of precipitation on the microstructure, shape memory characteristics and many other critical properties of Ni-rich NiTiZr and NiTiHf HTSMAs. Therefore, before detailed discussion of the shape memory characteristics of the alloys as a function of precipitation in the next chapters, it is crucial to report the generation, size, morphology, composition, coherency and crystal structures of the precipitates. Also, it is also important to study the microstructure and twinning relationships of the martensite phase when the precipitates are present. This chapter will cover all these aforementioned studies on the precipitates.

Systematic heat treatments were carried out on the studied alloys to control the precipitate size and volume fraction. Therefore, a range of precipitate size is expected to be observed, however it is beyond the scope of the present work to study all the thermal treatment cases. Instead, it is critical to determine the thermal treatments resulting in the differences in the microstructure. For this reason, examples of different precipitate size and their subsequent effect of martensite microstructure will be discussed in this part. The microstructural investigations for the individual alloy systems will be evaluated in

[*] "Reprinted from Acta Materialia, 63, Santamarta R, Arroyave R, Pons J, Evirgen A, Karaman I, Karaca HE, Noebe RD, TEM study of structural and microstructural characteristics of a precipitate phase in Ni-rich Ni-Ti-Hf and Ni-Ti-Zr shape memory alloys, 6191-6206, Copyright 2013, with permission from Elsevier."

the next chapters in detail for better understanding the relationship between the microstructure and shape memory characteristics.

4.1 The Size and Morphology of the Precipitates

The room temperature TEM/HRTEM investigations of solution heat treated alloys (Alloys A to E shown in Table 3.1) reveal the B2 austenite or B19' martensite phases depending on their Zr or Hf content. The following aging treatments at temperatures from 400 ^{o}C to 600 ^{o}C for various durations result in formation of precipitates with different particle sizes and interparticle distances as a function of aging temperature and duration. Generally, a dense distribution of nanometer size precipitates are formed after low temperature aging treatments (400 ^{o}C, 500 ^{o}C or 550 ^{o}C) for relatively short durations (a few hours) while the precipitates are coarsened to sizes of several hundred of nanometers after longer duration aging at these or higher temperatures (i.e. 600 ^{o}C). Such microstructures with large precipitates can be obtained after furnace cooling treatments as well. The approximate particle sizes obtained for different thermal treatments and studied via TEM are summarized in Table 4.1. The reader should note that there is always an error regarding the apparent dimensions since TEM reveals a 2D image of the 3D sample. However, repeatability of the TEM investigations are confirmed through studying several specimens of each alloy and thermal treatments and the TEM images given in the present study represent the overall microstructure of each condition.

Table 4.1 Nominal compositions, thermal treatments and approximate precipitate sizes of the studied alloys.

Alloy (at. %)	Treatment	Precipitate size (nm) Length	Width
$Ni_{50.3}Ti_{34.7}Zr_{15}$	200h @ 500 ^{o}C	20-70	10-16
	24h @ 550 ^{o}C	20-50	10-20
	100h @ 550 ^{o}C	75-160	15-30
	100h @ 600 ^{o}C	120-400	25-50
$Ni_{50.3}Ti_{29.7}Zr_{20}$	3h @ 500 ^{o}C	10-25	5-11
	48h @ 500 ^{o}C	20-40	10-15
	3h @ 550 ^{o}C	18-45	7-14
	FC 700-100 ^{o}C 48h	200-500	35-55
	FC 700-100 ^{o}C 3h	90-280	25-45
$Ni_{50.3}Ti_{34.7}Hf_{15}$	10h @ 450 ^{o}C	4-7	3-4
	3h @ 500 ^{o}C	7-20	3-6
	3h @ 550 ^{o}C	10-20	7-12
	10h @ 600 ^{o}C	60-300	20-50
$Ni_{50.3}Ti_{29.7}Hf_{20}$	3h @ 500 ^{o}C	6-8	2-4
	48h @ 500 ^{o}C	8-20	3-8
	3h @ 550 ^{o}C	7-20	4-6
	FC 700-100 ^{o}C 48h	70-250	20-70

Figure 4.1 shows the bright field TEM images of the $Ni_{50.3}Ti_{34.7}Zr_{15}$ (Figs. 4.1a and b) and $Ni_{50.3}Ti_{29.7}Zr_{20}$ (Figs. 4.1c and c) aged under different conditions. In both NiTiZr alloys, in the initial stages of precipitation, the nanometer size particles are ellipsoidal in shape that is close to be spherical. With further aging, when the particles grow to several tens of nanometer in size, they become oblate spindle-like in shape with

the ~ $<110>_{B2}$ long direction and the $\{001\}_{B2}$ habit plane (Figs. 4.1a and c). When the precipitates reach to several hundreds of nanometers in size after aging for longer durations or at higher temperatures, they adopt a plate-like shape similar to the martensite variants (Figs. 4.1b and d where the precipitates are indicated with letter P).

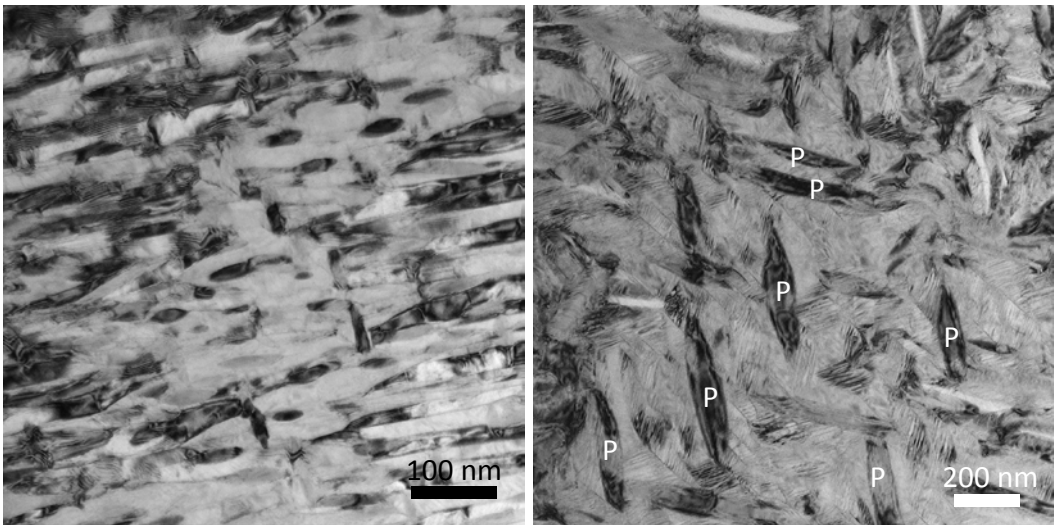

(a) (b)

Figure 4.1 Bright field TEM images of $Ni_{50.3}Ti_{34.7}Zr_{15}$ samples aged at (a) 550 °C for 24 h, (b) 600 °C for 100 h and $Ni_{50.3}Ti_{29.7}Zr_{20}$ samples (c) aged at 550 °C for 3 h, (d) furnace cooled in 48 h from 700 °C to 100 °C. Precipitates are labeled with letter "P" in image (b) and (d).

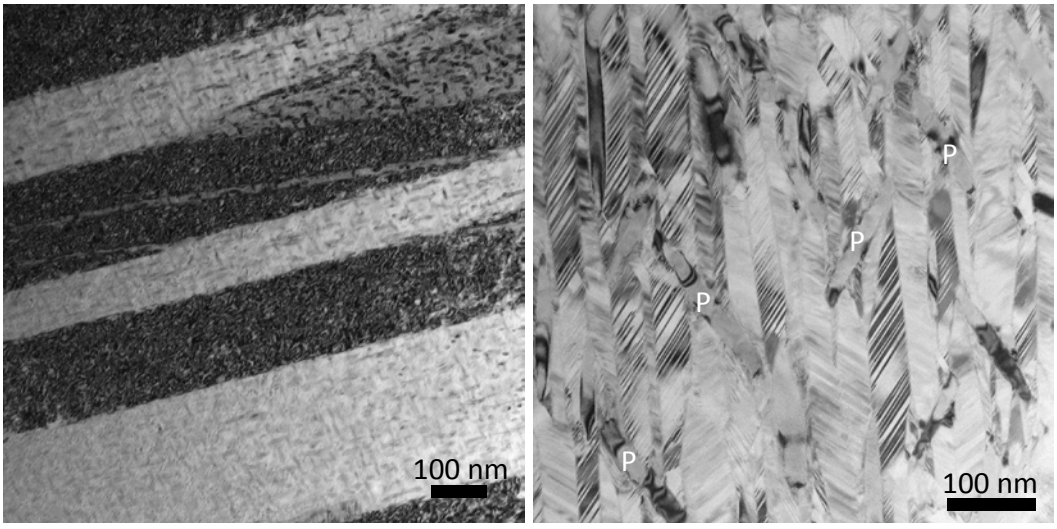

(c) (d)

Figure 4.1 Continued.

Similar conclusions on the precipitate morphology can be drawn for the NiTiHf alloys too. Figure 4.2 shows the bright field TEM images of the $Ni_{50.3}Ti_{34.7}Hf_{15}$ (Figs. 4.2a and b) and $Ni_{50.3}Ti_{29.7}Hf_{20}$ (Figs. 4.2c and d) aged under different conditions. The initially spherical precipitates (Fig. 4.2a) become spindle like in shape after reaching to several hundred of nanometers in size (Fig. 4.2b). When the precipitates are several tens of nanometers as seen in Fig. 4.2c, they are spindle-like in shape but again transform to plate-like shape upon particle coarsening (Fig. 4.2d) as a consequence of furnace cooling. Therefore, as seen from Figs. 4.1 and 4.2, it can be concluded that the precipitate morphology is same in both alloy systems and so are the recorded selected area diffraction patterns (SADPs) and HRTEM images which will be discussed in the coming sections. Therefore, the precipitate phase in both alloy systems is also same.

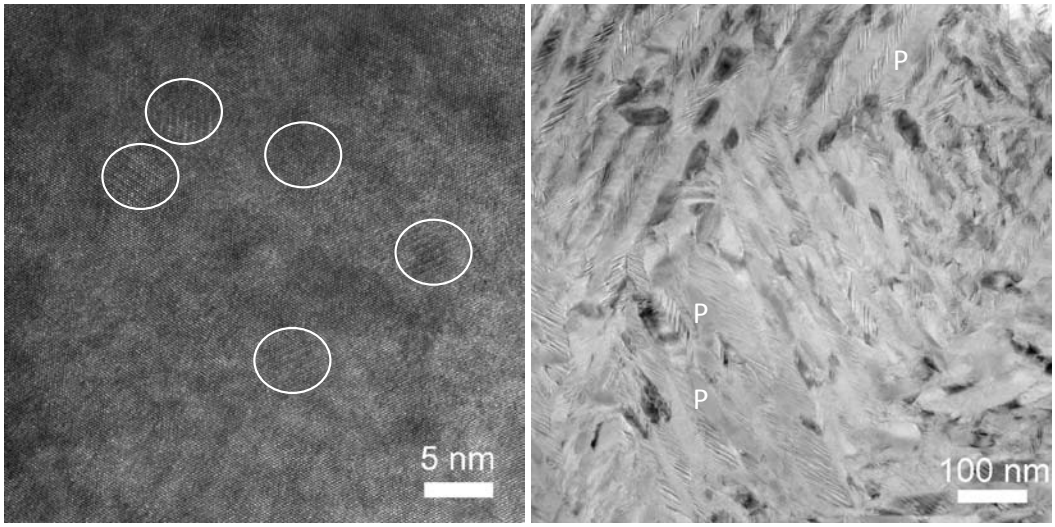

(a) (b)

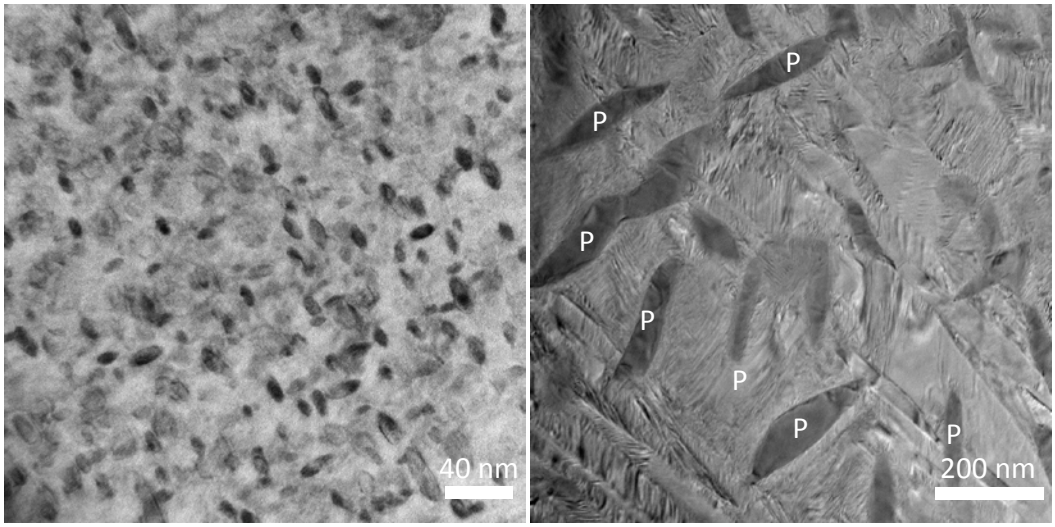

(c) (d)

Figure 4.2 Bright field TEM images of $Ni_{50.3}Ti_{34.7}Hf_{15}$ samples aged at (a) 450 °C for 10 h, (b) 600 °C for 10 h and $Ni_{50.3}Ti_{29.7}Hf_{20}$ samples (c) aged at 550 °C for 3 h, (d) furnace cooled in 48 h from 700 °C to 100 °C. Precipitates are labeled with letter "P" in image (b) and (d).

Concerning all the investigated samples as summarized in Table 4.1, it can be concluded that increasing the ternary element addition (15 at.% vs 20 at.%) in Ni-rich

NiTiZr alloys fastens the precipitate growth kinetics for a fixed Ni content. For instance, the precipitate size in the $Ni_{50.3}Ti_{34.7}Zr_{15}$ alloy after aging at 500 ^{o}C for 200 h is almost same with the precipitate size in $Ni_{50.3}Ti_{29.7}Zr_{20}$ alloy after aging at 500 ^{o}C for only 48 h. However, for the Ni-rich NiTiHf alloys, concerning similar aging conditions the precipitate size is almost same for $Ni_{50.3}Ti_{34.7}Hf_{15}$ and $Ni_{50.3}Ti_{29.7}Hf_{20}$ alloys whereas the precipitate volume fraction is higher in the latter (please see the next chapters of the present study for all the representative TEM images). This conclusion indicates that increasing the Hf content does not effectively accelerates precipitate growth kinetics but instead nucleation kinetics are fastened and hence precipitate volume fractions gets larger with the increased Hf addition for similar aging conditions. Furthermore, as seen from Table 4.1, for similar aging conditions $Ni_{50.3}Ti_{29.7}Zr_{20}$ samples possess larger precipitates compared to $Ni_{50.3}Ti_{29.7}Hf_{20}$ samples. Hence, it can be stated that for a fixed composition and for similar aging durations NiTiZr alloys will have larger precipitates compared to NiTiHf alloys.

4.2 Composition of the Precipitates

In order to study the composition of the precipitates, EDX microanalysis was performed on the samples with large precipitates which were assumed as the ones closest to the equilibrium conditions. Furthermore, more accurate measurement of the composition were able to be made on the samples with large precipitates since the smallest probe size that can be used in TEM is 15 nm and less interference would be obtained from the surrounding matrix. As a representative of each alloy systems, a

$Ni_{50.3}Ti_{29.7}Zr_{20}$ sample furnace cooled from 700 ^{o}C to 100 ^{o}C in 48 h (Fig. 4.1d) and a $Ni_{50.3}Ti_{34.7}Hf_{15}$ sample aged at 600 ^{o}C for 10 h (Fig. 4.2b) were investigated and the results were given in Table 4.2. The precipitates are richer in the ternary element (Zr or Hf) and slightly richer in Ni and poorer in Ti compared to nominal alloy compositions. Although there is an experimental error inherent to EDX technique, the Ni content of the precipitate phase is around 52.5 at.% for both alloys. The ternary element content (Zr or Hf) of the precipitate phases seems to be dependent on the nominal alloy composition and it is almost 10 at.% more than the nominal ternary element addition. The results given in Table 4.2 are the averages of 10 measurements each from the matrix and the precipitate. In spite of the small statistical error of the measurements, the estimated error is around 0.8 at.% taking into account the interference from the regions outside the main beam of electrons or differences in the thickness of he studied areas.

Table 4.2 Precipitate and matrix compositions with their estimated error measured via EDX for Ni-rich NiTiZr and NiTiHf alloys.

Alloy/Treatment	Phase	Ni at.% (±0.8 at.%)	Ti at.% (±0.8 at.%)	Zr at.% (±0.8 at.%)	Hf at.% (±0.8 at.%)
$Ni_{50.3}Ti_{34.7}Hf_{15}$, 10h @ 600 ^{o}C	Precipitate	52.5	21.2	-	26.3
	Matrix	48.9	34.3	-	16.8
$Ni_{50.3}Ti_{29.7}Zr_{20}$, FC 700/100 ^{o}C 48h	Precipitate	52.6	18.8	28.6	-
	Matrix	49.6	30.8	19.6	-

4.3 Coherency of the Precipitates

The alloy systems with low Zr or Hf content (15 at.%) are generally in austenitic state at room temperature after short duration aging treatments at 450 ^{o}C, 500 ^{o}C or 550 ^{o}C. In such cases, the formed nanometer size precipitates are fully embedded in the B2 (BCC) austenite phase. Two examples of this relationship of the B2 matrix with the precipitates are shown in Fig. 4.3, for a $Ni_{50.3}Ti_{34.7}Hf_{15}$ sample aged at 450 ^{o}C for 10 h (Fig. 4.3a) and for a $Ni_{50.3}Ti_{34.7}Zr_{15}$ sample aged at 500 ^{o}C for 200 h (Fig. 4.3b) with precipitate sizes of ~ 5 nm and ~ 20 nm, respectively. As seen from the enlarged images given in insets, there is a perfect coherency and continuity of the $\{110\}_{B2}$ atomic planes across the precipitate/matrix interface in both alloys systems. Two internal domains are also visible inside the revealed precipitate shown in Fig. 4.3b, however the domain boundary looks diffuse because the precipitate is inclined compared to the foil plane. It looks like there is an antiphase domain boundary across the boundary which is actually a translation of the contrast modulation characteristic of the HRTEM images. These antiphase domain boundaries are intrinsic formations to the ordered structure of the precipitates. Similar internal domain boundaries were also observed in precipitates with sizes of several tens of nanometers or more. Indeed, the large precipitates several hundred if nanometers in size, always exhibit several internal domains. These domains are probably a consequence of the coalescence of small particles nucleated independently and having the atoms in anti-site positions. Yang et al. reported similar internal domains on a Ni-rich NiTiHf alloy previously [114]. In the present study it is

probable that these internal domains are the reason for the Ni-rich character of the precipitates (~ 52.5 at.%).

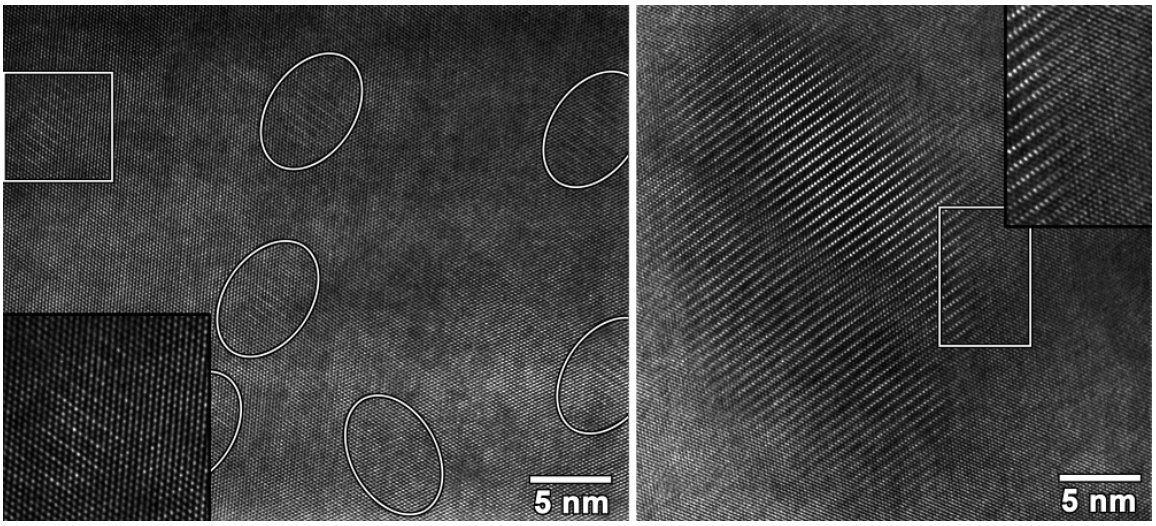

(a) (b)

Figure 4.3 HRTEM images of (a) $Ni_{50.3}Ti_{34.7}Hf_{15}$ alloy aged at 450 °C for 10 h containing several precipitates marked with white ellipses and (b) $Ni_{50.3}Ti_{34.7}Zr_{15}$ alloy aged at 500 °C for 200 h exhibiting a single precipitate. The corresponding inset images of the framed region show a perfect coherency and continuity of the atomic planes across the precipitate/B2 matrix interface.

The enlarged images of interface between the precipitates and the B19' martensite matrix are shown in Figs. 4.4a and b for the $Ni_{50.3}Ti_{29.7}Zr_{20}$ alloy FC in 48 h from 700 ^{o}C to 100 ^{o}C and for the $Ni_{50.3}Ti_{34.7}Hf_{15}$ alloy aged at 550 ^{o}C for 3 h, respectively. The images were taken in a zone axis parallel to $[110]_{B2}$. As seen from Fig. 4.4a, perfect continuity of the atomic planes with a small amount of tilt is visible across the interface after the martensitic transformation. A white line parallel to these atomic

planes is also shown to show continuity. This observation shown that the precipitates maintain their coherency, i.e same original orientation with the B2 matrix, upon the martensitic transformation whereas the surrounding matrix undergoes shear strain with the transformation and leading to the atomic plane tilt. For the specific martensite variant in the sample shown in Fig. 4.4a, the change in the interplanar distance with the martensitic transformation is small and the atomic planes across the matrix/precipitate interface still shows good continuity. But for other variants, larger changes in interplanar distances may take place which will result in a remarkable loss of the coherency between the nondeformed precipitates and the martensite matrix. Such an example is shown in Fig. 4.4b where the interface (shown with white circles) between the martensite and the two precipitates (marked as P1 and P2) reveals large distortions of the atomic planes and loss of the high resolution contrast.

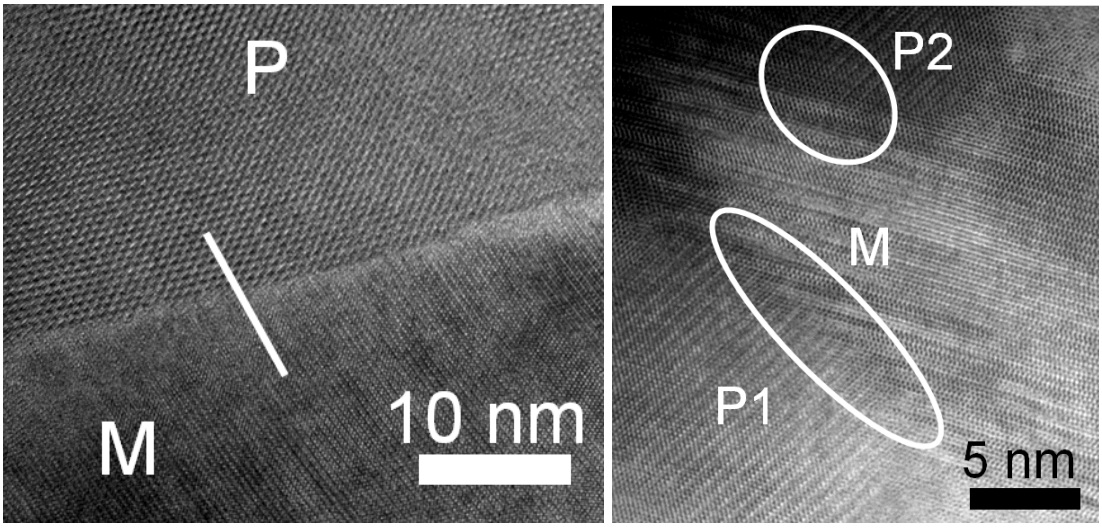

(a) (b)

Figure 4.4 Enlarged bright field TEM images of interfaces between the precipitates (P) and B19' martensite matrix (M) in (a) $Ni_{50.3}Ti_{29.7}Zr_{20}$ alloy furnace cooled in 48 h from 700 ^{o}C to 100 ^{o}C showing good continuity of planes outlined with straight line and (b) $Ni_{50.3}Ti_{34.7}Hf_{15}$ alloy aged at 550 ^{o}C for 3 h showing the lattice defects at the P1/M interface.

4.4 Crystal Structure of the Precipitates

As mentioned previously, the precipitates formed in NiTiZr and NiTiHf alloys show totally same electron diffraction patterns concluding that the precipitates in both systems have same crystal structure. All the SADPs obtained indicated fixed orientation relationships between the precipitate structure and the austenite B2 phase. The major characteristics of the precipitate crystal structure are presented in Figs. 4.5 and 4.6. Fig. 4.5 consists of three SADP obtained from $Ni_{50.3}Ti_{34.7}Zr_{15}$ alloy aged at 550 ^{o}C for 100 h (Figs. 4.5a and b) and from $Ni_{50.1}Ti_{24.9}Hf_{25}$ alloy aged at 450 ^{o}C for 3 h (Fig. 4.5c). The fundamental reflection spots are coincident with those of the austenite B2 structure in all the diffraction patterns, therefore they are indexed according to this phase. Two sets of

satellite spots along the [201] and [201] directions are visible in the SADP pattern taken in the [010] zone axis (Fig. 4.5a, marked with white circles). These satellite spots are in the ¼ of the distance to the fundamental reflections, therefore they will be denoted as ¼<210> satellites. Since a large selecting area aperture was used, some other mixed diffraction patterns were obtained coming from several orientation variants of the precipitates. Yellow circles in Fig. 4.5a show weak satellite spots belonging to a second variant of precipitates. Two other complex SADP are shown in Figs, 4.5b and c. Fig. 4.5b shows four variants of precipitates: two sets of 1/3<110> satellites labeled with white and red triangles and two other sets of ¼<210> satellites labeled with green and yellow triangles. Furthermore, three variants of precipitates with different 1/3<110> satellite directions (only one variant is marked with white labels) are revealed in the SADP shown in Fig. 4.5c.

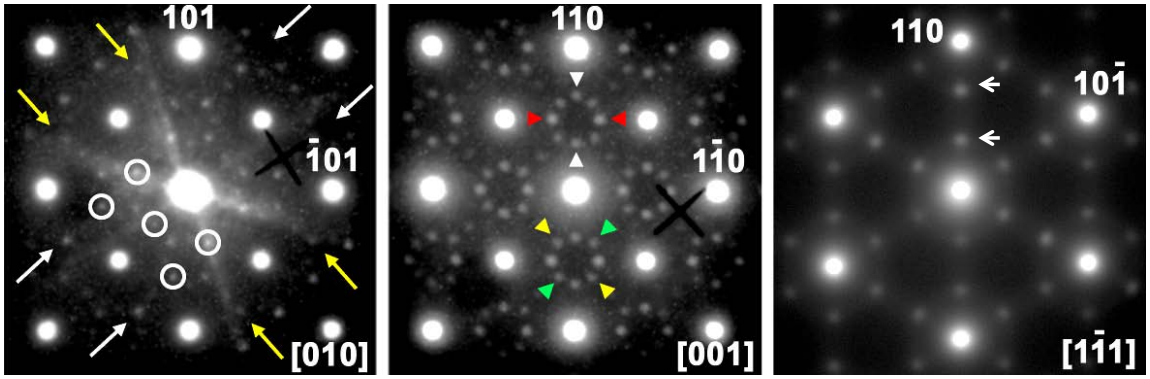

(a) (b) (c)

Figure 4.5 SADPs of the (a) $[010]_{B2}$ and (b) $[001]_{B2}$ zone axes obtained in $Ni_{50.3}Ti_{34.7}Zr_{15}$ alloy aged at 550 °C for 100 h. (c) SADP of the $[1\bar{1}1]_{B2}$ zone axis obtained in $Ni_{50.1}Ti_{24.9}Hf_{25}$ alloy aged at 450 °C for 3 h. 1/4<210> satellite spots produced by the precipitates are marked with white circles in (a); two sets of 1/3<110> and two additional sets of 1/4<210> satellites are pointed out with coloured triangles in (b). 1/3<110> additional spots from the precipitates are also observed along all $<110>_{B2}$ directions in (c).

The former results stated that the precipitate crystal structure can be considered as a superstructure of the cubic B2 austenite phase. This is provided through a fourfold symmetry along $<210>_{B2}$ directions and a threefold symmetry along a $<110>_{B2}$ direction lying on an orthogonal plane. The HRTEM images given in Fig. 4.6a and b for the $Ni_{50.3}Ti_{34.7}Zr_{15}$ alloy aged at 500 ^{o}C for 200 h and at 550 ^{o}C for 100 h, respectively, confirm the mentioned symmetries of the precipitate phase. The SADPs in Fig. 4.6a and b were recorded in the $[1\bar{1}0]$ and [010] zone axis, respectively. Fig. 4.6a clearly shows an enhanced contrast every three (110) planes corresponding to 1/3<110> satellites in the reciprocal lattices as shown in the SADPs given in Fig. 4.5. However, the intensity modulations of the (201) and $(20\bar{1})$ planes with a period of four planes are visible in

Fig. 4.6b. The corresponding Fast Fourier Transforms (FFT) of this image clearly reproduce the 1/4<210> satellites (given as the inset image in Fig. 4.6b).

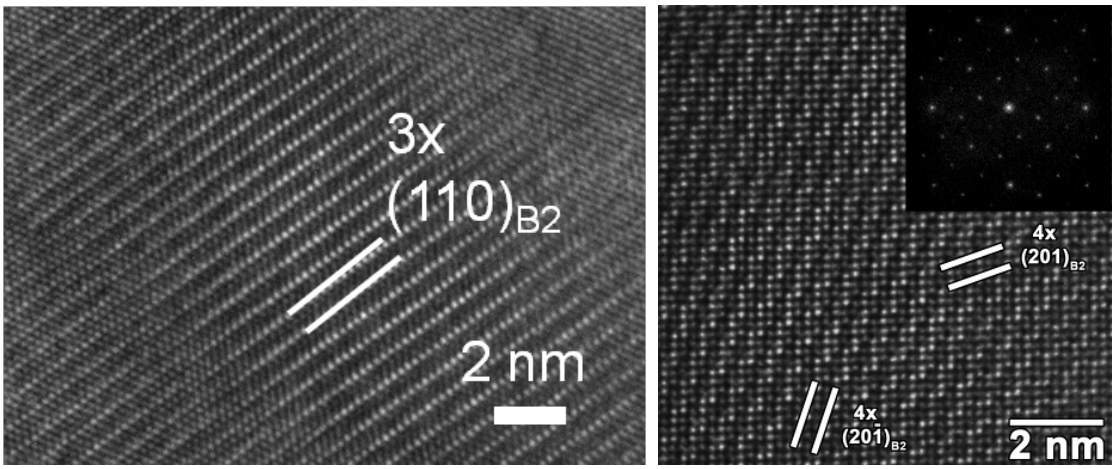

(a) (b)

Figure 4.6 HRTEM images of precipitates in $Ni_{50.3}Ti_{34.7}Zr_{15}$ alloy aged at (a) 500 °C for 200 h recorded in $[1\bar{1}0]_{B2}$ zone axis and (b) aged at 550 °C for 100 h recorded in $[010]_{B2}$ zone axis with the corresponding FFT of the precipitates.

The threefold symmetry of the {110} planes implies that the precipitate unit cell forms along the $[001]_{B2}$, $[1\bar{1}0]_{B2}$ and $[110]_{B2}$ directions where the latter axis possess three times larger unit vector. The additional fourfold symmetry of the $\{210\}_{B2}$ planes requires the extension of the unit cell further along these axes. Therefore, the following lattice correspondences of the precipitate phase (P) and the B2 structures can be proposed: $a_P \approx 4\, c_{B2}$; $b_P = 2\,(a_{B2} - b_{B2})$; $c_P = 6\,(a_{B2} + b_{B2})$. Then the lattice parameters are given as $a_P \approx 4a_0$, $b_P = 2\sqrt{2}\, a_0$, $c_P = 6\sqrt{2}\, a_0$, where a_0 is the lattice parameter of the B2 phase.

The SADPs obtained in the present study are coincident with the observations of Han et al. [91] and Yang et al. [114] and with some other recent papers that do not give any structural description of the precipitates [52]. Given the range of compositions and thermal conditions investigated in the present study, the possibility of the formation of $Ni_4(Ti + Zr/Hf)_3$-type precipitate phases in Ni-rich NiTiZr and NiTiHf alloys should be disregarded contrary to what was reported earlier. However, considering the SADPs and the given lattice parameters of the precipitates, it can be concluded that the precipitate phase in both alloy systems studied in the present study has the same type of unit cell proposed by Han et al. and Yang et al. with *Fddd* symmetry [91,114]. The newly identified phase is defined as "H phase" by Yang et al. with a face-centered orthorhombic lattice [114].

Based on the proposed unit cell and symmetry of the cubic B2 structure, there are six different variant orientations of the precipitates (a consequence of the six equivalent $<110>_{B2}$ directions for the c_p axis). A full description of their orientations with respect to the B2 matrix is reported in reference [91]. Yang et al. [114] reported on an atomic structural model for Ni-rich NiTiHf alloys (H-phase) which is a superstructure of B2 phase consists of 96 B2 units obtained from a reorganization of the Hf and Ti atoms in their sublattice with an additional refinement of the atomic positions using Density Functional Theory Calculations (DFT) calculations.

4.5 Twinning and Orientation Relationships of Martensite with Precipitates

Considerable amount of work has been performed on the binary NiTi alloys and (Ti + Hf/Zr)-rich NiTiHf and NiTiZr alloys in order to study the twinning relationships and the orientations of intervariant boundaries of the B19' martensite phase. In the case of binary NiTi alloys, <011>-Type II twins are the most widely seen twining mode providing the lattice invariant shear (LIS) regarding to the phenomenological crystallographic theory of martensitic transformation. On the other hand, although (011)-Type I twins are also suitable for LIS, they are rarely observed [5,115]. Moreover, (001)-compound twins are also reported to be present in binary alloys and they are assumed as deformation twins since they are not suitable for LIS [115,116]. In the case of (Ti + Hf/Zr)-rich NiTiHf and NiTiZr alloys, the most frequently observed twinning systems of the B19' martensite reported are the (001)-compound and (011)-Type I twins [117-120]. In these alloys, containing large $(Ti + Hf/Zr)_2Ni$-type precipitates, the (001)-compound twins appear as internal twins inside the martensite plates providing the lattice invariant shear (LIS), in spite that they are not a solution of the phenomenological crystallographic theory. This explained through introducing an adjustable dilatation parameter to the Bowles Mackenzie theory. Hence, an isotropically distorted habit plane (a consequence of the large monoclinic angle of the B19' unit cell in ternary alloys) is possible to form due to the use of (001) twins as LIS [28,119]. Beside these, an interesting effect of precipitation was reported by Nishida et al. that nanometric Ni_4Ti_3 precipitates can change the dominant twinning mode in binary NiTi [121]. The dominant <011>-Type II and (011)-Type I twinning modes are changed to (011)-compound

twinning in the presence of Ni_4Ti_3 precipitates. Therefore, detailed TEM work was performed to determine the effect of the nanoprecipitates on the martensitic microstructure of the ternary Ni-rich NiTiZr and NiTiHf alloys.

Complicated diffraction patterns along the zone axis derived from $<111>_{B2}$ directions such as the one given in Fig. 4.7a are widely observed in the present NiTiZr and NiTiHf alloys. The SADP and the corresponding bright field TEM images shown in Figs. 4.7a and b, respectively belong to $Ni_{50.3}Ti_{34.7}Hf_{15}$ alloy aged at 500 ^oC for 3 h. As seen from the SADP, three sets of twinned variants with (001)-compound twinning planes (labeled as AT, BT and CT) where the six variants are oriented in a specific $<1\bar{1}0>_{B19'}$ zone axis are visible. Among the others, only set A is completely indexed using white indices and the main variant spots are indicated with letter "A" and the twin spots are labeled with letter "T". The common 002 reflections for both the twin and main variants for sets B and C are shown with yellow and green indices, respectively. There is nearly 120^o between the 002 reflections of the three sets of variants since they are derived from {110} planes of the B2 austenite. The traces of three sets of $\{001\}_{B19'}$ planes are labeled with green, yellow and red lines together with the traces of $\{113\}_{B19'}$ and $\{111\}_{B19'}$ planes that are coincident with the intervariant boundaries are visible in the corresponding bright field image given in Fig. 4.7b. It is obvious from the image that many $(001)_{B19'}$ compound twins are revealed as internal twins in many of the martensite variants providing LIS similar to (Ti + Zr/Hf)-rich NiTiZr and NiTiHf alloys. The irregularities in the thickness of the internal twins as seen in Fig. 4.7b are probably the reason of the streaks appearing in the SADPs (Fig. 4.7a).

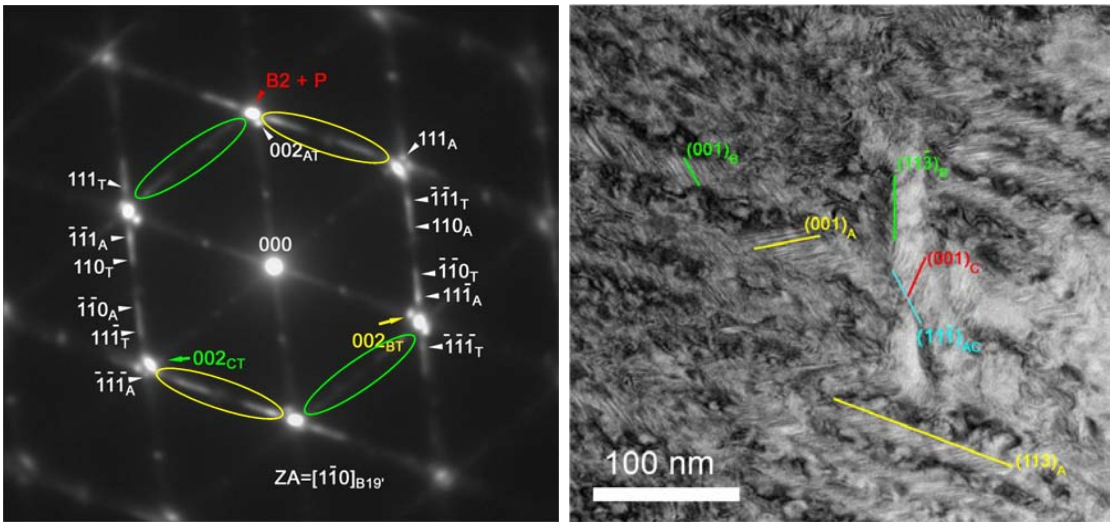

(a) (b)

Figure 4.7 (a) SADP and (b) corresponding bright field TEM image of the $Ni_{50.3}Ti_{34.7}Hf_{15}$ alloy aged at 500 ^{o}C for 3 h showing three sets of twinned variants with (001) compound twinning plane (labeled as AT, BT and CT). The traces of the three sets of $\{001\}_{B19'}$ planes are marked in (b) as well as the traces of $\{113\}_{B19'}$ and $\{111\}_{B19'}$ planes, which are coincident with the intervariant boundaries.

Another example of frequently seen SADP and the corresponding bright field TEM image in the present study is given in Figs. 4.8a and b, respectively for the $Ni_{50.3}Ti_{29.7}Zr_{20}$ alloy FC in 48 h from 700 ^{o}C to 100 ^{o}C. As seen from the pattern, two martensite variants on the $[100]_{B19'}$ zone axis (white labels) with a (011)-Type I common twin plane (yellow labels) are present. Furthermore, additional diffraction spots coming from the precipitates, ¼<210> satellites and the fundamental reflections (marked with red triangles and arrows, respectively) are also indexed. Moreover, additional spots belonging to other martensite variants are also obtained and shown with green triangles. As shown in the bright field image in Fig. 4.8b, the (011)-Type I twin plane is parallel to the intervariant boundary. Moreover as seen from Fig. 4.8a, the zone axis $[100]_{B19'}$ is

parallel to the $[100]_{B2}$ zone axis and reflections from $(011)_{B19'}$ and $(001)_{B2}$ planes are coincident. Therefore the crystallographic orientation relationship between B19' martensite and B2 austenite lattices in the present alloys is coincident with the well known relationship for the NiTi binary alloy, namely: $[100]_{B19'} \parallel [100]_{B2}$, $(011)_{B19'} \parallel (001)_{B2}$.

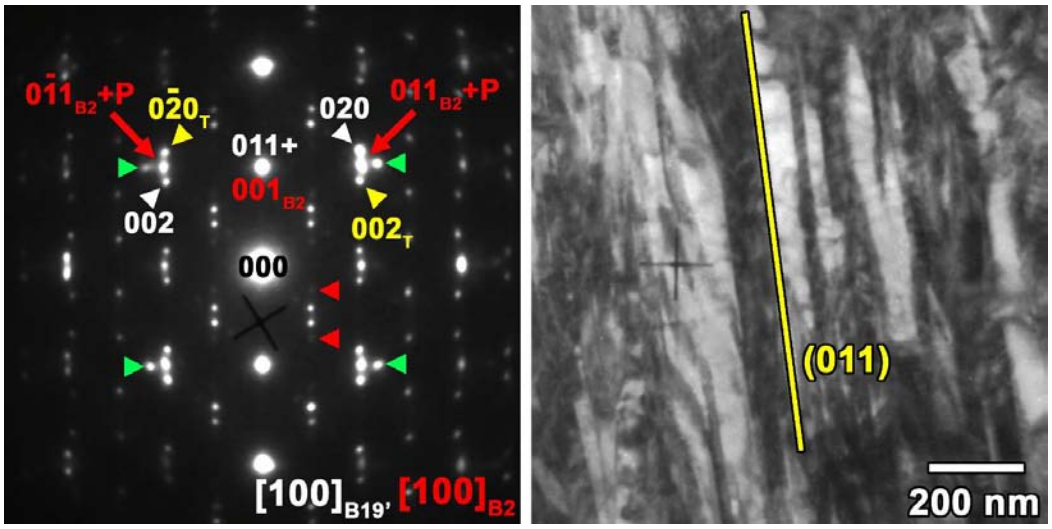

(a) (b)

Figure 4.8 (a) SAEDP of $Ni_{50.3}Ti_{29.7}Zr_{20}$ alloy furnace cooled in 48 h from 700 ^{o}C to 100 ^{o}C exhibiting two martensite variants on the $[100]_{B19'}$ zone axis with a $(011)_{B19'}$ common type I twin plane (white and yellow labels, respectively), together with additional ¼<210> satellites and fundamental reflections from the precipitates, marked with red triangles, and spots arising from other variants, marked with green triangles. (b) Corresponding bright-field image, where the trace of $(011)_{B19'}$ plane is marked.

In the present study, in all the investigations carried out, the intervariant boundaries are mainly parallel to the $\{111\}_{B19'}$ or $\{113\}_{B19'}$ planes as well as parallel to the $(011)_{B19'}$ twin plane. The HRTEM image given in Fig. 4.9a ($Ni_{50.3}Ti_{34.7}Hf_{15}$ sample

aged at 550 ^{o}C for 3 h) shows the large irregularities in the {111} and {113}-type boundaries. The micrograph compose of two segments of the boundary almost parallel to the $\{111\}_{B19'}$ plane and a largely distorted and wavy boundary that is seen in the middle region (shown with red lines). The two variants (A and B) of the fine (001) internal twins with irregular twin thicknesses are also shown with yellow and green lines. However differing than the others, the $(011)_{B19'}$ intervariant boundaries are very straight as visible in Fig. 4.9b ($Ni_{50.3}Ti_{34.7}Hf_{15}$ sample aged at 600 ^{o}C for 10 h).The interface is continuous following a single atomic plane in most of the image and only presents a single plane step on the right side of the micrograph (shown with an arrow). Similar conclusions were also drawn for (Ti + Hf)-rich NiTiHf ternary alloys reported by Han et al. [117] and Zheng et al. [118].

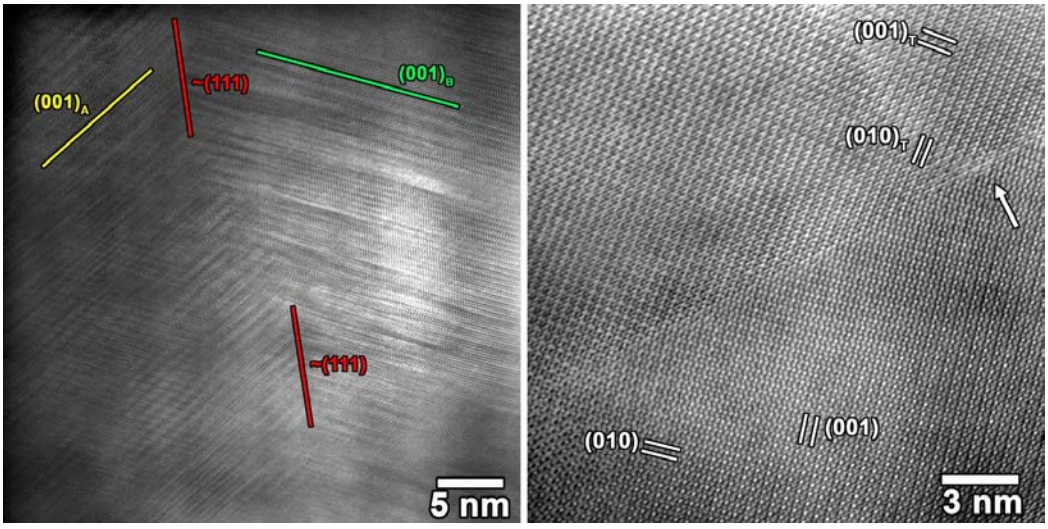

(a) (b)

Figure 4.9 HRTEM images of $Ni_{50.3}Ti_{34.7}Hf_{15}$ alloy (a) aged at 550 °C for 3 h showing wavy and distorted {111}-type boundaries and (b) aged at 600 °C for 10 h showing a very flat $(011)_{B19'}$ intervariant boundary with a single plane step marked by an arrow.

Based on all of the TEM/HRTEM work performed on the present study, it can be concluded that (001)-compound twins as LIS and (011)-Type I twins shown in Figs. 4.7 and 4.8 are the most widely seen twinning modes in the NiTiZr and NiTiHf alloys. However, (011)-Type I twins have higher volume fraction compared to (001)-compound twins when the precipitate size is small and they are absorbed by the martensite variants. But when the precipitate size is several hundred of nanometers and hence martensite variants grow in between the large particles, both types of twinning modes have more or less equal volume fractions. It can be stated that the H-phase precipitates formed in these Ni-rich alloys do not change the crystallography of the twinning relationships existing in these ternary alloys being same to those reported in (Ti Zr/Hf)-rich alloys not with this

new H-phase. Instead, the precipitate size and its subsequent effect on themartensite morphology do affect the proportion of the various twin systems observed.

4.6 Effect of Precipitates on the Martensite Microstructure

Further microstructural analysis of the precipitation heat treated Ni-rich NiTiZr and NiTiHf HTSMAs indicated that precipitate size has a strong effect on the martensite morphology. During the martensitic transformation, considerable amount of strain fields develop around the nontransforming particles. If the precipitate size is sufficiently small, i.e. several tens of nanometer, such strain fields can still be accommodated. Therefore, once the martensitic nucleation starts, martensite plates are able to grow without any interference and completely absorb the particles encountered and probably increasing the strain energy term in the thermoelastic balance. Such a case is given in Figs. 4.10a and b for $Ni_{50.3}Ti_{29.7}Zr_{20}$ alloy aged at 500 ^{o}C for 48 h and for $Ni_{50.3}Ti_{34.7}Hf_{15}$ alloy aged at 500 ^{o}C for 3 h, respectively. It is interesting to note that the martensite variants reach to a size of several hundred of nanometers in thickness in the $Ni_{50.3}Ti_{29.7}Zr_{20}$ alloy and they can cover a large number of precipitates with sizes up to ~ 40 nm (Fig. 4.10a) while the martensite thickness in $Ni_{50.3}Ti_{34.7}Hf_{15}$ alloy is much thinner (Fig. 4.10b) and although the precipitate size is two times smaller (~ 20 nnm) only a few particles are absorbed within the martensite variant width. The (011) and (113) planes parallel to the intervariant boundaries in this type of structures are also shown in Fig. 4.10. Similar observations are also made in samples subjected to other thermal treatments stating that the accommodation of transformation strain around the precipitates is much easier in

NiTiZr alloys than in NiTiHf ones. This conclusion may be true if the transformation strain levels are significantly lower in NiTiZr alloys than the NiTiHf alloys. In order to verify this and quantify the transformation strains, the lattice parameters of the transforming phases are necessary. The lattice parameters of the SHT and aged samples of the alloys were determined with XRD studies and will be discussed in Chapter VI and Chapter VII, however in this part of the thesis literature and some preliminary experimental data are used to calculate the transformation strains. Han et al. [117] reported the following lattice parameters for the $Ni_{48.5}Ti_{36.5}Hf_{15}$ alloy: $a_{B19'}$ = 0.293 nm, $b_{B19'}$ = 0.411 nm, $c_{B19'}$ = 0.473 nm, $\beta_{B19'}$ = 100.4º and a_0 = 0.309 nm. Since there is no data on the lattice parameters of Ni-rich NiTiZr alloys, preliminary XRD measurements were performed on a furnace cooled $Ni_{50.3}Ti_{29.7}Zr_{20}$ alloy. The measured lattice parameters are $a_{B19'}$ = 0.297 nm, $b_{B19'}$ = 0.412 nm, $c_{B19'}$ = 0.472 nm, $\beta_{B19'}$ = 98.6º and a_0 = 0.309 nm. Using these data, the computed strain values along the $a_{B19'}$, $b_{B19'}$ and $c_{B19'}$ axes are -5.2, -5.9 and +10.0% for the $Ni_{48.5}Ti_{36.5}Hf_{15}$ alloy and -3.8, -5.5 and +9.2% for the present $Ni_{50.3}Ti_{29.7}Zr_{20}$ alloy. As expected, the transformation strains in the NiTiZr alloy are lower than those in the NiTiHf alloy. Similarly, in the present study NiTiZr alloys should be exhibiting smaller transformation strains than the NiTiHf alloys facilitating the absorption of the precipitates by the growing martensite variants in NiTiZr alloys.

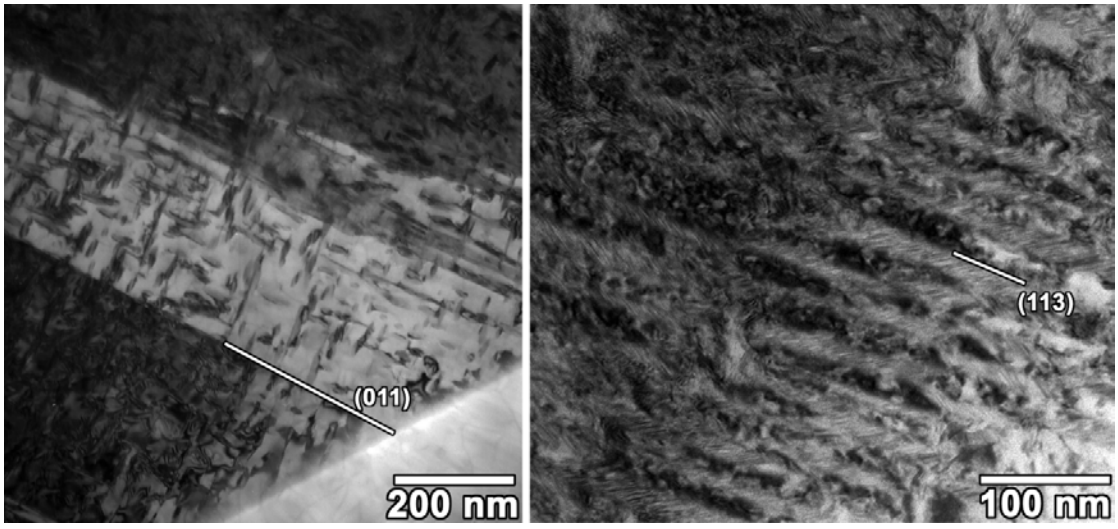

(a) (b)

Figure 4.10 Bright-field images of (a) $Ni_{50.3}Ti_{29.7}Zr_{20}$ alloy aged at 500 °C for 48 h showing martensite variants completely absorbing a large number of relatively large particles and (b) $Ni_{50.3}Ti_{34.7}Hf_{15}$ alloy aged at 500 °C for 3 h exhibiting thinner martensitic plates that can span few precipitates in their width. The traces of $(011)_{B19'}$ and $(113)_{B19'}$ planes are marked in the images.

As an addition to the transformation strain levels, the strain energy stored around the precipitates upon the transformation is also a function of the materials stiffness. The elastic constants for the precipitates and the B2 matrix were calculated with DFT using the relaxed crystal structures and the stress-strain method outlined by Le Page and Saxe and implemented in the Alloy Theoretic Automated Toolkit (ATAT) package. Table 4.3 shows the calculated elastic constants of the precipitates and the matrix for the NiTiZr and NiTiHf systems and also the experimental B2 elastic constant of the binary NiTi alloy for comparison [122] (to the author's knowledge there is no experimental data for the ternary alloys available in the literature). As shown in the table, the NiTiHf alloys are stiffer than the NiTiZr alloys. Therefore, lower energy will be necessary to

accommodate the strain fields around the precipitates in the NiTiZr alloys than in the NiTiHf alloys.

Table 4.3 Calculated stiffness tensors (in GPA) for the precipitates and B2 matrix in NiTiZr and NiTiHf alloys and the experimental values for the binary NiTi alloy given in reference [122].

	NiTiZr precipitates	NiTiHf precipitates	NiTiZr B2	NiTiHf B2	NiTi B2 experimental
C_{11}	180	210	193	200	162
C_{22}	188	204			
C_{33}	186	201			
C_{44}	24	33	35	49	35
C_{55}	26	38			
C_{66}	22	33			
C_{12}	127	126	130	136	129
C_{13}	127	127			
C_{23}	125	138			

When the precipitates get larger and reach to as size of several hundred of nanometers in size they become impenetrable obstacles for the martensitic plates and take a similar role like grain boundaries. Therefore, the large precipitates are not being absorbed anymore but instead they limit the martensitic growth in between the space between the particles. Hence, a large number very thin martensite variants forms containing very fine internal twins. Two examples of such microstructures are shown in Figs. 4.11a and b for the $Ni_{50.3}Ti_{29.7}Zr_{20}$ alloy FC in 48 h from 700 ^{o}C to 100 ^{o}C and for the $Ni_{50.3}Ti_{34.7}Hf_{15}$ alloy aged at 600 ^{o}C for 10 h, respectively. The large particles are indicated with letter “P” in both images and the fine internal (011)-compound twins are

shown in Fig. 4.11b with a (011) type I twin plane parallel to intervariant boundaries. In these type of microstructures, the nanometer size regions between two very close large particles remains untransformed even at temperatures below the nominal M_f temperature. This is analogous to the phenomena where a large decrease in transformation temperatures is seen in grain-refined polycrystals with nanometer size grains obtained after crystallization of an amorphous alloy or in severely deformed materials after recrystallization. Furthermore, in such cases the macroscopic transformation strains decrease as a consequence of the increase in the volume fraction of the material unable to transform due to size dependence of the MT together with the volume fraction of the precipitate phase. On the other hand, all these internal stress fields generated by either the large or small particles may improve the functional properties like reduction of the unrecovered strain levels, improvement in the stability of the microstructure and the transformation temperatures upon thermal cycling.

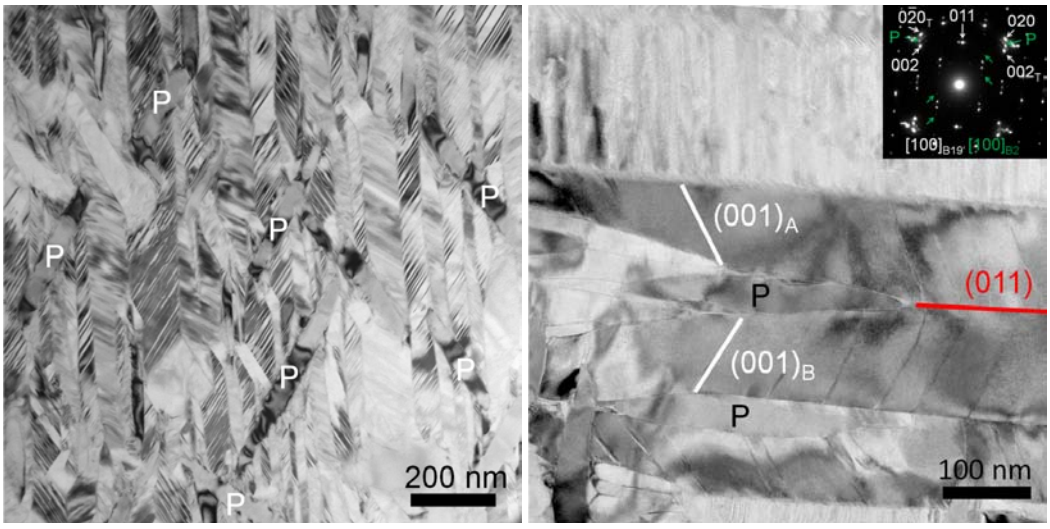

(a) (b)

Figure 4.11 The bright field TEM images of (a) $Ni_{50.3}Ti_{29.7}Zr_{20}$ alloy furnace cooled in 48 h from 700 ^{o}C to 100 ^{o}C and (b) $Ni_{50.3}Ti_{34.7}Hf_{15}$ alloy aged at 600 ^{o}C for 10 h. Two variants of (001) compound twins with the (011) type I twin plane parallel to intervariant boundaries are visible in (b). The precipitates are marked with letter "P".

4.7 Summary and Conclusions

In this part of the study, the size, shape, composition, coherency, crystal structure of the precipitates and their subsequent effect on the microstructure and the twinning and orientation relationships of the martensite were shown and discussed. The main observations and the conclusions can be summarized as following:

1. For a fixed Ni content, the growth rate of the precipitates is faster when the ternary element content (Zr or Hf) is increased. In the initial stages of precipitation, spherical precipitates form and they become oblate spindle like in shape when they are several tens of namometer in size. Precipitates, hundreds of nanometers in size, exhibit a plate-like shape similar to martensite variants or

fixed compositions and aging durations, NiTiZr alloys have larger precipitate sizes than the NiTiHf alloys.

2. The precipitates are richer in the ternary element, Zr or Hf, and poorer in Ti and slightly richer in Ni content compared to nominal compositions of the bulk alloys. This is in accordance with the observed coarsening kinetics of the precipitates.
3. When the precipitates are embedded in austenite, they are fully coherent with the matrix. Perfect continuity of the atomic planes across the interface is observed over large distances. After martensitic transformation, the particles conserve their orientation and lose some coherency with the martensite matrix as a consequence of the transformation strain undergone by the surrounding matrix. When the precipitates are nanometer size, they do not interfere with the martensite growth and be absorbed totally within the martensite variants. For equal particle sizes, the martensite variants are generally thicker in NiTiZr alloys and they span a large number particles compared to NiTiHf alloys due to the easier accommodation of the strain around the precipitates in NiTiZr alloys during martenstic transformation. This conclusion is in agreement with the lower transformation strain values and stiffness seen in the NiTiZr alloys. On the other hand, when the precipitates reach to several hundred nanometer in size they act as obstacles and martensite growth is restricted to the space between the precipitates in both systems.

4. The precipitate phase is same in both alloy systems and it coincides with the phase described earlier by Han et al. and Yang et al (H-phase). It is a superstructure of the B2 phase obtained from a recombination of the Zr/Hf and Ti atoms in their sublattice.
5. The new precipitate phase in these Ni-rich alloys does not modify the crystallography of the B19' martensite twinning modes. Same twinning and orientation relationships reported in (Ti +Zr/Hf)-rich NiTiZr and NiTiHf alloys. A mixture of (011)-compound and (011)-Type I twins are the most frequently seen twinning modes while the intervariant boundaries are mostly on $\{111\}_{B19'}$, $\{113\}_{B19'}$ and $\{011\}_{B19'}$ planes. However, precipitate size seems to affect the distribution of the particular twin systems identified. (011)-Type 1 twins are the major twinning system in samples with fine precipitates whereas more or less equal distribution of (011)-compound and (011)-Type 1 twins are present in the samples with large precipitates.

CHAPTER V

MICROSTRUCTURAL CHARACTERIZATION AND SHAPE MEMORY RESPONSE OF Ni-RICH $Ni_{50.3}Ti_{34.7}Zr_{15}$ AND $Ni_{50.3}Ti_{34.7}Hf_{15}$ ALLOYS

It is known that alloying of binary NiTi alloys with Zr and Hf increases its transformation temperatures. When the Ni content of the ternary alloys exceed 50 at.%, the transformation temperatures decrease dramatically. However, aging in Ni-rich compositions leads precipitation of Ni-rich particles which recovers transformation temperatures relatively. In this part of the study, effect of precipitation on the microstructures and the shape memory response of Ni-rich NiTiZr and NiTiHf SMAs with low ternary content (15 at.% Zr or Hf) were investigated. The studied alloy compositions are $Ni_{50.3}Ti_{34.7}Zr_{15}$ and $Ni_{50.3}Ti_{34.7}Hf_{15}$ (all in at.%)**.** Systematic precipitation heat treatments at temperatures from 450 ^{o}C to 600 ^{o}C for various durations were carried out on both alloy systems. Then, the transformation characteristics such as transformation temperatures, thermal hysteresis and thermal stability were studied using DSC. Moreover, the TTT diagrams for both alloy systems are generated to reveal the effect of precipitation on the transformation temperatures. The thermo-mechanical shape memory response of the alloys was studied via load-biased thermal cycling tests in tension. Using the obtained results, the evolution of transformation and unrecovered strain levels, transformation temperatures and thermal hysteresis as a function of applied stress were studied. This chapter is divided to two parts and results for each alloy system are given and discussed individually.

In order to reveal the effect of precipitation on the microstructure and hence on the shape memory characteristics extensive TEM studies were performed. Although the size of the precipitates were discussed in Chapter III, all the TEM investigations for various heat treatments were summarized and discussed in this section too to correlate the thermo-mechanical responses with the microstructural features.

5.1 Microstructural Characterization and Shape Memory Response of $Ni_{50.3}Ti_{34.7}Zr_{15}$

Prior to the systematic aging treatments carried out on $Ni_{50.3}Ti_{34.7}Zr_{15}$ alloy, the samples were first subjected to SHT at 900 ^{o}C for 1 h in order to have a single phase structure. A slight loss of Zr (~ 0.15 at.%) and a slight gain in Ni (~ 0.1 at.%) compared to nominal bulk alloy compositions are seen in the WDS analysis of samples after SHT as shown in Table 5.1.

Table 5.1 Composition of the present $Ni_{50.3}Ti_{34.7}Zr_{15}$ SMA after solution heat treatment at 900 ^{o}C for 1 h measured through WDS. ± indicates the standard deviation from a total of 10 measurements over the specimens.

	Ni (at.%)	Ti (at.%)	Hf (at.%)
Measured	50.4 ± 0.08	34.75 ± 0.05	14.85 ± 0.13
Nominal	50.3	34.7	15.0

Fig. 5.1 represents the BSE image taken at room temperature where a homogeneous structure of austenite with a grain size ranging from 25 to 100 μm is

present. Heterogeneously distributed white particles, <3 μm in size, are identified as zirconium carbide particles through EDS. These carbides were probably formed as a consequence of carbon diffusion from the crucibles to the molten metal during vacuum induction melting of the alloy in accordance with the slight Zr loss compared to the nominal composition. Since the distribution of the carbide particles are not homogeneous, no accurate measurement of their volume fraction is possible. However, their volume fraction is small enough to assume these particles as irrelevant for the present study.

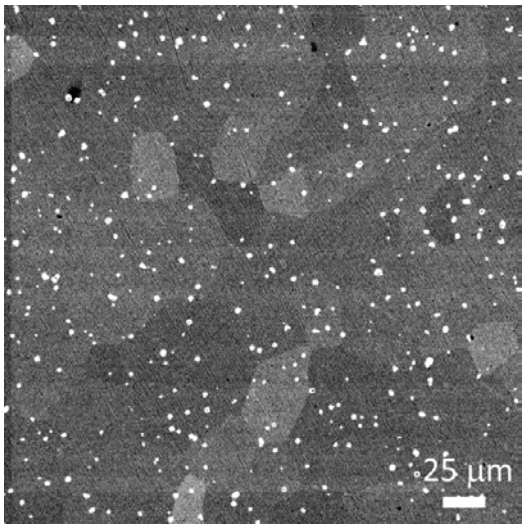

Figure 5.1 Back scattered electron micrograph of the solution heat treated $Ni_{50.3}Ti_{34.7}Zr_{15}$ SMA. White particles are found to be carbide inclusions (mainly ZrC) through EDS. The sample is at austenite state at room temperature and the grain size ranges from 25 μm to 100 μm.

5.1.1 Microstructure

Concerning the transformation characteristics such as transformation temperatures, thermal hysteresis and thermal stability which will be discussed in detail in section 5.1.2, the microstructures of the samples showing relatively low thermal hysteresis (sample aged at 500 ^{o}C for 200 h), relatively good thermal stability (sample aged at 550 ^{o}C for 24 h and 100 h) and relatively high transformation temperatures (sample aged at 600 ^{o}C for 100 h) were investigated with TEM. The bright field and high resolution TEM images of the aged $Ni_{50.3}Ti_{34.7}Zr_{15}$ samples are shown in Fig. 5.2. A dense distribution of spindle like precipitates, 20-70 nm in length and 10-16 nm in width, are present after aging at 500 ^{o}C for 200 h (Fig. 5.2a). The precipitates maintain their shape and are around 20-50 nm in length and 10-20 nm in width after aging for 24 h at 550 ^{o}C (Fig. 5.2b). However, precipitates coarsen with further aging at 550 ^{o}C for 100 h and reach to a size of 75-160 nm in length and 15-30 nm width (Fig. 5.2c). The inset SADP given (taken along the $[001]_{B2}$ zone axis) shows the two variant of precipitates with 1/3<110> satellites (red arrows) and other two variant with ¼<210> satellites (blue arrows) confirming the presence of H-phase precipitates. The precipitates grow to several hundred of nanometers, 120-400 nm in length and 25-50 nm in width, after aging at 600 ^{o}C for 100 h as seen from Fig. 5.2d where the precipitates are shown with arrows. As explained in Chapter IV (section 4.6), precipitates can be absorbed through martensite variants if their size is sufficiently small (Fig. 5.2b) while they cannot be absorbed and limit martensite growth when they reach to several hundred of nanometers in size (Fig. 5.2d).

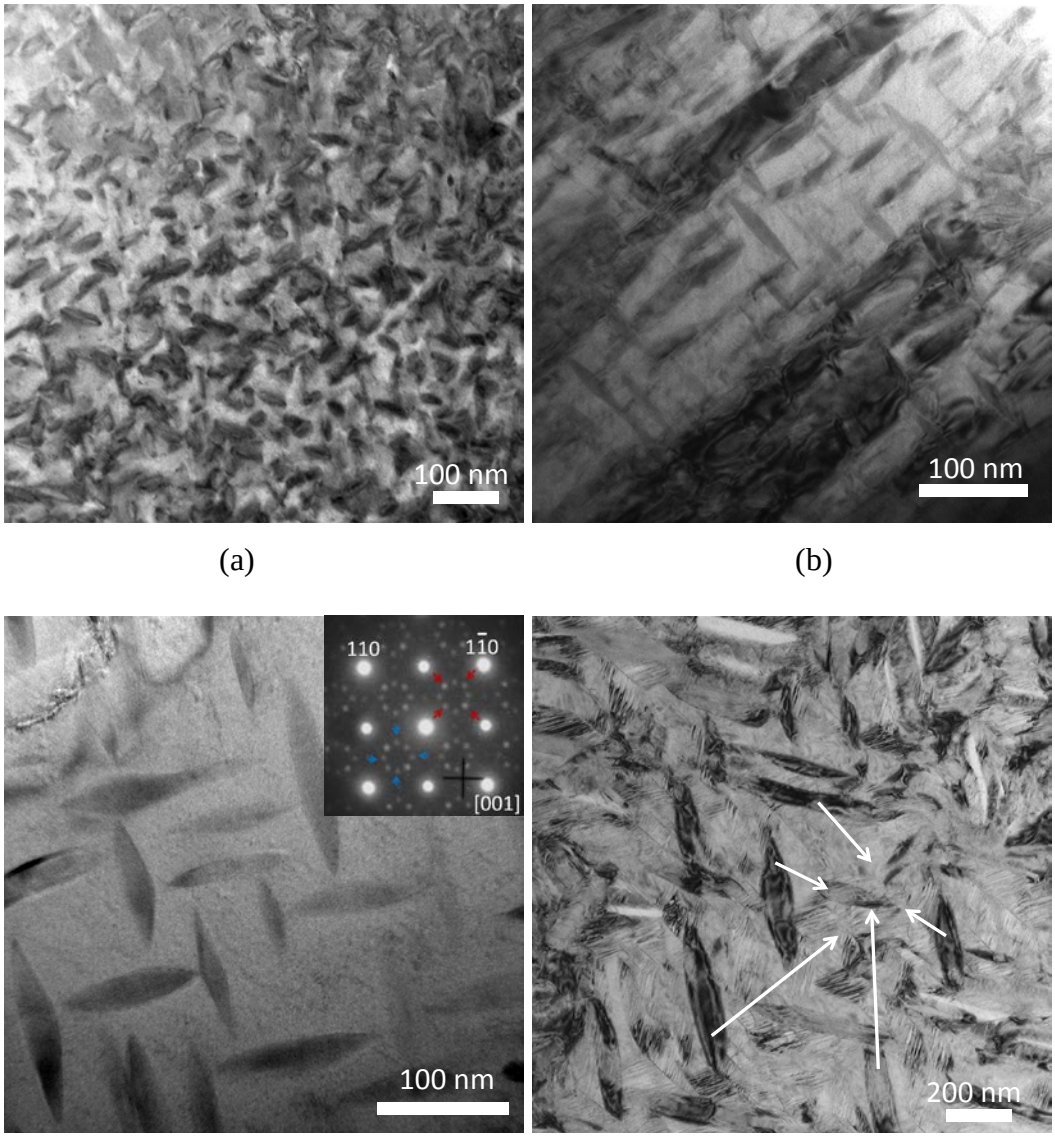

Figure 5.2 Bright field TEM images of $Ni_{50.3}Ti_{34.7}Zr_{15}$ samples aged at (a) 500 ^{o}C for 200 h, (b) 550 ^{o}C for 24 h, (c) 550 ^{o}C for 100 h and (d) 600 ^{o}C for 100 h. For clarity, precipitates are shown with arrows in image (d).

5.1.2 Transformation Temperatures and Characteristics

In this part of the work, the results of the DSC measurements carried out on the aged $Ni_{50.3}Ti_{34.7}Zr_{15}$ samples are given and discussed. The stress free DSC cycles of the

specimens aged at 500 ^{o}C, 550 ^{o}C and 600 ^{o}C are shown in Figs. 5.3a to c, respectively. The experiments were performed between -60 ^{o}C to 200 ^{o}C and no DSC signal is recorded for the samples subjected to SHT or aged at 450 ^{o}C or for samples aged at 500 ^{o}C for 1 h and 3 h between this measurement range. As seen from Fig. 5.3, all the aged samples undergo a single step phase transformation during forward and reverse transformations. It is clearly seen that for fixed aging temperatures, the transformation temperatures increase with the increase in aging duration. This is due to the continuous Ni depletion of the matrix with aging and hence formation of Ni-rich particles.

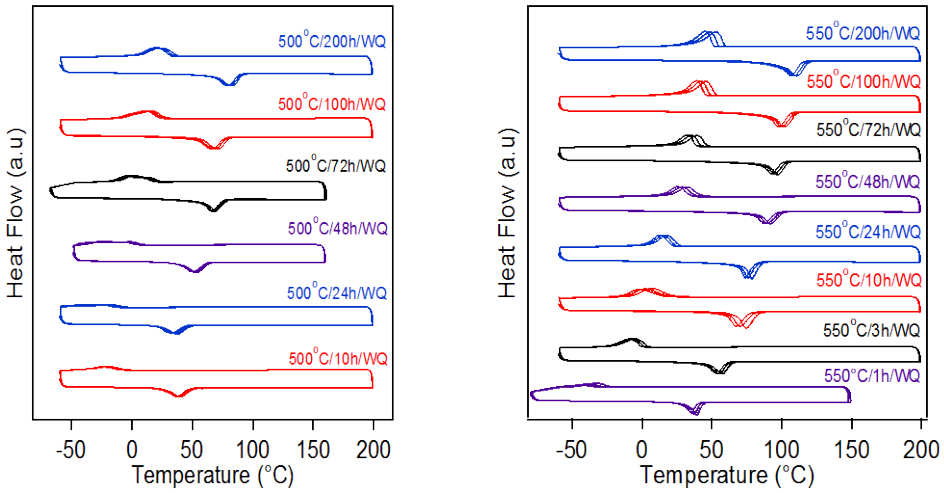

(a) (b)

Figure 5.3 The stress free DSC cycles of $Ni_{50.3}Ti_{34.7}Zr_{15}$ alloy aged at (a) 500 °C, (b) 550 °C and (c) 600 °C for various durations.

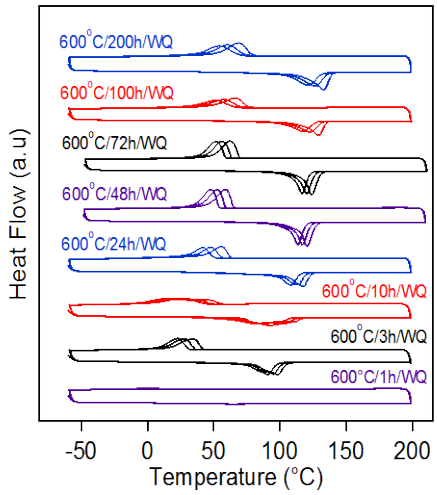

(c)

Figure 5.3 Continued.

Figs. 5.4 a and b represent the summary of A_f and M_s temperatures, respectively, derived from the DSC curves shown in Fig. 5.3 for the samples aged at 500 ^oC, 550 ^oC and 600 ^oC for different durations. For the target actuation applications, it is crucial to determine at what temperature the austenitic transformation is completed and where the martensitic transformation starts. Therefore, throughout the present study only A_f and M_s temperatures of the aged samples are reported and discussed. As seen from Fig. 5.4a and b, the transformation temperatures of $Ni_{50.3}Ti_{34.7}Zr_{15}$ SMA show a large flexibility as a result of precipitation: from 49 ^oC to 139 ^oC for A_f, a 90 ^oC temperature window, and from -5 ^oC to 79 ^oC for M_s, a 84 ^oC temperature window. It is visible from Fig. 5.4 that the transformation temperatures increase rapidly during the initial stages of aging, i.e. up to 24 h of aging, and increase gradually with further aging up to 200 h.

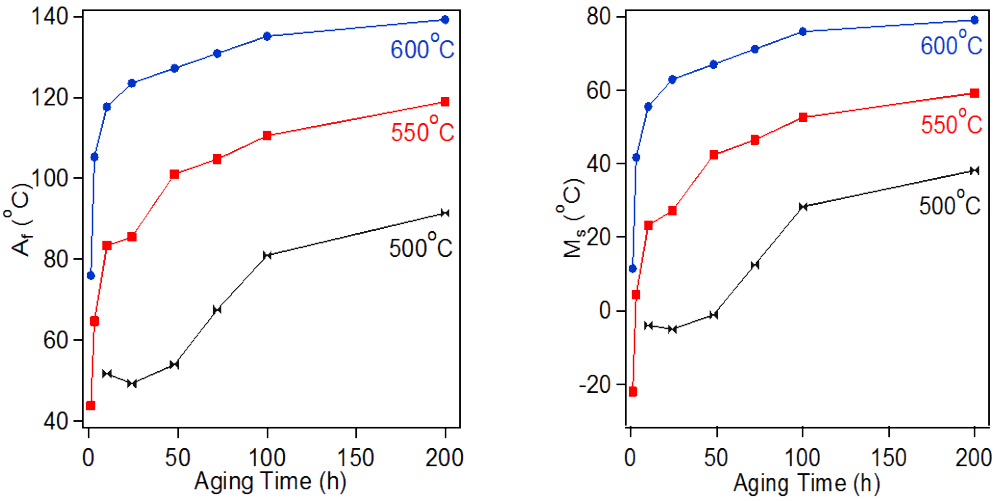

(a) (b)

Figure 5.4 The summary of the transformation temperatures of $Ni_{50.3}Ti_{34.7}Zr_{15}$ alloy aged at 500 °C, 550 °C and 600 °C for various durations (a) A_f and (b) M_s.

Fig. 5.5a represents the thermal hysteresis values of the aged $Ni_{50.3}Ti_{34.7}Zr_{15}$ samples calculated as the difference between the A_f and M_s temperatures (A_f - M_s) which are derived from DSC measurements. The thermal hysteresis values change between 53 ^oC lowest to 66 ^oC highest. Although, there is no clear relationship between the aging time and thermal hysteresis, it is obvious that the thermal hysteresis values generally decrease up to 100 h of aging and increase again with 200 h of aging. Generally in SMAs, the increase in matrix strength due to precipitation hardening decreases the energy dissipation during transformation and hence the thermal hysteresis decreases. At fixed aging temperatures, the increase in precipitate volume fraction with aging increase matrix strength more and decrease thermal hysteresis. However, when the precipitate size gets considerably larger such as in the cases of aging times as long as 200 h, the

precipitates do not increase the matrix strength as efficient as the nanosize precipitates do. Therefore, thermal hysteresis increases after 100 h of aging. Furthermore, with the increase in aging temperature the thermal hysteresis values also increase. This is probably due to the larger precipitate sizes obtained at higher aging temperatures and hence lower matrix strength. Moreover, when the precipitate size is several hundred of nanometers large and cannot be absorbed into martensite variants, the number of intervariant boundaries increases. This can result in an increase the thermal hysteresis such as in the samples aged at 600 ^{o}C.

Three DSC cycles were carried out on the samples in order to assess the thermal stability of the transformation temperatures. Fig. 5.5b shows the shift in M_s temperatures as indicated by the difference between the first and the third DSC cycles (M_{s1} - M_{s3}). The change in M_s during thermal cycling is actually a measure of thermal stability and a material showing negligible or no change in M_s can be assumed as “thermally stable”. Similar to the behaviors seen in hysteresis, increase in aging time results in an increase in the shift in M_s. The smallest temperature shifts are obtained after aging at 500 ^{o}C, however still over 4 ^{o}C while the largest shifts are present in the samples aged at 600 ^{o}C (>10 ^{o}C). This is again due to the difference in the precipitate sizes between the thermal treatments and probably matrix hardening is more efficient due to presence of dense small particles after low temperature aging. The change in transformation temperatures with stress free thermal cycling occurs as a consequence of the repetitive motion of the transformation interface and the accommodation of the transformation shape change with dislocations and other defects [111].

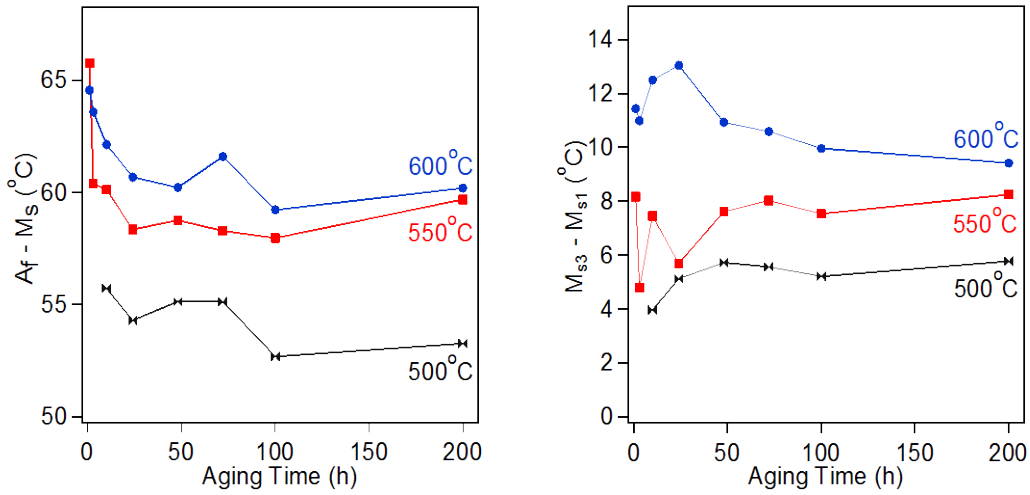

(a) (b)

Figure 5.5 The summary of (a) the shift in M_s (M_{s1} - M_{s3}) and (b) thermal hysteresis (A_f - M_s) during stress free DSC cycling of $Ni_{50.3}Ti_{34.7}Zr_{15}$ alloy aged at 500 °C, 550 °C and 600 °C for various durations.

5.1.3 Time-Temperature-Transformation Temperature Diagrams

The data derived from the DSC curves shown in Fig. 5.3, were re-plotted to generate the Time-Temperature-Transformation Temperature diagram (TTT) for the A_f and M_s temperatures of $Ni_{50.3}Ti_{34.7}Zr_{15}$ and shown in Figs. 5.6a and b, respectively. These TTT diagrams are very useful from the materials science perspective since it is possible to pick the aging conditions for specific transformation temperatures necessary for any type of application. The aging durations are converted to minutes and the horizontal axis of the diagrams is given in logarithmic scale in order to clearly express the trends in transformation temperatures as a function of aging time and temperature. Each curve in the diagrams represents the loci of a constant A_f or M_s. As seen from Fig. 5.6, the transformation temperatures always increase with the increase of aging time for

a fixed aging temperature (i.e. negative slope of the curves with time). Similarly, the transformation temperatures consistently increase with the increase of aging temperature at fixed aging durations. In $Ni_{50.3}Ti_{34.7}Zr_{15}$, there is either no transformation or no DSC signal within the measurement range (the DSC used in the present study can operate down to -80 ^{o}C) for short aging durations below 550 ^{o}C (i.e. 1 h or 3 h at 500 ^{o}C) as shown at the bottom left part of the TTT diagrams. These observations are completely in accordance with the trends seen in the DSC curves given in Fig. 5.3.

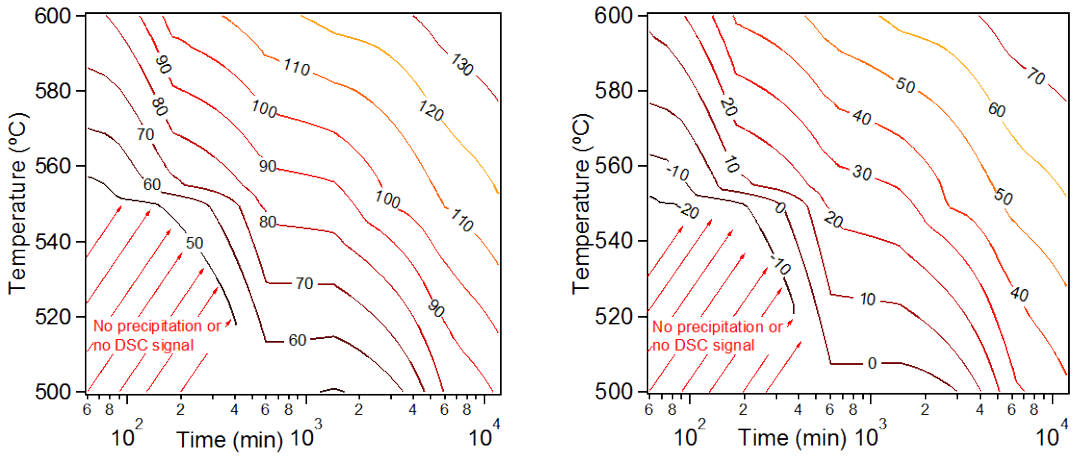

Figure 5.6 The Time-Temperature-Transformation Temperature (TTT) diagram of the $Ni_{50.3}Ti_{34.7}Zr_{15}$ alloy for (a) A_f and (b) M_s. Each curve in the plots corresponds to a loci of a constant A_f or M_s.

5.1.4 Load-biased Shape Memory Response

The shape memory response of the $Ni_{50.3}Ti_{34.7}Zr_{15}$ alloy was studied via load-biased thermal cycling tests in tension. Experiments were carried out on the samples

showing good thermal stability, relatively low thermal hysteresis and relatively high transformation temperatures. The evolution of transformation temperatures, recovered and unrecovered strain levels and thermal hysteresis as a function of applied stress were measured using the thermal cycles as shown in Fig. 3.2. The load-biased thermo-mechanical cycles of these samples are given in Fig. 5.7. The thermo-mechanical response under various applied stress levels are shown with different colors and the heat treatment applied to the samples are indicated on top left corners of the graphs. Except the sample aged at 600 ^{o}C for 100 h (Fig. 5.7d) all the samples show perfect shape recovery, i.e no open strain loops, even under 300 MPa applied stress levels due to increased matrix strength with precipitation.

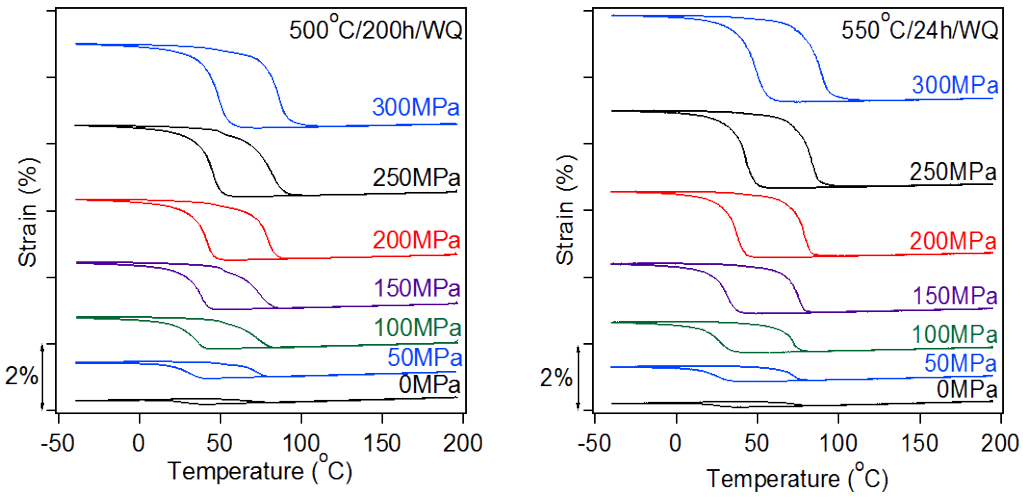

(a) (b)

Figure 5.7 Strain vs temperature response of the $Ni_{50.3}Ti_{34.7}Zr_{15}$ alloy in tension for the samples aged at (a) 500 ^{o}C for 200 h, (b) 550 ^{o}C for 24 h, (c) 550 ^{o}C for 100 h and (d) 600 ^{o}C for 100 h.

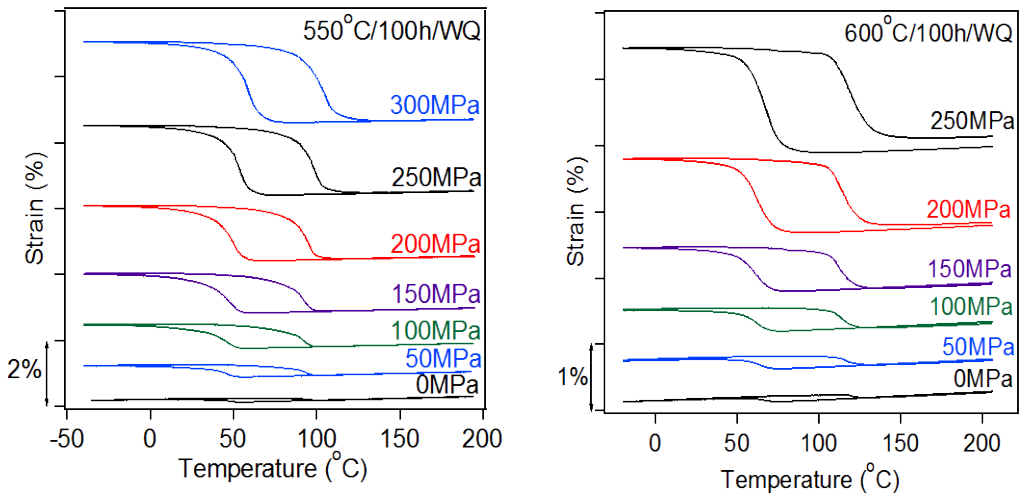

(c) (d)

Figure 5.7 Continued.

The recovered and unrecovered strain (which is a measure of dimensional stability in an SMA) levels of the aged $Ni_{50.3}Ti_{34.7}Zr_{15}$ specimens derived from Fig. 5.7 are given in Fig. 5.8. The strain levels show a continuous increase with the applied stress and reach to around 2.45% for the samples aged at 500 ^{o}C for 200 h and at 550 ^{o}C for 24 h and 100 h under 300 MPa applied stress. However, the sample aged at 600 ^{o}C for 100 h fails at applied stress levels above 250 MPa and show a maximum recovered strain level of 1.2%. The unrecovered strain levels were measured at temperatures 30 ^{o}C above the A_f for each applied stress as the difference in strain between the heating and cooling curves. Except the sample aged at 600 ^{o}C for 100 h, all the aged samples show perfect dimensional stability up to 300 MPa stress levels as a consequence of the increased resistance for plastic deformation due to precipitation hardening. However, since the precipitates gets remarkably larger for aging 100 h at 600 ^{o}C, the precipitation hardening

is less prominent as compared to other aged samples with smaller nanoparticles. Therefore this sample starts to show unrecovered strain already under 200 MPa applied stress (0.05%) and this increases up to 0.15% under 250 MPa.

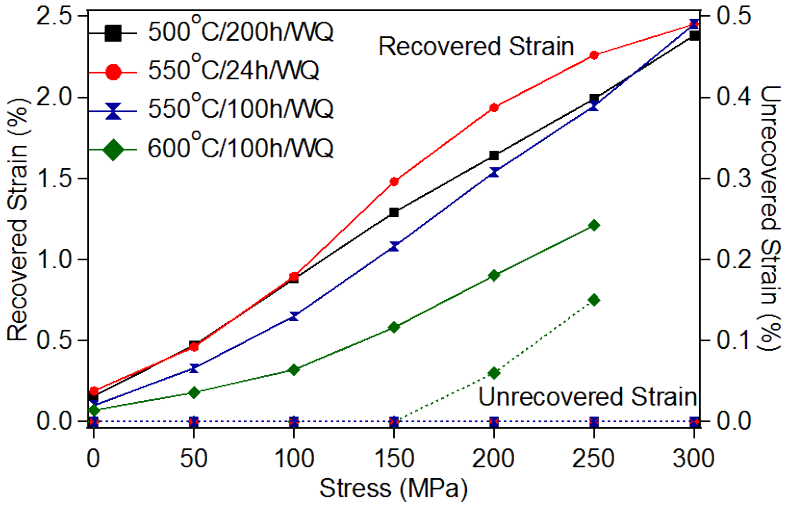

Figure 5.8 Recovered and unrecovered strain levels of the aged $Ni_{50.3}Ti_{34.7}Zr_{15}$ samples during thermal cycling in tension.

In most of the aged samples there is no sign of plastic deformation as seen from Fig. 5.8. Therefore one can argue that the applied stress levels are still lower than the stress levels where plastic slip becomes dominant over martensitic twinning which will result in a decrease in recovered strain levels due to the incomplete transformation of martensite to austenite. This significant increase to the plastic deformation is provided through formation of nanosize precipitates. This effect is more obvious in the transformation thermal hysteresis values as seen from Fig. 5.9a. As commented above, the precipitation hardening is probably less prominent in the sample aged at 600 ^{o}C for

100 h, hence larger thermal hysteresis is obtained in this sample compared to the samples with smaller precipitates. It can also be argued that the increased number of precipitate-martensite variant interfaces due to large precipitate sizes in this sample can result in increased energy dissipation and larger thermal hysteresis. Furthermore, the initial decrease in the hysteresis and increase after 150 MPa applied stress level is consistent with the unrecovered strain levels seen in Fig. 5.8 where the sample aged at 600 ^{o}C for 100 h starts to undergo plastic deformation and defect generations such as dislocations occurring under applied stress levels of 200 MPa or above increases the hysteresis. The decrease in the thermal hysteresis with the increase in applied stress seen in the other samples is probably due to the change in lattice parameters of the transforming phases with the applied stress. The lattice compatibility between austenite and martensite is a function of lattice parameters and it may be improved under applied stress which could decrease the thermal hysteresis. The thermal hysteresis obtained in aged $Ni_{50.3}Ti_{34.7}Zr_{15}$ samples are higher than the $Ni_{50.3}Ti_{29.7}Hf_{20}$ HTSMA (<28 ^{o}C) probably due to the differences in the lattice parameters and hence in the lattice compatibility [23].

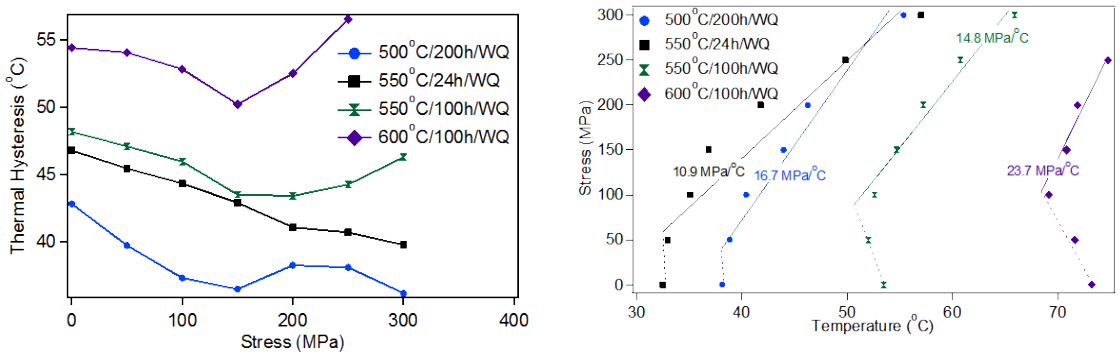

(a) (b)

Figure 5.9 The evolution of the (a) thermal hysteresis and (b) M_s temperatures of aged $Ni_{50.3}Ti_{34.7}Zr_{15}$ samples during thermal cycling in tension as a function of applied stress.

The evolution of the M_s temperatures as a function of applied stress, i.e. Clausius-Clapeyron (CC) relationship, with the best linear fit lines for the aged samples is given in Fig. 5.9b. The transformation temperatures corresponding to zero stress thermal cycle well match with the stress free DSC temperatures. As seen from Fig. 5.9b, M_s does not follow a linear stress dependence at low stress levels: up to 50 MPa for the samples aged at 500 ^oC for 200 h and at 550 ^oC for 24h and up to 100 MPa for the samples aged at 550 ^oC for 100 h and at 600 ^oC for 100 h while they show linear stress dependence at higher applied stress levels with slopes of 16.7 MPa/^oC, 10.9 MPa/^oC, 14.8 MPa/^oC and 23.7 MPa/^oC, respectively. Although, the reason why the CC-relationship is not valid at low applied stress levels and needs further investigation, it is probably due to the modified strain energy around the precipitates with the external applied stress. The strain energy is increased when the martensitic variant distribution is modified by an external stress and hence a tendency to decrease the transformation

temperatures occurs. At low applied stress levels this effect may overcome the expected increase in transformation temperatures caused by the external stress and hence M_s may initially decrease under low applied stress levels. Furthermore, as seen from Fig. 5.9b, higher stresses are needed to increase M_s in the samples with large precipitates (600 ^oC/100 h aged sample with 23.7 MPa/^oC slope) compared to the samples with smaller precipitates.

5.2 Microstructural Characterization and Shape Memory Response of $Ni_{50.3}Ti_{34.7}Hf_{15}$

As it was applied to all the studied alloys in the present work, the $Ni_{50.3}Ti_{34.7}Hf_{15}$ samples were first SHT at 900 ^oC for 1 h and subsequently aged at various aging temperatures for different durations. The WDS analysis of samples after SHT given in Table 5.2 showed a loss of ~ 0.7 at.% Hf, a gain of ~ 0.8 at.% Ti and a slight loss of Ni compared to the nominal compositions.

Table 5.2 Composition of the present $Ni_{50.3}Ti_{34.7}Hf_{15}$ SMA after solution heat treatment at 900 ^oC for 1 h measured through WDS. ± indicates the standard deviation from a total of 10 measurements over the specimens.

	Ni (at.%)	Ti (at.%)	Hf (at.%)
Measured	50.23 ± 0.2	35.50 ± 0.2	14.27 ± 0.04
Nominal	50.3	34.7	15.0

The BSE image given in Fig. 5.10 shows that the matrix has a homogeneous structure with heterogeneously distributed bright particles <3 μm in size which were identified as hafnium carbide particles through EDS. These carbides are likely to be formed by diffusion of some amount of carbon from the graphite crucibles into the molten material during vacuum induction melting of the alloy, promoting a small Hf loss compared to the nominal composition. The accurate measurement of the volume fraction of the carbide particles was not possible since they were not homogeneously distributed throughout the matrix but it is small enough to consider these particles as irrelevant for the present study.

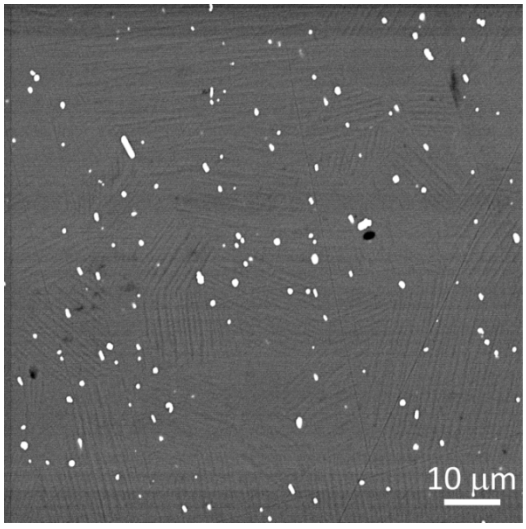

Figure 5.10: Back scattered electron image of solution heat treated $Ni_{50.3}Ti_{34.7}Hf_{15}$ SMA. Bright particles are identified as carbide inclusions (mainly HfC) via EDS.

5.2.1 Microstructure

On the basis of the DSC results that will be shown later, the microstructures of the samples showing best thermal stability (sample aged at 450 ^{o}C for 10 h, hereafter labeled as NTH450WQ), samples showing relatively low thermal hysteresis (samples aged at 500 ^{o}C for 3 h and 550 ^{o}C for 3 h, hereafter labeled as NTH500WQ and as NTH550WQ, respectively) and samples showing the highest M_s temperature (sample aged at 600 ^{o}C for 10 h, hereafter labeled as NTH600WQ) were investigated by TEM to reveal the general microstructure and precipitate size. The bright field and high resolution TEM images of the aged $Ni_{50.3}Ti_{34.7}Hf_{15}$ samples are given in Figs. 5.11a to d in which precipitates are marked with white circles in Figs 5.11a to c to emphasize their shape and size; some precipitates are labeled with letter P in Fig. 5.11d to better distinguish them from the martensitic variants. After aging at 450 ^{o}C for 10 h (Fig. 5.11a), the precipitates are ellipsoidal in shape with 4-7 nm in length and 3-4 nm in width and are coherent with B2 phase matrix. The SADP given in the inset image in Fig. 5.11a (recorded along the $[111]_{B2}$ zone axis) shows extra diffraction spots at 1/3 and 2/3 of the distances along the fundamental 110_{B2} spots that correspond to the H-phase precipitates [114]. After aging at 500 ^{o}C for 3 h, the precipitates are still ellipsoidal in shape but grow to 7-20 nm in length and 3-6 nm in width (Fig. 5.11b) and further grow to 10-20 nm in length and 7-12 nm in width after aging at 550 ^{o}C for 3 h (Fig. 5.11c). On the other hand, aging at 600 ^{o}C for 10 h results in significant coarsening of the precipitates that are spindle-like in shape with a size of 60-300 nm in length and 20-50 nm in width (Fig. 5.11d). As explained in detail in Chapter IV (section 4.6), the

martensite variants can accommodate the strain fields around the small precipitates and therefore totally absorb them (Figs. 5.11a, b and c) whereas they become impenetrable obstacles for the variants and limit their growth when they are several hundred of nanometers in size (Fig. 5.11d). Similar effects of precipitate size on the martensite morphology were reported on Ni-rich binary NiTi [121] and other SMA systems like Cu-Zn-Al [123,124] or Co-Ni-Ga [125] before.

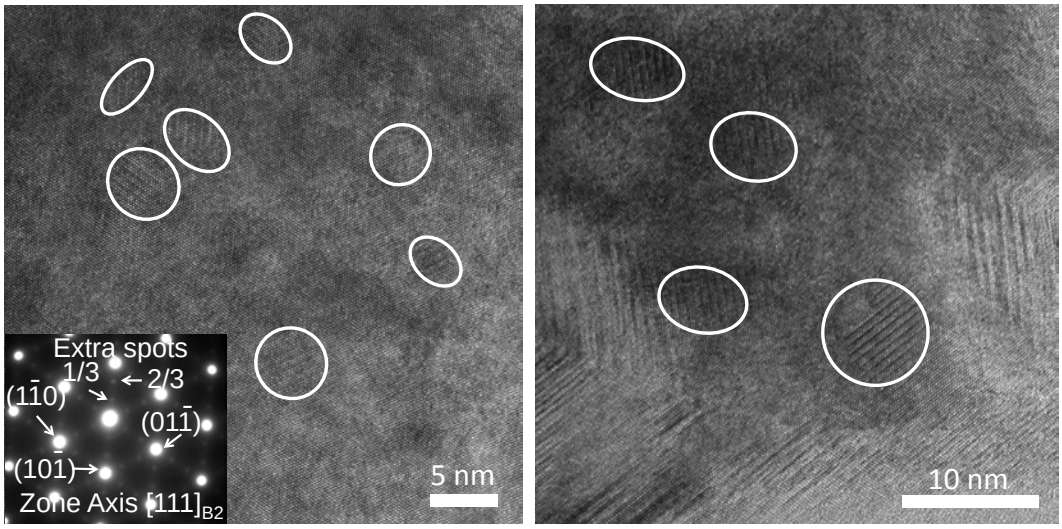

(a) (b)

Figure 5.11: Bright field TEM of $Ni_{50.3}Ti_{34.7}Hf_{15}$ samples aged at (a) 450 ^{o}C for 10 h together with the SADP (inset) showing the fundamental spots of the B2 austenite and the additional 1/3(110) spots of the precipitate phase. (b) 500 ^{o}C for 3 h, (c) 550 ^{o}C for 3 h and (d) 600 ^{o}C for 10 h. For clarity reasons, the precipitates are circled in images a, b and c and denoted with letter "P" in image d.

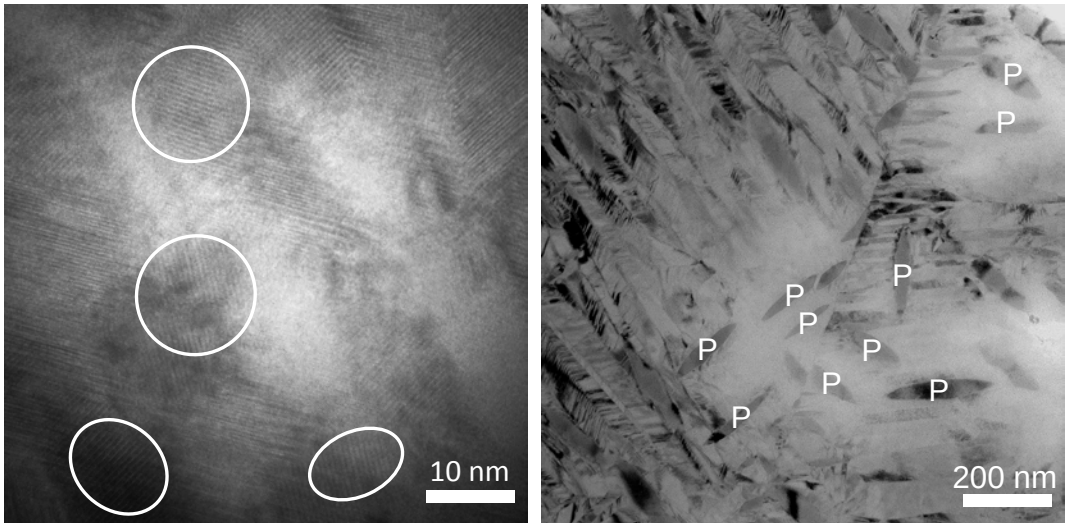

(c) (d)

Figure 5.11: Continued.

5.2.2 Transformation Temperatures and Characteristics

This section of the present work covers the results of the DSC experiments performed on the solution heat treated and aged $Ni_{50.3}Ti_{34.7}Hf_{15}$ samples. Figs. 5.12a to d show the stress free DSC cycles of the SHT and aged samples at 450 ^{o}C, 500 ^{o}C, 550 ^{o}C and 600 ^{o}C, respectively. The DSC curve for the SHT sample was given at the bottom of each plot for comparison with the aged samples. Fig. 5.12 indicates that $Ni_{50.3}Ti_{34.7}Hf_{15}$ samples always undergo one step transformation during the forward and reverse transformation. Hence, it can be concluded that there is no R-phase transformation seen which is in contradiction to the results of Javadi et al. [126] on $Ni_{50.3}Ti_{34.7}Hf_{15}$ and Meng et al. [53-55] on several Ni-rich NiTiHf alloys. Furthermore, transformation temperatures are expected to be increased due to the precipitation and hence Ni-depletion of the matrix compared to SHT state (900 ^{o}C/1 h/WQ). However, as seen from

Fig. 5.12a and b, the transformation temperatures initially decrease after aging at 450 ^{o}C and 500 ^{o}C for short durations such as 1 h and 3 h and increased with further aging at those temperatures. Moreover, along with the decrease in transformation temperatures, i.e. for the samples aged at 450 ^{o}C for 1 h and 3 h, sharp DSC peaks are obtained during the forward transformation. The reasons or the initial decrease in transformation temperatures and for the sharp DSC peaks seen are further commented below. At relatively higher aging temperatures such as 550 ^{o}C and 600 ^{o}C, the transformation temperatures show a constant increase with aging as expected due to the Ni-depletion of the matrix.

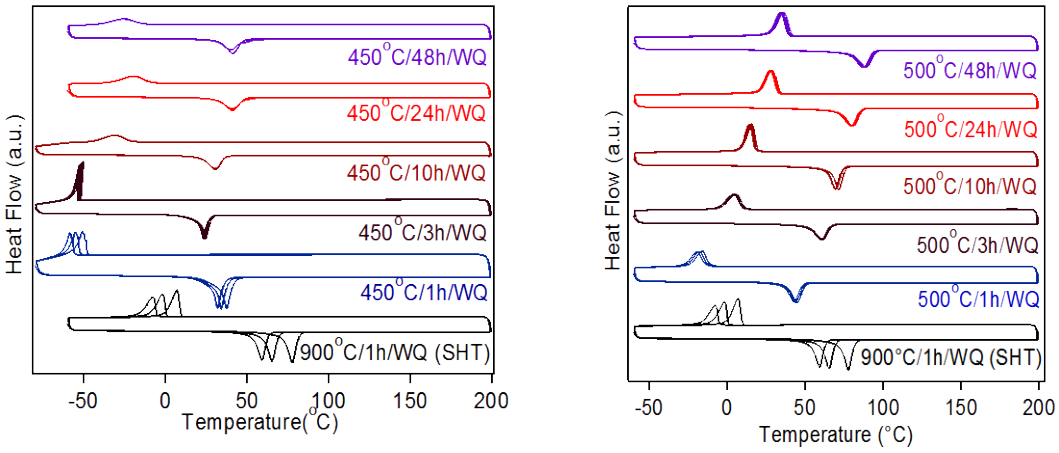

(a) (b)

Figure 5.12 The stress free DSC cycles of $Ni_{50.3}Ti_{34.7}Hf_{15}$ alloy aged at (a) 450 °C, (b) 500 °C, (c) 550 °C and (d) 600 °C for various durations.

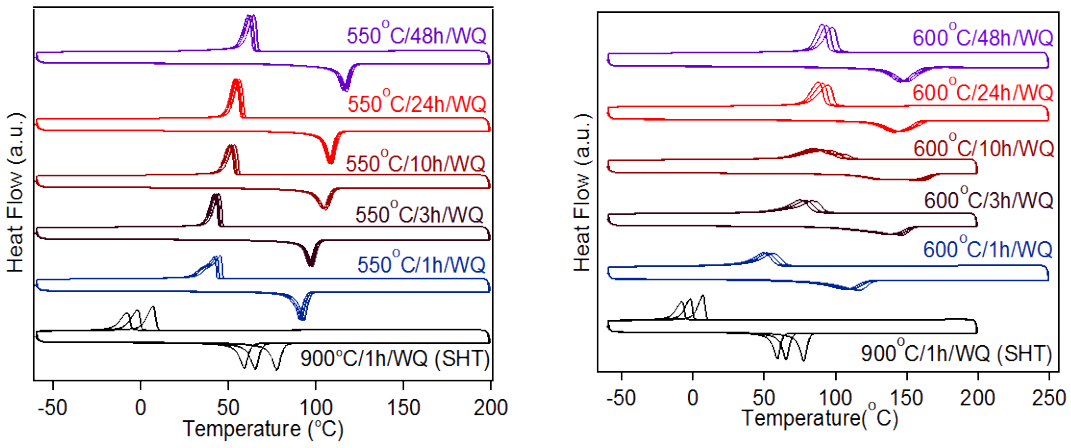

(c) (d)

Figure 5.12 Continued.

The summary of A_f and M_s temperatures for the SHT and the samples aged at 450 ^oC, 500 ^oC, 550 ^oC and 600 ^oC for different durations are given in Figs. 5.13a and b, respectively. The transformation temperatures measured after SHT (A_f ~ 82 ^oC and M_s ~ 10 ^oC) are given as the zero hour aging in the plots and assumed as the initial transformation temperatures of the alloy for comparison with those obtained after aging. It is obvious from Figs. 5.13a and b that the transformation temperatures of $Ni_{50.3}Ti_{34.7}Hf_{15}$ SMA can be altered in a wide temperature range as a consequence of precipitation: from 25 ^oC to 170 ^oC for A_f, i.e. a 145 ^oC temperature window and from -45 ^oC to 115 ^oC for M_s (160 ^oC temperature window). Furthermore, as seen from Figs. 5.13a and b, two trends on the A_f and M_s temperatures are visible: i) an initial decrease after short duration aging at the lowest temperatures (1 h and 3 h at 450 ^oC and 1 h at 500 ^oC) and a subsequent increase with further aging, ii) a constant increase after aging

at 550 ^{o}C and 600 ^{o}C. It should be noted that transformation temperatures reach a plateau region at temperatures slightly lower than the ones observed after aging for 10 h at 600 ^{o}C. As seen from Figs. 5.4 and 5.13, the transformation temperatures of the $Ni_{50.3}Ti_{34.7}Zr_{15}$ SMA are inferior compared to $Ni_{50.3}Ti_{34.7}Hf_{15}$ SMA.

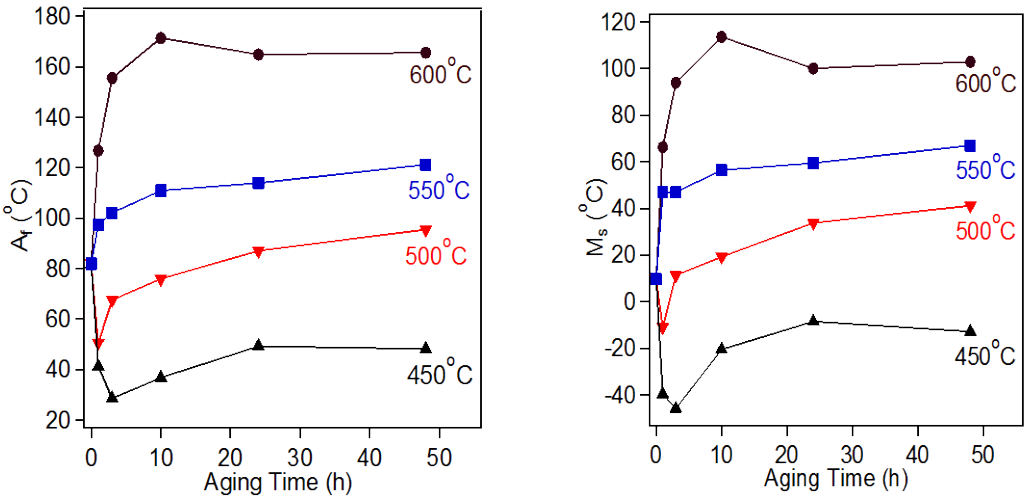

(a) (b)

Figure 5.13 Summary of the transformation temperatures of $Ni_{50.3}Ti_{34.7}Hf_{15}$ alloy aged at 450 ^{o}C, 500 ^{o}C, 550 ^{o}C and 600 ^{o}C for different durations (a) A_f and (b) M_s. A_f and M_s for the SHT sample are 10 ^{o}C and 82 ^{o}C, respectively.

The thermal hysteresis (A_f - M_s) values of the SHT and aged $Ni_{50.3}Ti_{34.7}Hf_{15}$ samples are shown in Fig. 5.14a. Although there is no clear trend in thermal hysteresis values with aging time, in most of cases the values lie between 50 ^{o}C and 65 ^{o}C. These thermal hysteresis values are generally comparable to $Ni_{50.3}Ti_{34.7}Zr_{15}$ samples as seen from Fig. 5.5a. The thermal hysteresis values of aged samples are lower than the

thermal hysteresis exhibited by the SHT samples (~ 72 ^{o}C). This is attributed to the precipitation hardening of the matrix, which results in a decrease of the energy dissipation during transformation. However, exceptions are visible for aging conditions resulting in a decrease in transformation temperatures, such as aging at 450 ^{o}C for 1 h and 3 h. The M_s decreases more remarkably compared to A_f which significantly increase the thermal hysteresis values, as seen in Fig. 5.14a. This case will be further commented below. The reduction in thermal hysteresis observed in the $Ni_{50.3}Ti_{34.7}Hf_{15}$ samples containing H phase precipitates constitutes a remarkable difference in relation to other SMAs containing precipitates, like Ni_4Ti_3 in Ni-rich binary NiTi [47], Nb-rich BCC nanoprecipitates in Ni-Ti-Nb [127], γ phase in Cu-Zn-Al [124] or γ' phase in Co-Ni-Ga [125] in which the precipitates increase the MT hysteresis in relation to the single phase (solution heat treated) state. For Ni-Ti-Nb, Cu-Zn-Al or Co-Ni-Ga alloys, the transformation hysteresis can be particularly enhanced up to a factor ~ 6 in the case of dense dispersions of large precipitates, when the particles cannot be absorbed by the growing martensite plates [35,36,42]. The large increase in hysteresis is attributed to remarkable difficulties for accommodating the transformation strain around the non transforming particles as well as to the significant increase on the number of intervariant boundaries when the martensite phase growth is limited to the space between particles [124,125,127]. A very small lattice misfit between precipitates and B2 matrix has been seen for the H phase in Ni-rich NiTiHf and NiTiZr alloys (Chapter IV). The reduced transformation hysteresis observed in $Ni_{50.3}Ti_{34.7}Hf_{15}$ alloy indicates a relatively easier accommodation of the transformation strain around the non transforming H phase

particles compared to other SMAs. Thus, the matrix strengthening as a consequence of the H phase precipitation, especially in the case of nanometric particles, would decrease the defect generation during MT and, hence, reduce the transformation hysteresis. However, the increase in the number of intervariant boundaries when the martensite phase growth is limited to the space between particles, like in the NTH600WQ samples, actually increases the energy dissipation during MT and results in higher hysteresis values compared to the samples with nanometric particles absorbed by the growing martensite plates (NTH450WQ, NTH500WQ and NTH550WQ), as seen in Fig. 5.14a.

The thermal stability of the transformation temperatures were investigated via stress free thermal cycles in DSC. Fig. 5.14b represents the change in M_s temperatures after three thermal cycles. The change in M_s in the SHT sample is remarkably large (15 ^oC), but it decreases significantly with aging and almost saturates after 10 h, at different values as a function of the aging temperature due to precipitation hardening. Samples aged at 450 ^oC show the best thermal stability whereas samples aged at 600 ^oC show the largest shifts in M_s. The thermal stability of the $Ni_{50.3}Ti_{34.7}Hf_{15}$ alloy is much better than the $Ni_{50.3}Ti_{34.7}Zr_{15}$ alloy. This is probably due to the better lattice compatibility of the transforming phases in $Ni_{50.3}Ti_{34.7}Hf_{15}$ alloy.

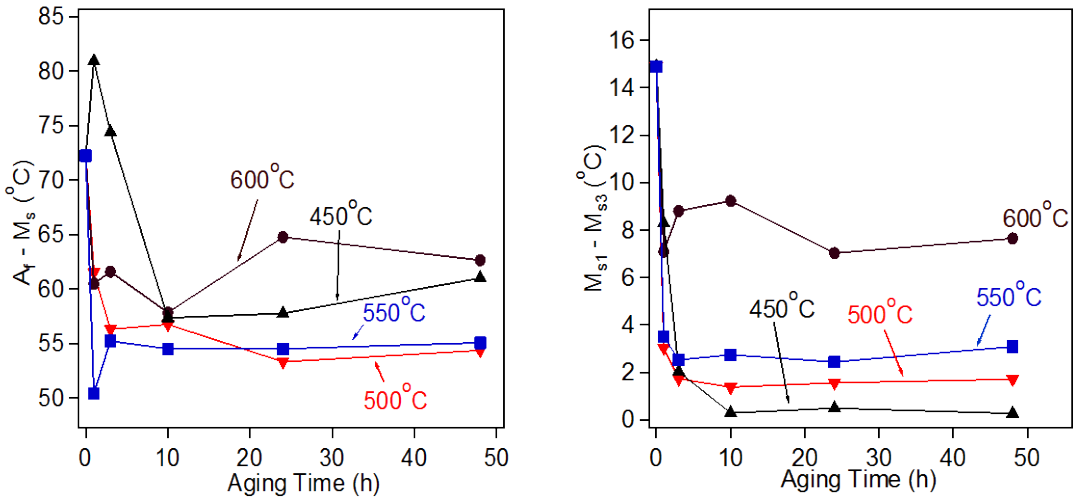

(a) (b)

Figure 5.14 The summary of (a) the shift in M_s (M_{s1} - M_{s3}) and (b) thermal hysteresis (A_f - M_s) during stress free DSC cycling of $Ni_{50.3}Ti_{34.7}Hf_{15}$ alloy aged at 450 °C, 500 °C, 550 °C and 600 °C for various durations.

5.2.3 Effect of Microstructure on Transformation Temperatures and Characteristics

Combining the microstructural observations by TEM with the observed evolution of transformation temperatures in the aged $Ni_{50.3}Ti_{34.7}Hf_{15}$ SMA, two different mechanisms affecting the martensitic transformation can be considered namely "interparticle spacing" which is a function of several factors such as precipitate size and the volume fraction and "compositional effect", in which precipitates also play a role through changing the matrix composition. Panchenko et al. showed in a binary Ni-rich NiTi SMA that interparticle spacing is a function of precipitate size and volume fraction which can be modified with aging [47]. In the present study, the TEM images reveal that interparticle spacing is very small when the precipitates are a few nm in size, but it gets

larger with the increase in particle size for a given volume fraction of precipitates (Figs. 5.11a to d). For a case when the critical size for the nucleation of martensite is larger or comparable to the interparticle spacing, the nucleation of martensite and thus martensitic transformation may be suppressed. In such a condition, the extra energy necessary to overcome the precipitate barriers in order to reach critical size for nucleation should be provided through undercooling. On the other hand, the irregular development of the transformation once the nucleation barriers are overcome increases the energy dissipation which is well in accordance with the increase in thermal hysteresis seen in Fig. 5.14a. Thus, a decrease in the martensitic transformation temperatures (M_s) is expected when the interparticle spacing is very small. This is the case of NTH450WQ and NTH500WQ samples, with interparticle spacing below ~10 nm (Figs. 5.11a and b). At the same time, since the Ni content of the matrix decreases with the precipitation of Ni-rich particles, a continuous increase in M_s with the precipitate volume fraction should also be expected. However, despite the Ni-content of the matrix also diminishes during short duration aging at 450 ^{o}C or 500 ^{o}C, the suppression effect of interparticle spacing is the dominant mechanism on martensitic transformation and hence M_s decreases. In turn, aging at elevated temperatures (550 ^{o}C or 600 ^{o}C) generates larger interparticle distances and precipitate volume fractions from the beginning and the compositional change of the matrix become the dominant effect leading to a continuous increase in transformation temperatures. It should be noted that M_s starts to increase after 3 h aging at 450 ^{o}C but it does not reach the SHT level even after 48 h aging (Fig. 5.13b). It means that the two mechanisms, namely “interparticle spacing” and “compositional effect”, are

in competition during the whole aging series at 450 ^{o}C and the precipitate volume fraction does not sufficiently increase to recover M_s to the SHT case level with aging. Similar conclusions can be made for aging at 500 ^{o}C for 3 h where precipitate volume fraction is barely enough for M_s to get back to SHT level.

In order to further analyze the competition between these two mechanisms, additional aging treatments for durations less than 1h (e.g. 20 min and 50 min) at intermediate temperatures between 450 ^{o}C and 550^{o}C (i.e. 450 ^{o}C, 475 ^{o}C, 500 ^{o}C and 525 ^{o}C) were performed and the corresponding DSC curves are given in Fig. 5.15. DSC curve of the SHT sample is shown at the bottom of the figure for comparison. Fig. 5.15 shows that M_s decreases almost by 55 ^{o}C and 65 ^{o}C after aging for 20 minutes and 50 minutes at 450 ^{o}C, respectively, compared to M_s in SHT case (~10 ^{o}C). Very small precipitates already form during the first few ten minutes of aging at 450 ^{o}C and the change in precipitate size with aging up to 50 minutes is probably negligible but instead, the volume fraction of these small precipitates increases. Hence, the interparticle spacing gets smaller and M_s continues to decrease. Additionally, the DSC curves of samples aged at 450 ^{o}C (Figs. 5.12a and 5.15) demonstrate very sharp martensitic transformation peaks indicating that the forward transformation is strongly nucleation controlled. Indeed, these sharp DSC peaks are in accordance with harder nucleation of martensite and extra undercooling necessary to start martensitic transformation. The extra energy provided through undercooling allows the martensite to reach the critical nuclei size and, then, propagate instantly resulting in a very sharp DSC peak. As a matter of fact, the rapid release of transformation heat produces small heating of the sample and DSC

sensor, which slightly tilts the DSC peak to higher temperatures. The MT temperatures also decrease during aging at 475 ^{o}C and 500 ^{o}C for 20 and 50 minutes compared to the SHT case (Fig. 5.15). Sharp beginning of DSC peaks is also observed during aging at 475 ^{o}C which shows that martensitic transformation is still strongly nucleation controlled. In turn, the DSC peak is not sharp anymore after aging at 500 ^{o}C and 525 ^{o}C in coincidence with the increase of MT temperatures, indicating that nucleation difficulties are less prominent.

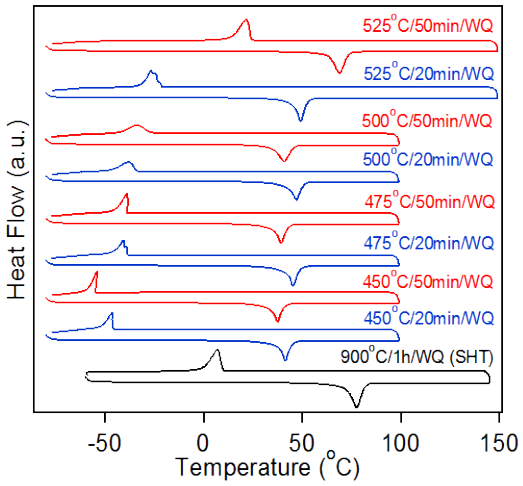

Figure 5.15 The stress free DSC cycles of $Ni_{50.3}Ti_{34.7}Hf_{15}$ alloy aged at temperatures from 450 ^{o}C to 525 ^{o}C for 20 and 50 minutes. DSC curves show very sharp peaks indicating martensitic transformation is nucleation controlled for aging at 450 °C and 475 °C. Transformation temperatures decreased significantly compared to solution heat treated sample due to suppressed martensitic transformation during aging at 450 ^{o}C, 475 ^{o}C and 500 ^{o}C. M_s starts to increase after the initial decrease during aging at 500 ^{o}C and 525 ^{o}C.

The DSC curves corresponding to the aging at 500 ^{o}C, 550 ^{o}C and 600 ^{o}C (Figs. 5.12b, c and d), represent the continuous increase in M_s for aging times longer than 1 h, as a consequence of the Ni-depletion of the matrix with precipitation. Though an initial decrease compared to SHT case can still be observed for 1 h aging at 500 ^{o}C. Considering the observations in Figs. 5.13b and 5.15, one can conclude that M_s will show a decrease in the early stages of aging at low temperatures (e.g. 450 ^{o}C, 475 ^{o}C, 500 ^{o}C and 525 ^{o}C) due to the presence of nanometric particles, followed by an increase for long aging times, whereas M_s will continuously increase upon aging at elevated temperatures (e.g. 550 ^{o}C and 600 ^{o}C) as a consequence of large precipitate size and high volume fraction. The effect of these two mechanisms, "interparticle spacing" and "*compositional change*", on M_s as a function of aging time and temperature is schematically represented in Fig. 5.16.

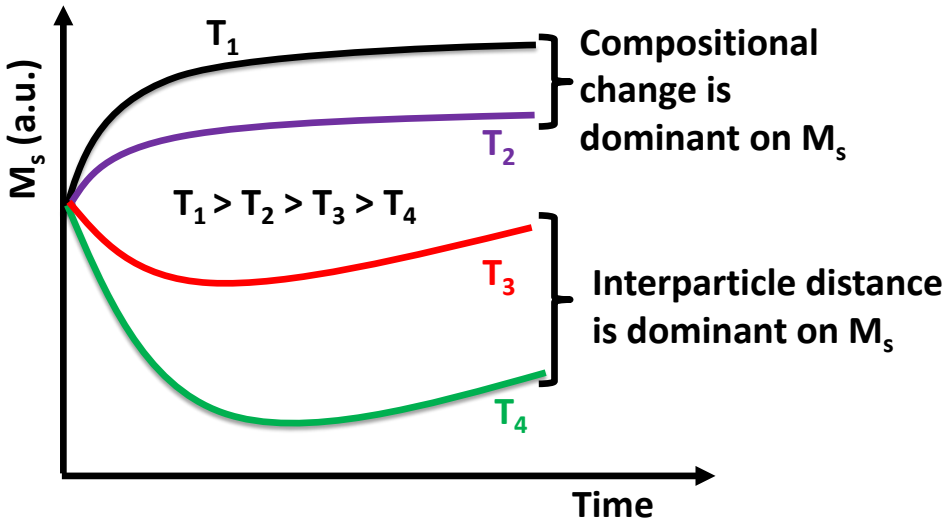

Figure 5.16 The representation of the effect of "*interparticle spacing*" and "*compositional change*" on M_s as a function of aging temperature and time. T_1, T_2, T_3 and T_4 indicate the aging temperatures. M_s decreases initially during low temperature aging (T_3 and T_4) due to small interparticle spacing and increases with further aging. M_s increases continuously due to remarkable compositional change of matrix during aging at elevated temperatures like T_1 and T_2.

5.2.4 Time-Temperature-Transformation Temperature Diagrams

The data derived from the DSC measurements were re-plotted to generate the Time-Temperature-Transformation Temperature diagram (TTT) for the A_f and M_s temperatures of $Ni_{50.3}Ti_{34.7}Hf_{15}$ SMA as shown in Figs. 5.17a and b, respectively. The trends of A_f and M_s seen in Figs. 5.13 and 5.15 as a function of aging time and temperature may seem to be counter intuitive concerning the "*interparticle spacing and compositional effects*" on the transformation temperatures discussed above. Thus, the diagrams in Fig. 5.17 have been split into two regions namely "Region 1 and Region 2" where these two mechanisms are effectively dominant. For instance, DSC measurements showed that transformation temperatures always increase for aging durations longer than

3 h at 450 ^{o}C and 475 ^{o}C; in its turn, a horizontal line in Fig. 5.17 at 450 ^{o}C or 475 ^{o}C will cross curves with increasing transformation temperatures for times higher than 180 min (i.e. negative slope of the curves with time). On the other hand, when the aging temperature is between 475 ^{o}C and 550 ^{o}C, transformation temperatures start to increase if the samples are aged for more than 1 h. However, aging durations exceeding 30 minutes will be sufficient to result in an increase in transformation temperatures at aging temperatures as high as 575 ^{o}C. This is more obvious during aging at 600 ^{o}C since there is a constant increase without any initial decrease of transformation temperatures (lines of constant transformation temperatures have only negative slope). The zone corresponding to the aging conditions where the change in the matrix composition continuously increases A_f and M_s with the increase in aging temperature or aging duration, as in the case of 600 ^{o}C, is labeled as Region 1 in Fig. 5.17.

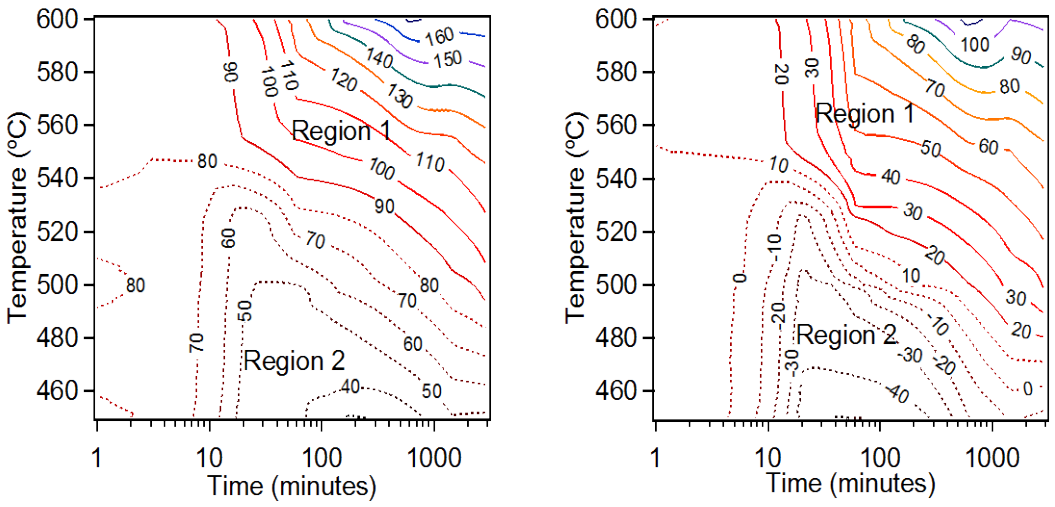

Figure 5.17 Effect of aging temperature and duration on the transformation temperatures of $Ni_{50.3}Ti_{34.7}Hf_{15}$ SMA. TTT diagram illustrating both the interparticle spacing (Region 1) and compositional effect (Region 2) on (a) A_f and (b) M_s. The loci of a constant transformation temperature in Region 1 is indicated with solid lines and dashed lines in Region 2. Initial A_f and M_s are 82 ^oC and 10 ^oC, respectively.

However, the trends of A_f and M_s as a function of aging time and temperature in Region 2 of Figs. 5.17a and b are more complicated as interparticle spacing becomes the dominant factor on the transformation temperatures. For a given aging temperature (i.e. an imaginary horizontal line in Fig. 5.17), the increase in aging time decreases transformation temperatures as a consequence of the further diminish in interparticle distances along with the increase in precipitate volume fraction. But after a certain amount of aging time, A_f and M_s starts to increase due to the increase in the precipitate size and volume fraction. These peculiarities of Region 1 and 2 are governed by two factors: *i)* nucleation and *ii)* diffusional growth of the H-phase precipitates [128]. Indeed, precipitate volume fractions and precipitate sizes, and hence the interparticle distances,

are strongly controlled by these two factors. At high aging temperatures, the thermal energy is high enough to allow rapid diffusion of atoms to the first particle nuclei created. Thus, instead of the formation of new precipitate nuclei, the ones already formed tend to grow and change the matrix composition rapidly. But at low aging temperatures nucleation rates are higher whereas diffusion occurs more slowly. Therefore, the precipitate density per unit area is large and the interparticle spacing is small. It is beyond the scope of the present article to accurately determine how the interparticle distances will be modified when these two factors are competing at various aging temperatures in Region 2, but this competition plays a crucial role in the observed fluctuations of MT temperatures.

5.2.5 Load-biased Shape Memory Response

The shape memory response of the SHT and several aged $Ni_{50.3}Ti_{34.7}Hf_{15}$ samples were investigated via load-biased thermal cycling tests. Experiments were performed on the aged samples showing relatively better thermal stability, low thermal hysteresis as well as relatively high transformation temperatures. The strain-temperature response of these thermal cycling experiments in tension is given in Figs. 5.18a to f, for all the tested samples. Independent of the precipitate size, the strain-temperature loops seen in Fig. 5.18 are nearly closed even at stress levels as high as 300 MPa indicating that the unrecovered strain levels are very small or negligible and thus the alloy shows excellent dimensional stability. Interestingly, the SHT sample without any precipitates can still shows very good dimensional stability (Fig. 5.18a). However, the effect precipitation

hardening becomes more dominant on transformation thermal hysteresis which will be further commented below.

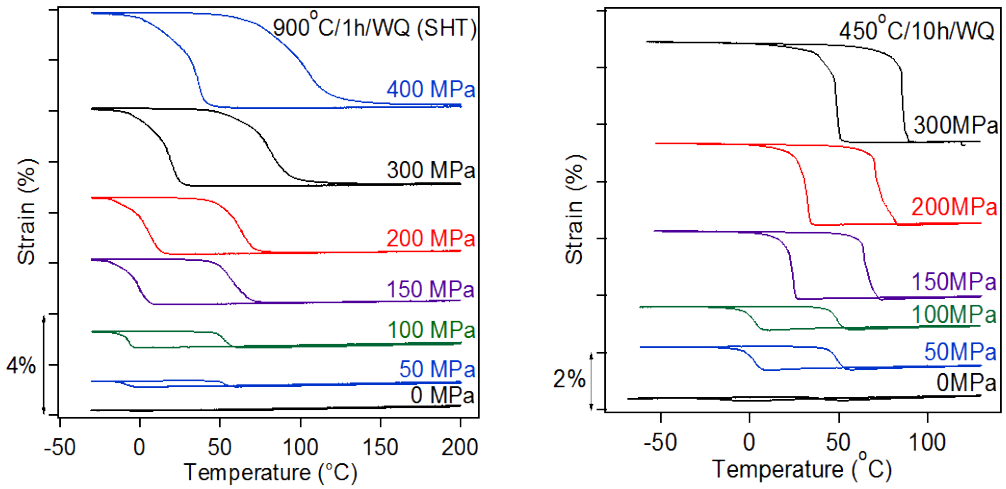

(a) (b)

Figure 5.18 Strain vs temperature response of the $Ni_{50.3}Ti_{34.7}Hf_{15}$ alloy in tension for the samples (a) SHT (at 900 °C for 1 h), (b) 450 °C for 10 h, (c) 500 °C for 3 h, (d) 550 °C for 3 h, (e) 550 °C for 10 h and (f) 600 °C for 10 h. Near close strain-temperature loops indicated excellent dimensional stability of the alloy up to 300 MPa stress level.

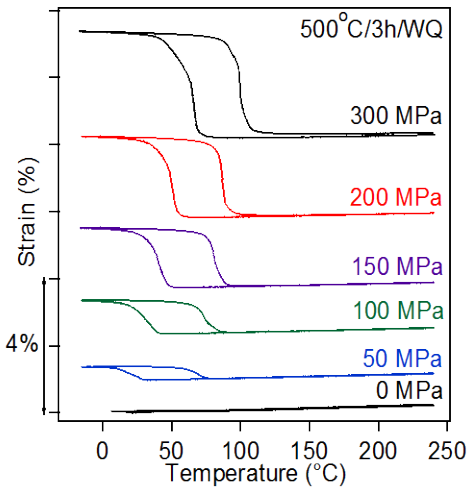

(c)

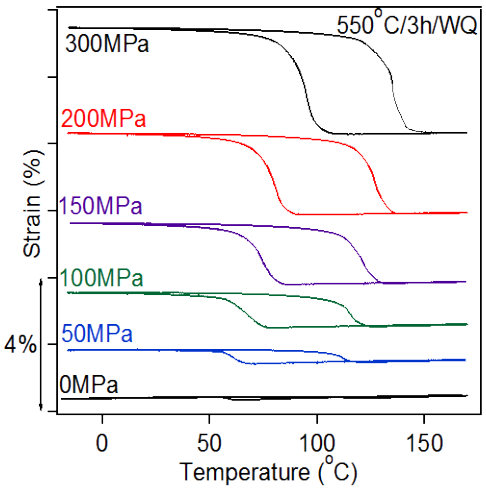

(d)

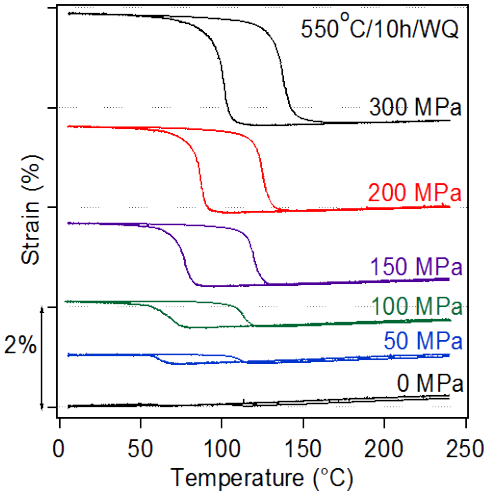

(e)

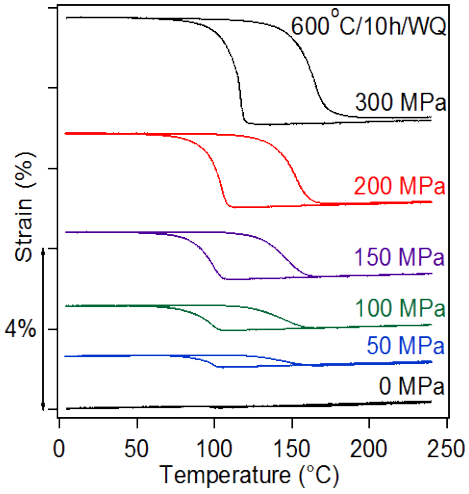

(f)

Figure 5.18 Continued.

The recovered and unrecovered strains of the SHT and aged samples for various applied stress levels are summarized in Fig. 5.19. The recovered strain levels are continuously increasing with the applied stress and they vary between 2.2% (sample

aged at 550 ^{o}C for 10 h) and 3.3% (sample aged at 450 ^{o}C for 10 h) under 300 MPa applied stress. On the other hand, the SHT sample can resist higher stress levels and reached to a maximum recovered strain level of 3.5% under 400 MPa. The unrecovered strain levels were measured at temperatures 30 ^{o}C above the A_f for each applied stress as the difference in strain between the heating and cooling curves. All the aged samples exhibit almost excellent dimensional stability and show no unrecovered strain up to 200 MPa and only 0.1% or less under 300 MPa stress level due to the increased critical stress for slip with precipitation hardening. However, the SHT sample starts to undergo plastic deformation under 150 MPa (0.02% unrecovered strain) but still shows good dimensional stability up to 400 MPa (0.1% unrecovered strain). Since these small or negligible unrecovered strain values are obtained already during the first few thermal cycles, it can be concluded that no prior training is necessary on the $Ni_{50.3}Ti_{34.7}Hf_{15}$ SMA to provide dimensional stability. Similar conclusions can be drawn for $Ni_{50.3}Ti_{34.7}Zr_{15}$ SMA too since the alloy shows almost excellent dimensional stability. Furthermore, the shape recovery of the present Ni-rich $Ni_{50.3}Ti_{34.7}Zr_{15}$ and $Ni_{50.3}Ti_{34.7}Hf_{15}$ SMAs is significantly better than other (Ti + Hf/Zr)-rich NiTiHf/Zr SMAs [29,55]. These two alloys also demonstrate better shape recovery compared to the Ni-rich NiTiHf alloy with the same stoichiometry reported by Javadi et al [126]. $Ni_{50.3}Ti_{34.7}Hf_{15}$ also shows higher transformation strain values than the $Ni_{50.3}Ti_{34.7}Zr_{15}$ alloy probably due to difference in the lattice parameters of the transforming phases.

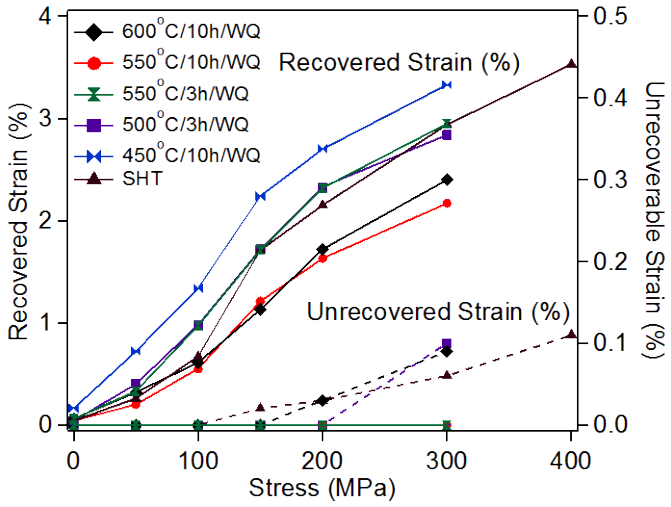

Figure 5.19 Recovered and unrecovered strain levels of the SHT and aged $Ni_{50.3}Ti_{34.7}Hf_{15}$ samples during thermal cycling in tension.

The maximum transformation strains obtained in $Ni_{50.3}Ti_{34.7}Hf_{15}$ alloy are lower than $Ni_{50.3}Ti_{29.7}Hf_{20}$ HTSMA or binary NiTi alloys. Two reasons could be responsible for the lower strain levels: the difference in the theoretical transformation strains or the incomplete martensite reorientation/detwinning under the stress levels applied. The theoretical transformation strains are probably lower in the $Ni_{50.3}Ti_{34.7}Hf_{15}$ alloy since they are a function of the lattice parameters of the transforming phases. However, $Ni_{50.3}Ti_{34.7}Hf_{15}$ SMA shows higher transformation strains than the $Ni_{50.3}Ti_{34.7}Zr_{15}$ SMA probably due to the difference in the lattice parameters and thus in the theoretical maximum strain levels. Moreover, as seen from Fig. 5.19, the strain levels continuously increase with the bias stress and they have not reached to a saturation point even under 300 MPa for aged samples and under 400 MPa for the SHT sample. Therefore, higher strain levels would be observed if the samples do not fracture when higher stresses are

applied. Although, the precipitate free SHT sample is slightly more ductile compared to aged samples and fails when tested above 400 MPa, the aged samples show always fracture when tested above 300 MPa probably due to the increase in matrix hardness with precipitation hardening. Similar conclusions can also be stated for the $Ni_{50.3}Ti_{34.7}Zr_{15}$ SMA where larger strains could be obtained if the specimens do not show failure.

Interestingly, the SHT $Ni_{50.3}Ti_{34.7}Hf_{15}$ SMA without precipitates already exhibits good dimensional stability since it shows comparable unrecovered strain levels to the precipitation hardened samples. This clearly indicates that the applied stresses have not reached the levels where plastic deformation becomes dominant over martensitic twinning and lead to a decrease in recovered strain through incomplete transformation of martensite to the austenite. Beside the dimensional stability, the effect of precipitation hardening becomes significantly prominent on the transformation thermal hysteresis levels which are summarized in Fig. 5.20a. The thermal hysteresis values are significantly smaller in the aged samples compared to the SHT sample, which is attributed to the harder generation of defects as a consequence of precipitation hardening, as commented above. Except the NTH600WQ sample in which thermal hysteresis remains nearly constant after the initial decrease, the thermal hysteresis values generally decrease with the increase in applied stress and are comparable to each other for all aged samples. It was argued formerly for the NiTiHfPd [129] and Co-Ni-Ga [130] SMAs that the lattice parameters of the austenite and martensite around the precipitates may change under applied stress and therefore better compatibility between the

transforming phases and hence smaller thermal hysteresis can be obtained. Since the thermal hysteresis is a function of the lattice compatibility between austenite and martensite, the decreasing thermal hysteresis seen in the $Ni_{50.3}Ti_{34.7}Hf_{15}$ SMA is probably a consequence of the change in the lattice parameters of the transforming phases and the improvement in the lattice compatibility. As mentioned above, the relatively higher thermal hysteresis obtained in the NTH600WQ sample is probably due to the difference in the precipitate size and martensite morphology. Higher amount of energy will be dissipated during the growth of large number of martensite variants and intervariant boundaries when the particles are coarsened and limit the growth of martensite plates. The increase in thermal hysteresis with the applied stress observed in SHT sample for stress levels above 150 MPa is consistent with the unrecovered strains shown in Fig. 5.19. The SHT sample started to show plastic deformation under 150 MPa stress level and defect formations such as dislocations with the increased applied stress leads to an increase in thermal hysteresis. Similar increase in transformation thermal hysteresis due to plastic deformation with the applied stress is also reported for an aged Ni-rich binary NiTi [131]. The present thermal hysteresis values are higher than the $Ni_{50.3}Ti_{29.7}Hf_{20}$ HTSMA (<28 ^{o}C) probably due to the differences in the lattice parameters and hence in the lattice compatibility [57] but are comparable to the $Ni_{50.3}Ti_{34.7}Zr_{15}$ alloy concerning the aged samples.

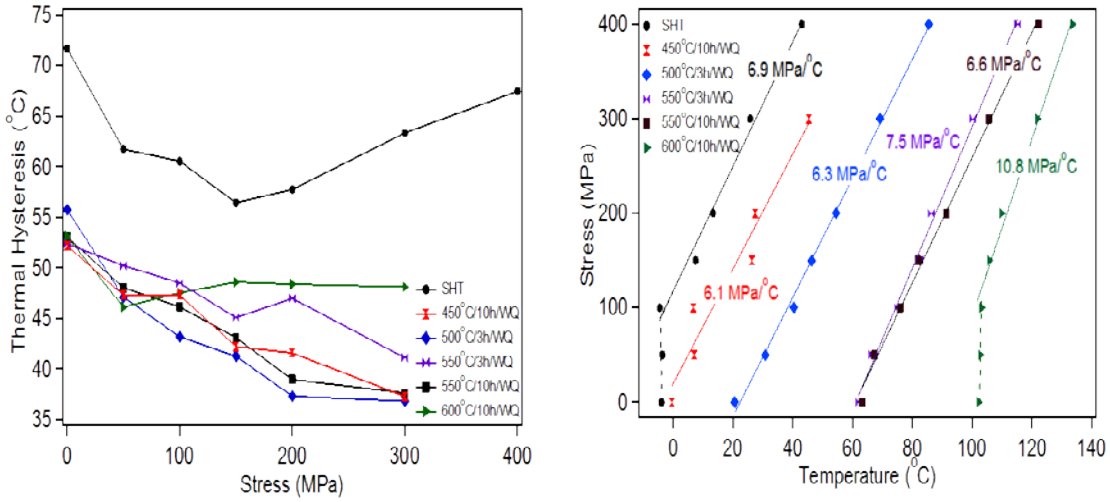

Figure 5.20 The evolution of the (a) thermal hysteresis and (b) M_s temperatures of SHT and aged $Ni_{50.3}Ti_{34.7}Hf_{15}$ samples during thermal cycling in tension as a function of applied stress.

The stress dependency of the M_s temperatures with the best linear fit lines for the SHT and aged samples are represented in Fig. 5.20b. The transformation temperatures measured from the zero stress thermo-mechanical cycle generally did not match with the stress free transformation temperatures obtained from DSC experiments (~ ± 10 ^oC). However, the strain-temperature responses under zero applied stress levels are generally very weak as seen in Fig. 5.18. Therefore, when the transformation temperatures are measured using the slope extension method as it is shown in Fig.3.2, some deviations from the original DSC values can be seen. As seen from Fig. 5.20b, the M_s temperatures of SHT sample and NTH600WQ sample were not changing with the applied stress up to 100 MPa but follow a linear stress dependence, i.e. a Clausius-Clapeyron (CC) relation, with slopes of 6.9 MPa/^{o}C and 10.8 MPa/^{o}C, respectively with the further increase in applied stress. However, M_s temperatures show a linear stress dependence over the entire

applied stress range for all the other aged samples. It is obvious from Fig. 5.20b that samples with no precipitates (SHT) or with very small precipitates (< 20nm) such as NTH450WQ, NTH500WQ and NTH550WQ, show smaller CC slope compared to the NTH600WQ with large precipitates. TEM investigations showed that the martensite variants can absorb the precipitates when they are small (<20 nm) and hence there is negligible interference during the martensitic transformation. On the other hand, the precipitates become impenetrable obstacles for the martensite plates when they are coarsened such as in the case of NTH600WQ sample. Considering the CC relationships shown in Fig. 5.20b and the TEM observations (Fig. 5.11), it can be concluded that less stress is necessary to increase M_s when the samples have no or small precipitates compared to the samples with large precipitates in $Ni_{50.3}Ti_{34.7}Hf_{15}$ SMA.

5.3 Summary and Conclusions

This part of the present work focuses on the microstructure, transformation characteristics and shape memory response of the Ni-rich $Ni_{50.3}Ti_{34.7}Zr_{15}$ and $Ni_{50.3}Ti_{34.7}Hf_{15}$ SMAs with low ternary content (15% Zr or Hf) as a function of aging conditions. On the basis of all the results, the following conclusions can be made:

1. H-phase precipitation in both alloy systems leads to a wide range of flexibility to modify transformation temperatures. No multi-step or R-phase transformations are obtained in both of the alloy systems. In $Ni_{50.3}Ti_{34.7}Hf_{15}$ SMA, two mechanisms, "*interparticle spacing*" and "*compositional change*", are found to be effective on the transformation temperatures; the dominant one of those two

determines the final trends in transformation temperatures. Small and dense particles formed after low temperature aging for short durations lead to small interparticle spacing which in turn makes martensite nucleation harder and decreases M_s initially (Region 2 in TTT diagram). Sharp DSC peaks are observed for these samples aged at low temperatures for short durations in accordance with the harder nucleation of martensite. Longer duration aging at low temperatures or elevated temperature aging increase precipitate volume fraction remarkably and therefore M_s increases continuously (Region 1 in TTT diagram).

2. Both alloy systems show excellent dimensional stability due to precipitation hardening of the matrix. A maximum recovered strain of 2.45% is obtained in the $Ni_{50.3}Ti_{34.7}Zr_{15}$ alloy after proper heat treatments. The $Ni_{50.3}Ti_{34.7}Hf_{15}$ alloy shows almost perfect shape recovery even without precipitates and a maximum of 3.3% recovered strain is observed during load-biased thermal cycling experiments after precipitation heat treatments. Effect of precipitation hardening becomes more prominent on the transformation hysteresis levels and hysteresis gets lower for the heat treated samples as a consequence of harder defect generation when the precipitates are present. Applied stress has less effect to increase the M_s temperatures of the samples with large precipitates compared to the ones with no precipitates or small precipitates due to their steeper Clausius-Clapeyron slopes.
3. $Ni_{50.3}Ti_{34.7}Hf_{15}$ alloy has higher transformation temperatures than the $Ni_{50.3}Ti_{34.7}Zr_{15}$ alloy. Moreover, $Ni_{50.3}Ti_{34.7}Hf_{15}$ SMA exhibits better thermal stability and also shows higher recovered strain levels compared to

$Ni_{50.3}Ti_{34.7}Zr_{15}$ SMA due to difference in the lattice parameters of the transforming phases.

CHAPTER VI

MICROSTRUCTURAL CHARACTERIZATION AND SHAPE MEMORY RESPONSE OF Ni-RICH $Ni_{50.3}Ti_{29.7}Zr_{20}$ HIGH TEMPERATURE SHAPE MEMORY ALLOY*

The initially processed Ni-rich NiTiZr and NiTiHf alloys ($Ni_{50.3}Ti_{34.7}Zr_{15}$ and $Ni_{50.3}Ti_{34.7}Hf_{15}$) in the present study exhibit almost perfect shape recovery up to applied stress levels as high as 300 MPa as shown in Chapter V. Although, precipitation provides a wide flexibility to modify transformation temperatures, they are still limited and M_s barely exceeds 100 ^oC in a few aging conditions. Therefore, they cannot be used at elevated temperatures and further increase in ternary element addition is necessary to increase the transformation temperatures. A Ni-rich composition of $Ni_{50.3}Ti_{29.7}Hf_{20}$ SMA was already shown to have promising shape memory response as well as having relatively high transformation temperatures but comparable studies have not been carried out on its Zr counterpart which is the $Ni_{50.3}Ti_{29.7}Zr_{20}$ alloy. Therefore, work was initiated on the $Ni_{50.3}Ti_{29.7}Zr_{20}$.

The present chapter focuses on the microstructural and shape memory response characterizations of $Ni_{50.3}Ti_{29.7}Zr_{20}$ high temperature alloy. Samples were subjected to systematic aging treatments at temperatures from 450 ^oC to 600 ^oC for various durations

---

* "Reprinted from Scripta Materialia, 81, Evirgen A, Karaman I, Santamarta R, Pons J, Noebe RD, Microstructural characterization and superelastic response of a $Ni_{50.3}Ti_{29.7}Zr_{20}$ high-temperature shape memory alloy, 12-15, Copyright 2014, with permission from Elsevier."

and also another set of samples were furnace cooled from 700 ^{o}C to 100 ^{o}C for various durations. The transformation temperatures, thermal hysteresis and thermal stability as a function of thermal treatment conditions were studied via DSC. Using the DSC data, the TTT diagram for the $Ni_{50.3}Ti_{29.7}Zr_{20}$ alloy was generated to understand the effect of precipitation on transformation temperatures. The shape memory response of the alloy was investigated through load-biased isobaric thermal cycling tests and isothermal and constant strain superelasticity tests under tension. The evolution of transformation temperatures, thermal hysteresis, transformation and unrecovered strain levels as well as the temperature dependency of stress induced martensitic transformation (SIMT) stress were studied through analyzing the obtained thermal cycling and superelasticity curves. Furthermore, the TEM investigations for various heat treatments were given and discussed in order to correlate the obtained results from the experiments with the microstructural features.

Beside The NiTiZr alloy, a characterization attempt was also made on the $Ni_{50.1}Ti_{24.9}Hf_{25}$ alloy to study its shape memory response and transformation characteristics. Although, the alloy may show A_f and M_s as high as 370 °C and 240 °C, respectively, they were very brittle and always showed failure when tested above 150 MPa. Therefore, no further studies were performed on this alloy. The reader is suggested to refer “Appendix” for the preliminary studies on this material.

6.1 Microstructure

Prior to the thermal treatments applied to the $Ni_{50.3}Ti_{29.7}Zr_{20}$ samples, a SHT at 900 ^{o}C for 1 h was performed on the as received samples. The WDS results showed some deviation from the nominal composition as shown in Table 6.1 (a gain of ~ 0.6 at.% Zr and a loss of ~ 0.7 at.% Ni). However, contrary to WDS results, the ICP – AES investigations indicated ~ 0.5 at.% Ni gain, ~ 0.3 at.% Ti loss and ~ 0.2 at.% Zr loss. It should be noted that both of these methods involve some percent of error and despite the statistical error for the averaged compositions being lower, the estimation of the error is increased up to 0.7 at.% concerning the nominal compositions.

Table 6.1 Composition of the present $Ni_{50.3}Ti_{29.7}Zr_{20}$ SMA after solution heat treatment at 900 ^{o}C for 1 h measured through WDS and ICP - AES methods. ± indicates the standard deviation from a total of 10 measurements over the specimens with WDS.

	Ni (at.%)	Ti (at.%)	Zr (at.%)
WDS	49.60 ± 0.2	29.80 ± 0.3	20.60 ± 0.25
ICP - AES	50.8	29.4	19.8
Nominal	50.3	29.7	20.0

The matrix is in martensitic state at room temperature and has a homogeneous structure with heterogeneously distributed bright particles which are smaller than 3 μm in size as seen from the BSE image shown in Fig. 6.1. The EDS measurements performed on the bright particles indicated that they are zirconium carbide particles probably formed during the vacuum induction melting of the alloy in the graphite

crucibles. Their volume fractions cannot be measured since they are heterogeneously distributed throughout the matrix and moreover their volume fractions are not relevant for the present work because they are very small.

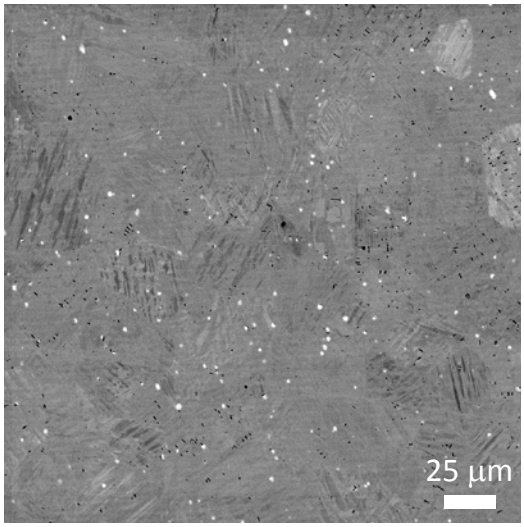

Figure 6.1 Back scattered electron image of solution heat treated $Ni_{50.3}Ti_{29.7}Zr_{20}$ SMA. Bright particles are identified as carbide inclusions (mainly ZrC) via EDS.

6.1.1 Precipitate Size and Martensite Microstructure

After the samples were solution heat treated, two sets of samples were prepared with precipitation heat treatments. The first of samples were aged at temperatures ranging from 450 ^{o}C to 600 ^{o}C for durations of 1 h to 48 h and a second set of samples were furnace cooled (FC) from 700 ^{o}C to 100 ^{o}C in durations from 3 h to 48 h in order to study the effect of controlled thermal treatment on the transformation characteristics and shape memory response. Regarding the DSC results which will be discussed in detail below, the microstructures of the samples showing best thermal stability (samples FC in

3 h and 48 h from 700 ^{o}C to 100 ^{o}C, hereafter labeled as NTZFC3 and NTZFC48, respectively), low thermal hysteresis (samples aged at 500 ^{o}C for 3 h, hereafter labeled as NTZ5003) and relatively high transformation temperatures (samples aged at 500 ^{o}C for 48 h and 550 ^{o}C for 3h, hereafter labeled as NTZ50048 and NTZ5503, respectively) were investigated with TEM to study the average precipitate sizes and the overall microstructure of the $Ni_{50.3}Ti_{29.7}Zr_{20}$ alloy. Figs. 6.2a to e correspond to the bright field TEM images of precipitation heat treated $Ni_{50.3}Ti_{29.7}Zr_{20}$ samples. The precipitates are marked with letter "P" in Figs. 6.2d and e to clearly indicate their size and distinguish them from the martensite variants. The precipitate morphology is in well accordance with the previous observations on $Ni_{50.3}Ti_{34.7}Zr_{15}$ and $Ni_{50.3}Ti_{34.7}Hf_{15}$. Their morphology change from oblate spindle-like shape when they are several tens of nanometers in size (NTZ5003, NTZ50048 and NTZ5503, Figs. 6.2a to c) to a plate-like shape similar to martensite variants when they reach to several hundred of nanometer in size after furnace cooling (NTZFC3 and NTZFC48, Figs. 6.2d and e). For the precipitate size corresponding to individual thermal treatment cases, the reader should refer to Table 4.1 in Chapter IV. The TEM images given in Fig. 6.2 reveal an interesting effect of precipitate size on the martensite morphology. If the precipitates are sufficiently small, the strain fields developing around the precipitates which do not transform during the martensitic transformation are able to be accommodated. In such conditions, the small precipitates (< 45 nm for the $Ni_{50.3}Ti_{29.7}Zr_{20}$ samples) do not interfere with the martensitic growth after the nucleation starts and hence large variants completely absorbing these small precipitates are generated. Examples of such microstructures are

shown as the inset images in Figs. 6.2a, b and also in Fig. 6.2c for the samples NTZ5003, NTZ50048 and NTZ5503, respectively where several hundred nanometer thick martensite variants are visible. This type of structures are generally formed after low temperature aging, i.e at 450 ^{o}C, 500 ^{o}C or 550 ^{o}C, for short durations and hereafter indicated as *"Type A microstructures"*. On the other hand, when precipitates are coarsened to several hundred of nanometers after furnace cooling as shown in Figs. 6.2d and e for the NTZFC3 and NTZFC48 samples, respectively, they limit the martensitic growth and therefore refine the variant thickness. These large precipitates cannot be absorbed and a large number of martensite variants generally comparable to the size of large precipitates are visible in this type of microstructures. This type of microstructures will be hereafter stated as *"Type B microstructures"*. The large precipitates in these samples are shown with letter "P" in Figs. 6.2d and e.

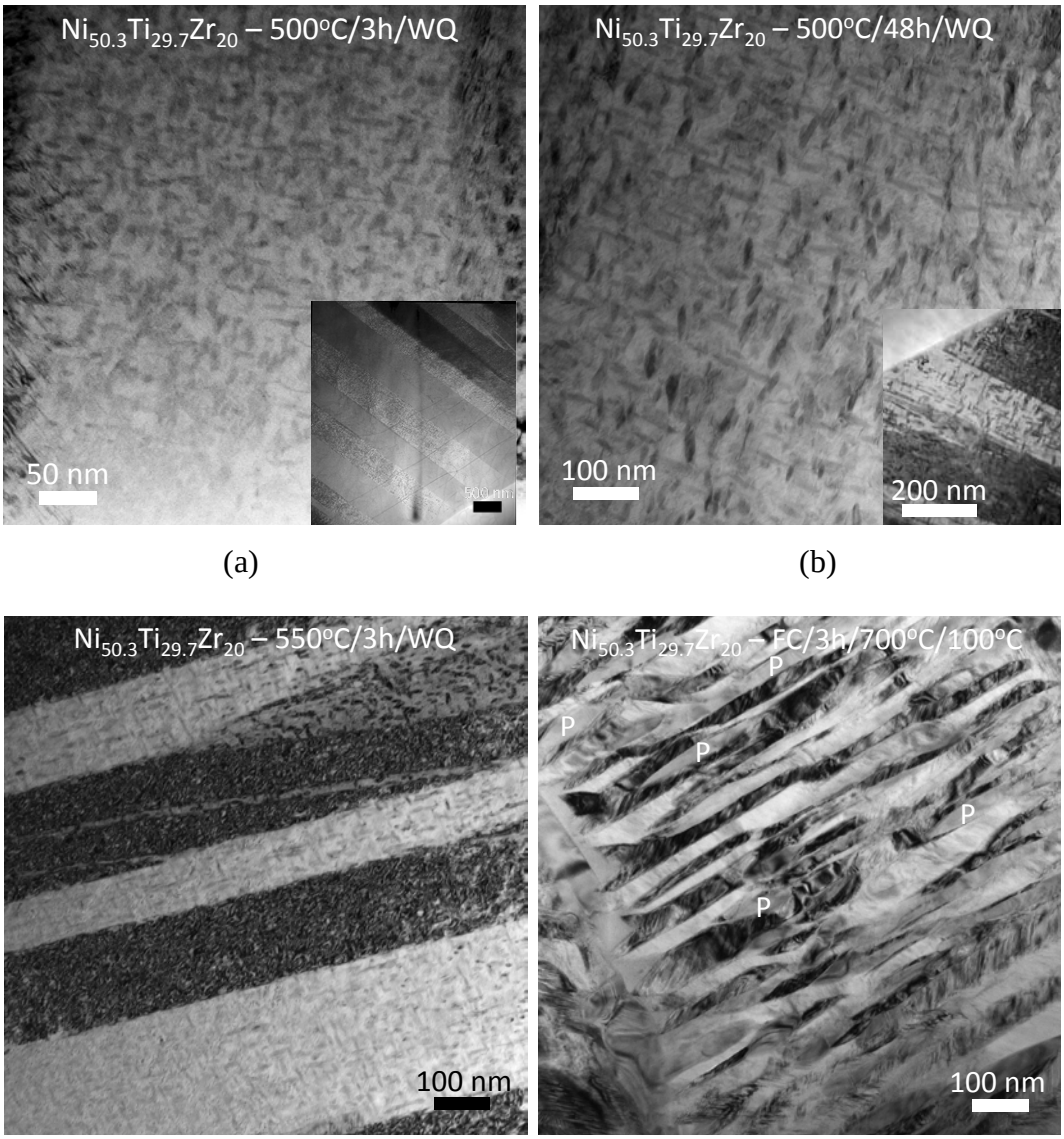

Figure 6.2 Bright field TEM images of $Ni_{50.3}Ti_{29.7}Zr_{20}$ samples (a) aged at 500 ^{o}C for 3 h, (b) 500 ^{o}C for 48 h, (c) 550 ^{o}C for 3 h and furnace cooled from 700 °C to 100 ° in (d) 3 h and (e) 48 h. The inset images given in (a) and (b) show the large variants absorbing the precipitates. For clarity, the precipitates are labeled with letter "P" in images (d) and (e).

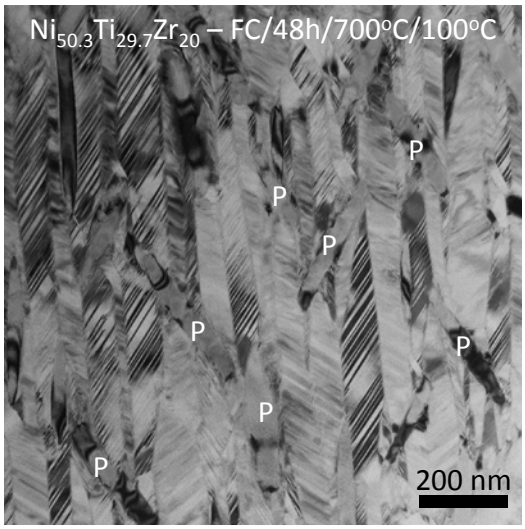

(e)

Figure 6.2 Continued.

6.2 Transformation Temperatures and Characteristics

Figs. 6.3a to f represent the stress free DSC curves of the aged (at 400 °C, 450 °C, 500 °C, 550 °C and 600 °C) and furnace cooled (from 700 °C to 100 °C) $Ni_{50.3}Ti_{29.7}Zr_{20}$ samples for various durations, respectively. For comparison, the DSC measurement corresponding to the SHT sample is given at the bottom of each graph. Similar to the Ni-rich NiTiZr and NiTiHf systems with low ternary content (15 at.%), $Ni_{50.3}Ti_{29.7}Zr_{20}$ samples also always show one step transformation indication that no R-phase is present. Moreover, although a continuous increase in transformation temperatures are expected due to the precipitation of Ni-rich particles, an initial decrease in A_f and M_s is visible after aging at 400 °C for 1 h or 3 h (Fig. 6.3a) and at 450 °C for 1 h (Fig. 6.3b) as compared to the SHT state with a similar fashion seen in $Ni_{50.3}Ti_{34.7}Hf_{15}$ SMA. The transformation temperatures start to increase after the initial decrease with

longer aging at these temperatures due to the further decrease in the Ni content of the matrix. Furthermore, sharp DSC peaks are observed for the aging cases where an initial decrease is observed, i.e. for the samples aged at 400 °C for 1 h and 3 h, indicating that the forward transformation is nucleation controlled. At aging temperatures relatively high such as 500 °C, 550 °C and 600 °C (Figs. 6.3c to e) or for prolonged aging treatments, a constant increase in transformation temperatures is observed due to Ni-depletion of the matrix as expected. Interestingly, the transformation temperatures show a constant decrease with the increase of cooling time after furnace cooling treatments as seen from Fig. 6.3f. This will be further commented below.

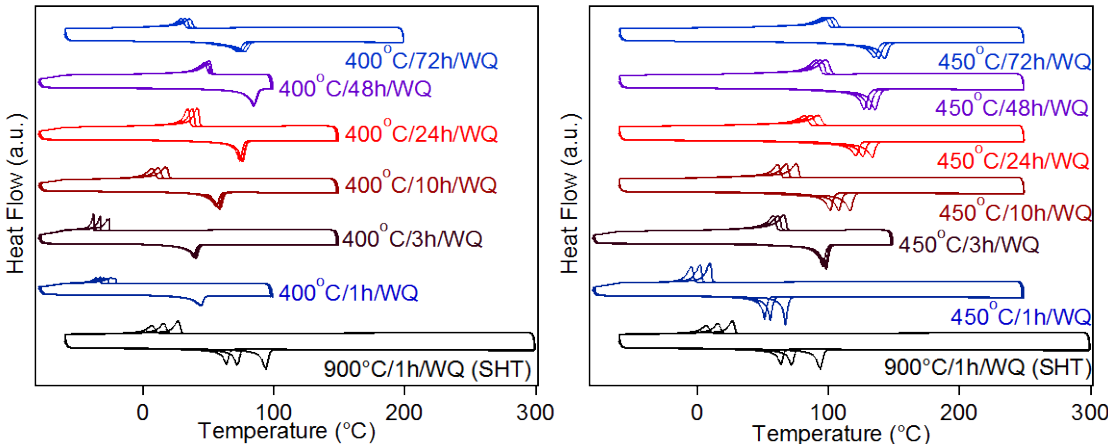

(a) (b)

Figure 6.3 The Stress free DSC cycles of the $Ni_{50.3}Ti_{29.7}Zr_{20}$ samples aged at (a) 400 °C, (b) 450 °C, (c) 500 °C, (d) 550 °C, (e) 600 °C and (f) furnace cooled from 700 °C to 100 °C for various durations of 1 h to 72 h. The DSC curve of the SHT sample is given at the bottom of each plot for comparison.

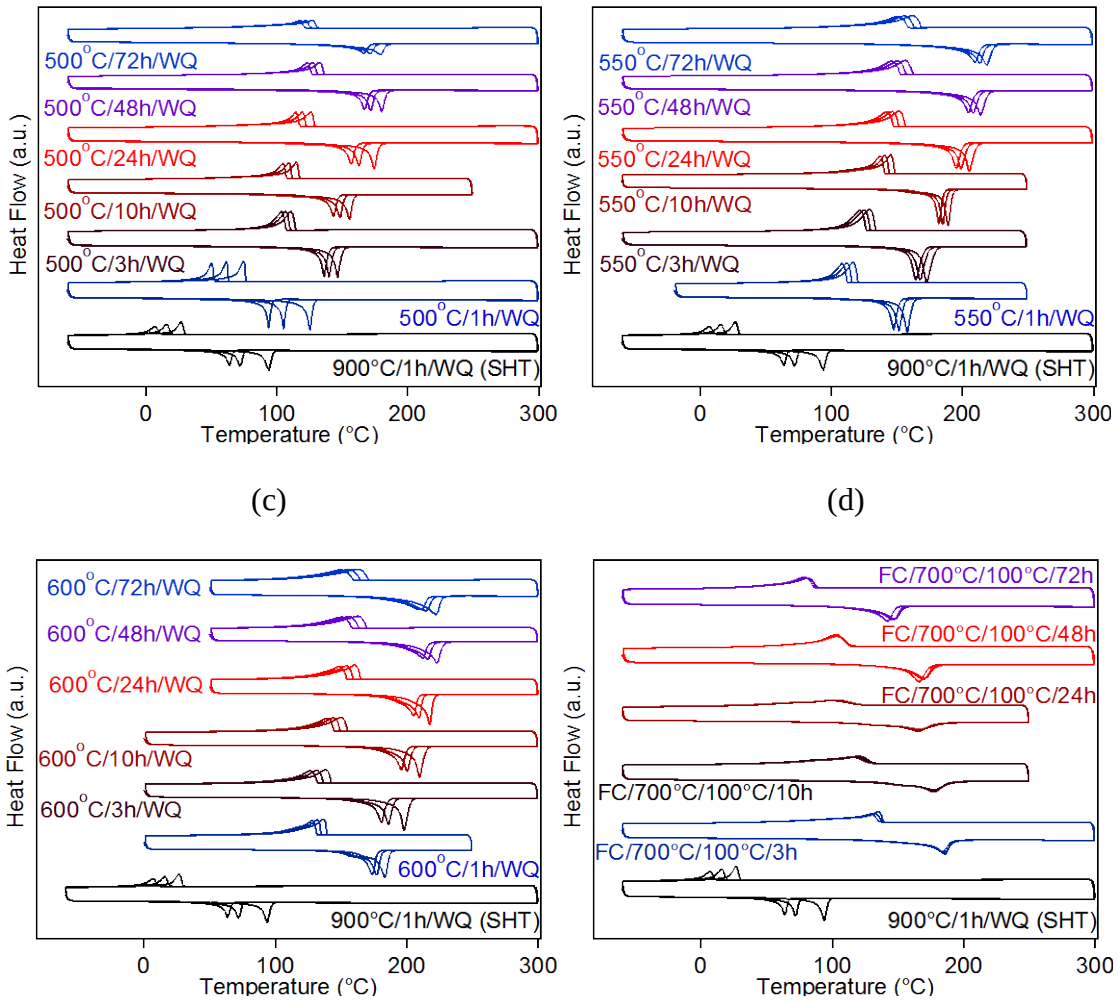

Figure 6.3 Continued.

The evolution of A_f and M_s temperatures as function of thermal treatment conditions for the $Ni_{50.3}Ti_{29.7}Zr_{20}$ samples are shown in Figs. 6.4a and b, respectively. The transformation temperatures corresponding to SHT (A_f ~ 97.5 ^oC and M_s ~ 30 ^oC) are plotted as the zero hour aging in the plots and assumed as the initial transformation temperatures of the alloy for comparison with those obtained after aging. Fig. 6.4

indicates that precipitation provides a wide range of transformation temperature flexibility: from 43.5 ^{o}C to 226.5 ^{o}C for A_f, i.e. a 183 ^{o}C temperature window and from -25.5 ^{o}C to 171 ^{o}C for M_s (160 ^{o}C temperature window). It is obvious from Fig. 6.4 that similar to $Ni_{50.3}Ti_{34.7}Hf_{15}$ SMA, two main trends are seen on the transformation temperatures of $Ni_{50.3}Ti_{29.7}Zr_{20}$ SMA: i) an initial decrease after short duration aging at the low aging temperatures (1 h and 3 h at 400 ^{o}C and 1 h at 450 ^{o}C) and a subsequent increase with further aging at these temperatures, ii) a constant increase after aging at 500 ^{o}C, 550 °C and 600 ^{o}C. It should be noted that transformation temperatures increase rapidly during the first few hours of aging at 500 °C, 550 °C and 600 °C, i.e. 1 h and 3 h aging durations, and do not change significantly thereafter. It is also obvious that transformation temperatures are do not differ remarkably for the samples aged at 550 °C or 600 °C for durations of 24 h or longer stating that the alloy almost reaches to equilibrium composition after 24 h aging at 550 °C. The present transformation temperatures for the $Ni_{50.3}Ti_{29.7}Zr_{20}$ alloy are higher than those for the $Ni_{50.3}Ti_{34.7}Zr_{15}$ and $Ni_{50.3}Ti_{34.7}Hf_{15}$ alloys as expected since increase in ternary element addition is higher (20 at.% Zr).

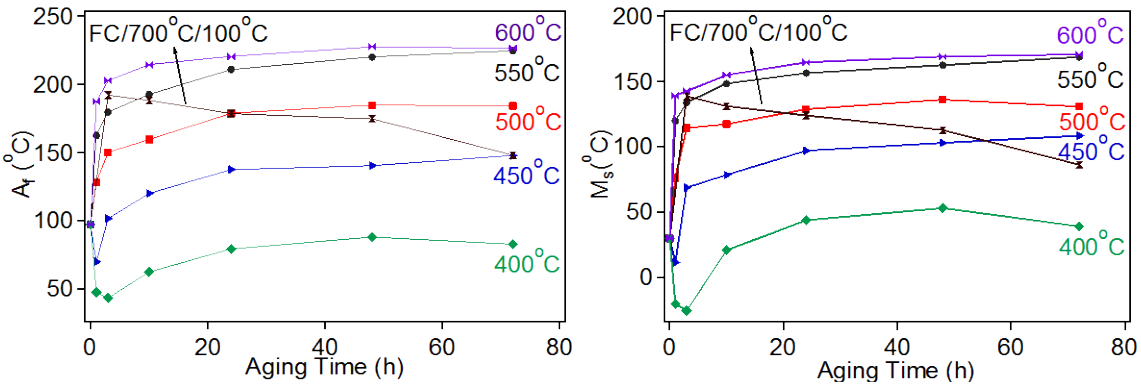

Figure 6.4 The evolution of transformation temperatures of the $Ni_{50.3}Ti_{29.7}Zr_{20}$ samples with precipitation: (a) A_f and (b) M_s. The transformation temperatures belonging to SHT case is given as the zero hour aged case (A_f ~ 97.5 °C and M_s ~ 30 °C).

In Chapter V (section 5.2.3), it has been discussed in detail that precipitate size is significantly influencing the transformation temperatures of $Ni_{50.3}Ti_{34.7}Hf_{15}$ SMA. Two mechanisms are identified to be effective on the transformation temperatures namely "interparticle spacing" and "compositional effect". Interparticle spacing is a function of particle size and volume fraction and hence may be controlled with thermal treatments. When a dense distribution of very fine (a few nm in size) particles is present after proper heat treatments, the interparticle spacing is small but the interparticle spacing gets larger with the increase in precipitate size for a given volume fraction of precipitates. In the $Ni_{50.3}Ti_{34.7}Hf_{15}$ SMA, martensitic transformation is suppressed to lower temperatures as compared to SHT case (precipitate free structure) when the samples are aged at low temperatures for short durations leading to formation of very fine precipitates and thus small interparticle spacing. The TEM investigation of the $Ni_{50.3}Ti_{29.7}Zr_{20}$ sample aged at

500 °C for 3h (Fig. 6.2a) showed that the particle size is 10-25 nm and it should be smaller when the samples are aged at 400 °C for 1 h or 3 h or at 450 °C for 1 h where an initial decrease in M_s is visible (Fig. 6.4b). Therefore, with a similar fashion to the $Ni_{50.3}Ti_{34.7}Hf_{15}$ SMA, the interparticle spacing in $Ni_{50.3}Ti_{29.7}Zr_{20}$ alloy after aging at 400 °C for 1 h or 3 h and at 450 °C for 1 h should be small or at least comparable to the precipitate sizes leading to decrease in M_s. Along with the small interparticle spacing under these aging conditions, one should also expect an increase in M_s with the increase in Ni-rich precipitate volume fractions and thus decrease in matrix Ni content. However, the suppressing effect of small interparticle spacing on M_s is more dominant and takes over the compositional change of the matrix resulting in decrease in M_s during short duration aging at 400 °C or 450 °C. Prolonged aging durations at these temperatures increase M_s since the precipitate volume fraction will be high enough to start increasing M_s again. On the other hand, aging at higher temperatures (500 °C, 550 °C and 600 °C) produces larger interparticle distances due to the increase in precipitate size and also larger volume fractions of the precipitates initially and therefore the compositional change of the matrix (compositional effect) becomes the dominant effect on M_s leading to continuous increase in transformation temperatures. It is suggested for the reader to refer to section 5.3.2 in Chapter V of the present work for more detail on the effect of "interparticle spacing" and "compositional effect" on M_s since the trends in M_s is identical in both $Ni_{50.3}Ti_{34.7}Hf_{15}$ and $Ni_{50.3}Ti_{29.7}Zr_{20}$ SMAs.

Additionally, the transformation temperatures of the samples furnace cooled from 700 °C to 100 °C show a decrease with the increase of cooling time. This

phenomenon cannot be explained only with small interparticle spacing since the particle sizes are very large (Fig. 6.2d and e). It is well known that at high aging temperatures, the kinetics for the nucleation of new particles are slow but instead the diffusion of atoms to the nuclei is faster. Therefore, instead of formation of new small precipitates, the growth of precipitates which are already formed is facilitated which will change the matrix composition rapidly. At low aging temperatures, nucleation becomes faster while diffusion is slower decreasing the growth rate of particles. Based on these thermodynamics, it can be argued that during furnace cooling of samples, large precipitates already form at high temperatures which will increase transformation temperatures remarkably. During cooling down to 100 °C and when the sample reaches to relatively low temperatures, small precipitates may form in between these large particles decreasing the interparticle spacing and hence suppressing M_s. These will be more prominent for longer cooling durations such as 48 h or 72 h since there will be longer time for generation of a large volume fraction of small precipitates which may suppress M_s to much lower temperatures. Indeed, increasing the furnace cooling durations leads to more decrease in M_s which supports this argument. Moreover, the microhardness experiments carried out on the furnace cooled samples indicated that microhardness values increase with the increase in cooling time. Microhardness is 444.4 ± 12.7 HV, 471.8 ± 8.5 HV, 478.3 ± 2.2 HV and 482.6 ± 6.7 HV for cooling times of 3 h, 10 h, 24 h and 48 h, respectively. It seems that the increase in the volume fraction of fine precipitates increases microhardness along with the increase in cooling durations which is in accordance with the suppression of M_s. However, TEM images given in Figs.

5.2d and e do not reveal the presence of small precipitates in the microstructure which may be due to the fine martensite microstructure. Therefore, further investigation is necessary to prove this statement.

The thermal hysteresis ($\Delta T = A_f - M_s$) of the SHT and thermal treated $Ni_{50.3}Ti_{29.7}Zr_{20}$ samples derived from the DSC curves shown in Fig. 6.3 is summarized in Fig. 6.5a. There is no clear trend in thermal hysteresis values with thermal treatment durations however they are smaller in the precipitation heat treated samples as compared to thermal hysteresis in SHT state (68 °C) due to precipitation hardening and hence less energy dissipation during transformation. One exception is visible for the samples where a decrease in M_s is seen such as after aging at 400 °C for 1 h and 3 h or at 500 °C for 1 h. In such cases, nucleation of martensite is harder due to small interparticle spacing and the extra energy needed to reach critical size for nucleation should be supplied through undercooling. This extra undercooling of the samples manifests itself as energy dissipation which is in accordance with the increase in thermal hysteresis seen in these samples. It is also obvious from Fig. 6.5a that for aging durations longer than 10 h, the samples aged at 400 °C and 450 °C exhibit smaller thermal hysteresis than the samples aged at higher temperatures or furnace cooled. This is probably due to higher matrix strength of the samples aged at 400 °C and 450 °C. Precipitation hardening is more efficient due to the presence of fine dense precipitates for those samples. Differing than the aged samples furnace cooled samples for durations of 24 h or longer also possess significantly large thermal hysteresis (> 60 °C). Due to limited martensite growth as a consequence of large particles in furnace cooled samples, a large number of thin

martensite variants are generated. This increases the number of intervariant boundaries and precipitate-variant interfaces which in turn increase the energy dissipation during transformation and large thermal hysteresis is present in the furnace cooled samples as compared to the samples with nanometric precipitates. The thermal hysteresis values obtained in the present $Ni_{50.3}Ti_{29.7}Zr_{20}$ alloy for aging conditions at 400 °C and 450 °C is lower than the $Ni_{50.3}Ti_{34.7}Zr_{15}$ and $Ni_{50.3}Ti_{34.7}Hf_{15}$ alloy but comparable for the rest of the thermal treatment conditions.

The thermal stability of the $Ni_{50.3}Ti_{29.7}Zr_{20}$ alloy was studied via measuring the difference between the first and third DSC cycle M_s temperature and the results are summarized in Fig. 6.5b. The shift in M_s in three DSC cycles for the SHT sample is very large (18.8 °C). The thermal stability gets better with precipitation hardening however the decrease in transformation temperatures is still generally above 7 °C for the aged samples. The thermal stability of the present $Ni_{50.3}Ti_{29.7}Zr_{20}$ alloy is comparable to $Ni_{50.3}Ti_{34.7}Zr_{15}$ alloy but worse than the $Ni_{50.3}Ti_{34.7}Hf_{15}$ alloy. These differences are a result of the differences in the lattice parameters of the transforming phases and hence the lattice compatibility of the alloys. One exceptional thermal treatment which results in very good thermal stability is the furnace cooling treatments as seen from Fig. 6.5b. The reason for the good thermal stability is not clear and needs further research however it has been argued before that small precipitates may form during cooling. These small precipitates may block dislocations more effectively in “Type B microstructures” along with the martensite growth limiting effect of large particles. Thus, defect generation

could be remarkably harder with thermal cycling enhancing thermal stability after furnace cooling.

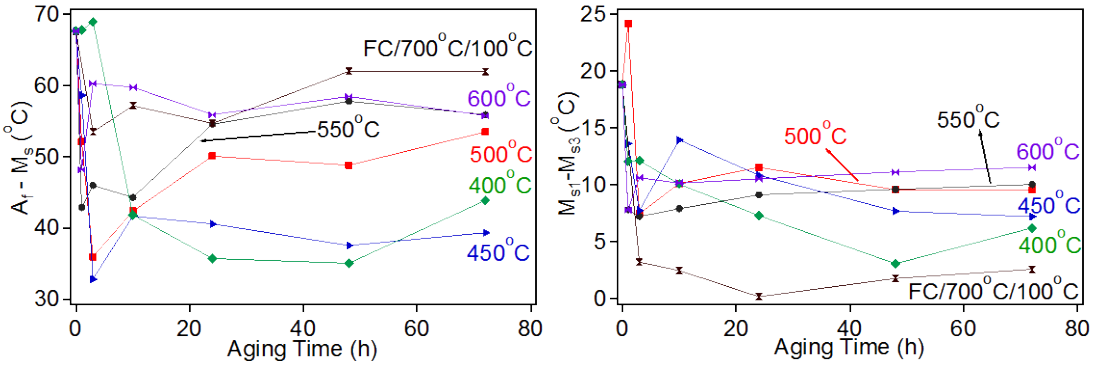

(a) (b)

Figure 6.5 The evolution of (a) thermal hysteresis and (b) thermal hysteresis of the precipitation heat treated the $Ni_{50.3}Ti_{29.7}Zr_{20}$ samples. The values given as the zero hour aging belongs to SHT sample (ΔT and M_{s1} - M_{s3} are 68 °C and 18.8 °C, respectively).

6.2.1 Time-Temperature-Transformation Temperature Diagrams

The Time-Temperature-Transformation Temperature (TTT) diagrams corresponding to the A_f and M_s temperatures of the $Ni_{50.3}Ti_{29.7}Zr_{20}$ alloy are generated using the DSC data and given in Figs. 6.6a and b, respectively. The TTT diagrams are split to two regions as “Region 1” and Region 2” to explain the peculiarities in the transformation temperatures seen in Fig. 6.4 and indicate under what aging conditions the “interparticle spacing or compositional effect” is dominantly effective on transformation temperatures. The DSC experiments indicated that any aging duration at 500 °C will increase the transformation temperatures as compared to SHT case.

Furthermore, any aging duration exceeding 1 h at 450 °C or 3 h at 400 °C also increases transformation temperatures but it takes time at these temperatures for A_f and M_s to recover back to SHT level and ultimately they exceed the levels of SHT case with further aging. This is rationalized with a boundary determined by the loci of A_f and M_s in the SHT case (A_f ~ 97.5 °C and M_s ~ 30 °C). The zone where aging always results in an increase in transformation temperatures due to "compositional effect" as compared to SHT case is labeled as "Region 1" in Fig. 6.6.

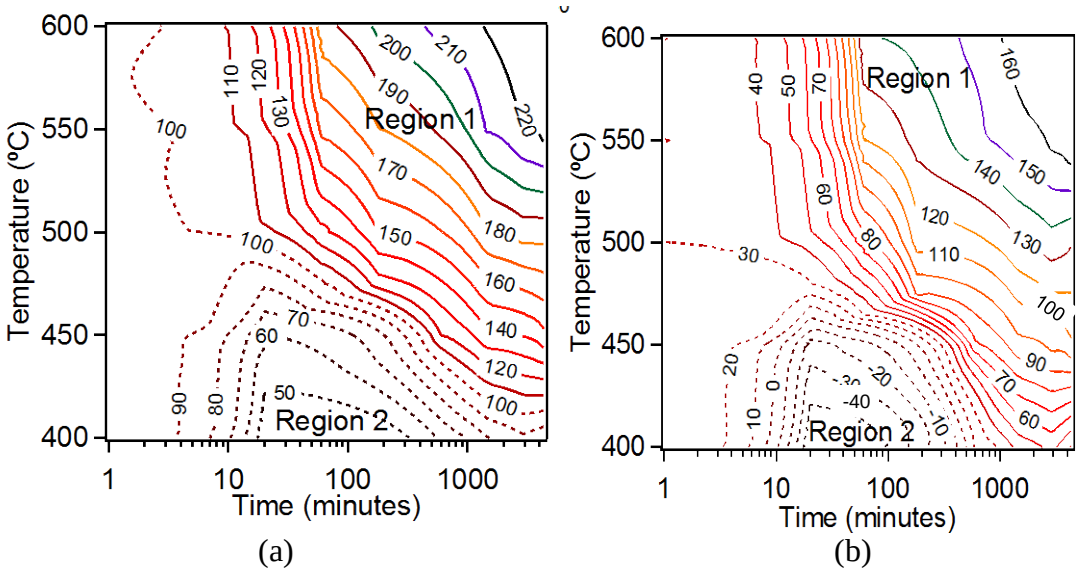

Figure 6.6 The Time-Temperature-Transformation Temperature diagram of the $Ni_{50.3}Ti_{29.7}Zr_{20}$ alloy illustrating both the interparticle spacing (Region 1) and compositional effect (Region 2) on the transformation temperatures. (a) for A_f and (b) for M_s. The loci of transformation temperatures in Region 1 is indicated with solid lines and with dashed lines in Region 2. Initial A_f and M_s are 97.5 °C and ~ 30 °C, respectively.

The peculiarities of A_f and M_s as a function of aging time and duration in "Region 2" needs more clarification since "interparticle spacing" becomes the dominat effect on the transformation temperatures. As explained previously, when interparticle spacing is small after aging at low temperatures for short durations, the nucleation of martensite and hence the martensitic transformation is suppressed leading to a decrease in M_s. Consequently, for an imaginary horizontal line in Figs. 6.6a and b, i.e. for a constant aging temperature, the increase in aging time decreases transformation temperatures along with the further decrease of interparticle spacing with the increase in the volume fraction of small precipitates initially. But with further aging at those temperatures, A_f and M_s increases with the increase in precipitate volume fraction remarkably and sufficiently enough to dominate suppression effect of small interparticle spacing. As concluded above, at these temperatures, once transformation temperatures starts to increase, it takes time to reach to levels of SHT case. So "interparticle spacing" is dominant for any aging condition leading to transformation temperatures smaller than SHT case: aging conditions below the loci of 100 °C for A_f and 30 °C for M_s and labeled as "Region 2". These differences in Region 1 and 2 where different trends on transformation temperatures are visible are driven by two main mechanisms namely nucleation and diffusional growth thermodynamics of the H-phase precipitates [128]. For further discussion on these two factors and their subsequent effect on TTT diagrams, the reader is suggested to refer section 5.2.4 in Chapter V.

6.3 Shape Memory Response

The shape memory response of the $Ni_{50.3}Ti_{29.7}Zr_{20}$ HTSMA is characterized through two types of mechanical experiments in tension. In the first set of experiments, the SHT and precipitation heat treated samples were subjected to load-biased thermal cycling experiments. The heat treated samples consist of sample sets showing two distinct microstructures explained formerly in section 6.1 as Type A and Type B microstructures. Samples showing “Type A microstructures” were chosen as NTZ5003, NTZ50048 and NTZ5503 while furnace cooled samples, NTZFC3 and NTZFC48 were chosen as the representatives of “Type B microstructures” for testing. The evolution of transformation temperatures, recovered and unrecovered strain levels and thermal hysteresis of the alloy as a function of applied stress were derived from the obtained thermo-mechanical cycles. In the second set of experiments, together with the precipitate free structure which could either be SHT or as received samples, one representative of the two microstructures were tested to study the superelastic response of the alloy. Since the SHT samples were found to be brittle, the as received samples were tested instead. NTZ5503 sample was chosen as the representative of “Type A microstructrues” and NTZFC48 sample was chosen as the representative of “Type B microstructures”. These experiments consist of isothermal and constant strain superelasticity tests to study the effect of precipitation on the superelastic properties. The maximum recoverable superelastic strain levels at A_f + 20°C temperature, the temperature range of superelasticity (defined as the temperature range where SIMT is the dominant

deformation mode over plastic deformation) and temperature dependency of stress necessary to induce martensitic transformation were studied using the obtained results.

6.3.1 Load-biased Thermal Cycling Experiments

The load-biased thermal cycles of the SHT and precipitation heat treated $Ni_{50.3}Ti_{29.7}Zr_{20}$ specimens under various applied stress levels in tension are shown in Figs. 6.7a to f. The precipitate free $Ni_{50.3}Ti_{29.7}Zr_{20}$ sample (SHT – Fig. 6.7a) already shows very good dimensional stability since a very small unrecovered strain is visible only after 400 MPa applied stress level characterized by the slightly open strain-temperature loop. The precipitation heat treated samples, either with “Type A microstructures” (Fig. 6.7b to d) or with “Type B microstructures” (Fig.6.7e and f) also show almost perfect shape recovery up to stress levels of 200 MPa and very small plastic deformation under 300 MPa applied stress level. Precipitation clearly increases the critical stress for slip and hardens the matrix however rather than the unrecoverable strain levels, effect of precipitation hardening is more prominent on the thermal hysteresis levels in samples with “Type A microstructures” which will be commented below.

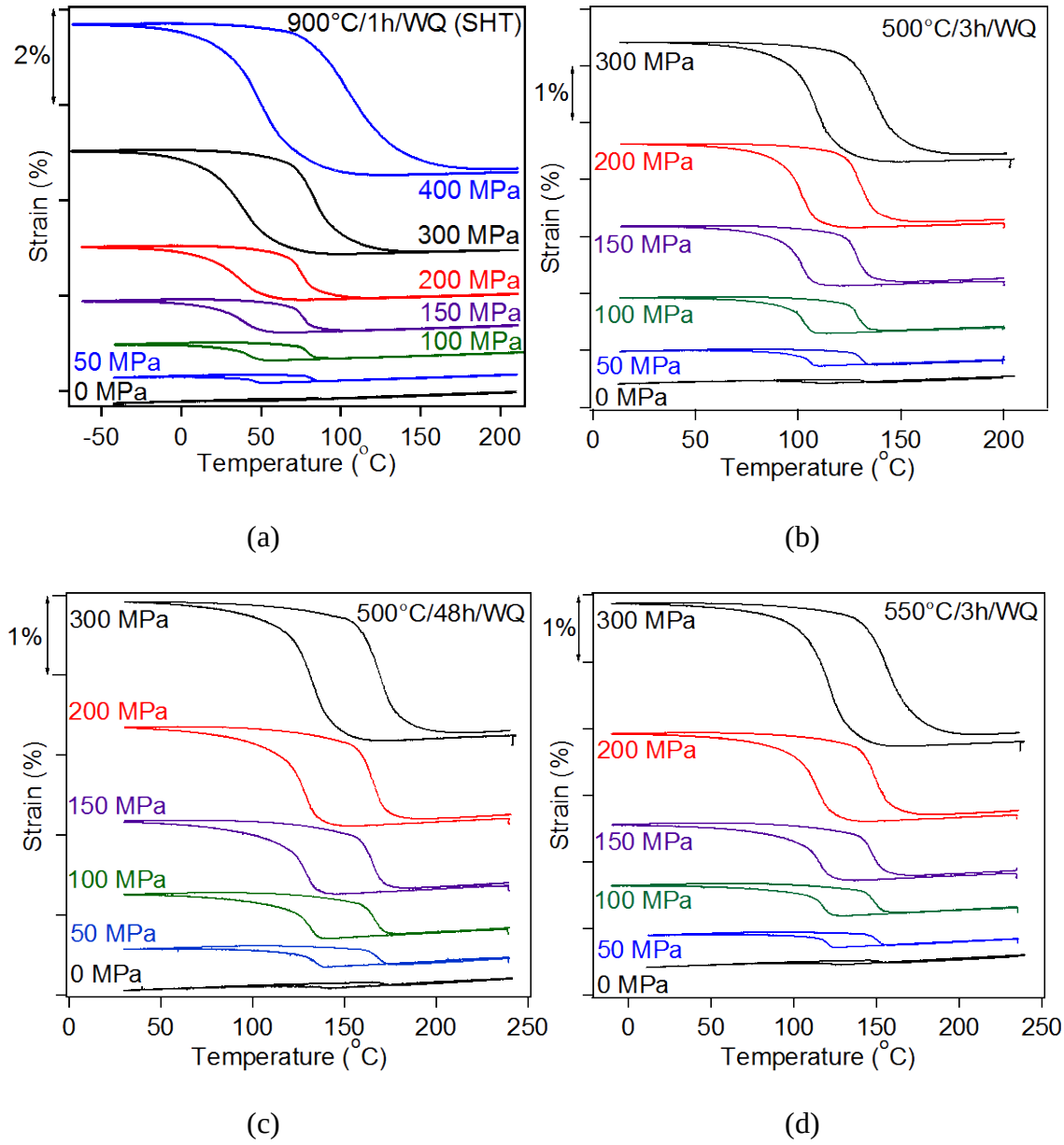

Figure 6.7 Strain vs temperature response of the $Ni_{50.3}Ti_{29.7}Zr_{20}$ specimens (a) solution heat treated (b) aged at 500 °C for 3 h, (c) aged at 500 °C for 48 h, (d) aged at 550 °C for 3 h, (e) furnace cooled in 48 h from 700 °C to 100 °C and (f) furnace cooled in 3 h from 700 °C to 100 °C, under various applied stress levels in tension.

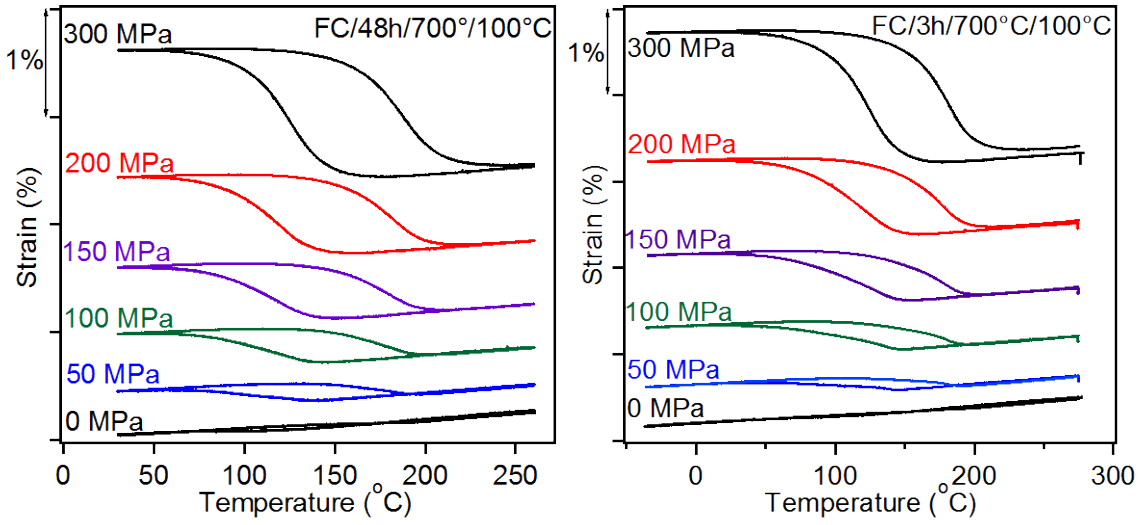

Figure 6.7 Continued.

The thermal cycles given in Figs. 6.7b to f for the precipitation heat treated specimens clearly reveal that the samples with different microstructures show notably different shape memory response under applied stress. For a better comparison, the behavior of all samples under 200 MPa applied stress levels is shown in Fig. 6.8. It is obvious from the graph that samples with type A and type B microstructures show differences in terms of transformation strain levels, thermal hysteresis and martensitic transformation ranges (defined as M_s - M_f) while the SHT sample without precipitates behaves similar to samples with type A microstructures. Therefore, it can be stated that these differences in shape memory responses are a function of microstructure which will be discussed in detail below.

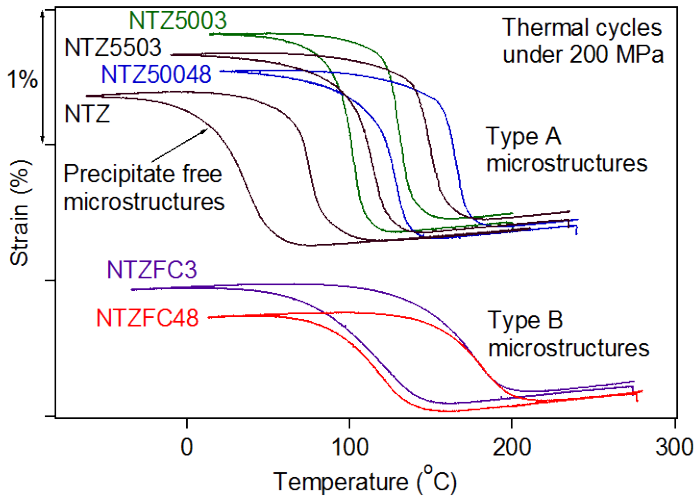

Figure 6.8 Comparison of the thermal cycles for the $Ni_{50.3}Ti_{29.7}Zr_{20}$ specimens under 200 MPa applied stress level exhibiting different microstructures. Samples with type A and type B microstructures clearly show differences in terms of transformation strain levels, thermal hysteresis and martensitic transformation ranges (M_s - M_f) while the precipitate free SHT sample behaves similar to samples with type A microstructures.

The evolution of recovered and unrecovered strain levels as a function of bias stress is summarized in Fig. 6.9. The recovered strain levels increase with the applied stress from almost zero at zero stress to a maximum of 2.1 % (NTZ5503) under 300 MPa in the samples with type A microstructures and to 1.6 % (NTZFC48) in the samples with type B microstructures. Precipitation heat treated samples show failure at stress levels above 300 MPa however the SHT sample can resist 400 MPa applied stress and a recovered strain level of 3.1 % is obtained. The unrecovered strain levels were determined at A_f + 30 ^oC for each stress level as the difference in strain between the heating and cooling curves. No unrecovered strain levels are present in any of the samples up to 100 MPa applied stress levels and increases around 0.1 % under 300 MPa applied stress for all the samples. Thus, it can be concluded that independent of the

microstructure, the precipitation heat treated samples exhibit very good dimensional stability under these stress levels due to the precipitation hardening. It should also be noted that this inherent stability observed during the very first thermal cycles without any prior training. Also, the shape recovery of the present Ni-rich $Ni_{50.3}Ti_{29.7}Zr_{20}$ alloy is significantly better than the shape recovery in (Ti+Zr)-rich NiTiZr alloys [29].

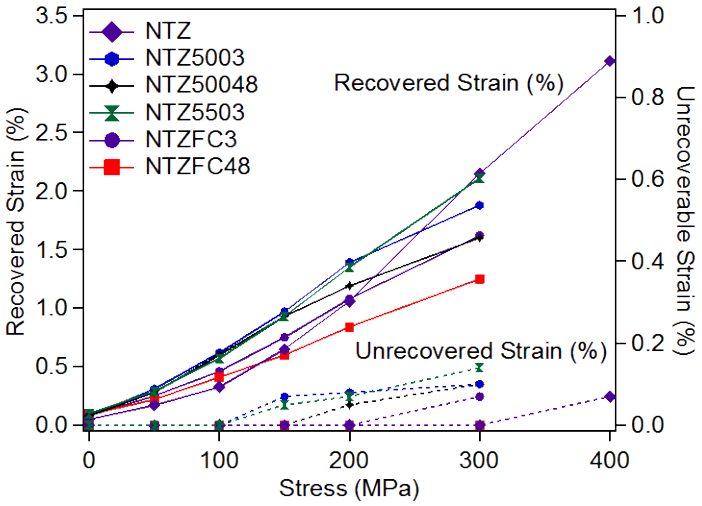

Figure 6.9 The summary of the recovered (solid lines) and unrecovered (dashed lines) strain levels of SHT and precipitation heat treated $Ni_{50.3}Ti_{29.7}Zr_{20}$ samples during thermal cycling in tension.

The recovered transformation strain levels of the present $Ni_{50.3}Ti_{29.7}Zr_{20}$ alloy are lower than those in binary NiTi SMAs. The smaller strain levels of the present alloys are probably due to the lattice incompatibility of B2 and B19′ phases which is a consequence of the lattice parameters of transforming phases. Additionally, the maximum strain of an SMA system may be also dependent on the active variant planes

during transformation which could be different in $Ni_{50.3}Ti_{29.7}Zr_{20}$ than the active ones in binary NiTi hence resulting in lower strain levels. Nevertheless, the continuous increase in the transformation strain with stress indicates that the maximum possible transformation strain was not reached even at 300 MPa for all NiTiZr samples, *i.e.* higher transformation strains should be obtained if higher stresses are applied. However, the precipitation heat treated samples failed during thermal cycling under 400 MPa indicating the brittle nature of the materials, an area of further investigation.

Fig. 6.9 shows that the solution heat treated $Ni_{50.3}Ti_{29.7}Zr_{20}$ samples show very good dimensional stability even without any precipitation heat treatment since it shows comparable or smaller unrecovered strain levels as compared to precipitation heat treated samples. Therefore, it can be concluded that the current applied stress levels (up to 300 MPa) are still below the stress levels required to induce plastic deformation as the dominant deformation mode over the martensitic twinning and hence decrease the recovered strain levels through incomplete transformation of martensite to austenite. However, instead of the unrecovered strain levels, precipitation greatly influences the thermal hysteresis levels after precipitation heat treatments which are summarized in Fig. 6.10. The thermal hysteresis lie between 25 to 35 °C for the samples exhibiting type A microstructures (NTZ5003, NTZ50048 and NTZ5503) while it is nearly 20-30 °C larger in the furnace cooled samples (~ 55 °C for NTZFC3 and ~ 65 °C for NTZFC48) with type B microstructures. The NTZ (SHT) sample initially exhibit higher thermal hysteresis (~ 55 °C) under zero stress as compared to precipitation hardened samples with type A microstructures. Thermal hysteresis gradually decreases with applied stress

around to 30 °C followed by a sharp increase over 60 °C under 400 MPa applied stress for the NTZ sample. This is well in accordance with the low matrix strength due to the lack of precipitates and plastic deformation seen in the NTZ sample at or above stress levels of 300 MPa. The fluctuations in thermal hysteresis in all precipitation heat treated samples with the bias stress is probably due to the change in lattice parameters of austenite and martensite and hence the lattice compatibility. More importantly than the trends in thermal hysteresis, the cooling curves of the samples in the course of transformation have significantly different slopes for the samples with precipitate free, type A and type B microstructures (Fig. 6.8). In other words, the martensitic transformation range (defined as M_s - M_f) under external stress, is notably smaller in samples with precipitate free (NTZ) and type A microstructures (NTZ5003, NTZ50048 and NTZ5503) than that in furnace cooled samples with type B microstructures (NTZFC48 and NTZSFC3). This indicates that the martensite variant growth/reorientation is more difficult and the elastic stored energy is higher in the furnace cooled samples. This is in agreement with the TEM observations in Fig. 6.2. The larger precipitates in furnace cooled samples are strong barriers against martensite variant boundary motion as they clearly stop the variant growth and control the variant size while the martensite boundaries can more easily propagate through the field of small precipitates in type A microstructures and precipitate free microstructures resulting in larger martensite lathes.

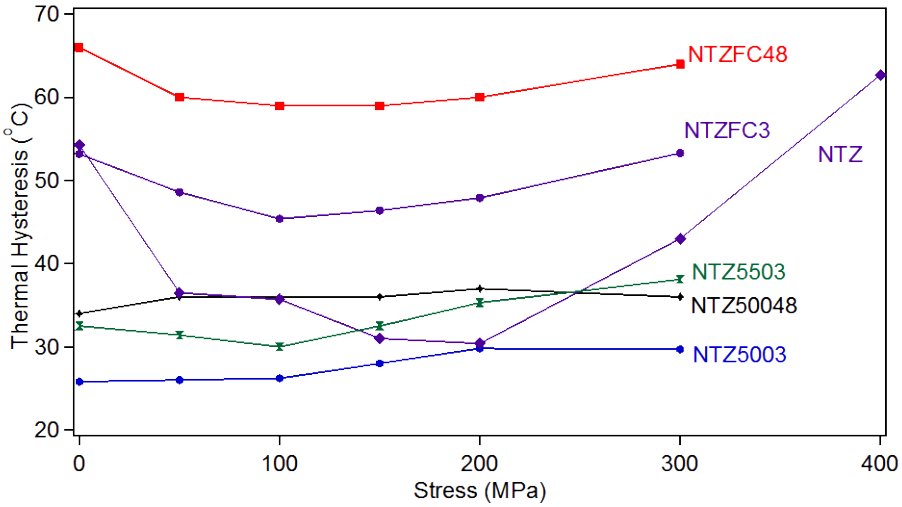

Figure 6.10 The evolution of thermal hysteresis in SHT and precipitation heat treated $Ni_{50.3}Ti_{29.7}Zr_{20}$ samples as function of applied stress during thermal cycling in tension.

Based on the strain temperature responses given in Fig. 6.7, the stress vs. transformation temperature phase diagrams for the M_s temperatures were constructed (Fig. 6.11). The M_s of type A microstructures decrease initially with increasing stress up to about 100 MPa or 150 MPa , but with further increase in stress they follow a linear stress dependence, i.e. a Clausius-Clapeyron (CC) relation, having slopes of 10.9 MPa/^{o}C, 16.1 MPa/^{o}C and 15.5 MPa/^{o}C for NTZ5003, NTZ50048 and NTZ5503 samples, respectively (Fig. 6.11). For the NTZ sample, no change is observed in M_s with the bias stress up to 50 MPa but it follows a linear stress dependency under higher applied stress levels with a slope of 15.1 MPa/°C. The M_s temperatures of type B microstructures, i.e. NTZFC48 and NTZFC3, on the other hand, show a positive CC relationship over the entire stress range with slopes of 15.2 MPa/^{o}C and 24.2 MPa/^{o}C, respectively (Fig. 6.11). These differences in the stress-temperature phase diagrams can

be attributed to the differences in size and distribution of the precipitates in both types of microstructures. Considerable strain fields develop around the small, densely-populated and coherent precipitates upon martensitic transformation when they are completely absorbed by the martensite plates in type A microstructures due to the transformation experienced by the matrix surrounding the untransformed particles. Therefore, the configuration of martensite variants becomes dependent on the local distribution of precipitate orientations, *i.e.* the variants formed are those that minimize the extra strain energy around the particles existing at each zone. However, since no macroscopic strain is detected under zero external stress, a global self-accommodated microstructure is still formed. Thus, when the martensitic variant distribution is modified by an external stress, an increase in the extra strain energy around the particles occur, which tends to decrease the transformation temperatures. For low applied stresses, this effect overcomes the natural increase in transformation temperatures caused by the external stress, as observed in the type A microstructure samples. On the other hand, this effect is not observed in furnace cooled samples due to the drastic change in the martensitic microstructure caused by the large precipitates, which become impenetrable obstacles for the martensite plates. With such configuration, the indivual martensite domains have only a small fraction of their volume interacting with the particles, and the interfaces are probably semi-coherent. Thus, the change in the extra strain energy around the particles when the martensitic microstructure is modified by the external stress is practically negligible.

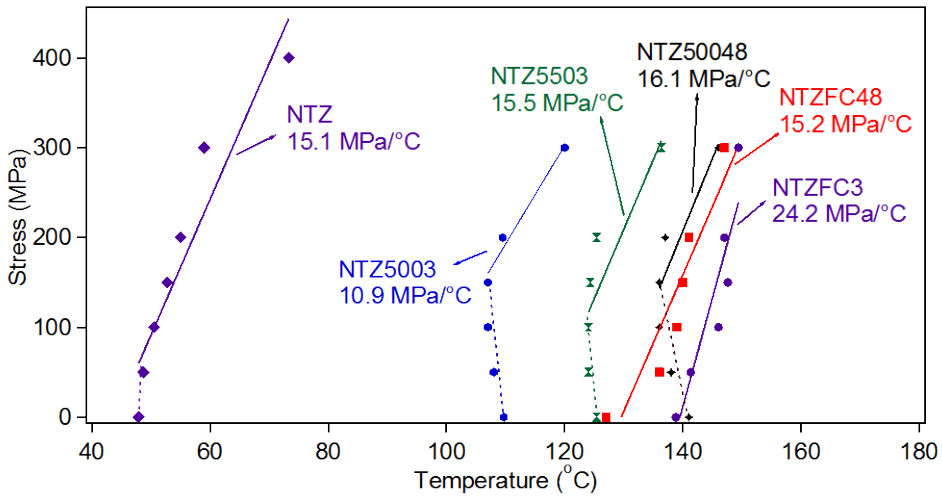

Figure 6.11 The stress vs temperature phase diagrams for the M_s temperatures of SHT and precipitation heat treated $Ni_{50.3}Ti_{29.7}Zr_{20}$ samples during thermal cycling in tension.

Concerning the TEM observations and load-biased test results, it can be concluded that type A and type B microstructure samples exhibit totally different behaviors in terms of thermal hysteresis, martensitic transformation range (M_s-M_f) and recovered transformation strain levels as a consequence of their microstructures. TEM images showed that when the precipitate size is small (< 45 nm), large martensite variants absorbing the particles form due to the no or negligible interference of precipitates with martensite growh during transformation (Figs. 6.2a to c). This type of microstructures were identified for the NTZ5003, NTZ50048 and NTZ5503 samples and defined as "Type A microstructures". When there are no precipitates in the microstructure such as in the case of SHT, there will be no precipitate barriers to overcome and there will be no interference with the martensitic transformation. However, in type B microstructures in which several hundred of nanometer precipitates

are present, there is a strong interference with martensitic growth leading to formation of large number of thin variants. Furthermore, these large particles act as obstacles the reorientation/detwinning of martensite under applied stress. This type of structures is generated after furnace cooling such as in the case of NTZFC48 and NTZFC3 samples. This significant difference in the manner in which the martensite phase interacts with the precipitates manifests itself as the following differences in shape memory behavior: a) thermal hysteresis under stress is higher in type B microstructures as compared to that in type A microstructures or precipitate free conditions due to the higher energy dissipation during the growth of a larger number of thinner martensite variants and intervariant boundaries, b) martensitic transformation occurs over a broader temperature range since more undercooling is necessary to complete the transformation within the barriers and therefore the transformation range under stress is significantly higher in type B microstructures, and c) the transformation strain levels are lower in type B microstructures since higher stresses are necessary for the reorientation/detwinning of the martensite.

6.3.2 Superelasticity Experiments

The incremental strain superelastic responses of the as received (labeled as NTZASR) and heat-treated $Ni_{50.3}Ti_{29.7}Zr_{20}$ samples was investigated at a constant temperature 20 °C above their A_f temperature (A_f + 20 °C) and the results are presented in Fig. 6.12. A_f of all the samples was measured by DSC to be 10, 150 and 190 °C for NTZASR, NTZ5503 and NTZFC48, respectively. The reader should note that these

values deviate from the DSC data given in Fig. 6.4 since a new batch of vacuum induction melted $Ni_{50.3}Ti_{29.7}Zr_{20}$ alloy was used for the present superelasticity tests. Therefore, these deviations are a consequence of the sample to sample variations between these two batches of melted material. When precipitates are not present (NTZASR), the material shows complete recovery only for applied strains up to 2% (Fig. 6.12). The material starts to show a small amount of unrecovered strain (0.2% under 3% applied strain) beyond this strain, which increased progressively to ~5.3% unrecovered strain for a cumulative of 8.0% applied strain. Contrary to the behavior of NTZASR sample, the resistance to plastic deformation significantly increased due to the generation of very fine and coherent precipitates after aging at 550 °C for 3 h (NTZ5503). NTZ5503 shows only 0.08% and 0.2% unrecovered strain levels under 5% and 6% total applied strains, respectively (Fig. 6.12). The amount of recovered transformation strain increased to 5% with an increase in the applied strain to 6% (NTZ5503). To the author's best knowledge, this present recovered transformation strain values for NTZ5503 sample are higher than any strain values reported to date for a polycrystalline NiTiZr or NiTiHf HTSMA. On the other hand, the NTZFC48 sample which has very large precipitates, become very brittle. It can undergo only one mechanical cycle up to 1% applied strain and shows failure in the subsequent loading cycle at 1.4% applied strain, as shown in Fig. 6.12.

As a characteristic of the SIMT, only a short plateau region is visible during the first few percent applied strain in NTZASR sample (Fig. 6.12). After this plateau region and with the increase of applied strain level, a significant amount of hardening is

observed since the material starts to undergo plastic deformation and thus a high density of dislocations are generated. Therefore, the external applied stress increases rapidly well over to 1 GPa with failure occurring at a strain of 8.7%.

In contrast, NTZ5503 sample does not experience a flat plateau region during the SIMT. Instead, a two-stage hardening behavior is seen, with an initial plateau-like region with moderate work hardening for about the first 3% strain followed by a region of much higher hardening. The initial region of moderate work hardening is due to the strengthening of the parent B2 phase with generation of fine and coherent precipitates requiring extra elastic energy to accommodate the transformation strain around the non-transforming particles. While these fine precipitates are being absorbed through the growing martensite variants during SIMT, the stress should continuously increase in order to accommodate the strain energy around the precipitates. Such increase in the elastic energy accumulated around small and coherent precipitates has been observed in other SMA systems, such as β-Cu-Zn-Al containing fine γ-phase precipitates [132,133], or Co–Ni–Ga with nanometer-sized γ’ particles [125]. The transformation strain around the γ -phase particles in β-Cu–Zn–Al alloys cannot be completely accommodated only by elastic strain and therefore dislocation loops form around the particles. Once generated, accommodation of transformation strain is facilitated by these dislocation loops in the subsequent cycles, resulting in a significant decrease in the stress to induce SIMT (or increase in transformation temperature) in a few consecutive cycles [132,133]. A similar phenomenon is not visible in the present NTZ5503 samples, i.e. the direct martensitic transformation followed exactly the same curve for the initial cycles

performed during the incremental applied strain tests (Fig. 6.12). The transformation strain between austenite and martensite is probably lower in the $Ni_{50.3}Ti_{29.7}Zr_{20}$ alloy than in β-Cu–Zn–Al and the intrinsic stiffnesses of the austenite and martensite phases are significantly higher. As a consequence, the strain around the particles occurring during transformation seems to be elastically accommodated in NTZ5503 samples. Additionally, previously formed martensite variants and the grain boundaries are constraining the austenitic domains transforming at high applied strains and stresses leading to formation of thinner martensite variants in these regions to provide geometric compatibility. Therefore, the variant-variant interactions are increased and along with the start of plastic deformation, it leads to the second region of higher work hardening in the σ-ε curves (Fig. 6.12).

When the precipitate size is very large such as in the case of NTZFC48 (type B microstructures), the strain hardening during SIMT is more dominant (Fig. 6.12) and as a result early failure occurs at very low strains. For the martensitic transformation driven by the change in temperature, such as in the case of load-biased thermal cycling tests, a complex multivariant martensitic microstructure is necessary to provide the geometrical compatibility with the internal stress fields created by the large precipitates (see Fig. 6.2e). However for the SIMT, a limited number of martensite variants are activated through the applied external stress which decreases the geometrical compatibility with the large precipitates. As a result, local stress and strain concentrations increase remarkably, leading to high strain hardening during SIMT and early failure.

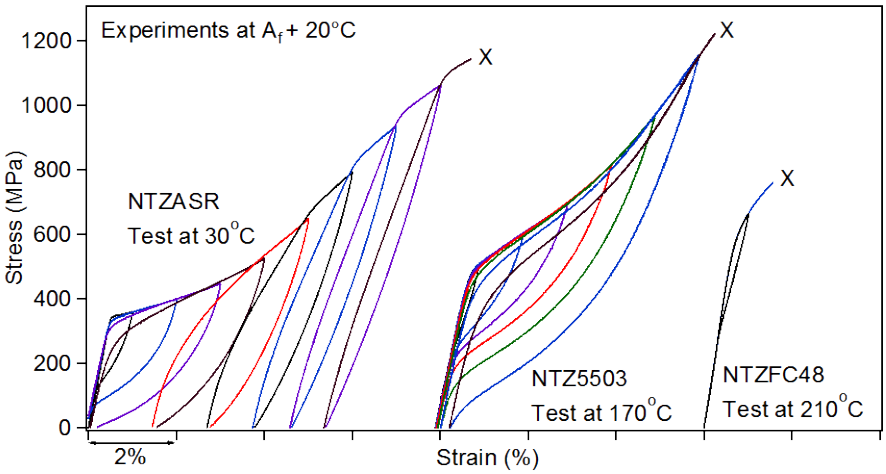

Figure 6.12 Incremental strain superelastic responses of as-extruded and heat-treated $Ni_{50.3}Ti_{29.7}Zr_{20}$ samples. The tests were carried out at A_f + 20 °C for each sample.

The superelastic responses of the NTZASR and NTZ5503 samples as a function of temperature under constant applied strain levels are shown in Fig. 6.13a. The applied strain level was restricted to 3% for the NTZ5503 specimens, but was limited to 2% for NTZASR, in order not to plastically deform the materials and provide full recovery upon unloading. Furthermore, the superelastic stress-strain cycles of NTZASR samples corresponding to testing temperatures above 180 °C, i.e. 210 °C, 250 °C and 290 °C are given in Fig. 6.13b. The NTZFC48 samples always show failure at <1% applied strain when tested at temperatures above 210 °C, and therefore no data for this condition was included in Fig. 6.13a. The experiments were repeated several times on different samples for the NTZASR and NTZ5503 samples, and the transformation stress levels for each test temperature were measured using the 0.2% strain offset method and are summarized in Fig. 6.14 together with the best linear fit through the data.

Fig. 6.13a indicates that the NTZASR sample possesses perfect superelasticity up to 180 °C (A_f + 170 °C) (Fig. 6.13a) but start to show irrecoverable strains at temperatures above 180 °C, i.e. 0.08% unrecovered strain at 210 °C and 0.31% at 290 °C when 2% strain was applied (Fig. 6.13b). The samples show failure before reaching to 2% applied strain when tested above 290 °C. The precipitation hardened sample (NTZ5503), on the other hand, exhibits near-perfect superelasticity up to 250 °C (A_f + 100 °C) only with 0.05 and 0.08% unrecovered strains at 230 °C and 250 °C, respectively, and fails at 270 °C before reaching the 3% applied strain level (Fig. 6.13a).

The stress hysteresis ($\Delta\sigma$) decreases from 198 to 166 MPa with the increase in test temperature from 30 to 180 °C (Fig. 6.13a) in the NTZASR samples. The stress hysteresis changes slightly with the testing temperature for NTZ5503 sample (i.e. 197 MPa at 170 °C and 203 MPa at 250 °C). However, it is not possible to directly compare these stress levels since they were cycled under different applied strain levels and the amount of transformed volume was different, which has a clear effect on the stress hysteresis, as evidenced in Fig. 6.12. For this reason, the temperature hysteresis measured via DSC provides a more reliable comparison of the three microstructures, being 59, 45 and 69 °C for NTZASR, NTZ5503 and NTZFC48 samples, respectively. It is worth to note that the current stress hysteresis values are smaller than the ones obtained in $Ni_{50.3}Ti_{29.7}Hf_{20}$ HTSMA [57].

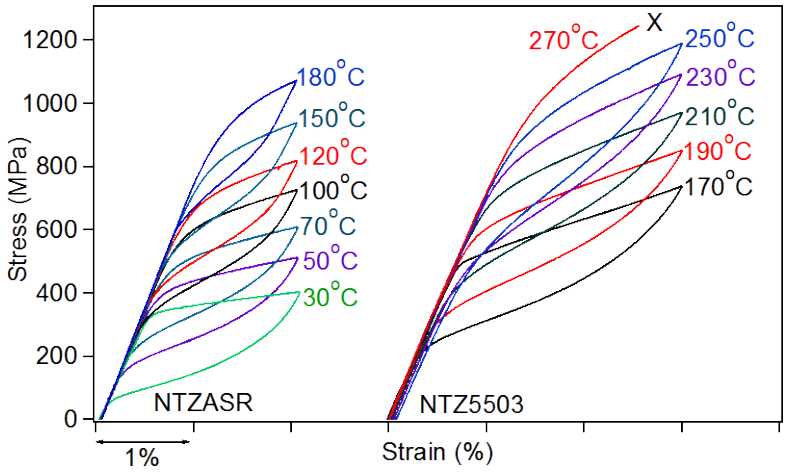

(a)

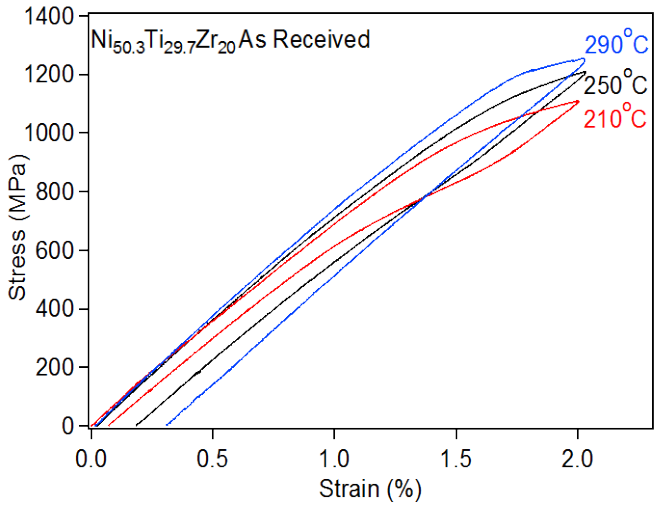

(b)

Figure 6.13 (a) Temperature-dependent superelastic responses of the as received and heat-treated $Ni_{50.3}Ti_{29.7}Zr_{20}$ samples and (b) superelastic stress-strain curves of as received $Ni_{50.3}Ti_{29.7}Zr_{20}$ samples for testing temperatures above 180 °C.

The evolution of critical stress for SIMT (σ_{SIM}) as a function of testing temperature, is summarized in Fig. 6.14. σ_{SIM} increases linearly with temperature, i.e.

Clausius–Clapeyron relationship, and attain conspicuously high values (i.e. 1230 MPa at 290 °C for NTZASR and 990 MPa at 270 °C for NTZ5503). These σ_{SIM} values for the $Ni_{50.3}Ti_{29.7}Zr_{20}$ HTSMA are comparable to those of $Ni_{50.3}Ti_{29.7}Hf_{20}$ [57,59] and higher than the values for $Ni_{52}Ti_{42}Zr_6$ [51] alloys. The Clausius–Clapeyron slopes, $d\sigma_{SIM}/dT$, are 3.54 MPa/C^{-1} for NTZASR and 4.87 MPa/C^{-1} for NTZ5503. It is obvious from Fig. 6.14 that for a given test temperature, NTZASR samples show higher σ_{SIM} values than their heat-treated counterparts (NTZ5503), due to its lower transformation temperatures. Additionally for both samples, the M_d temperature, defined as the temperature at which the stress-induced transformation no longer occurs and plasticity is the dominant deformation mode, is not reached.

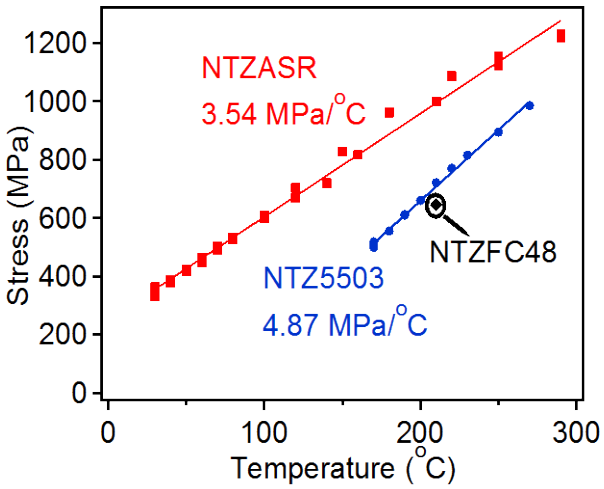

Figure 6.14 Temperature dependence of the critical stress for stress-induced martensitic transformation (determined via 0.2% offset method) for the as received and heat-treated $Ni_{50.3}Ti_{29.7}Zr_{20}$ samples.

The present experiments describe for the first time the superelastic response of a Ni-rich NiTiZr HTSMA as a function of the different microstructures obtained after aging. The as-extruded samples without precipitates exhibit nearly perfect superelasticity up to 180 °C, but only when the total applied strain is restricted to 2%. The precipitate-free microstructure show little resistance to plastic deformation at higher applied strain levels even at temperatures as low as 30 °C. The furnace-cooled material does not show favorable superelasticity and fails at very low values of applied strain as the precipitated large particles act as obstacles to martensite growth. However, the superelastic response of the material is remarkably improved through the precipitation of nanosize particles in samples aged at 550 °C for 3 h. The nanometer-sized coherent precipitates are effective in strengthening the material and inhibit plastic deformation without a dramatic interference with the martensite growth. In this way, a maximum of 5% fully recoverable strain at 170 °C and near-perfect superelasticty under 3% applied strain up to 250 °C were obtained when 22–40 nm long and 13-20 nm wide particles of the H-phase were formed after aging at 550 °C for 3 h. To the best of the authors' knowledge, these superelastic strain levels are the highest values reported for a polycrystalline NiTiZr SMA.

6.4 Summary and Conclusions

This chapter of the present study covers the effect of precipitation on the microstructure, transformation characteristics and shape memory response of the Ni-rich

$Ni_{50.3}Ti_{29.7}Zr_{20}$ HTSMA with a higher ternary content (20% Zr). The following remarks and conclusions can be drawn concerning the obtained results:

1. Formation of Ni-rich H-phase precipitates provides a wide range of flexibility to alter transformation temperatures. SHT and precipitation heat treated samples always undergo a single step transformation. With a similar fashion to $Ni_{50.3}Ti_{34.7}Hf_{15}$ SMA, two mechanisms, "*interparticle spacing*" and "*compositional change*", are found to be influencing the transformation temperatures and it is the dominant one of those two determines the final behaviors in transformation temperatures. Short aging durations at low temperatures result in generation of small interparticle spacing which suppresses martensite nucleation and lowers M_s initially (Region 2 in TTT diagram). Ms continuously increases along with the remarkable increase in the volume fraction of precipitates after longer duration aging at low temperatures or elevated temperature aging (Region 1 in TTT diagram).
2. Precipitate size is found to be strongly affecting the martensite morphology. During low temperature aging, i.e. at 450 ^{o}C, 500 ^{o}C or 550 ^{o}C, for short durations, sufficiently small precipitates are formed (< 45 nm for the $Ni_{50.3}Ti_{29.7}Zr_{20}$ samples) which do not interfere with the martensitic transformation and hence several hundred of nanometer wide variants form absorbing the precipitates (Type A microstructures). Furnace cooling coarsens precipitates to several hundred of nanometers long and they limit the martensite

growth and refine variant thickness. Thus a large number of variants with a comparable size to the precipitates are formed (Type B microstructures).

3. $Ni_{50.3}Ti_{29.7}Zr_{20}$ HTSMA shows very good dimensional stability as a consequence of the increase in resistance to plastic deformation with precipitation. Samples with type A and B microstructures show totally distinct shape memory responses such as thermal hysteresis, martensitic transformation range (M_s - M_f) and recovered transformation strain levels. Type B microstructures have higher thermal hysteresis and wider transformation range as compared to type A microstructures due to the formation of a large number of thin variants and extra undercooling necessary to complete transformation within precipitate barriers. Lower transformation strains are obtained in type B microstructures due to the harder reorientation/detwinning of martensite.
4. The precipitate free $Ni_{50.3}Ti_{29.7}Zr_{20}$ samples already show perfect superelasticity under 2% applied strain up to 180 °C but has little resistance to plastic deformation under higher applied strain levels even at temperatures as low as 30 °C. The limited martensite growth due to the precipitate barriers in furnace cooled samples with type B microstructures results in early failure at low applied strain levels and no favorable superelasticity is obtained. Precipitation hardening in type A microstructures with nanosize particles improves superelasticity remarkably leading to 5% fully recoverable strain at 170 °C and perfect superelastic shape recovery under 3% applied strain up to 250 °C with more than 1 GPa of stress.

CHAPTER VII

DIFFERENCES AND SIMILARITIES IN THE MICROSTRUCTURAL FEATURES AND SHAPE MEMORY RESPONSE OF Ni-RICH $Ni_{50.3}Ti_{29.7}Zr_{20}$ AND $Ni_{50.3}Ti_{29.7}Hf_{20}$ HIGH TEMPERATURE SHAPE MEMORY ALLOYS

As discussed in Chapter V of the present work, the $Ni_{50.3}Ti_{34.7}Zr_{15}$ and $Ni_{50.3}Ti_{34.7}Hf_{15}$ SMA show very good dimensional stability but they are not suitable to be used at elevated temperatures (above 100 ^{o}C) since they show transformation temperatures below 100 ^{o}C. However, SMAs with increased ternary addition are able to show higher transformation temperatures as well as good dimensional stability and excellent superelasticity such as in the case of $Ni_{50.3}Ti_{29.7}Zr_{20}$ HTSMA discussed in Chapter VI. The Hf counterpart of this Ni-rich NiTiZr alloy, namely $Ni_{50.3}Ti_{29.7}Hf_{20}$ HTSMA, was shown to exhibit high transformation temperatures and very good shape memory properties chronologically before the experimental progress carried out in the present thesis. Although, the NiTiZr and NiTiHf SMA systems were reported to show similar transformation characteristics and shape memory responses, there has been no detailed analysis comparing the differences and similarities of their microstructural features and their shape memory response as a function of aging conditions.

The previous chapter showed that microstructure, which is a function of aging conditions, has a strong effect on the transformation characteristics and shape memory response of $Ni_{50.3}Ti_{29.7}Zr_{20}$. Therefore, as the primary goal, this chapter covers the investigations on the microstructural features and their subsequent effect on the shape

memory characteristics of $Ni_{50.3}Ti_{29.7}Hf_{20}$ in an approach similar to that applied to $Ni_{50.3}Ti_{29.7}Zr_{20}$. The experimental observations are compared and the differencies as well as similarities are discussed for each alloy.

7.1 Precipitate Size and Martensite Morphology

In the $Ni_{50.3}Ti_{29.7}Zr_{20}$ alloy, short duration aging treatments at low aging temperatures, i.e. at 450 ^{o}C, 500 ^{o}C or 550 ^{o}C, lead to precipitation of fine nanoparticles, which could be completely absorbed by the large martensite variants (type A microstructures). On the other hand, prolonged treatments at these or higher temperatures generate large particles with sizes of several hundred nanometers. These large particles are not capable of being absorbed by the martensite plates, but they limit the martensite growth and refine the variant size instead (type B microstructures). Such microstructures are generally provided by slow controlled furnace cooling treatments such as the cases shown in Chapter VI for the $Ni_{50.3}Ti_{29.7}Zr_{20}$ alloy. Several heat treatments, representative resulting in typical type A and type B microstructures were also applied to the $Ni_{50.3}Ti_{29.7}Hf_{20}$ alloy and detailed TEM investigations were performed. In order to provide type A microstructures, the samples were heat treated at 500 ^{o}C for 3 h and 48 h and also at 550 ^{o}C for 3h. To generate type B microstructures, the samples were subjected to furnace cooling in 48 h from 700 ^{o}C to 100 ^{o}C. From hereafter, all the investigations discussed in the present chapter are based on these thermal treatments since they are typical examples of two different microstructures as indicated above. Furthermore, to study the microstructures with no precipitates, the SHT

samples were also studied and analyzed. Microstructural features such as precipitate size and martensite morphology for both the NiTiZr and NiTiHf alloys are compared and discussed.

Figs. 7.1a to h show the bright field TEM images taken from the same zone axis to reveal the precipitate size in $Ni_{50.3}Ti_{29.7}Zr_{20}$ (right hand side images) and $Ni_{50.3}Ti_{29.7}Hf_{20}$ (left hand side images) for different thermal treatments. The thermal treatment performed on each sample is indicated on the top part of each image. Table 7.1 summarizes the precipitate size of all the heat treated samples for both alloys. The labels for each sample given in Table 7.1 are used hereafter to indicate the corresponding heat treatments applied to the samples. As seen from the images, the precipitate morphology is same in both alloys: spindle like when they are nanometric size (Figs. 7.1a to f) and oblate ellipsoids or nearly plate like shape similar to martensite variants when they reach several hundred nanometers in size (Figs. 7.1g and h). Similar to the observations in the $Ni_{50.3}Ti_{29.7}Zr_{20}$ alloy, when the precipitates are small (<20 nm) they do not interfere with the martensitic transformation and they are absorbed by the martensite variants in the $Ni_{50.3}Ti_{29.7}Hf_{20}$ (Figs. 7.1a, c and e). Moreover, as a consequence of furnace cooling, very large precipitates (>100 nm) form and they limit martensitic growth leading to martensite variants with comparable sizes to the precipitates (Fig. 7.1g). Furthermore, it is clear from images that $Ni_{50.3}Ti_{29.7}Zr_{20}$ samples have significantly larger precipitates compared to $Ni_{50.3}Ti_{29.7}Hf_{20}$ samples under similar aging conditions. Based on the TEM images given, it can be concluded that precipitation coarsening kinetics are faster in the NiTiZr alloy than the NiTiHf alloy for the same relative stoichiometry. For instance, it

takes 3 h at 500 ^{o}C in the NiTiZr (Fig. 7.1b) for the precipitates to grow to 10-25 nm in length and 5-11 nm in width, whereas it takes 48 h at the same aging temperature in the NiTiHf (Fig. 7.1c) to produce similar size precipitates. Moreover, considering the further coarsening of the precipitates, in the NiTiZr it takes only three hours for the precipitates to reach several hundred of nanometers during the furnace cooling of the specimens from 700 ^{o}C to 100 ^{o}C while the precipitates in the NiTiHf reach similar size after 48 h of furnace cooling. However, the reader should note that even slight differences in the initial composition of both alloys which could not be detected through WDS may result in the differences in precipitate size.

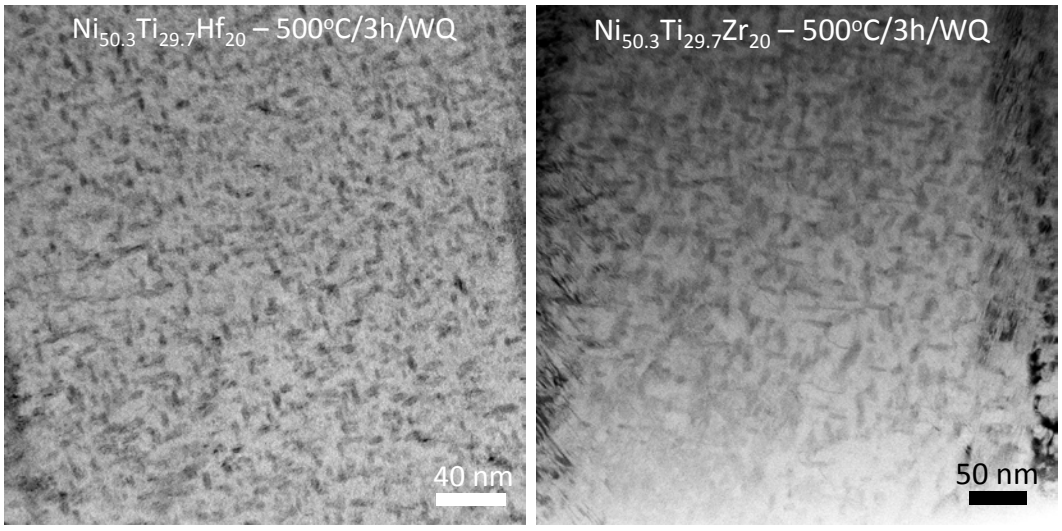

(a) (b)

Figure 7.1 Bright field TEM images of samples aged at 500 °C for 3 h (a) $Ni_{50.3}Ti_{29.7}Hf_{20}$ (b) $Ni_{50.3}Ti_{29.7}Zr_{20}$, at 500 °C for 48 h (c) $Ni_{50.3}Ti_{29.7}Hf_{20}$ (d) $Ni_{50.3}Ti_{29.7}Zr_{20}$, at 550 °C for 3 h (e) $Ni_{50.3}Ti_{29.7}Hf_{20}$ (f) $Ni_{50.3}Ti_{29.7}Zr_{20}$ and furnace cooled from 700 °C to 100 °C in 48 h (g) $Ni_{50.3}Ti_{29.7}Hf_{20}$ (h) $Ni_{50.3}Ti_{29.7}Zr_{20}$.

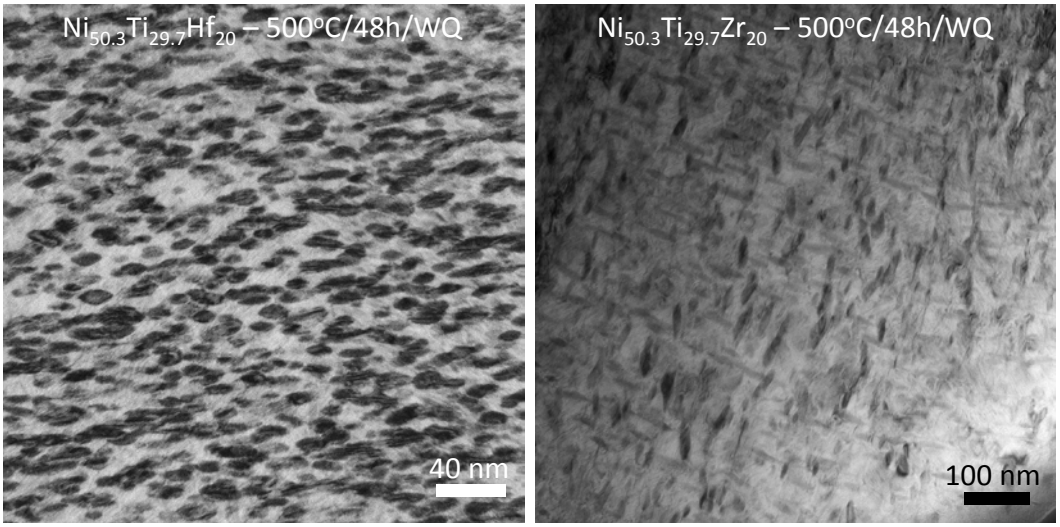

(c) (d)

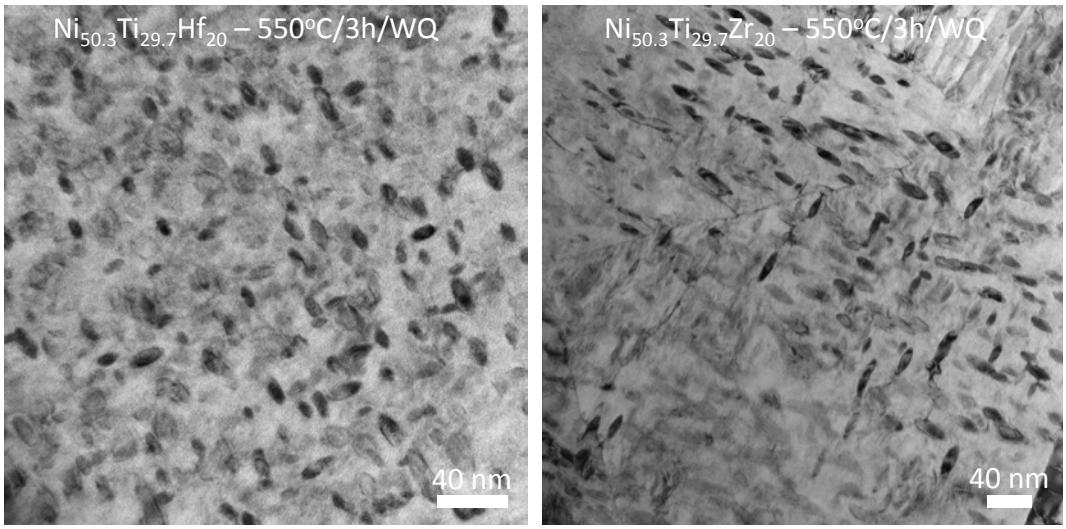

(e) (f)

Figure 7.1 Continued.

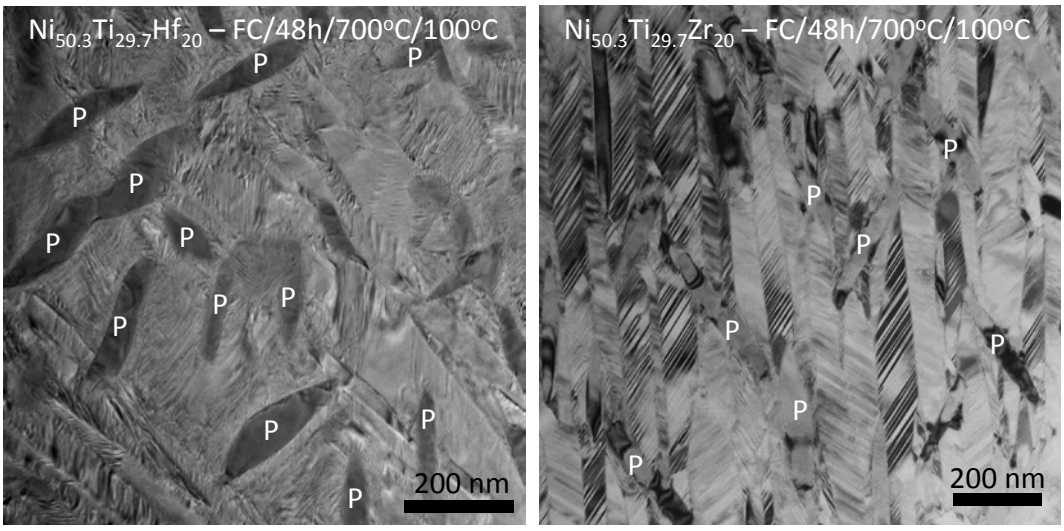

(g) (h)

Figure 7.1 Continued.

Table 7.1 Approximate precipitate sizes of $Ni_{50.3}Ti_{29.7}Zr_{20}$ and $Ni_{50.3}Ti_{29.7}Hf_{20}$ HTSMA alloys as a function of thermal treatment conditions.

Alloy	Treatment	Label	Precipitate size (nm) Length	Width
$Ni_{50.3}Ti_{29.7}Zr_{20}$	3h @ 500 °C	NTZ5003	10-25	5-11
	48h @ 500 °C	NTZ50048	20-40	10-15
	3h @ 550 °C	NTZ5503	18-45	7-14
	FC 700-100 °C 48h	NTZFC48	200-500	35-55
	FC 700-100 °C 3h	NTZFC3	90-280	25-45
$Ni_{50.3}Ti_{29.7}Hf_{20}$	3h @ 500 °C	NTH5003	6-8	2-4
	48h @ 500 °C	NTH50048	8-20	3-8
	3h @ 550 °C	NTH5503	7-20	4-6
	FC 700-100 °C 48h	NTHFC48	70-250	20-70

The small precipitates in NiTiZr (< 45 nm) and in NiTiHf (< 20 nm) could be absorbed by the martensite variants while the large precipitates in the furnace cooled

samples (>100 nm) act as obstacles for martensite growth. Therefore, there is no change in the basic martensite morphology for either alloy for similar aging conditions. Since precipitate size is shown to have strong effect on the martensite morphology, it is also important to investigate the effect of precipitate size on the martensite thickness. For this purpose, the samples with similar precipitate sizes and also representatives of the two distinct microstructures were investigated in more detail by TEM to study the martensite plate thickness. The corresponding TEM images taken from the same zone axis are given in Fig. 7.2. As seen from Table 7.1, precipitate size after aging at 500 ^{o}C for 3 h in $Ni_{50.3}Ti_{29.7}Zr_{20}$ alloy (NTZ5003) is similar to the precipitate size in the $Ni_{50.3}Ti_{29.7}Hf_{20}$ alloy after aging at 500 ^{o}C for 48h (NTH50048). These samples exhibit type A microstructures (Figs. 7.2a and b). For type B microstructures, furnace cooling treatments were applied to both alloy systems (Figs. 7.2c and d). Furnace cooling in 3 h from 700 ^{o}C to 100 ^{o}C in the $Ni_{50.3}Ti_{29.7}Zr_{20}$ alloy (NTZFC3) generates similar size precipitates to the $Ni_{50.3}Ti_{29.7}Hf_{20}$ alloy after furnace cooling in 48 h from 700 ^{o}C to 100 ^{o}C (NTHFC48) (Table 7.1).

For type A microstructures, comparing Fig. 7.2a and b for NTH5003 and NTZ50048, respectively, variant thickness in the NiTiZr alloy is much larger than the NiTiHf system considering similar precipitate sizes in both systems. This is due to the easier accommodation of transformation strain around the precipitates in NiTiZr alloys than the NiTiHf alloys as discussed in Chapter IV. Another reason why the martensite variants are larger in the NiTiZr alloy, for fine precipitates, is the relative stiffness of the precipitates and the parent phase in both alloys. As given in Table 4.3 (Chapter IV), the

H-phase precipitates in NiTiHf are stiffer than those in NiTiZr alloys. Additionally, the parent phase (B2 austenite) in the NiTiHf alloy has higher stiffness than in the NiTiZr alloy. As a consequence, lower energy will be necessary to accommodate the strain fields around the precipitates in the NiTiZr alloy than the NiTiHf alloy.

For type B microstructures such as in the case of NTHFC48 (Fig. 7.2c) and NTZFC3 (Fig. 7.2d), the martensite variants are generally comparable in size with the precipitates. For such cases, no obvious difference in the martensite variant thickness was observed between the two alloys. In this type of microstructure, martensite variants can nucleate only within the space between the precipitates and are restricted in size by the microstructure and therefore do not differ remarkably in both alloys.

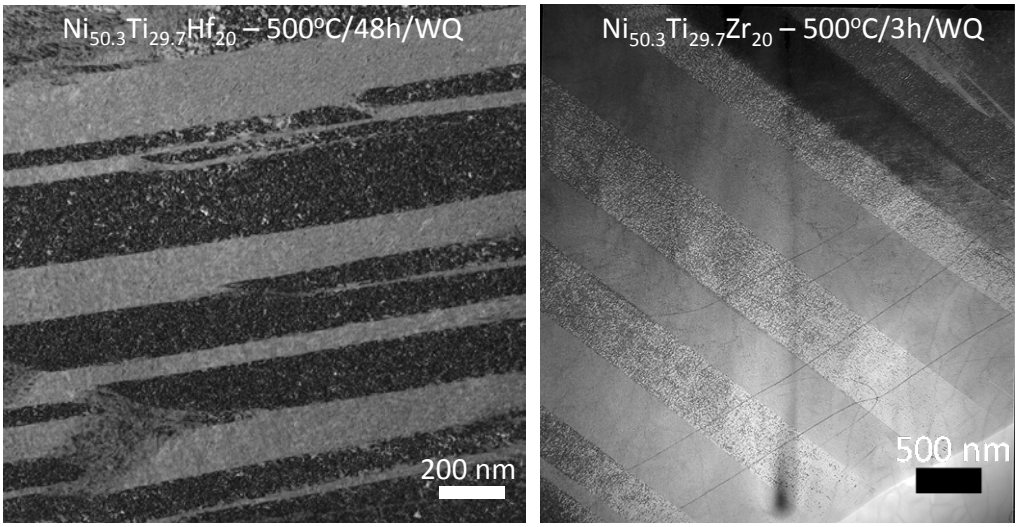

(a) (b)

Figure 7.2 Bright field TEM images for the similar precipitate sizes in (a) $Ni_{50.3}Ti_{29.7}Hf_{20}$ aged at 500 °C for 48 h (b) $Ni_{50.3}Ti_{29.7}Zr_{20}$ aged at 500 °C for 3 h, (c) $Ni_{50.3}Ti_{29.7}Hf_{20}$ furnace cooled in 48 h from 700 °C to 100 °C, (d) $Ni_{50.3}Ti_{29.7}Zr_{20}$ furnace cooled in 3 h from 700 °C to 100 °C.

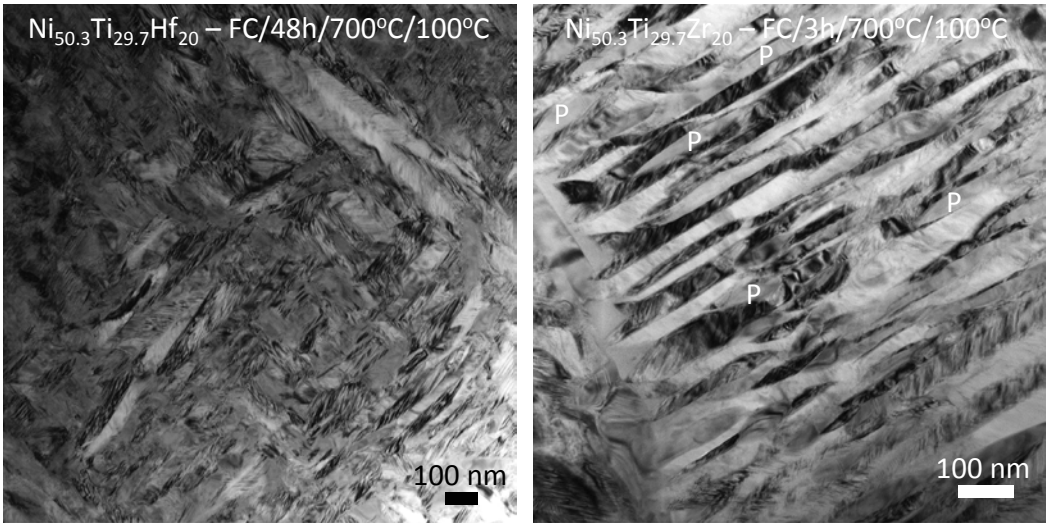

(c) (d)

Figure 7.2 Continued.

7.2 Transformation Temperatures and Characteristics

To provide examples of the two different microstructure types in the $Ni_{50.3}Ti_{29.7}Hf_{20}$ alloy, samples were aged at 500 ^{o}C for 3 h and 48 h (NTH5003 and NTH50048, respectively) and at 550 ^{o}C for 3 h (NTH5503) and also subjected to furnace cooling in 48 h from 700 ^{o}C to 100 ^{o}C (NTHFC48). Moreover, to analyze the initial transformation temperatures and characteristics, the SHT sample (hereafter labeled as NTH) was also investigated. The transformation temperatures of these samples were measured via DSC and the corresponding DSC curves are shown in Fig. 7.3. As seen from Fig. 7.3, the transformation temperatures increase with aging due to the precipitation and hence Ni-depletion of the matrix. Furthermore, the thermal hysteresis decreases with aging (38 ^{o}C for the SHT sample and less than 30 ^{o}C for the aged samples) as a consequence of precipitation hardening. However, similar to the

observations in $Ni_{50.3}Ti_{29.7}Zr_{20}$, the thermal hysteresis increased significantly for the NTHFC48 sample. In this case large density of small martensite variants are generated, controlled by the large precipitate obstacles, and therefore energy dissipation is increased and so is the thermal hysteresis. Additionally, the thermal stability of the alloy improves when precipitates are present. The shifts in consecutive cycles in M_s temperature is very small due to harder defect generation with precipitation hardening in the aged and furnace cooled samples compared to the SHT sample.

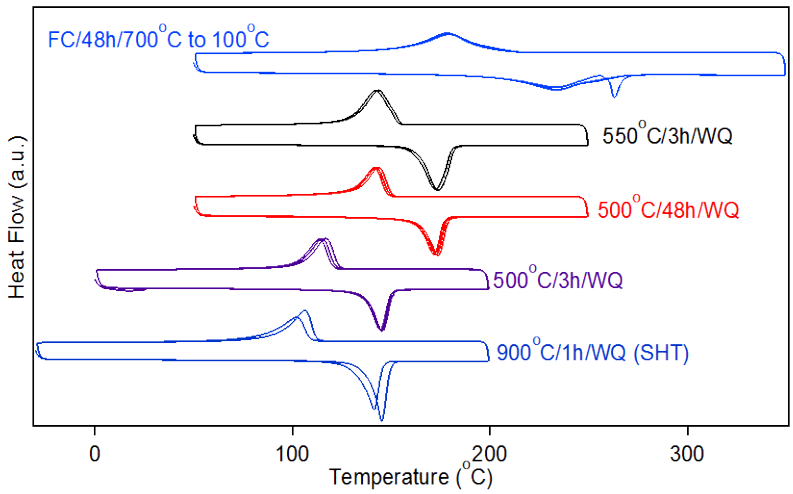

Figure 7.3 The stress free DSC cycles of $Ni_{50.3}Ti_{29.7}Hf_{20}$ HTSMA subjected to various precipitation heat treatments.

To compare the transformation temperatures and transformation characteristics of the $Ni_{50.3}Ti_{29.7}Hf_{20}$ alloy with the $Ni_{50.3}Ti_{29.7}Zr_{20}$ counterpart, all the DSC data (A_f, M_s, ΔT and $M_{s1} - M_{s3}$) for both systems are summarized in Table 7.2. As seen from the table, when there are no precipitates (SHT samples at 900 °C for 1 h), the NiTiHf alloy

shows much higher transformation temperatures. But with precipitation (after aging at 500 ^{o}C for 3 h and 48 h or at 550 ^{o}C for 3 h), the A_f temperatures are almost same whereas the M_s temperatures are 10 to 20 ^{o}C higher in the $Ni_{50.3}Ti_{29.7}Hf_{20}$ alloy for similar aging conditions. This observation is consistent with previous studies since Hf is reported to increase transformation temperatures more effectively than Zr does [25]. However, in the case of furnace cooling, the transformation temperatures of the NiTiHf alloy are ~ 90 ^{o}C higher than the NiTiZr. Since the precipitate sizes are very large after furnace cooling, the dominant mechanism leading to the increase in transformation temperatures is the compositional change.

Table 7.2 Comparison of transformation temperatures, thermal hysteresis and the change in M_s (M_{s1} - M_{s3}) of the $Ni_{50.3}Ti_{29.7}Zr_{20}$ and $Ni_{50.3}Ti_{29.7}Hf_{20}$ HTSMAs for various thermal treatment conditions.

		A_f (^{o}C)	M_s (^{o}C)	ΔT (^{o}C)	M_{s1}- M_{s3} (^{o}C)
$Ni_{50.3}Ti_{29.7}Zr_{20}$	SHT (900^{o}C/1h/WQ)	98	30	68	18.8
	500^{o}C/3h/WQ	151	114	37	7.5
	500^{o}C/48h/WQ	185	136	49	9.5
	550^{o}C/3h/WQ	180	134	46	7.3
	FC/48h/700^{o}C to 100^{o}C	175	113	62	-1.8
$Ni_{50.3}Ti_{29.7}Hf_{20}$	SHT (900^{o}C/1h/WQ)	150	112	38	3.3 (2 cycles)
	500^{o}C/3h/WQ	151	123.5	27.5	3.2
	500^{o}C/48h/WQ	179	150	29	2.3
	550^{o}C/3h/WQ	182	155	27	1.5 (2 cycles)
	FC/48h/700^{o}C to 100^{o}C	268.50	202	66.5	3.9

As seen from Table 7.2, the thermal hysteresis (ΔT) values are significantly smaller in the NiTiHf alloy (38 ^{o}C) compared to the NiTiZr alloy (68 ^{o}C) in precipitate free conditions (SHT). When small precipitates are present (after aging at 500 ^{o}C for 3 h and 48 h or at 550 ^{o}C for 3 h), ΔT values are 10 to 20 ^{o}C higher in the NiTiZr alloy. On the other hand, ΔT values get closer in both systems when the precipitates are larger than 100 nm in size (after furnace cooling). The shift in M_s temperatures ($M_{s1} - M_{s3}$), which is a measure of thermal stability is also smaller in the NiTiHf alloy as compared to the NiTiZr alloy when there are no precipitates or when the precipitates are very small, indicating that the NiTiHf alloy is more stable thermally. When precipitate size is large, the thermal stability of both alloys seems to be similar, since there is very little change in M_s temperatures with thermal cycling. These differences in the thermal hysteresis and thermal stability of both alloys are due to the difference in the lattice parameters and hence in the lattice compatibility of transforming phases which will be further discussed below.

7.3 Load-biased Shape Memory Response

Load-biased thermal cycling tests were carried out on the SHT and aged $Ni_{50.3}Ti_{29.7}Hf_{20}$ specimens in order to study the shape memory response. Samples of the two different microstructures (NTH5003, NTH50048, NTH5503, NTHFC48) as well as the precipitate free sample (SHT) were tested. Figs 7.4a to e show the thermo-mechanical cycles under different applied bias stress levels for the $Ni_{50.3}Ti_{29.7}Hf_{20}$ samples. As seen from Fig. 7.4, after precipitation heat treatments, the $Ni_{50.3}Ti_{29.7}Hf_{20}$

HTSMA shows excellent shape recovery up to applied stress levels of 300 MPa. However, NTHFC48 sample (Fig. 7.4e) fails earlier (under 300 MPa) than the other samples probably due to the increased brittleness of these samples due increased variant to variant interactions and local strains. On the other hand, the NTH sample (Fig. 7.4a) without precipitates still shows very good dimensional stability, however it starts to undergo plastic deformation under 200 MPa applied stress. It is also evident that except the NTHFC48 sample (Fig. 7.4e), precipitation hardening decreases the thermal hysteresis in a similar fashion to the $Ni_{50.3}Ti_{34.7}Hf_{15}$ SMA.

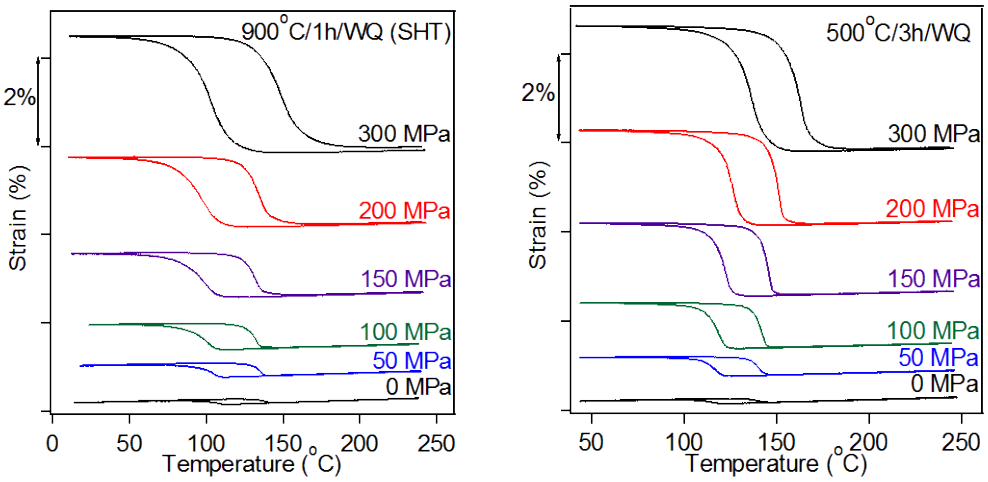

(a) (b)

Figure 7.4 Strain vs temperature response of the $Ni_{50.3}Ti_{29.7}Hf_{20}$ specimens (a) solution heat treated (b) aged at 500 °C for 3 h, (c) aged at 500 °C for 48 h, (d) aged at 550 °C for 3 h and (e) furnace cooled in 48 h from 700 °C to 100 °C under various applied stress levels in tension.

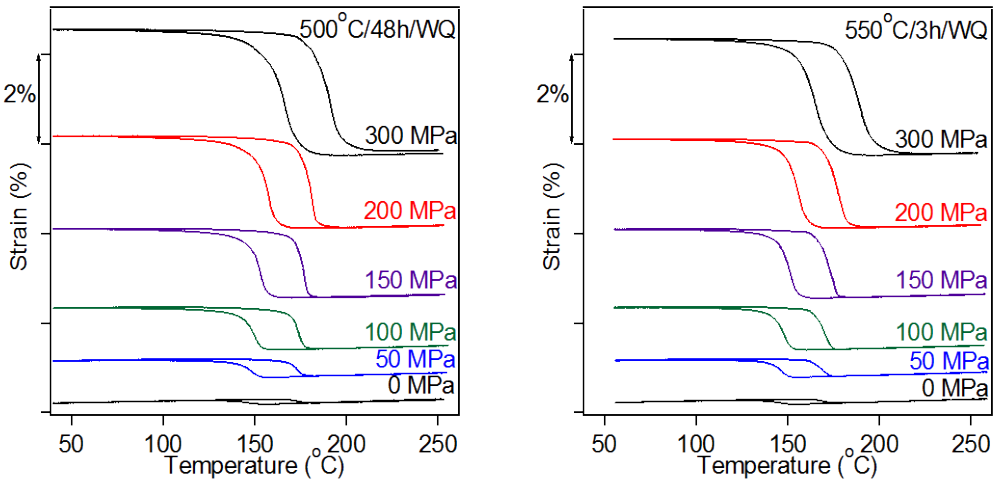

(c)

(d)

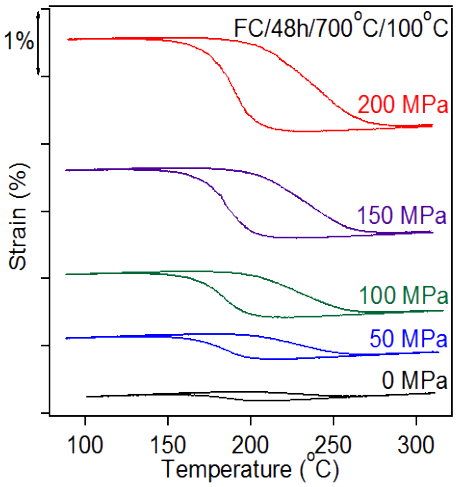

(e)

Figure 7.4 Continued.

Fig. 7.5 summarizes the recovered and unrecovered strain levels of the SHT and aged $Ni_{50.3}Ti_{29.7}Hf_{20}$ samples under various applied stress levels. As expected, the recovered strain levels increase with increasing bias stress and they reach similar levels

(~ 2.7%) under 300 MPa stress for the NTH, NTH5003, NTH50048 and NTH5503 samples. However, NTHFC48 shows a maximum recovered strain level of only 1.4% under 200 MPa which is significantly lower than the aged samples at this stress since it is very brittle and shows early failure. No unrecoverable strain is measured even in the NTH sample up to 150 MPa applied stress and only 0.13% unrecovered strain is observed under 300 MPa. As a consequence of increased resistance to slip due to precipitation hardening, no plastic deformation is seen up to 200 MPa applied stress in the thermal treated samples and only 0.09% plastic deformation is visible in NTH50048 sample under 300 MPa. Similar to $Ni_{50.3}Ti_{34.7}Zr_{15}$, $Ni_{50.3}Ti_{34.7}Hf_{15}$ and $Ni_{50.3}Ti_{29.7}Zr_{20}$ SMAs discussed previously, no prior thermo-mechanical training is necessary to provide dimensional stability in the $Ni_{50.3}Ti_{29.7}Hf_{20}$ SMA, since these very small or negligible unrecovered strain levels are already obtained during the first few thermal cycles.

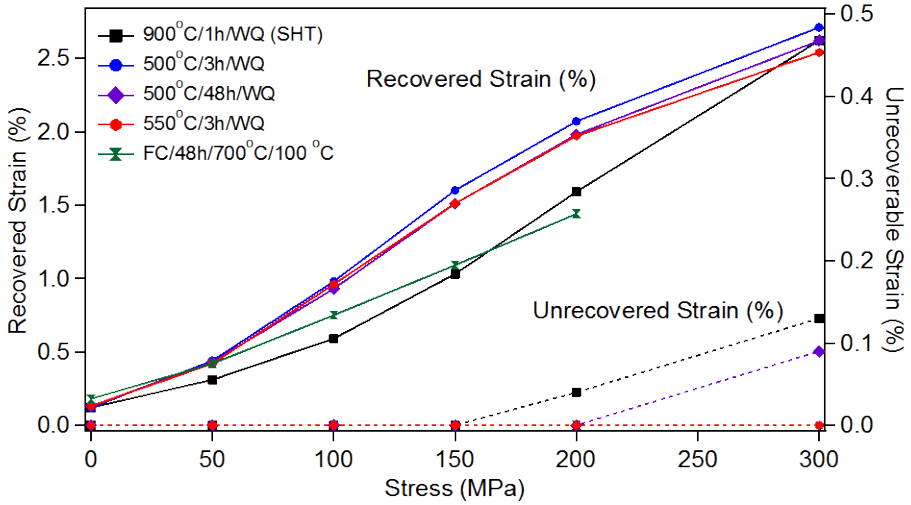

Figure 7.5 Recovered and unrecovered strain levels of the SHT and precipitation heat treated $Ni_{50.3}Ti_{29.7}Hf_{20}$ samples during thermal cycling in tension.

Similar to the observations in $Ni_{50.3}Ti_{34.7}Hf_{15}$ and $Ni_{50.3}Ti_{29.7}Zr_{20}$, the thermal hysteresis is also remarkably influenced by precipitation hardening. The transformation thermal hysteresis of the $Ni_{50.3}Ti_{29.7}Hf_{20}$ HTSMA derived from the thermal cycles (Fig. 7.4) is given in Fig. 7.6a. As compared to the SHT sample, which has hysteresis over 30 ^{o}C, the samples with small precipitates (NTH5003, NTH50048 and NTH5503) have smaller hysteresis levels (< 30 ^{o}C) due to harder defect generation under applied stress. In these samples with fine precipitates, thermal hysteresis is similar to each other and does not change significantly with the increase in bias load. The thermal hysteresis values remain constant up to 150 MPa applied stress in the NTH sample and increases thereafter, which is in accordance with the plastic deformation seen after 150 MPa stress level. Furthermore, as seen from Fig. 7.6a, the NTHFC48 sample with very large precipitates follows a different behavior as compared to other samples. The thermal hysteresis (~ 56 ^{o}C) is significantly larger than those in the NTH sample and nearly two times that of the samples with small precipitates (~ 28 ^{o}C). A large number of martensite variants are formed when the large precipitates limit the martensite plate growth and hence more intervariant boundaries or precipitate-martensite variant boundaries are present in the NTHFC48 sample. Therefore, during transformation more energy is dissipated and hence the thermal hysteresis is very large. Similar conclusions were also drawn for the furnace cooled $Ni_{50.3}Ti_{29.7}Zr_{20}$ samples.

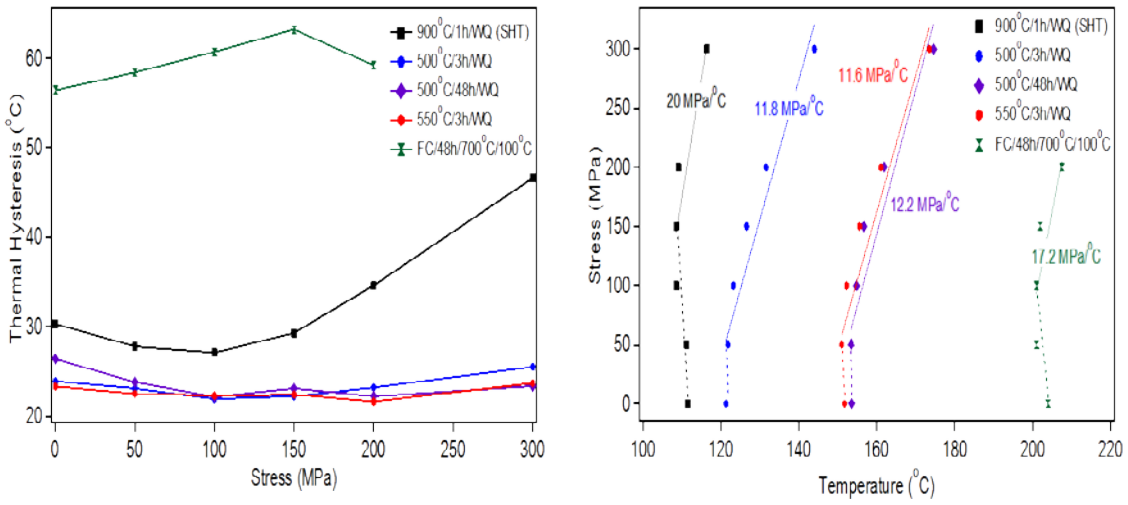

(a) (b)

Figure 7.6 The evolution of the (a) thermal hysteresis and (b) M_s temperatures of SHT and heat treated $Ni_{50.3}Ti_{29.7}Hf_{20}$ samples during thermal cycling in tension as a function of applied stress.

The change in the M_s temperatures with the best linear fit lines of the SHT and aged $Ni_{50.3}Ti_{29.7}Hf_{20}$ samples as a function of applied stress is shown in Fig. 7.6b. The M_s temperatures measured from the zero stress thermal cycle compare well with the M_s temperatures measured via DSC (± 2 ^oC). The M_s temperatures follow a bilinear stress dependence at low applied stress levels: up to 50 MPa for the NTH5003, NTH50048 and NTH5503 and up to 100 MPa for the NTH and NTHFC48 samples where M_s is insensitive to stress. Above these stress levels, they all follow linear stress dependence with slopes of 20 MPa/^{o}C, 11.8 MPa/^{o}C, 12.2 MPa/^{o}C, 11.6 MPa/^{o}C and 17.2 MPa/^{o}C for the NTH, NTH5003, NTH50048, NTH5503 and NTHFC48 samples, respectively. The reason that M_s does not follow a linear increase at low applied stress levels is probably due to a change in strain energy around the precipitates with the external

applied stress as explained in section 5.1.4 in Chapter V similar to the other Ni-rich NiTiZr and NiTiHf SMAs studied in the present study.

Throughout this chapter, the microstructure, transformation characteristics and shape memory response of the $Ni_{50.3}Ti_{29.7}Hf_{20}$ and $Ni_{50.3}Ti_{29.7}Zr_{20}$ HTSMAs were compared for two different microstructures, explained in section 7.1. It is also crucial to investigate samples with similar microstructures in order to better understand the similarities and differences in the behavior of the two alloys. For this purpose, representative thermal treatments leading to similar precipitate size in the $Ni_{50.3}Ti_{29.7}Hf_{20}$ and $Ni_{50.3}Ti_{29.7}Zr_{20}$ HTSMAs were chosen and the shape memory behaviors compared. Table 7.2 suggests that NTH50048 and NTZ5003 contain precipitates similar in size and type A microstructures. As representatives of type B microstructures, NTHFC48 and NTZFC3 samples were found to be similar (Table 7.2). Finally, the load-biased shape memory response of the NTZ50048 and NTZFC48 samples are also discussed to compare the shape memory response of both systems under similar aging conditions.

Fig. 7.7 represents the thermo-mechanical cycles of the $Ni_{50.3}Ti_{29.7}Hf_{20}$ (shown with dashed lines) and $Ni_{50.3}Ti_{29.7}Zr_{20}$ (solid lines) samples under 200 MPa applied bias stress for similar precipitate sizes (NTH50048 vs NTZ5003 and NTHFC48 vs NTZFC3) and also for similar aging conditions (NTH50048 vs NTZ50048 and NTHFC48 vs NTZFC48). It is obvious from Fig. 7.7 that precipitate size and hence the martensite morphology has the same general effect on the shape memory characteristics of the $Ni_{50.3}Ti_{29.7}Hf_{20}$ alloy (NTH50048, NTHFC48) as they do on $Ni_{50.3}Ti_{29.7}Zr_{20}$ HTSMA (NTZ5003, NTZ50048, NTZFC48, NTZFC3). Martensitic transformation and martensite

reorientation/detwinning are easier in type A microstructures (NTH50048, Figs. 7.1c and 7.2a) due to the limited interference of precipitates with the transformation. However in type B microstructures (NTHFC48, Fig. 7.1g and 7.2c), martensite reorientation/detwinning is harder since particles are now obstacles for the martensitic growth. As a consequence, larger thermal hysteresis, and broader transformation range (defined as $M_s - M_f$) as well as smaller transformation strain are obtained in NTHFC48 sample as compared to NTH50048. These observations are completely in accordance with the behavior of the $Ni_{50.3}Ti_{29.7}Zr_{20}$ alloy with similar microstructures. For instance, larger transformation strain, smaller transformation range and smaller thermal hysteresis are seen in the NTZ5003 and NTZ50048 samples as compared to NTZFC48 and NTZFC3 samples. The reader should refer to Chapter VI for detailed discussion on the effect of microstructure on the shape memory characteristics of $Ni_{50.3}Ti_{29.7}Zr_{20}$.

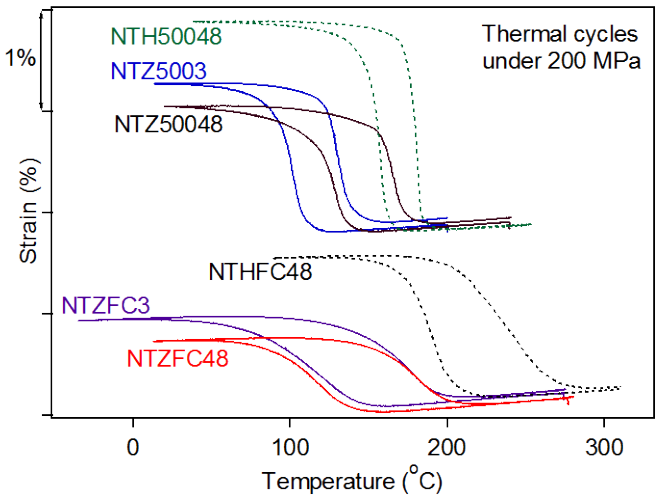

Figure 7.7 Comparison of the thermal cycles for the $Ni_{50.3}Ti_{29.7}Zr_{20}$ and $Ni_{50.3}Ti_{29.7}Hf_{20}$ specimens under 200 MPa applied stress level. NTZ5003, NTZ50048 and NTH50048 are representatives of type A microstructures while NTZFC3, NTZFC48 and NTHFC48 samples are examples of type B microstructures in both alloys. Samples with type A and type B microstructures clearly show differences in terms of transformation strain levels, thermal hysteresis and martensitic transformation ranges (M_s - M_f) in both alloys.

Fig. 7.7 indicates that although the thermo-mechanical response of both alloy systems is similar when similar microstructures are compared, they still possess differences in transformation strain levels and thermal hysteresis levels when directly compared to each other. Fig. 7.8 shows the evolution of strain levels of both alloy systems for similar aging conditions and for similar precipitate sizes. For similar thermal treatments, comparing NTH50048 with NTZ50048 and NTHFC48 with NTZFC48 samples, the $Ni_{50.3}Ti_{29.7}Hf_{20}$ HTSMA shows much higher recovered transformation strain levels. NTH50048 samples show 2.6% recoverable strain under 300 MPa while NTZ50048 sample show nearly 1% less transformation strain (~ 1.6%). For the large precipitate cases, even though NTHFC48 sample fails at stress levels above 200 MPa

and shows only 1.4% recoverable strain, it is still higher than the transformation strain that NTZFC48 sample exhibits (1.25%) under 300 MPa stress level. The $Ni_{50.3}Ti_{29.7}Hf_{20}$ alloy shows still higher transformation strain levels than the $Ni_{50.3}Ti_{29.7}Zr_{20}$ alloy when samples with similar precipitate sizes are compared. NTH50048 samples also possess higher recovered strain levels (2.6%) than the NTZ5003 sample (1.9%) showing similar precipitate sizes. For the microstructures where large precipitates refine variant thickness, 1.4% strain is observed in NTHFC48 under 200 MPa, which is higher than that obtained in NTZFC3 sample (1.1%) under same stress level. But, the NTZFC3 sample exceeds the strain level of the NTHFC48 sample under 300 MPa (1.6%). However, as seen from Fig. 7.8, the strain levels do not reach to a plateau region in either alloy system, suggesting that higher strain levels may be obtained if samples do not fracture under the applied stress levels in the present study. It can be argued the NTHFC48 sample would exceed the strain level of NTZFC3 sample if it did not fail during testing at 300 MPa stress level. Since the strain levels that would be obtained in an SMA under a certain applied stress is a function of the volume fraction of the martensite detwinned, it would not be conclusive to state that the maximum strain levels of $Ni_{50.3}Ti_{29.7}Hf_{20}$ HTSMA will necessarily be larger than those in $Ni_{50.3}Ti_{29.7}Zr_{20}$. The reason why two materials show different theoretical strain levels may be the difference in their lattice parameters, which will be further discussed below. However, based on the current results, it can be argued that during practical applications up to 300 MPa applied stress levels, $Ni_{50.3}Ti_{29.7}Hf_{20}$ samples will show larger transformation strains than the $Ni_{50.3}Ti_{29.7}Zr_{20}$ counterpart with similar microstructural features or thermal treatments.

Both systems show very good dimensional stability and no or very small (< 0.1%) unrecovered strain levels are obtained up to 300 MPa (Fig. 7.8). Therefore, the applied stress levels are still well below the stress levels where plastic deformation begins to compete with martensitic twinning and decreases the recoverable strain levels as a result of incomplete transformation of martensite to austenite.

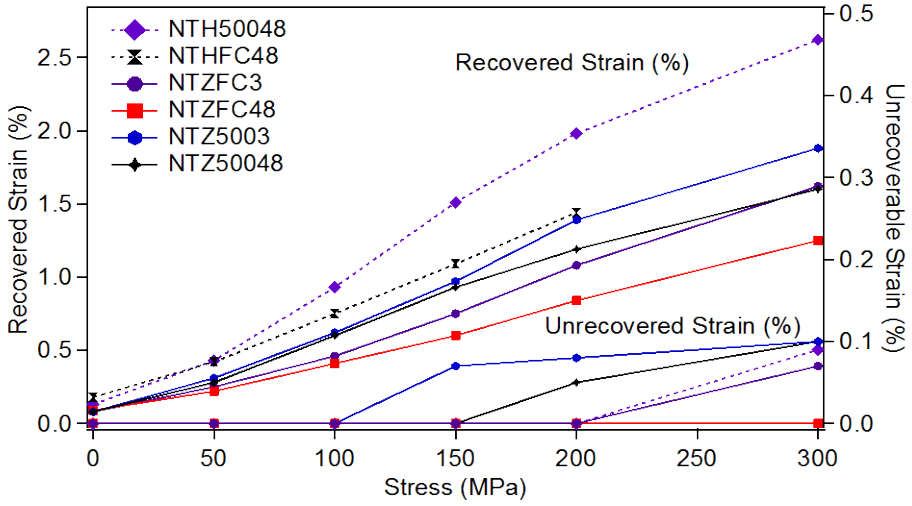

Figure 7.8 The comparison of the recovered and unrecovered strain levels of $Ni_{50.3}Ti_{29.7}Zr_{20}$ (solid lines) and $Ni_{50.3}Ti_{29.7}Hf_{20}$ (dashed lines) during isobaric thermal cycling in tension with representative type A and B microstructures.

Beside the transformation strain levels, the transformation thermal hysteresis is also an important criteria for practical applications. SMAs with low thermal hysteresis generally provide better transformation reversibility and less energy dissipation during transformation. Hence, it is also important to study the differences and similarities in the thermal hysteresis response of the Ni-rich NiTiZr and NiTiHf alloys as a function of

applied stress. The thermal hysteresis of the $Ni_{50.3}Ti_{29.7}Hf_{20}$ and $Ni_{50.3}Ti_{29.7}Zr_{20}$ samples treated under same thermal conditions and having similar precipitate size are given in Fig. 7.9. When samples of both alloys are furnace cooled for 48 h, (NTHFC48 and NTZFC48), the thermal hysteresis (ΔT) values are comparable (~ 60 ^{o}C) and do not change notably with an increase in stress. But for similar precipitate sizes after furnace cooling, NTZFC3 samples show almost 10 ^{o}C less hysteresis (~ 50 ^{o}C) as compared to NTHFC48 samples. The thermal hysteresis is much less than those in the furnace cooled specimens in both alloys because the precipitates are smaller. For similar aging conditions which generate fine precipitates, NTH50048 has thermal hysteresis (~ 25 ^{o}C) around 10 ^{o}C smaller than the NTZ50048 sample (~ 35 ^{o}C) and with an exception under zero applied stress level, around 5 ^{o}C smaller than the NTZ5003 (~ 30 ^{o}C), which has precipitates similar in size with the NTH50048 sample. ΔT values of the samples with small precipitates generally do not change with the applied stress over the range of stresses investigated.

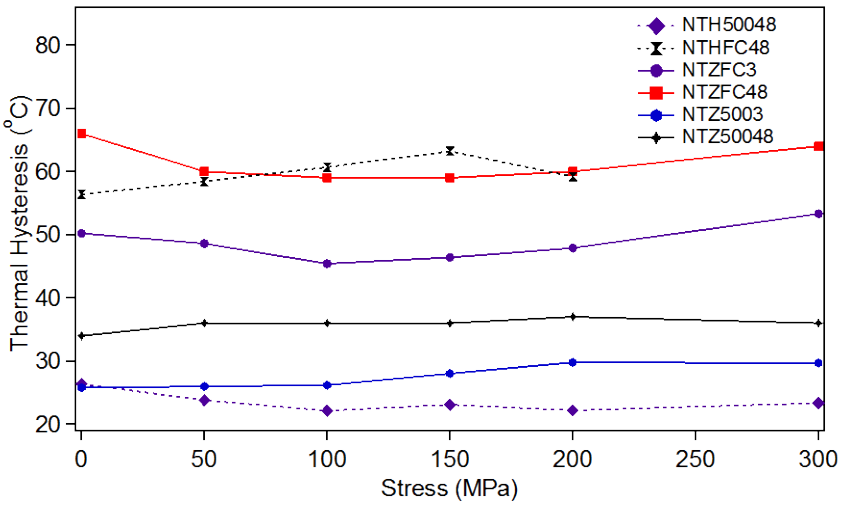

Figure 7.9 Comparison of the evolution of thermal hysteresis in $Ni_{50.3}Ti_{29.7}Zr_{20}$ (solid lines) and $Ni_{50.3}Ti_{29.7}Hf_{20}$ (dashed lines) for various heat treatments as a function of applied stress during thermal cycling in tension.

7.4 Mechanisms Responsible for Differences in the Microstructure and Shape Memory Characteristics

It has been shown that the $Ni_{50.3}Ti_{29.7}Hf_{20}$ samples show higher recovered strain levels than the $Ni_{50.3}Ti_{29.7}Zr_{20}$ alloys at applied stress levels below 300 MPa. Furthermore, aging treatments leading to smaller precipitate sizes results in lower thermal hysteresis levels in $Ni_{50.3}Ti_{29.7}Hf_{20}$ HTSMA yet NTZ5003 is not that different. However, thermal hysteresis values are closer in both alloys systems when large particles are present in the microstructure as a consequence of furnace cooling. These differences in strain levels and thermal hysteresis are probably due to the difference in their lattice parameters and hence their lattice compatibility and their maximum theoretical strain levels. In this part of the report, the effect of these properties on shape memory characteristics are discussed.

Furthermore, the larger variant sizes seen in $Ni_{50.3}Ti_{29.7}Zr_{20}$ alloy for type A microstructures is probably because of the difference in strain energy around the precipitates. This conclusion can be verified through comparing the elastic constants of both alloy systems, which will be reviewed below.

7.4.1 Lattice Compatibility of Transforming Phases

Thermal hysteresis arises from the energy dissipation that is instilled to the system through undercooling or applied stress. It is a consequence of frictional losses due to lattice friction and generation of new interfaces or point and line defects like vacancies, self-interstitials or dislocations to accommodate transformation shear and volume change. Lower thermal hysteresis is obtained when the matrix of an SMA material is strengthened due to precipitation hardening or solid solution strengthening and hence defect formation and accommodation of transformation shear through defect formation becomes more difficult. In such cases, the transformation shear is accommodated generally in an elastic manner leading to lower thermal hysteresis [111]. Furthermore, it has been discussed in Chapter II that “geometric non-linear theory of martensite” (GNLTM) explains the relationship between the shape memory effect and symmetry of the crystal and crystallographic compatibilities. The theory states that transformation hysteresis in SMA systems is a consequence of the crystallographic incompatibilities between the austenite and martensite phases and the hysteresis can be significantly decreased through the improvement of the lattice compatibility. According to the GNLTM, one of the criteria that will lead to small hysteresis in an SMA is the $\lambda_2 =$

1 condition where λ_2 is the second eigenvalue of the transformation matrix U. For an SMA that λ_2 deviates from 1, the energy dissipation is large and thus thermal hysteresis is large. In case of better or full compatibility between the transforming phases ($\lambda_2 = 1$), the hysteresis is minimized since there is no need for the elastic transition layer or the interfacial energy on the twin boundaries [111].

For an SMA, the transformation matrix, U, can be built up using the lattice parameters of the austenite and martensite phases. Hence, the second eigenvalue of this matrix, λ_2, becomes a function of the lattice parameters of the transforming phases. For the B19' to B2 transformation, the eigenvalues can be found as $\lambda_1 = a/a_0$, $\lambda_2 = b/\sqrt{2}\ a_0$ and $\lambda_3 = c/\sqrt{2}\ a_0$ where a, b and c are the lattice parameters of monoclinic martensite unit cell and a_0 is the lattice parameter of the cubic austenite unit cell. Therefore, in order to study the lattice compatibility and the thermal hysteresis in the $Ni_{50.3}Ti_{29.7}Zr_{20}$ and $Ni_{50.3}Ti_{29.7}Hf_{20}$ HTSMAs, the lattice parameters of austenite and martensite phases should be determined. For this purpose, all the samples were investigated first at room temperature to obtain the martensite peaks and the corresponding XRD patterns are shown in Figs. 7.10a and b for the $Ni_{50.3}Ti_{29.7}Hf_{20}$ and $Ni_{50.3}Ti_{29.7}Zr_{20}$ alloys, respectively. As seen from the patterns, seven individual peaks belonging to B19' martensite can be indexed. The martensite lattice parameters were calculated using the obtained peaks shown in Fig. 7.10. In order to calculate the austenite lattice parameters, the materials were first heated to 20 °C or 30 ^{o}C above their A_f temperature to transform the material fully to austenite. Examples of such an approach for both alloy systems are shown in Figs. 7.11a and b for the samples NTH50048 and NTZFC3, respectively. As

seen from the figures, the martensite peaks obtained at room temperature are not present during XRD scan at elevated temperatures (above their A_f temperatures) and only the (110) peak of B2 austenite becomes visible over the limited range of 2Θ shown. Then the materials are slowly cooled to a temperature above their M_s temperatures (M_s + 10 ^oC). Then the XRD experiments were carried out on several temperatures above the M_s and A_f temperatures. An example of such high temperature XRD experiments at five different temperatures and the corresponding B2 patterns is shown in Fig. 7.12a for NTH50048 sample. It is clear that the peaks corresponding to $(110)_{B2}$ plane shifts to lower angles due to the thermal expansion of the austenite unit cell with the increase in experiment temperature. Thus, any lattice parameter calculation at these temperatures would deviate from the real lattice parameters of austenite at room temperature. Therefore, in order to provide thermodynamically equivalent conditions for both the austenite and martensite lattice parameter calculations, the 2Θ values measured from the $(110)_{B2}$ peaks at different temperatures were extrapolated to room temperature as shown in Fig. 7.12b. The diffraction angle estimated for the room temperature values as exemplified in Fig. 7.12b for each sample is used for the austenite lattice parameter calculations. Since precipitate crystal structure is a superstructure of the B2 austenite, the lattice parameters of the H-phase are also calculated using austenite lattice parameters.

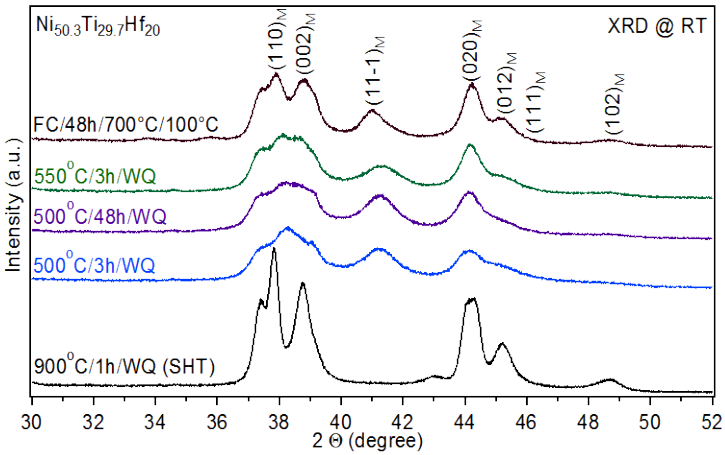

(a)

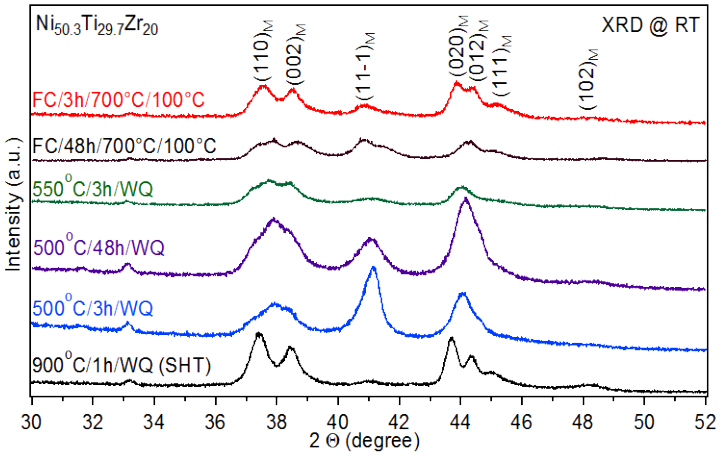

(b)

Figure 7.10 Room temperature XRD patterns of SHT and precipitation heat treated (a) $Ni_{50.3}Ti_{29.7}Hf_{20}$ and (b) $Ni_{50.3}Ti_{29.7}Zr_{20}$ alloys.

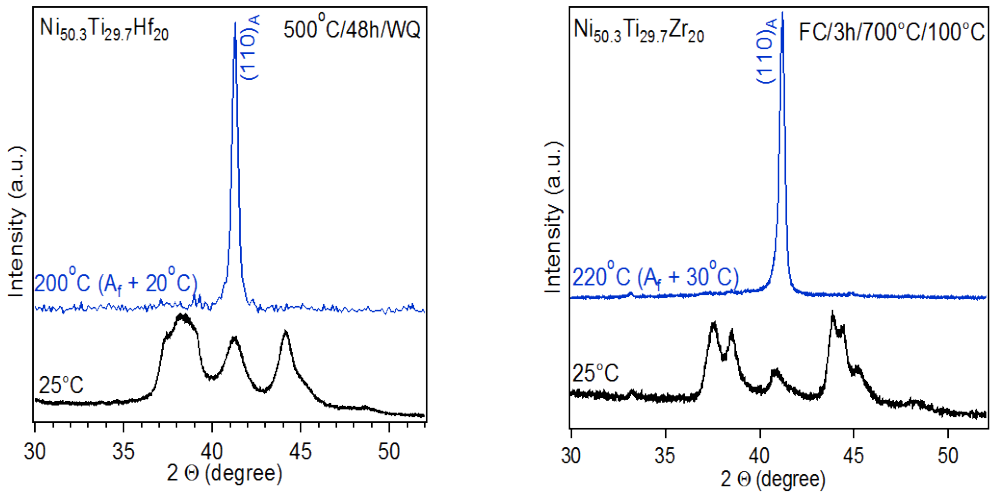

(a) (b)

Figure 7.11 The evolution of B19' diffraction peaks to the B2 peaks during elevated temperature XRD scan above A_f of the (a) $Ni_{50.3}Ti_{29.7}Hf_{20}$ sample aged at 500 °C for 48 h and (b) $Ni_{50.3}Ti_{29.7}Zr_{20}$ sample furnace cooled from 700 °C to 100 °C in 3 h.

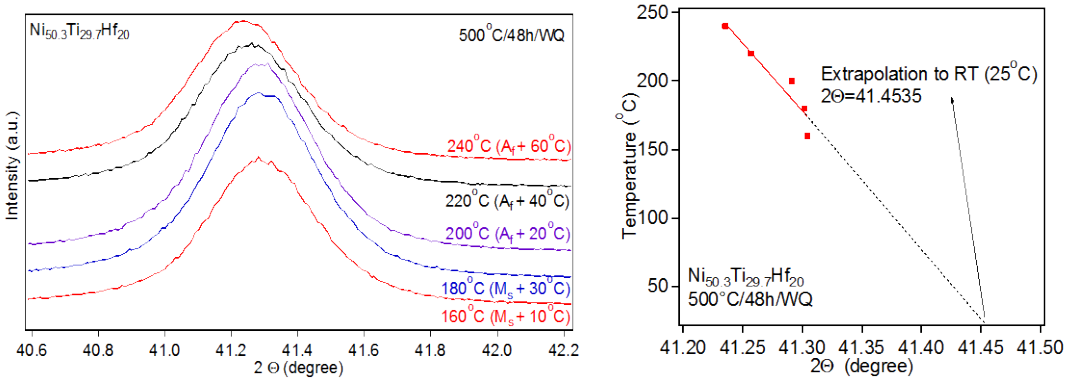

(a) (b)

Figure 7.12 (a) High temperature XRD patterns of $Ni_{50.3}Ti_{29.7}Hf_{20}$ sample aged at 500 °C for 48 h. The sample is in fully austenitic state at the experimental temperatures. (b) Interpolation of 2θ values to room temperature.

The lattice parameters for the SHT (no precipitates) and precipitation heat treated $Ni_{50.3}Ti_{29.7}Hf_{20}$ and $Ni_{50.3}Ti_{29.7}Zr_{20}$ samples are summarized in Tables 7.3 and 7.4, respectively. As seen from the tables, formation of precipitates results in a decrease in the lattice parameters of B19' martensite stating that the martensite unit cell shrinks when the precipitates are present. However, the lattice parameters of the austenite phase with precipitation do not change remarkably for both alloy systems. Precipitate lattice parameters are nearly constant for all the aged samples showing that they are not a function of aging time and temperature and hence precipitate size.

Table 7.3 The lattice parameters of martensite, austenite and H-phase precipitates in SHT and precipitation heat treated $Ni_{50.3}Ti_{29.7}Hf_{20}$ samples.

	B19' Martensite				B2 Austenite (Å)	H-Phase		
	a (Å)	b (Å)	c (Å)	β (degree)		a (Å)	b (Å)	c (Å)
SHT (900°C/1h/WQ	2.96	4.11	4.71	99.94	3.07	-	-	-
500°C/3h/WQ	2.88	4.11	4.65	97.34	3.08	12.32	8.71	26.13
500°C/48h/WQ	2.89	4.10	4.67	96.73	3.08	12.32	8.71	26.13
550°C/3h/WQ	2.90	4.10	4.68	96.11	3.08	12.32	8.71	26.13
FC/48h/700°C/ 100°C	2.93	4.09	4.67	96.71	3.08	12.32	8.71	26.13

Table 7.4 The lattice parameters of martensite, austenite and H-phase precipitates in SHT and precipitation heat treated $Ni_{50.3}Ti_{29.7}Zr_{20}$ samples.

	B19' Martensite				B2 Austenite (Å)	H-Phase		
	a (Å)	b (Å)	c (Å)	β (degree)		a (Å)	b (Å)	c (Å)
SHT (900°C/1h/WQ	2.98	4.14	4.72	97.87	3.09	-	-	-
500°C/3h/WQ	2.92	4.11	4.71	96.04	3.09	12.35	8.73	26.20
500°C/48h/WQ	2.92	4.10	4.73	96.36	3.09	12.34	8.73	26.19
550°C/3h/WQ	2.94	4.11	4.71	95.51	3.09	12.36	8.74	26.22
FC/48h/700°C/ 100°C	2.93	4.10	4.69	97.15	3.09	12.35	8.73	26.20
FC/3h/700°C/ 100°C	2.97	4.12	4.72	98.62	3.09	12.35	8.74	26.21

Using the lattice parameters given in Tables 7.3 and 7.4, the λ_2 values and its deviation from 1 (1 - λ_2) are calculated as a function of thermal treatment conditions. In order to study the lattice compatibility and the thermal hysteresis relationship in both alloy systems, the λ_2 and the corresponding thermal hysteresis values are summarized in Table 7.5. The thermal hysteresis values are derived from the stress free DSC measurements however all the conclusions drawn hereafter will be also valid for the hysteresis levels under applied stress since the peculiarities are almost same. In precipitate free conditions (SHT samples), $Ni_{50.3}Ti_{29.7}Zr_{20}$ HTSMA exhibit a slightly lower λ_2 value than the $Ni_{50.3}Ti_{29.7}Hf_{20}$ HTSMA. This difference in λ_2 manifests itself as a larger thermal hysteresis in $Ni_{50.3}Ti_{29.7}Zr_{20}$ (68 °C) than the $Ni_{50.3}Ti_{29.7}Hf_{20}$ alloy (38 °C). Both these systems have larger 1 - λ_2 values and hence larger incompatibility as compared to NiTiPd, NiTiPt and NiTiAu HTSMAs displaying themselves as much

larger thermal hysteresis in the present alloys [110]. When small precipitates are produced after aging at 500 ^{o}C or 550 ^{o}C, λ_2 parameters get smaller and hence larger deviations from 1 occur (1 - λ_2 values gets larger) as compared to SHT cases in both alloy systems. Therefore, the thermal hysteresis values are expected to be larger due to worsened lattice compatibility. But instead much smaller hysteresis values are obtained after generation of small precipitates. In such cases, although the lattice compatibility is not as good as in the case of SHT samples, the dominant mechanism affecting the thermal hysteresis is the matrix strengthening that increases the resistance for defect formation and lowering the thermal hysteresis. Comparing the samples treated under similar aging conditions (NTZ5003, NTZ50048 and NTZ5503 with NTH5003, NTH50048 and NTH5503) and the samples showing similar precipitate sizes (NTZ5003 with NTH50048), the $Ni_{50.3}Ti_{29.7}Hf_{20}$ alloy has thermal hysteresis lower than the $Ni_{50.3}Ti_{29.7}Zr_{20}$ alloy.

When the precipitates are large such as in the case of furnace cooled samples (type B microstructures), there is again no correlation between the λ_2 and thermal hysteresis values. In the case of NiTiZr samples, the λ_2 decreases and but in contradiction ΔT also decreases in NTZFC48 sample. On the other hand, while λ_2 increases, the ΔT decreases in the NTZFC3 sample as expected as compared to SHT sample. In the case of NiTiHf samples, smaller λ_2 and higher thermal hysteresis is obtained as compared to SHT sample in NTHFC48. Comparing NTHFC48 sample (λ_2 = 0.9407 and ΔT of 66.5 ^{o}C) with the NTZFC48 sample (λ_2 = 0.9380 and ΔT of 62 ^{o}C), lattice compatibility seems to better in the NiTiHf sample but it shows higher hysteresis

interestingly. On the other hand, NTZFC3 sample which has similar precipitate size with NTHFC48 sample, has better lattice compatibility and lower hysteresis than NTHFC48 specimen. Concerning the irregularities in the relationship between "λ_2 and ΔT" seen in the NiTiZr furnace cooled specimens, it should be noted that the trends in thermal hysteresis values are mainly because of the large precipitate sizes in these samples. A lot of precipitate – variant and variant – variant interfaces form which will increase the energy dissipation and the hysteresis. Therefore, beside the lattice compatibility, the thermal hysteresis is mainly dependent on the precipitate size for the samples with type B microstructures.

Table 7.5 The summary of the λ_2, 1 - λ_2 and ΔT values of the $Ni_{50.3}Ti_{29.7}Zr_{20}$ and $Ni_{50.3}Ti_{29.7}Hf_{20}$ HTSMAs for SHT and precipitation heat treated samples determined using the experimental lattice parameters and DSC measurements.

	$Ni_{50.3}Ti_{29.7}Zr_{20}$			$Ni_{50.3}Ti_{29.7}Hf_{20}$		
	λ_2	1 - λ_2	ΔT (^oC)	λ_2	1 - λ_2	ΔT (^oC)
SHT (900^oC/1h/WQ)	0.9418	0.0582	68	0.9466	0.0534	38
500^oC/3h/WQ	0.9406	0.0594	37	0.9455	0.0545	27.5
500^oC/48h/WQ	0.9391	0.0609	49	0.9422	0.0578	29
550^oC/3h/WQ	0.9393	0.0607	46	0.9412	0.0588	27
FC/48h/700^oC to 100^oC	0.9380	0.062	62	0.9407	0.0593	66.5
FC/3h/700^oC to 100^oC	0.9438	0.0562	53	-	-	-

7.4.2 Elastic Constants of Transforming Phases

Another reason that may be leading to differences in thermal hysteresis in the NiTiZr and NiTiHf alloys could be the material stiffness. Moreover, the strain energy stored around the precipitates upon the martensitic transformation is also a function of material stiffness. If one system has less stiffness and easiness to accommodate the transformation strain around the precipitates, larger martensite variants will be obtained in that system. The elastic constants of B2 parent phase and H-phase precipitates in both alloy systems have already been given in Table 4.3 in Chapter IV. The elastic constants and stiffness tensors as well as the mechanical properties of the B19' martensite in $Ni_{50.3}Ti_{29.7}Zr_{20}$ and $Ni_{50.3}Ti_{29.7}Hf_{20}$ alloys are calculated as explained in Section 3.4.3 using the lattice parameters of the SHT materials given in Tables 7.3 and 7.4. Tables 7.6 and 7.7 summarize the elastic constants and stiffness tensors of the $Ni_{50.3}Ti_{29.7}Hf_{20}$ and $Ni_{50.3}Ti_{29.7}Zr_{20}$ alloys, respectively. The comparison of the mechanical properties such as bulk modulus, shear modulus, elastic modulus and poisson's ratio of $Ni_{50.3}Ti_{29.7}Zr_{20}$ and $Ni_{50.3}Ti_{29.7}Hf_{20}$ HTSMAs is shown in Table 7.8. It is obvious from the table that the NiTiHf alloys tend to be stiffer than the NiTiZr alloys and therefore lower energy is necessary to accommodate the strain around the precipitates in NiTiZr alloys. As a consequence, martensite variants may reach to larger sizes in NiTiZr alloys due to easier absorption of precipitates when precipitate size is sufficiently small which is indeed the case in type A microstructures as seen in the TEM images given in Figs. 7.2a and b.

Due to higher stiffness, the defect generation in NiTiHf alloys with fine precipitates will be much harder as compared to NiTiZr alloys. Therefore, for similar

aging conditions generating nanoscale precipitates, NiTiHf alloys will exhibit smaller thermal hysteresis than the NiTiZr alloys such as in the samples aged at 500 ^{o}C or 550 ^{o}C.

Table 7.6 The elastic constants and stiffness matrix of $Ni_{50.3}Ti_{29.7}Hf_{20}$ HTSMA calculated using the experimental lattice parameters for the SHT sample.

Cij					
189.87	119.52	110.18	0	2.62	0
119.52	245.74	133.41	0	9.72	0
110.18	133.41	248.64	0	11.38	0
0	0	0	72.00	0	-5.50
2.62	9.72	11.38	0	11.86	0
0	0	0	-5.50	0	79.72

Sij					
0.00841	-0.00297	-0.00226	0	0.00274	0
-0.00297	0.00683	-0.00222	0	-0.00281	0
-0.00226	-0.00222	0.00639	0	-0.00381	0
0	0	0	0.01396	0	0.00096
0.00274	-0.00281	-0.00381	0	0.08967	0
0	0	0	0.00096	0	0.01261

Table 7.7 The elastic constants and stiffness matrix of $Ni_{50.3}Ti_{29.7}Zr_{20}$ HTSMA calculated using the experimental lattice parameters for the SHT sample.

Cij					
177.24	116.43	120.53	0	4.83	0
116.43	205.63	136.41	0	-0.99	0
120.53	136.41	188.68	0	-19.6	0
0	0	0	71.71	0	0.04
4.83	-0.99	-19.6	0.00	14.87	0
0	0	0	0.04	0.00	68.6

Sij					
0.0133	-0.0016	-0.009	0	-0.0163	0
-0.0016	0.0109	-0.0078	0	-0.009	0
-0.009	-0.0078	0.0196	0	0.0282	0
0	0	0	0.0139	0	0
-0.0163	-0.009	0.0282	0	0.1091	0
0	0	0	0	0	0.0146

Table 7.8 The comparison of the mechanical properties such as bulk modulus, shear modulus, elastic modulus and poisson's ratio of $Ni_{50.3}Ti_{29.7}Zr_{20}$ and $Ni_{50.3}Ti_{29.7}Hf_{20}$ HTSMAs calculated using the lattice parameters of the SHT samples.

		Bulk Modulus (GPa)	Shear Modulus (GPa)	Elastic Modulus (GPa)	Poisson's Ratio
$Ni_{50.3}Ti_{29.7}Zr_{20}$	Voigt Approximation	146.48	44.25	132.74	0.3628
	Reuss Approximation	142.86	22.67	68.02	0.4246
	Average	144.67	33.46	100.38	0.3926
$Ni_{50.3}Ti_{29.7}Hf_{20}$	Voigt Approximation	156.72	54.12	162.38	0.3451
	Reuss Approximation	148.60	32.25	96.76	0.3988
	Average	152.66	43.19	129.57	0.3707

The higher stiffness of $Ni_{50.3}Ti_{29.7}Hf_{20}$ alloy as compared to its Zr counterpart, $Ni_{50.3}Ti_{29.7}Zr_{20}$, is also consistent with the microhardness of the alloys. For the precipitate free (SHT) materials, the microhardness is 444.4 ± 9.3 HV and 426.8 ± 8.7 HV for the $Ni_{50.3}Ti_{29.7}Hf_{20}$ and $Ni_{50.3}Ti_{29.7}Zr_{20}$, respectively. Precipitation hardening improves the microhardness remarkably in both systems and increases to 520.3 ± 8.8 HV, 502.3 ± 11.9 HV, 478.3 ± 2.2 HV and 523.6 ± 7.02 HV for the NTZ5503, NTH5503, NTZFC48 and NTHFC48 samples, respectively. This also explains the early failure seen in the furnace cooled NiTiHf sample (NTHFC48). Although, precipitate size is large, not effectively hardening the matrix as the fine precipitates, the volume fractions of particles should be considerably high to make the sample brittle. This is also in accordance with the remarkable increase in the transformation temperatures of the NTHFC48 sample.

7.4.3 Maximum Theoretical Transformation Strains

Using the lattice parameters given in Tables 7.3 and 7.4, the maximum theoretical strains that can be obtained in the single crystal orientations of $Ni_{50.3}Ti_{29.7}Hf_{20}$ and $Ni_{50.3}Ti_{29.7}Zr_{20}$ HTSMA is calculated as a function of aging conditions. The inverse pole figures corresponding to maximum theoretical strains in single crystal directions for each sample under tension are shown in Fig. 7.13. In tension, the largest strains are calculated in <110> directions while in compression single crystals in <001> orientations would give the highest strains. However both in tension and compression, <100> directions display least amount of strain levels. It should be noted that these

calculations show higher transformation levels than those can be calculated with the energy minimization theory taking into account the corresponding variant pairs (CVPs). These types of calculations were performed on NiTi [103] and FeNiCoTi [134] SMAs with energy minimization theory by Sehitoglu et al. Differing than their calculations, in the present study it is assumed that martensite will be 100% detwinned and finally there will be one single variant martensite and hence the calculated strains will be larger in the present study.

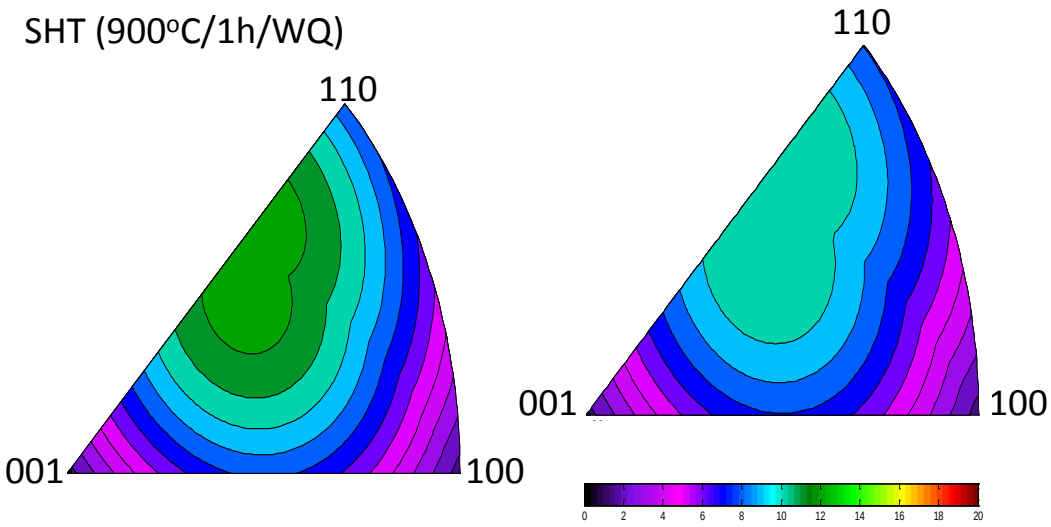

(a) (b)

Figure 7.13 Inverse pole figures of the theoretical maximum transformation strains in tension for single crystal directions of the SHT (a) $Ni_{50.3}Ti_{29.7}Hf_{20}$ (b) $Ni_{50.3}Ti_{29.7}Zr_{20}$, samples aged at 500 °C for 3 h (c) $Ni_{50.3}Ti_{29.7}Hf_{20}$ (d) $Ni_{50.3}Ti_{29.7}Zr_{20}$, at 500 °C for 48 h (e) $Ni_{50.3}Ti_{29.7}Hf_{20}$ (f) $Ni_{50.3}Ti_{29.7}Zr_{20}$, at 550 °C for 3 h (g) $Ni_{50.3}Ti_{29.7}Hf_{20}$ (h) $Ni_{50.3}Ti_{29.7}Zr_{20}$ and furnace cooled from 700 °C to 100 °C in 48 h (i) $Ni_{50.3}Ti_{29.7}Hf_{20}$ (j) $Ni_{50.3}Ti_{29.7}Zr_{20}$.

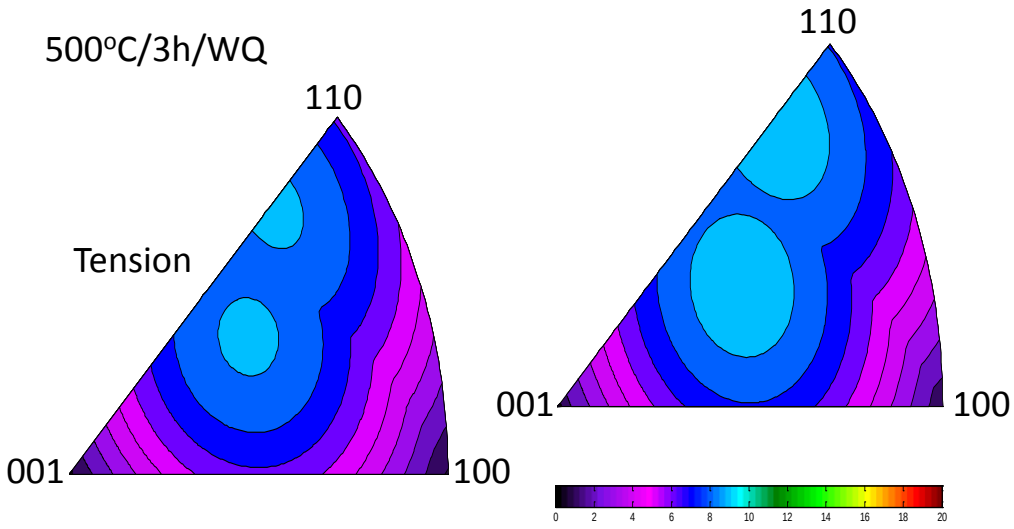

(c) (d)

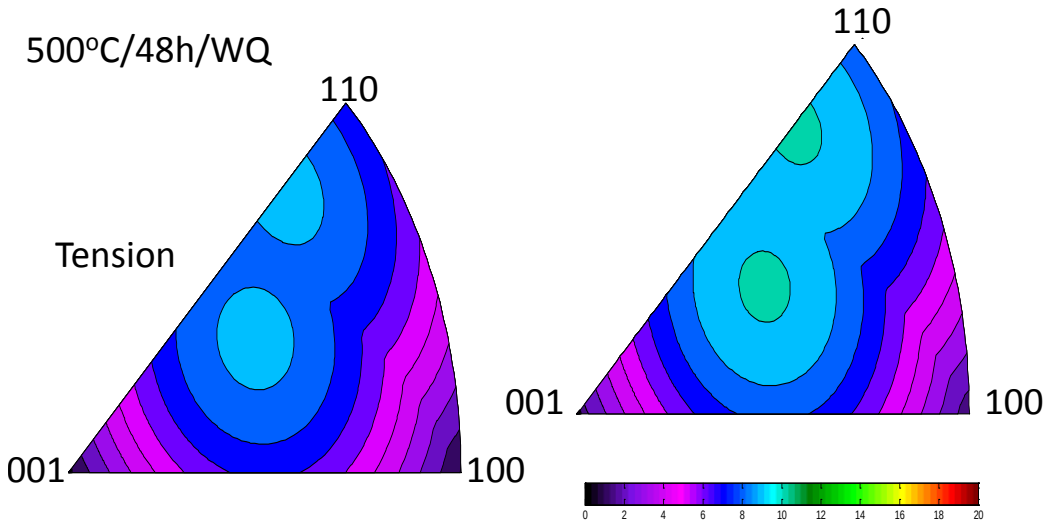

(e) (f)

Figure 7.13 Continued.

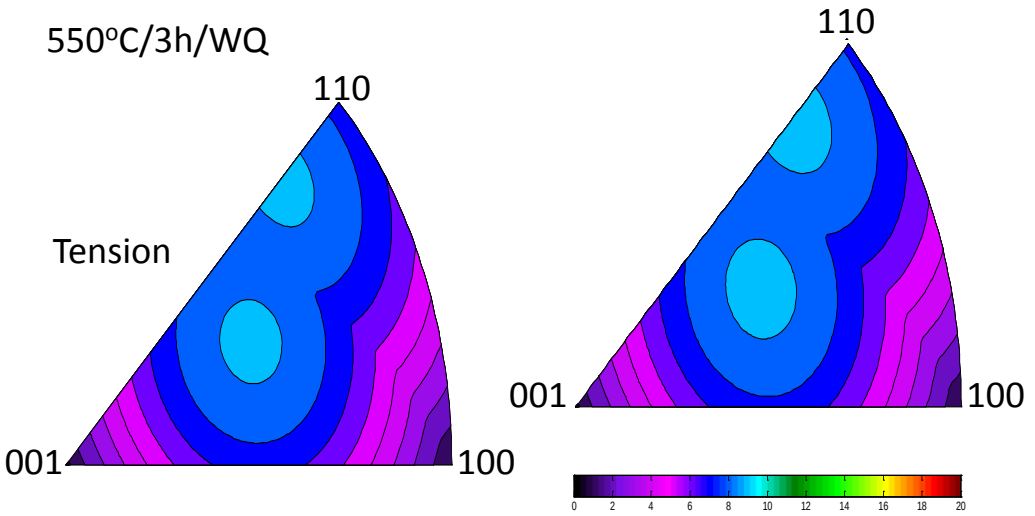

(g) (h)

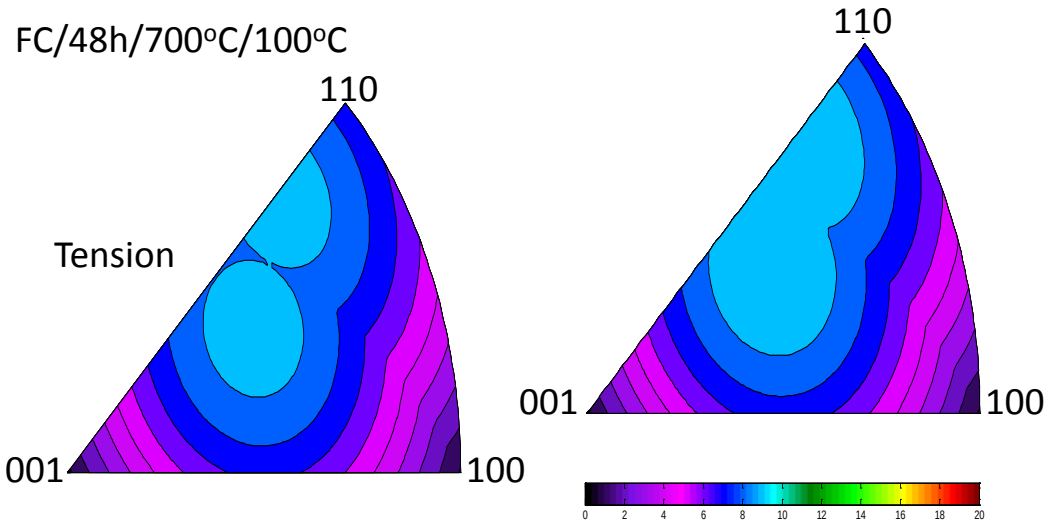

(i) (j)

Figure 7.13 Continued.

The comparison of maximum theoretical strain levels for $Ni_{50.3}Ti_{29.7}Zr_{20}$ and $Ni_{50.3}Ti_{29.7}Hf_{20}$ alloys is represented in Table 7.9. For comparison, calculations for the maximum theoretical strains of $Ni_{49.2}Ti_{50.8}$ binary alloy are also given in the table.

$Ni_{50.3}Ti_{29.7}Hf_{20}$ HTSMA may show higher transformation strains in tension and compression than the $Ni_{50.3}Ti_{29.7}Zr_{20}$ HTSMA in precipitate free conditions (SHT samples). After aging at 500 ^{o}C and 550 ^{o}C, the $Ni_{50.3}Ti_{29.7}Zr_{20}$ HTSMA shows higher transformation strains in tension while lower in compression as compared to $Ni_{50.3}Ti_{29.7}Hf_{20}$ HTSMA. This statement is valid when samples treated under same aging conditions or samples with similar precipitate size are compared (NTH50048 vs NTZ5003). However, when large particles are generated after furnace cooling, it is the $Ni_{50.3}Ti_{29.7}Zr_{20}$ HTSMA exhibiting larger theoretical strains with an exception in the NTZFC48 sample showing smaller strain in <100> directions in compression. As a comparison, both alloy systems show smaller maximum strain levels than the binary NiTi alloy in tension as expected [135]. Indeed, the transformation strains obtained during actual load-biased testing of the present alloys are much smaller than the binary NiTi alloys.

However, these calculations are not conclusive to explain why $Ni_{50.3}Ti_{29.7}Hf_{20}$ HTSMA show higher transformation strains than the $Ni_{50.3}Ti_{29.7}Zr_{20}$ HTSMA as seen from Fig. 7.8 under the applied stress levels in the present study. But it is obvious from Fig. 7.8 that the unrecovered strain levels of the present alloys are either very low or negligible and also the recovered transformation strain levels have not reached to a peak point. Therefore, it can be argued that the maximum applied stress, 300 MPa, is not sufficient in order to initiate plastic deformation as the dominant deformation mode rather than the martensite detwinning. This concludes that martensite under 300 MPa applied stress is not completely detwinned and hence the strain levels seen Fig. 7.8 do

not reflect the maximum strain capability of the alloys. Instead, they are a function of the volume fraction of detwinned martensite under the specific applied stress level. Although, $Ni_{50.3}Ti_{29.7}Zr_{20}$ alloy may show larger strains under higher stress levels, at stress levels up to 300 MPa, volume fraction of detwinned martensite should be higher in $Ni_{50.3}Ti_{29.7}Hf_{20}$ alloy. Hence, under similar aging conditions or with similar microstructures, more recovered transformation strain will be obtained in $Ni_{50.3}Ti_{29.7}Hf_{20}$ due to easier detwinning of martensite.

Table 7.9 Comparison of theoretical maximum transformation strains in single crystal directions of the SHT and precipitation heat treated $Ni_{50.3}Ti_{29.7}Zr_{20}$, $Ni_{50.3}Ti_{29.7}Hf_{20}$ and $Ni_{49.2}Ti_{50.2}$ alloys.

		<001>		<100>		<110>	
		Comp.	Tens.	Comp.	Tens.	Comp.	Tens.
$Ni_{50.3}Ti_{29.7}Zr_{20}$	SHT (900°C/1h/WQ)	6.91	6.64	3.78	1.5	6.32	7.95
	500°C/3h/WQ	7.32	6.54	5.47	1.22	6.02	7.89
	500°C/48h/WQ	7.28	6.87	5.22	1.35	6.09	8.27
	550°C/3h/WQ	6.63	6.4	4.92	1.08	6.07	7.75
	FC/3h/700°C/100°C	7.34	6.81	3.79	1.51	6.85	8.17
	FC/48h/700°C/100°C	7.66	6.13	5.08	0.86	6.76	7.48
$Ni_{50.3}Ti_{29.7}Hf_{20}$	SHT (900°C/1h/WQ)	8.13	6.85	3.89	1.52	7.79	8.22
	500°C/3h/WQ	8.68	5.57	6.26	0.86	7.40	6.79
	500°C/48h/WQ	8.12	5.95	5.97	0.94	6.84	7.24
	550°C/3h/WQ	7.61	6.13	5.76	1.00	6.30	7.45
	FC/48h/700°C/100°C	7.08	5.96	4.65	0.89	6.25	7.27
$Ni_{49.2}Ti_{50.2}$ [135]		6.42	7.17	4.18	2.68	5.17	8.4

7.5 Summary and Conclusions

Primarily, this chapter covers the microstructural investigations, transformation characteristics and load-biased shape memory response of the $Ni_{50.3}Ti_{29.7}Hf_{20}$ HTSMA alloy with an emphasis on the two distinct microstructures formerly discovered in the $Ni_{50.3}Ti_{29.7}Zr_{20}$ HTSMA. Secondly, the obtained results on the $Ni_{50.3}Ti_{29.7}Hf_{20}$ alloy are compared with its $Ni_{50.3}Ti_{29.7}Zr_{20}$ counterpart and finally the mechanisms resulting in the similarities and differences on the microstructure, transformation characteristics and shape memory responses are discussed. The main conclusions can be stated as following:

1. Under similar thermal treatment conditions, $Ni_{50.3}Ti_{29.7}Zr_{20}$ alloy has larger precipitates due to faster precipitate coarsening kinetics than the $Ni_{50.3}Ti_{29.7}Hf_{20}$ alloy. Similar to the NiTiZr alloy, small precipitates do not interfere with martensite growth and they can be absorbed through the variants leading to large martensite plates (type A microstructures) in the NiTiHf alloy. Furnace cooling generates large precipitates limiting martensite growth and refining the variant size (type B microstructures). Concerning thermal treatments resulting in similar precipitate sizes in type A microstructures, $Ni_{50.3}Ti_{29.7}Zr_{20}$ has larger variant sizes since accommodation of strain energy is easier which is due to the lower stiffness of $Ni_{50.3}Ti_{29.7}Zr_{20}$ alloy than the $Ni_{50.3}Ti_{29.7}Hf_{20}$ alloy. In type B microstructures, precipitate size is comparable to variant size in both systems.
2. $Ni_{50.3}Ti_{29.7}Hf_{20}$ alloy show much higher transformation temperatures than the $Ni_{50.3}Ti_{29.7}Zr_{20}$ alloy in precipitate free conditions. After generation of small

particles, A_f temperatures get closer while M_s is higher in NiTiHf. Furnace cooling accelerates precipitation more efficiently in the NiTiHf alloy and much higher transformation temperatures are obtained as compared to furnace cooled $Ni_{50.3}Ti_{29.7}Zr_{20}$. NiTiHf shows smaller thermal hysteresis in SHT case than the NiTiZr due to better lattice compatibility. However, there is no direct correlation of the lattice compatibility with the thermal hysteresis when precipitates are present. Thermal hysteresis decreases in both alloys due to precipitation hardening while high thermal hysteresis is observed after furnace cooling in both alloys due to the presence of large particles. Thermal stability is better in NiTiHf alloy due to better lattice compatibility.

3. Precipitate size and its subsequent effect on the martensite morphology manifest themselves in a similar fashion to the $Ni_{50.3}Ti_{29.7}Zr_{20}$ alloy in the $Ni_{50.3}Ti_{29.7}Hf_{20}$ samples. Higher strain levels, lower thermal hysteresis and narrower transformation range (M_s – M_f) are obtained in type A microstructures as compared to type B microstructures.
4. Larger recovered transformation strain levels are obtained in the $Ni_{50.3}Ti_{29.7}Hf_{20}$ alloy for all the samples with precipitates as compared to $Ni_{50.3}Ti_{29.7}Zr_{20}$. Contrary to the results, NiTiZr alloy show larger theoretical transformation strains in tension with an exception in precipitate free conditions where NiTiHf alloy would possess larger strains. This shows that, the applied stress levels, with a maximum of 300 MPa, are not sufficient to completely detwin the martensite

and detwinning is easier in NiTiHf for present applied stress levels leading to higher strains.

5. When samples have small precipitates, thermal hysteresis is smaller under applied stress in the $Ni_{50.3}Ti_{29.7}Hf_{20}$ alloy as compared to $Ni_{50.3}Ti_{29.7}Zr_{20}$ alloy. Thermal hysteresis is comparable for the furnace cooled samples under applied stress in both alloy systems since large number of variants and hence interfaces are present which increase energy dissipation.

CHAPTER VIII

MAIN CONLUSIONS AND FUTURE DIRECTIONS

The poor shape memory response, high thermal hysteresis and poor dimensional stability seen in the (Ti + Hf/Zr)-rich NiTiHf and NiTiZr alloys can be overcome through processing of Ni-rich compositions of these alloys which allow precipitating hardening of the matrix on that side of stoichiometry. The present work investigated the effect of precipitation on the microstructure and the shape memory response of Ni-rich $Ni_{50.3}Ti_{34.7}Hf_{15}$, $Ni_{50.3}Ti_{34.7}Zr_{15}$, $Ni_{50.3}Ti_{29.7}Hf_{20}$ and $Ni_{50.3}Ti_{29.7}Zr_{20}$ shape memory alloys. Systematic precipitation heat treatments were carried out on these alloy systems in order to control the precipitate size and volume fraction. The transformation characteristics such as transformation temperatures, thermal hysteresis and thermal stability of transformation temperatures as a function of aging conditions were studied via DSC experiments. The microstructural evolution during precipitation heat treatments in terms of precipitate size, martensite morphology, twinning and orientation relationships of martensite and coherency of precipitates were revealed using TEM/HRTEM. Furthermore, the composition of precipitates and their crystal structure were investigated and discussed along with the microstructural evolution. Based on the DSC data and microstructural investigations, the time-temperature-transformation temperature (TTT) diagrams of the individual alloy systems were generated revealing the effect of precipitate size and composition on the ternary NiTi-based SMA for the first time in literature. The load biased shape memory response of the individual alloy systems in

tension was characterized through constant stress thermal cycling tests and the evolution of recovered and unrecovered strain levels, transformation temperatures and thermal hysteresis was extracted from the obtained results. Finally, since they are candidate materials for elevated temperature use, the differences and similarities in terms of microstructure, shape memory response and transformation characteristics of the $Ni_{50.3}Ti_{29.7}Hf_{20}$ and $Ni_{50.3}Ti_{29.7}Zr_{20}$ HTSMAs were discussed and the response mechanisms were investigated.

Based on the results of the present study the following conclusions can be made:

1. Precipitation heat treatments in Ni-rich NiTi(Hf,Zr) alloys lead to formation of precipitates with the same crystal structure in both alloy systems. The precipitate phase is identified as H-phase which is a superstructure of B2 austenite phase. The particles are richer in Ni and ternary element content (Hf or Zr) and poorer in Ti in composition. H-phase precipitates do not change the crystallography of the twinning modes in Ni-rich compositions as compared to (Ti + Hf/Zr)-rich compositions and a mixture of (011)-compound and (011)-type I twins with intervariant boundaries on $\{111\}_{B19'}$, $\{113\}_{B19'}$ and $\{011\}_{B19'}$ planes are present.
2. H-phase precipitation provides a great flexibility to modify transformation temperatures of the Ni-rich alloys. SHT and precipitation heat treated samples always undergo single step transformation and no R-phase transformation is seen. M_s is affected by two mechanisms in $Ni_{50.3}Ti_{34.7}Hf_{15}$ and $Ni_{50.3}Ti_{29.7}Zr_{20}$ SMA systems namely "*interparticle spacing*" and "*compositional change*". Fine and densely distributed particles generally occurring after low temperature aging

for short durations, result in small interparticle spacing. In turn, martensite nucleation is suppressed and M_s decreases which is rationalized by Region 2 in TTT diagrams. Prolonged aging at these temperatures or high temperature aging increase precipitate volume fraction and raises M_s in accordance with the behavior of alloys in Region 1 of TTT diagrams.

3. Both Ni-rich NiTiHf and NiTiZr alloys show very good dimensional stability and very small amount of unrecovered strain levels up to 300 MPa applied stress levels due to increased matrix strength with precipitation. Transformation thermal hysteresis under applied stress are more effectively influenced by precipitation hardening since defect generation gets harder in precipitation hardened materials. Energy dissipation and hence thermal hysteresis is low when nanosize precipitates are present.
4. Martensite morphology is found to be a function of precipitate size in $Ni_{50.3}Ti_{29.7}Zr_{20}$ HTSMA. When the precipitates are smaller than 45 nm in size, they do not interfere with the transformation and large martensite variants can grow absorbing the fine precipitates (Type A microstructures). Precipitates forming after furnace cooling treatments, several hundred nanometer in size, block martensite growth and refines variant thickness (Type B microstructures). Samples with type B microstructures exhibit larger thermal hysteresis and wider transformation range ($M_s - M_f$) as compared to the samples with type A microstructures since a large number of thin variants are formed and extra undercooling is needed for transformation within the precipitate barriers. Type B

microstructures also show smaller transformation strains due to harder reorientation/detwinning of martensite. Specimens without precipitates have little resistance to plastic deformation but samples with type A microstructures exhibit fully recoverable 5% strain at 170 °C and excellent superelastic shape recovery at temperatures as high as 250 °C up to 3% applied strain due to precipitation hardening. Type B microstructures kill the superelasticty and premature failure is seen even at low applied strain levels.

5. Effect of precipitation on the martensite morphology and on the shape memory response is identical both in $Ni_{50.3}Ti_{29.7}Zr_{20}$ and $Ni_{50.3}Ti_{29.7}Hf_{20}$ HTSMAs. However, for fixed thermal treatments, precipitation coarsening kinetics is faster in $Ni_{50.3}Ti_{29.7}Zr_{20}$ HTSMA and therefore larger precipitates are present as compared to $Ni_{50.3}Ti_{29.7}Hf_{20}$ alloys. For equivalent precipitate sizes in type A microstructures, the variant size is much larger in $Ni_{50.3}Ti_{29.7}Zr_{20}$ HTSMA due to easier accommodation of stain energy originating from the low matrix stiffness of the NiTiZr alloy.
6. Lattice compatibility is better in $Ni_{50.3}Ti_{29.7}Hf_{20}$ alloy as compared to its NiTiZr counterpart in SHT conditions and so the thermal hysteresis is smaller and the thermal stability is better in the former alloy. Thermal hysteresis decrease in both alloy systems after fine precipitates are generated (type A microstructures). Furnace cooling increases thermal hysteresis in both alloys independent of the lattice compatibilities.

Overall, the Ni-rich compositions of NiTiHf and NiTiZr alloys were proven to have much more promising shape memory responses with better dimensional stability, lower thermal hysteresis and better thermal stability than their (Ti + Hf/Zr)-rich counterparts. Although, alloys with low ternary additions (15 at.%) showed very good shape recovery, their transformation temperatures are still low for high temperature use. Instead, $Ni_{50.3}Ti_{29.7}Zr_{20}$ and $Ni_{50.3}Ti_{29.7}Hf_{20}$ systems are true candidates for high temperature applications with decent strain levels, improved shape recovery and relatively high transformation temperatures. $Ni_{50.3}Ti_{29.7}Zr_{20}$ HTSMA on the other hand provides at least 20% weight reduction than its NiTiHf counterpart. Moreover, $Ni_{50.3}Ti_{29.7}Zr_{20}$ was shown to exhibit the highest superelastic strain levels reported for a polycrystalline ternary Ni-rich NiTi-based HTSMA system up to date. Additionally, this study shows how to manipulate the shape memory responses and superelastic properties of these Ni-rich systems by just controlling the microstructure though simple precipitation heat treatments for the first time in literature. In terms of processing conditions, type A microstructures are more favorable for practical uses due to lower thermal hysteresis, higher strain levels and narrower transformation ranges. Still, the maximum capabilities of these Ni-rich HTSMAs are not revealed but the present work shows that $Ni_{50.3}Ti_{29.7}Zr_{20}$ and $Ni_{50.3}Ti_{29.7}Hf_{20}$ alloys are promising systems as cheaper and lighter alternatives to other already known precious metal alloyed NiTi-based HTMSAs.

Beside all these promising results, the characterization studies carried out in the present work do not reveal the behavior of the alloys under extended number of thermo-

mechanical cycles which is required for real applications. Therefore, as a future work, more research is necessary to assess the thermo-mechanical fatigue response of these HTSMAs. Furthermore, in order to reveal the effect of precipitation and hence the microstructure on the fatigue life and response, samples with type A and type B microstructures could be investigated.

Additionally, the fundamental knowledge obtained on these systems required extensive characterization studies which in turn bring in a quite high number of experiments to be performed. However, once the TTT diagrams of these systems are generated, one can select aging conditions to pick up desired transformation temperatures and use them as inputs to model the shape memory response of the alloy systems as a function of precipitation. This approach was successfully performed on a binary NiTi alloy already and can be extended to ternary systems in future [136]. By this way, a considerable amount of time would be saved and thermal treatment conditions may be easily selected for desired properties.

REFERENCES

[1] Chang LC, Read TA. Trans AIME 1951;189:47.

[2] Burkart MW, Read TA. Trans AIME 1953;197:1516.

[3] Basinski ZS, Christian JW. Acta Metall 1954;2:101.

[4] Buehler WJ, Gilfrich JW, Wiley RC. J Appl Phys 1963;34:1473.

[5] Otsuka K, Ren X. Prog Mater Sci 2005;50:511.

[6] Van Humbeeck J, Stalmans R. Characteristics of shape memory alloys. In: Otsuka K, Wayman CM, editors. Shape memory materials. 1st ed: Cambridge University Press, Cambridge, England; 1998.

[7] Otsuka K, Wayman CM. Shape memory materials. Cambridge University Press, Cambridge, England; 1998.

[8] Au YK, Wayman CM. Scripta Metall 1972;6:1209.

[9] Kim YD, Wayman CM. Scripta Metall Mater 1990;24:245.

[10] Kainuma R, Ohtani H, Ishida K. Metall Mater Trans A 1996;27:2445.

[11] Kainuma R, Nakano H, Ishida K. Metall Mater Trans A 1996;27:4153.

[12] Adachi K, Wayman CM. Metall Trans A 1985;16:1567.

[13] Yang WS, Mikkola DE. MRS Proceedings 1991;246:135.

[14] Sakamoto H, Shimizu K. Trans Japan Institute Metals 1986;27:601.

[15] Eucken S, Kobus E, Hornbogen E. Zeitschrift Fur Metallkunde 1991;82:640.

[16] Sade M, Damiani C, Gastien R, Lovey FC, Malarria J, Yawny A. Smart Mater Struct 2007;16:126.

[17] Kato H, Stalmans R, Van Humbeeck J. Mater Trans JIM 1998;39:378.

[18] Otsuka H, Sakamoto H, Shimizu K. Acta Metall 1979;27:585.

[19] Ma J, Karaman I, Maier HJ, Chumlyakov YI. Acta Mater 2010;58:2216.

[20] Maeshima T, Ushimaru S, Yamauchi K, Nishida M. Mater Sci Eng A 2006;438:844.

[21] Kim HY, Ohmatsu Y, Kim JI, Inamura T, Hosoda H, Miyazaki S. Mater Trans 2006;47:518.

[22] Kim HY, Ikehara Y, Kim JI, Hosoda H, Miyazaki S. Acta Mater 2006;54:2419.

[23] Ikeda M, Komatsu SY, Nakamura Y. Mater Trans 2004;45:1106.

[24] Buenconsejo PJS, Kim HY, Hosoda H, Miyazaki S. Acta Mater 2009;57:1068.

[25] Ma J, Karaman I, Noebe RD. Int Mater Rev 2010;55:257.

[26] Kumar PK, Lagoudas DC. Acta Mater 2010;58:1618.

[27] Eckelmeyer KH. Scripta Metall 1976;10:667.

[28] Mulder J. PhD Thesis, University of Twente, Enschede, The Netherlands; 1994.

[29] Hsieh SF, Wu SK. Mater Charact 1998;41:151.

[30] Hsieh SF, Wu SK. J Alloys Compd 1998;270:237.

[31] Hsieh SF, Wu SK. J Alloys Compd 1998;266:276.

[32] Firstov GS, Van Humbeeck J, Koval YN. Scripta Mater 2004;50:243.

[33] Angst DR, Thoma PE, Kao MY. J Phys IV 1995;C8:747.

[34] Olier P, Brachet J, Bechade J, Foucher C, Guenin G. J Phys IV 1995;C8:741.

[35] Thoma PE, Boehm JJ. Mater Sci Eng A 1999;273:385.

[36] Besseghini S, Villa E, Tuissi A. Mater Sci Eng A 1999;273:390.

[37] Meng X, Cai W, Zheng Y, Tong Y, Zhao L, Zhou L. Mater Lett 2002;55:111.

[38] Meng X, Zheng Y, Cai W, Zhao L. J Alloy Compd 2004;372:1806.

[39] Meng X, Zheng Y, Wang Z, Zhao L. Scripta Mater 2000;42:341.

[40] Wang Y, Zheng Y, Cai W, Zhao L. Scripta Mater 1999;40:1327.

[41] Santamarta R, Seguí C, Pons J, Cesari E. Scripta Mater 1999;41:867.

[42] Otsuka K, Ren X. Intermetallics 1999;7:511.

[43] Liang XL, Chen Y, Shen HM, Zhang ZF, Li W, Wang YN. Solid State Commun 2001;119:381.

[44] Kim HY, Jinguu T, Nam T, Miyazaki S. Scripta Mater 2011;65:846.

[45] Khalil-Allafi J, Dlouhy A, Eggeler G. Acta Mater 2002;50:4255.

[46] Gall K, Sehitoglu H, Chumlyakov YI, Zuev YL, Karaman I. Scripta Mater 1998;39:699.

[47] Panchenko E, Chumlyakov YI, Kireeva I, Ovsyannikov A, Sehitoglu H, Karaman I, Maier YHJ. Phys Metall Metallogr 2008;106:577.

[48] Kim JI, Miyazaki S. Acta Mater 2005;53:4545.

[49] Nishida M, Wayman CM, Honma T. Metall Trans 1986;17:1505.

[50] Frenzel J, George EP, Dlouhy A, Somsen C, Wagner MFX, Eggeler G. Acta Mater 2010;58:3444.

[51] Sandu AM, Tsuchiya K, Yamamoto S, Todaka Y, Umemoto M. Scripta Mater 2006;55:1079.

[52] Sandu AM, Tsuchiya K, M. Tabuchi M, Yamamoto S, Todaka Y, Umemoto M. Mater Trans 2007;48:432.

[53] Meng X, Cai W, Zheng Y, Zhao L. Mater Sci Eng A 2006;438:666.

[54] Meng X, Cai W, Chen F, Zhao LC. Scripta Mater 2006;54:1599.

[55] Meng XL, Cai W, Fu YD, Li QF, Zhang JX, Zhao LC. Intermet 2008;16:698.

[56] Karaca HE, Saghaian SM, Ded G, Tobe H, Basaran B, Maier HJ, Noebe RD, Chumlyakov YI. Acta Mater 2013;61:7422.

[57] Bigelow GS, Garg A, Padula II SA, Gaydosh DJ, Noebe RD. Scripta Mater 2011;64:725.

[58] Benafan O, Noebe RD, Padula SA, Vaidyanathan R. Metall Mater Trans A 2012;43:4539.

[59] Coughlin DR, Phillips PJ, Bigelow GS, Garg A, Noebe RD, Mills MJ. Scripta Mater 2012;67:112.

[60] Bhattacharya K, Kohn RV. Acta Mater 1996;44:529.

[61] Nishiyama Z. Martensitic transformations. Academic Press, New York; 1978.

[62] Kaufman L. Prog Met Phys 1958;7:165.

[62] Cheng YT, Grummon DS. Indentation in shape memory alloys. In: Yang F and Li JCM, editors. Micro and nano mechanical testing of materials and devices. Springer: New York; 2008.

[63] Cahn RW. Acta Metall 1953;1:49.

[64] Christian JW, Mahajan S. Prog Mater Sci 1995;39:1.

[65] Wechsler MS, Lieberman DS, Read TA. Trans AIME 1953;197:1503.

[66] Mackenzie JK, Bowles JS. Acta Metall 1957;5:137.

[67] Sehitoglu H, Karaman I, Anderson R, Zhang X, Gall K, Maier HJ, Chumlyakov Y. Acta Mater 2000;48:3311.

[68] Saburi T, Nenno S. Shape memory effect and related phenomena. In: Aaronson HI, Laughlin DE, Sekerka RF, Wayman CMl, editors. Proc Int Conf on Solid–Solid Phase Transformations, The Metallurgical Society of AIME. Warrendale, PA; 1982,p.1455-1479.

[69] Otsuka K. Mater Sci Forum 1990;56:393.

[70] Saburi T, Wayman CM. Acta Metall 1979;27:979.

[71] Miyazaki S, Otsuka K, Wayman CM. Acta Metall 1989;37:1873.

[72] Ball JM, James RD. Arch Ration Mech Anal 1987;100:13.

[73] Madangopal K. Acta Mater 1997;45:5347.

[74] Perez-Landazabal JI, Recarte V, No ML, San Juan J. Intermet 2003;11:927.

[75] George EP, Liu CT, Horton JA, Sparks CJ, Kao M, Kunsmann H, King T, Mater Charact 1994;32:139.

[76] Yang JH,Wayman CM. Intermet 1994;2:111.

[77] Noebe R, Biles T, Padula SA. NiTi-based high-temperature shape-memory alloys: Properties, prospects, and potential applications. In: Soboyejo WQ, Srivatsan TS, editors. Advanced Structural Materials: Properties, Design Optimization, and Applications, CRC Press Inc, Bosa Roca, FL; 2007,p.145.

[78] Hwang CM, Wayman CM. Scripta Metall 1983;17:1345.

[79] Honma T, Matsumoto M, Shugo Y, Yamazaki I. Effects of addition of 3D transition elements on the phase transformation. In: ICOMAT-79: Proceedings of the International Conference on Martensitic Transformations, Cambridge, MA; 1979;259–264.

[80] Suzuki Y, Horikawa H, Liu CT, Kunsmann H, Ostuka K, Wuttig M. MRS Proceedings 1992;246:389.

[81] Yang JH, Simpson JW. J Phys IV 1995:C8:771.

[82] Eremenko VN, Semenova EL, Tretyachenko LA, Domtyrko ZG. Dopovidi Akademii Nauk Ukrainskoi RSR, Seriya A: Fiziko-Matematichni Ta Tekhnichni Nauki 1998;50:76.

[83] Abu Judom D, Thoma P, Kao M, Angst D. US patent no. 5114504, 1992.

[84] Pu Z, Tseng H, Wu K. Proc SPIE 1995;2441:171.

[85] Han S, Zou W, Jin S, Zhang Z, Yang D. Scripta Metall Mater 1995;32:1441.

[86] Meisner LL, Grishkov VN, Sivokha VP. The martensitic transformations and the shape memory effect in the $Ni_{50}Ti_{50-x}Zrx$ alloys. In: Youyi C, Hailing TU editors. Proc Int Symp on Shape Memory Materials, International Academic Publishers, Beijing; 1994,p.263-266.

[87] Mulder JH, Maas JH, Beyer J. Martensitic transformations and shape memory effects in Ti-Ni-Zr alloys. In: Wayman CM, Perkins J. editors. ICOMAT-92: Proceedings of the International Conference on Martensitic Transformations, Monterey Institute for Advanced Studies, Carmel, CA; 1993,p.869–874.

[88] Meisner L, Sivokha V. J Phys IV 1995;C8:765.

[89] Meng XL, Cai W, Fu YD, Zhang JX, Zhao LC. Acta Mater 2010;58:3751.

[90] Noebe R. NASA Glenn Research Center, unpublished research.

[91] Han XD, Wang R, Zhang Z, Yang DZ. Acta Mater 1998;46:273.

[92] Meng X, Zheng Y, Wang Z, Zhao L. Mater Lett 2000;45:128.

[93] Russell S, Sczerzenie F. Proc Mater Res Soc Symp 1995;360:455.

[94] Hsieh SF, Wu SK. Mater Charac 2000;45:143.

[95] Nam TH, Saburi T, Shimizu K. Mater Trans, 1990;31:959.

[96] Meng X, Tong Y, Lau K, Cai W, Zhou L, Zhao L. Mater Lett 2002;57:452.

[97] Meng X, Cai W, Lau K, Zhao L, Zhou L. Intermet 2005;13:197.

[98] Hsieh S, Chang W. J Mater Sci 2002;37:2851.

[99] Dalle F, Kolomytsev V, Ochin P, Portier R. Scripta Mater 2001;44:929.

[100] Kockar B, Karaman I, Kim J, Chumlyakov Y. Scripta Mater 2006;54:2203.

[101] Chumlyakov YI, Efimenko SP, Kireeva IV, Panchenko EY, Sehitoglu H, Gall K, Yahia LH. Dokl Phys 2001;46:849.

[102] Jiang F, Liu YN, Yang H, Li L, Zheng YF. Acta Mater 2009;57:4773.

[103] Sehitoglu H, Jun J, Zhang X, Karaman I, Chumlyakov Y, Maier HJ, Gall K. Acta Mater 2001;49:3609.

[104] Gall K, Yang N, Sehitoglu H, Chumlyakov YI. Int J Fracture 2001;109:189.

[105] Eggeler G, Hornbogen E, Yawny A, Heckmann A, Wagner M. Mat Sci Eng A 2004;378:24.

[106] Wagner MFX, Dey SR, Gugel H, Frenzel J, Somsen C, Eggeler G. Intermetallics 2010;18:1172.

[108] Bhattacharya K, Conti S, Zanzotto G, Zimmer J. Nature 2004;428:55.

[109] Ball JM, James RD. Phil Trans R Soc Lond A 1992;338:389.

[110] Zarnetta R, Takahashi R, Young ML, Savan A, Furuya Y, Thienhaus S, Maass B, Rahim M, Frenzel J, Brunken H, Chu YS, Srivastava V, James RD, Takeuchi I, Eggeler G, Ludwig A. Adv Funct Mater 2010;20:1917.

[111] Atli KC. PhD Thesis, College Station, Texas A&M University; 2011.

[112] Bhattacharya K. Microstructure of Martensite, Oxford University Press; 2003.

[113] Le Page Y, Saxe P. Phys Rev B 2002;65:104104.

[114] Yang F, Coughlin DR, Phillips PJ, Yang L, Devaraj A, Kovarik L. Noebe RD, Mills MJ. Acta Mater 2013;61:3335.

[115] Nishida M, Ohgi H, Itai I, Chiba A, Yamauchi K. Acta Metall Mater 1995;43:1219.

[116] Gupta SP, Johnson AA. Trans JIM 1973;14:292.

[117] Han XD, Zou WH, Wang R, Zhang Z, Yang DZ. Acta Mater 1996;44:3711.

[118] Zheng YF, Zhao LC, Ye HQ. Scripta Mater 1998;38:1249.

[119] Dalle F, Perrin E, Vermaut P, Masse M, Portier R. Acta Mater 2002;50:3557.

[120] Wei Q, Han XD, Zhang Z. Mater Lett 2006;60:3054.

[121] Nishida M, Wayman CM, Chiba A. Metallogr 1988;21:275.

[122] Mercier O, Melton KN, Gremaud G, Hagi J. J Appl Phys 1980;51:1833.

[123] Pons J, Cesari E. Acta Metall Mater 1993;41:2547.

[124] Cesari E, Pons J, Chandrasekaran M. Trans Mater Res Soc Jpn 1994;18B:903.

[125] Kireeva IV, Pons J, Picornell C, Chumlyakov YI, Cesari E, Kretinina IV. Intermet 2013;35:60.

[126] Moshref-Javadi M, Seyedein SH, Salehi T, Aboutalebi MR. Acta Mater 2013;61:2583.

[127] Shi H, Pourbabak S, Van Humbeeck J, Schryvers D. Scripta Mater 2012;67:939.

[128] Aaronson H, Lee Y, Russell KC. Diffusional nucleation and growth. In: Russell KC, Aaronson HI, editors. Precipitation processes in solids, Warrendale, PA: AIME;1978,p.31–86.

[129] Karaca HE, Acar E, Ded GS, Basaran B, Tobe H, Noebe RD, Bigelow G, Chumlyakov YI. Acta Mater 2013;61:5036.

[130] Kireeva IV, Picornell C, Pons J, Kretinina IV, Chumlyakov YI, Cesari E. Acta Mater 2014;68:127.

[131] Karaca HE, Kaya I, Tobe H, Basaran B, Nagasako M, Kainuma R, Chumlyakov Y. Mater Sci Eng A 2013;580:66.

[132] Pons J, Sade M, Lovey FC, Cesari E. Mater Trans JIM 1993;34:888.

[133] Lovey FC, Torra V, Isalgue´ A, Roqueta D, Sade M. Acta Metall Mater 1994;42:453.

[134] Sehitoglu H, Zhang XY, Kotil T, Canadinc D, Chumlyakov Y, Maier HJ. Metall Mater Trans A 2002;33:3661.

[135] Kudoh Y, Tokonami M, Miyazaki S, Otsuka K. Acta Metall 1985;33:2049.

[136] Baxevanis T, Cox A, Lagoudas DC. Acta Mech 2014;225:1167.

APPENDIX

FIGURES

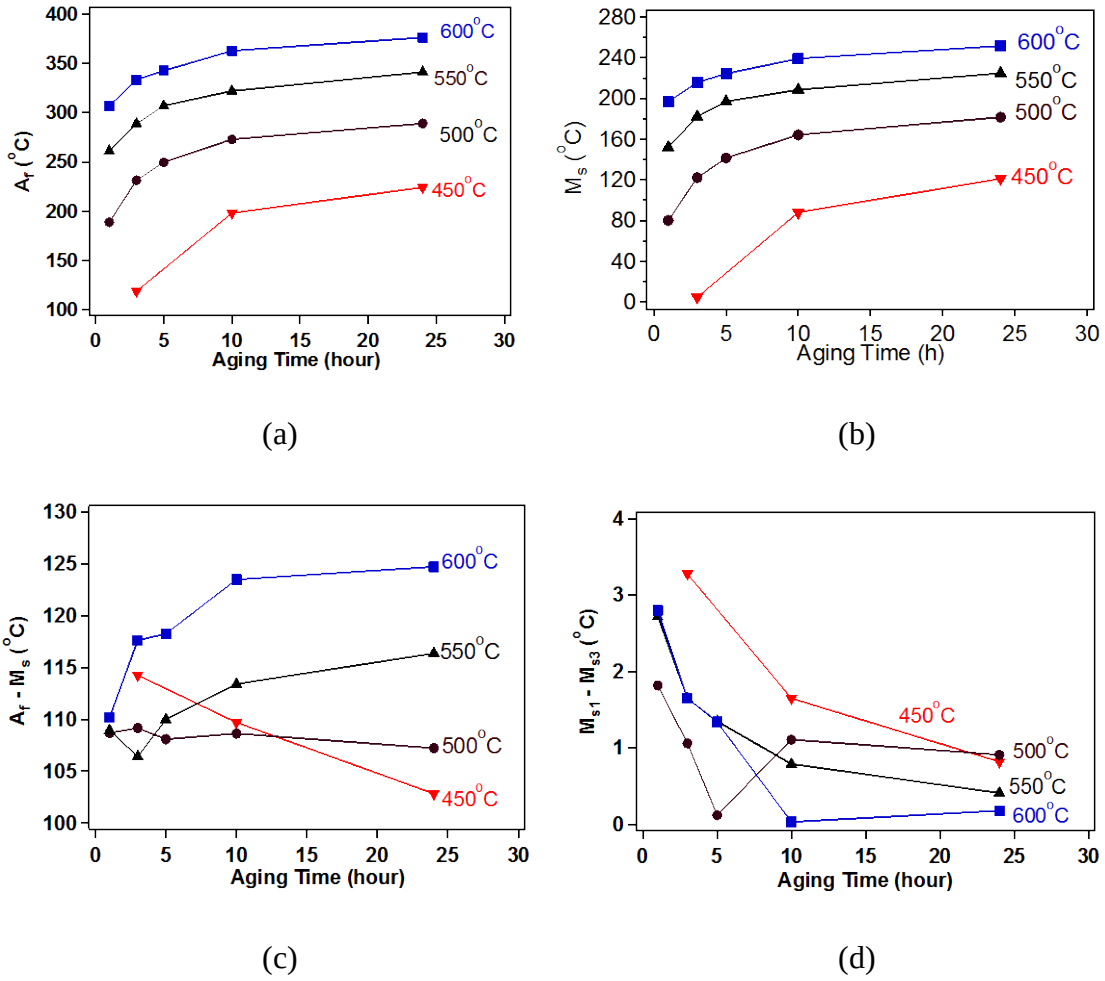

Figure A.1: The summary of the (a) the A_f temperatures, (b) M_s temperatures, (c) thermal hysteresis (A_f – M_s) and (d) thermal stability (M_{s1} - M_{s3}) of $Ni_{50.1}Ti_{24.9}Hf_{25}$ samples aged under various conditions.

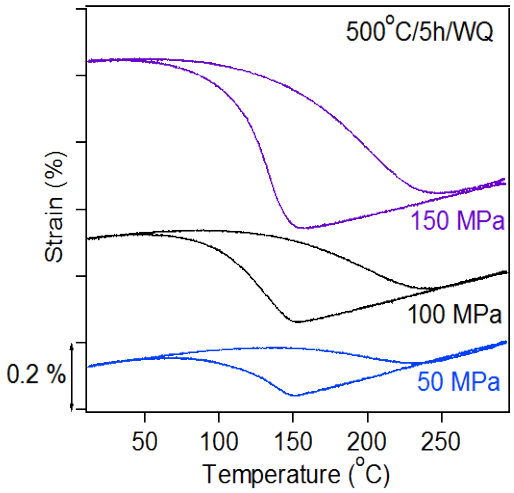

Figure A.2: The strain-temperature response of the $Ni_{50.1}Ti_{24.9}Hf_{25}$ samples aged at 500 °C for 5 h.